PURVIKA KULKARNI

ISOTOPE HYDROLOGY

A PRACTICAL APPROACH

Isotope Hydrology: A Practical Approach

Isotope Hydrology: A Practical Approach

Purvika Kulkarni

Table of Contents

Moisture Sources for Precipitation and Hydrograph Components of the Sutri Dhaka Glacier Basin, Western Himalayas

Ajit T. Singh *, Waliur Rahaman, Parmanand Sharma, C. M. Laluraj, Lavkush K. Patel, Bhanu Pratap, Vinay Kumar Gaddam and Meloth Thamban

ESSO-National Centre for Polar and Ocean Research, Headland Sada, Vasco-da-Gama, Goa 403804, India; waliur@ncaor.gov.in (W.R.); pnsharma@ncaor.gov.in (P.S.); lalucm@ncaor.gov.in (C.M.L.); lavkushpatel@ncaor.gov.in (L.K.P.); bhanu@ncaor.gov.in (B.P.); gaddam_vinay@ymail.com (V.K.G.); meloth@ncaor.gov.in (M.T.)

* Correspondence: ajit.t.singh@gmail.com

Abstract: Himalayan glaciers are the major source of fresh water supply to the Himalayan Rivers, which support the livelihoods of more than a billion people living in the downstream region. However, in the face of recent climate change, these glaciers might be vulnerable, and thereby become a serious threat to the future fresh water reserve. Therefore, special attention is required in terms of understanding moisture sources for precipitation over the Himalayan glaciers and the hydrograph components of streams and rivers flowing from the glacierized region. We have carried out a systematic study in one of the benchmark glaciers, "Sutri Dhaka" of the Chandra Basin, in the western Himalayas, to understand its hydrograph components, based on stable water isotopes (δ^{18}O and δ^2H) and field-based ablation measurements. Further, to decipher moisture sources for precipitation and its variability in the study region, we have studied stable water isotopes in precipitation samples (rain and snow), and performed a back-trajectory analysis of the air parcel that brings moisture to this region. Our results show that the moisture source for precipitation over the study region is mainly derived from the Mediterranean regions (>70%) by Western Disturbances (WDs) during winter (October–May) and a minor contribution (<20%) from the Indian Summer Monsoon (ISM) during summer season (June–September). A three-component hydrograph separation based on δ^{18}O and d-excess provides estimates of ice (65 ± 14%), snowpack (15 ± 9%) and fresh snow (20 ± 5%) contributions, respectively. Our field-based specific ablation measurements show that ice and snow melt contributions are 80 ± 16% and 20 ± 4%, respectively. The differences in hydrograph component estimates are apparently due to an unaccounted snow contribution 'missing component' from the valley slopes in field-based ablation measurements, whereas the isotope-based hydrograph separation method accounts for all the components, and provides a basin integrated estimate. Therefore, we suggest that for similar types of basins where contributions of rainfall and groundwater are minimal, and glaciers are often inaccessible for frequent field measurements/observations, the stable isotope-based method could significantly add to our ability to decipher moisture sources and estimate hydrograph components.

Keywords: Sutri Dhaka; Chandra Basin; Western Himalaya; hydrograph separation; stable water isotope; specific ablation

1. Introduction

The Himalayan-Karakorum mountain range has the largest concentration of glaciers outside the polar regions, out of which ~9600 glaciers lie in the Indian Himalayas, covering an area of

~40,000 km^2 [1]. These glaciers are the perennial source of runoff to major river systems, such as the Ganga, Brahmaputra and the Indus. These perennial rivers support more than a billion people living in the downstream region for their livelihood e.g., drinking, irrigation, industrial and sanitation [2–5]. Among all the major Himalayan river basins, the Indus Basin has the largest (~22,000 km^2) glacier extent [3]. The Ganga and the Brahmaputra River are primarily fed by monsoonal rain, whereas the Indus River receives the highest amount of water from snow and glacier melts [3,6]; the total glacier melt contribution to the Ganga, Brahmaputra and the Indus River estimated using snowmelt runoff model (SRM) are ~10%, ~12% and ~40%, respectively [3]. Previous studies have suggested that ~70% of Himalayan glaciers are receding at a faster rate, which has resulted in net loss of glacier volume [2,7,8]. As the Indus Basin receives its maximum runoff generated from the snow/ice-melt, it may face the most adverse effect of rising global temperatures [9], resulting in the initial rise in discharge, followed by the scarcity of freshwater supply leading to socio-economic instability in the downstream region [2,3]. Thus, considering a large number of Himalayan glaciers and their complex behavior and dynamics, it is imperative to have more studies and observations to improve our current knowledge and to address the pertinent questions related to moisture sources (rainfall/snowfall), snow/ice-melt contribution and their spatio-temporal variability.

Stable water isotope ratios of oxygen (δ^{18}O) and hydrogen (δ^2H), along with second order parameter, deuterium excess $\left(d - \text{excess} = \delta^2 H - 8\delta^{18}O\right)$, have been widely used to trace moisture sources for precipitation, identify mixing water from various sources and to quantify their relative contributions [10,11]. Several isotope-based studies have been conducted in the Himalayan and polar regions to trace moisture sources and estimate the hydrograph components [12–23]. Moisture sources for precipitation over the central and eastern Himalayas are primarily derived from the Indian Summer Monsoon (ISM) during June-September, while moisture sources to the western Himalayas are predominantly derived from the Mediterranean region due to Western Disturbances (WDs) during winter (October-May) [6,24]. A previous study based on stable water isotopes shows that the WDs contribute the maximum (>70%) to the total annual precipitation in the Kashmir valley (western Himalayas), which is more than the Indian Summer Monsoon (ISM) (<30%) [15]. In contrast, a study in the Parbati Basin, western Himalayas, shows that WDs contribute a maximum up to 30% to the annual precipitation [17]. These reports clearly indicate large spatial variability in annual precipitation over the western Himalayas, particularly during the WDs.

Several studies have been conducted to estimate the contribution of snow and glacier melts in the Himalayan regions. A model-based water balance approach shows that the snow and glacier melt contribution to the Beas River at Pandoh Dam, western Himalayas, contributes ~35% to the annual flow [25]. On the contrary, another study based on a stable isotopes study suggests that the snow/glacier melt contribution to the Beas River, Western Himalaya, is up to ~50% [12]. A similar study in the Parbati River, a major tributary of the Beas River, has reported that glacier melt contributes up to ~44% (±15%) [17]. A model-based water balance approach for other Himalayan rivers like the Sutlej, Ganga and the Chenab, estimates the annual snow and glacier melt contributions up to ~60% (at Bhakra Dam), ~28% (at Devpryag), and ~49% (at Akhnoor), respectively [26,27]. Another isotope-based study reported up to ~32% contribution of snow and glacier melts to the Ganga River [28]. Such diverging results of glacier melt contributions for the Himalayan rivers could be due to the differences in the methods employed, sampling strategies, such as sampling frequency and locations (distance from glacier), uncertainty in constraining the glacier and snow melts end members, differences in defining terminologies such as glacier, snow and ice-melts, and local influences due to the diverse topography and variable climate regimes. Further, underlying assumptions involved in various methods have not been tested in these basins, and this therefore has resulted in large uncertainty and differences in the estimates [29,30].

It should be noted that the relative contribution of snow and ice-melts can be better constrained at the head-ward region of the glaciated catchment, since the contribution of precipitation and subsurface water increases substantially in the downstream region. A recent isotope-based study near the

snout of the Gangotri Glacier (Upper Ganga Basin) have reported snow, glacier melts and direct runoff contributions of about 59.6, 36.8 and 3.6%, respectively [31]. Another study based on stable water isotope ($\delta^{18}O$) and Electrical Conductivity (EC) has estimated contributions of supraglacial melt (~65%) and subglacial melt (~35%) from the Chhota Shigri Glacier [32]. Furthermore, few attempts have been made to validate the isotope-based precipitation source and hydrograph separation of snow/ice-melts. Therefore, to provide a baseline data for understanding moisture sources for precipitation, and to estimate the hydrograph components (snow and ice-melts) of stream flow during the peak ablation period, we have carried out a systematic study of a benchmark glacier (Sutri Dhaka) in the Chandra Basin, western Himalayas. We have employed two independent methods for the hydrograph component estimates, i.e. the stable water isotope method and field-based specific accumulation/ablation measurements. Similarly, we have also deciphered moisture sources for precipitation over the study region using stable water isotopes, which is further corroborated with the back-trajectory analysis of air parcels.

2. Study Area

The Sutri Dhaka Glacier catchment (32°22′49″ N and 77°33′05″ E) falls in the Chandra basin of the Western Himalayan region (Figure 1) [33,34]. This glacier is a clean type glacier (C-type) with less than 5% of total debris cover [34,35]. The total watershed area of the Sutri Dhaka Glacier is ~42 km^2, of which the glacier occupies an area of ~20 km^2, covering approximately 50% of the total watershed. The glacier elevation ranges from ~4500 m a.s.l. near the snout to an elevation of ~6000 m a.s.l at the bergschrund, with a mean length of about 11 km (Figure 1) [34,35]. A meltwater stream flows from the snout of the Sutri Dhaka Glacier in a south-east direction for ~3 km downstream and confluences with the Chandra River in the downstream region. A recent study based on remote sensing has reported that the Sutri Dhaka Glacier has shown a retreating trend from 1962 to 2013, with an annual retreat rate of 11.4 ± 0.7 m a^{-1} [35].

The climate in this region is dominated by long winters (November–March), followed by spring which lasts until the end of May [24]. The summer season starts at the end of May and lasts until the end of September, while October and early November mark a short autumn period [24]. The predominant precipitation occurs during winters (>70%) compared to summer months (<30%) [36]. The elevated Pir-Panjal range acts as an orographic barrier for the monsoonal clouds to reach the upper region of the Chandra Basin, resulting in limited rainfall during summer. However, few summer precipitation events occur in the form of drizzle. The aridity in the region is also shown by the lack of vegetation [36,37]. Since the study region comes under the rain shadow zone with high altitudinal variations due to steep topography, the local aquifer at higher altitude does not get recharged sufficiently to act as a potential groundwater reservoir for discharge at later stages [37]. A recent study by the Central Ground Water Board (CGWB) in the region has reported that the groundwater yield in the upstream regions of the Chandra Basin is less than 5 liters per second, which is meager compared to the total amount of discharge generated by the snow and ice-melts in the region [37]. Therefore, a major source of freshwater to the downstream settlement is mainly supplied by combined contribution of snow and ice-melts runoff. Thus, considering uniqueness of the study area in terms of the limited contribution of summer precipitation and groundwater contribution to the total discharge, the estimation of hydrograph components involves less complexity.
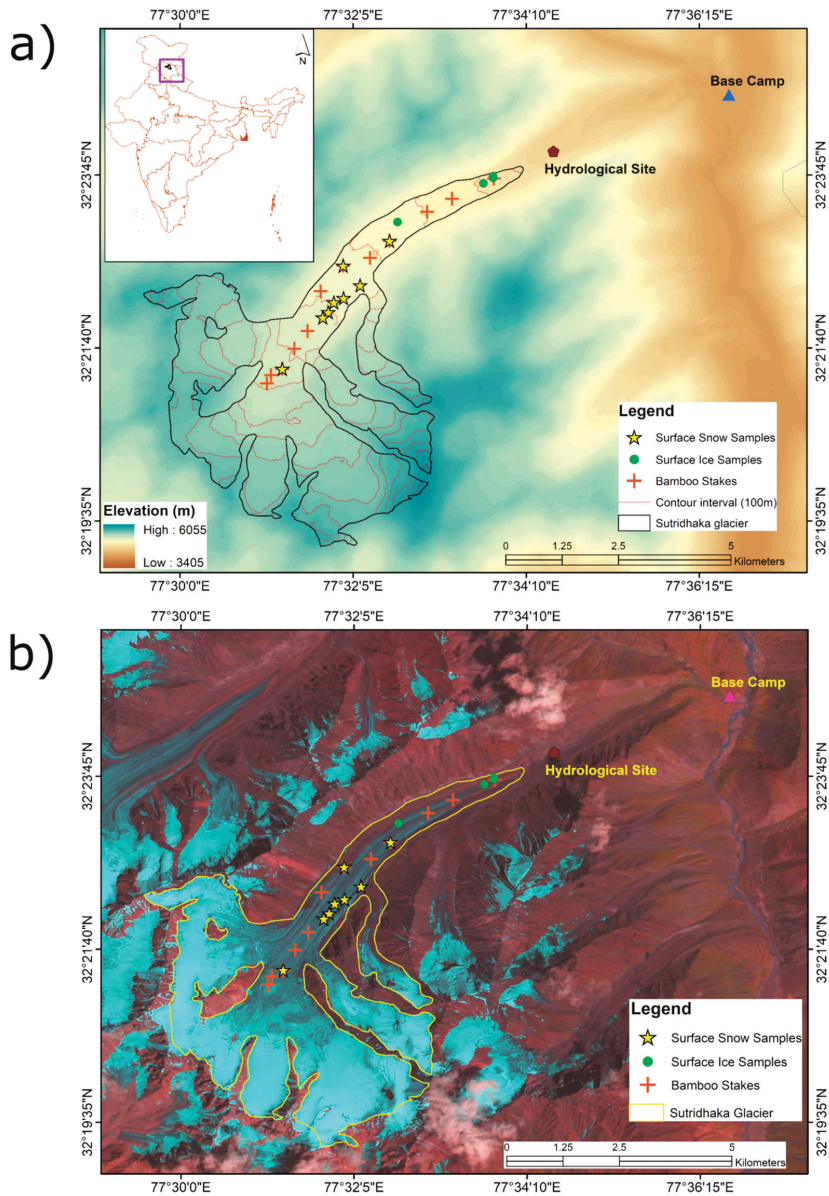
Figure 1. (**a**) Study area with Digital Elevation Model (DEM) derived from ASTER GDEM V2 along with sampling points; (**b**) Landsat 8 OLI image showing snow (light colored) and ice cover (dark colored) on the Sutri Dhaka glacier along with drainage (Image acquired on 20 August 2015).

3. Materials and Methods

An extensive field campaign was conducted in the Sutri Dhaka Glacier during summer–autumn (July–October) of the year 2015. Spatio-temporal samples of glacier snowpack, glacier ice, fresh snow, rainwater and stream (a combination of snow and ice-melts from the glacier) were collected systematically during the field campaign (Table 1 and Figure 1).

An overview of the sample collection and in-situ field measurements of the glaciological and hydrological parameters on the Sutri Dhaka Glacier are shown in Figure 2, Table 1. The main tongue of the Sutri Dhaka Glacier is shown in Figure 2a. To measure the discharge of the Sutri Dhaka stream, a hydrological station was established nearly 200 m downstream of the present glacier snout (Figure 2b). Meltwater samples (n = 133) from the Sutri Dhaka stream were collected twice in a day at 10:00 hrs and 17:00 hrs (Figure 2c). Further, snowpack samples (n = 8) were collected from the glacier surface at various locations and certain intervals (Figure 2d), whereas fresh snowfall samples (n = 15) were collected from the base camp and discharge site (near snout) during a major snowfall event (20–24 September 2015). Glacial surface ice samples (n = 9) were strategically collected at an elevation ranging from 4550 m a.s.l to 4750 m a.s.l from the debris-covered as well as the debris-free part of the Sutri Dhaka Glacier. Precipitation samples were collected near the hydrological station (Figure 1b). However, we missed collecting samples of few rain events due to a lack of adequate logistic support. Therefore, for the present study, we have also used isotopic data of precipitation published during the same season (June to October 2015) for the Chhota Shigri Glacier, upper Chandra Basin [32]. Considering the proximity of these two glaciers, i.e., Chhota Shigri and Sutri Dhaka Glaciers, with a distance less than 15 km, we expect similar hydro-meteorological conditions. Additionally, we conducted sampling at a similar altitude for the present study; therefore, we assume minimum changes in the isotopic characteristics of precipitation in the Sutri Dhaka and the Chhota Shigri catchments. To avoid any evaporation and atmospheric exchange with collected samples, they were filled in 20 mL scintillation vials without any headspace and air bubbles, and sealed immediately.

Table 1. Detailed description of end member components and stream (mixed component) sampling at the Sutri Dhaka Glacier.

Sr. No	Sample Type	Sampling Time	No. of Samples (n)
1	Glacier snowpack	1 July 2015	5
		17 October 2015	3
2	Fresh Snow	21–24 September 2015	15
3	Glacier Ice	1 July 2015	9
4	Sutri Dhaka Stream	7 July 2015 to 9 October 2015	133
5	Rainwater at Sutri Dhaka	7 July 2015 to 9 October 2015	9

Discharge of the Sutri Dhaka stream was measured using the area-velocity method [38]. Wooden floats and Flow tracker (Son Tek Flowtracker, Son Tek, San Diego, CA, US) were used to determine the velocity of the stream. Excessive velocities, depth, boulder movement in the bed of stream and the floating drift of the instrument prohibited us from using the SonTek flow tracker during high flow. Therefore, our SonTek flow tracker measurements were only conducted during low flow conditions which showed a similar velocity reading to the float-based velocity measurement with an accuracy better than ± 10%. Depth profiles were measured using a metal gauge. To estimate daily discharge, daily gauge measurements were conducted at 10:00 Hrs (low flow) and 17:00 Hrs (high flow), and a level versus discharge relationship was established. The mean of high and low flow was considered as a daily mean discharge [33]. Since the bed topography of high mountainous streams are unstable, and the surface velocity of the stream is higher than bed velocity, the obtained discharge value was multiplied with a factor of 0.84 to estimate the discharge [38]. The meteorological parameters, i.e., temperature and relative humidity (RH%) were measured continuously using a temperature sensor (RHT-20, Extech, Waltham, MA, US) installed at the Sutri Dhaka Glacier (~5000 m a.s.l). Due to a technical problem with our rain gauge instrument installed at our study site, we could not measure precipitation during the field campaign.

Therefore, we have used precipitation data measured at the base camp of an adjacent glacier; the Chhota Shigri Glacier, located ~15 km away from the study region using an Automatic Weather Station (AWS) with accuracy better than 1%.

Figure 2. Fieldwork on the Sutri Dhaka Glacier and catchment: (**a**) Downstream synoptic view of the Sutri Dhaka Glacier showing the accumulation and ablation zone; (**b**) hydrological observation site; (**c**) meltwater sampling; (**d**) snowpack sampling; (**e**) stakes coordination and measurements; (**f**) snow pit excavation and density measurements.

All collected snow, ice, rain and meltwater samples were analyzed for ^{2}H/^{1}H, and ^{18}O/^{16}O ratio using OA-ICOS laser absorption spectroscopy (LGR, Triple Isotope Water Analyzer (TIWA-45EP), Los Gatos Research (LGR) Process Automation, Mountain View, CA, USA) at the National Centre for Polar and Ocean Research, Goa, India. The Analyzer uses LGR's Off-axis ICOS technology, a fourth-generation cavity ring down spectroscopy (CRDS) technique [39], which employs an optical cavity to greatly enhance spectral absorption and enable us to achieve the fastest and highest precision measurements of δ^{18}O and δ^2H. The isotopic ratios are reported in the standard δ-notation with relative to VSMOW-SLAP [40] and expressed as

$$\delta(\permil) = \frac{\left(R_{sample} - R_{standard}\right)}{R_{standard}} \times 1000 \qquad (1)$$

where R represents either the ^{18}O/^{16}O or ^{2}H/^{1}H ratio. The overall accuracy of δ^2H and δ^{18}O measurements are better than ± 0.18‰ and ± 0.07‰, respectively, based on the known value of a laboratory standard with respect to V-SMOW-SLAP with six injections per samples. To understand the source of the precipitation in the study region and a better identification of end-member for hydrograph separation, d-excess $(d - excess = \delta^2H - 8\delta^{18}O)$ was calculated for all samples using δ^2H and δ^{18}O [41]. The relationship between δ^2H and δ^{18}O in precipitation was defined using the least square regression method [10].

Meltwater of the Sutri Dhaka stream is predominantly sourced from two components (snow and ice-melts) and therefore a simple two component hydrograph separation using single tracer (δ^{18}O) can be used to determine the snow and ice-melt contributions to the meltwater stream [42].

However, it was difficult to constrain the end member value of $\delta^{18}O_{snow}$ as a single component because they undergo several stages of post-depositional processes such as evaporation, sublimation

and repetitive melting-freezing cycles, which could cause large isotope fractionation. In earlier studies, based on modeling and field evidences, it was suggested that $\delta^{18}O$ values in a snowpack could be heavier up to 3 to 5‰ than the fresh snow due to preferential removal of lighter isotopes in melts resulting in large uncertainty in hydrograph separation [42,43]. Therefore, in the present study, fresh snow (isotopically depleted) and snowpack (isotopically enriched) were considered as two separate components of snow, covering the entire spectrum of snow contribution, and a three-component hydrograph separation was performed to estimate the contribution of fresh snow, snowpack and ice-melt to the Sutri Dhaka stream.

In the case of three-component hydrograph separations based on a geochemical and isotope mass balance approach, at least two tracers are required. Using $\delta^{18}O$ along with electrical conductivity (EC), silica (SiO_2) and chloride (Cl^-) are among the most common tracers, and are widely used for three-component hydrograph separation (Klauss and McDonnell, 2013). However, they have limitations in separating snow and ice-melt contributions to glacier stream since the EC, SiO_2 and other dissolved solutes may get enriched due to water-rock interaction. In order to circumvent this problem, several studies have suggested that $\delta^{18}O$ and d-excess can be successfully used to trace the contribution of hydrological components [44,45].

Thus, we have used $\delta^{18}O$ and d-excess as tracers in constraining the end members for a three-component hydrograph separation of the Sutri Dhaka stream. Since the contribution of rainwater to total discharge is insignificant, we have not considered it as a major hydrograph component in our calculations [32,36,37,46]. The equation for three-component hydrograph separation can be written as follows [44].

$$Q_{St} = Q_i + Q_o + Q_n \tag{2}$$

where Q_i, Q_o and Q_n are the contribution of ice-melts, old snow (snowpack), fresh snow to the Sutri Dhaka stream discharge (Q_{st}).

$$1 = f_i + f_o + f_n \tag{3}$$

$$\delta_{st} = \delta_i \cdot f_i + \delta_o \cdot f_o + \delta_n \cdot f_n \tag{4}$$

δ_{st}, δ_i, δ_o and δ_n and are $\delta^{18}O$ for the stream, ice, snowpack and fresh snow respectively.

$$d_s = d_i \cdot f_i + d_o \cdot f_o + d_n \cdot f_n \tag{5}$$

d_{st}, d_i, d_o and d_n are d-excess tracer for the stream, ice, snowpack and fresh snow respectively.

$$Q_i(\%) = \frac{(d_{st} - d_n)(\delta_o - \delta_n) - (d_o - d_n)\,(\delta_{st} - \delta_n)}{(d_i - d_n)(\delta_o - \delta_n) - (d_o - d_n)(\delta_i - \delta_n)} \times 100 \tag{6}$$

$$Q_o(\%) = \frac{(d_{st} - d_n)}{(d_o - d_n)} \times 100 - \frac{(d_i - d_n)}{(d_o - d_n)} \times Q_i \tag{7}$$

$$Q_n\ (\%) = 100 - Q_i - Q_o \tag{8}$$

The ice-melt, snowpack and fresh snow contributions to the total discharge were calculated using Equations (6)–(8) respectively.

The total snow and ice-melt contributions were also estimated using a field-based ablation measurement of total snow and ice during the study period. In order to measure snow and ice ablation of the Sutri Dhaka Glacier, a network of 12–15 ablation stakes of ~6–10 m deep was installed along the center line of glacier surface at different altitudes, following the standard protocols published elsewhere [35,47]. To measure net ablation during the subsequent ablation period (July–October 2015), stakes were installed at the end of the ablation season i.e., September 2014. The lengths of the exposed stakes were measured on a monthly basis from 5 July to 5 October 2015 for the summer ablation measurements (Figure 2e). Net ablation was estimated based on the ice cover loss at each point multiplied with the density of ice. Ice density was measured at nine different locations in the ablation

zone. The average density of 870 ± 10 kg m^{-3} based on nine measurements at different locations was used in ice ablation estimates in terms of water equivalent. For the snowmelt contribution, we have measured winter snow accumulation (4 July 2015) and annual/residual snow accumulation (September–October 2015) by excavating four snow pits followed by density measurements at different altitudes of the glacier surface (Figure 2f). The measured thickness was linearly extrapolated to the higher reaches (5350–6050 m a.s.l.) to accommodate the total snow accumulation in the glacierized zone. Total snowmelt during the study period (July to October 2015) was then calculated by subtracting winter accumulation from residual accumulation. A simple transient snow line (TSL)-snow pit method was also used to measure snow ablation. The snow line was measured before the study was conducted (27 June 2015), and at the maximum snowline elevation (30 August 2015), using Landsat 8 OLI satellite imagery [48]. Since the mean accumulated snow was known from snow pit estimates, the total snow cover area ablation estimated using the TSL method was multiplied with respective snow pit volume (m w.e.) and the total snow volume ablation for the study period were estimated [48]. Due to inaccessibility to the site for sampling during the spring season, our study was limited to the peak summer period (July–October 2015), when maximum melting occurs.

Further, to understand moisture sources for precipitation over the study region throughout the year, we performed monthly back trajectory analysis of air parcels reaching the sites using the NOAA HYSPLIT model together with a reanalysis model output from the Global Data Assimilation System (GDAS) dataset [49]. Four days back trajectory analysis was performed for all months of the year 2015. All trajectories were initialized at 1500 m above the surface because most of the water vapor in the atmosphere travel within 0–2 km above ground level [49]. Subsequently, trajectories obtained for each day for the respective months were clustered using Trajstat to obtain the mean monthly trajectories [50]. Similarly, four days back-trajectory analysis to capture major precipitation events was plotted using the Global Data Assimilation System (GDAS) dataset at different altitudes (100, 1500 and 2000 m AGL) and also using HYSPLIT online simulation developed by Air Resources Laboratory, NOAA [51,52].

4. Results and Discussion

4.1. Hydro-Meteorological Characteristics of the Sutri Dhaka Stream

Meteorological parameters play a significant role in controlling the glacier melt dynamics [3]. Temporal variations in air temperature, relative humidity, precipitation and discharge of the Sutri Dhaka Glacier are shown in Figure 3 and data provided in supplementary excel sheet. The discharge of the Sutri Dhaka stream during the study period varied between 0.2 m^3 s^{-1} to 20 m^3 s^{-1} with a mean of 8.9 m^3 s^{-1} (Figure 3a). The discharge during the study period increased from early July with rising temperatures and reached its peak by the end of July. The daily mean temperature during the study period ranged from -15.3 to 16.1 °C with a mean of 9.1 °C (Figure 3b). Similarly, daily mean RH varied from 34.8% to 99.9% with a mean of 59.8% (Figure 3c). The highest daily mean discharge (20 m^3 s^{-1}) and temperature (16.2 °C) were observed on 15 July 2015. A gradual declining trend in temperature and discharge were observed in the months of August, September and October. A significant correlation ($R^2 = 0.83$, n = 63; $p < 0.05$) was observed between the daily mean discharge and temperature (Figure 3), suggesting a dominant control of temperature on discharge. This relationship implies a ~9% increase in daily mean discharge per degree rise in daily mean air temperature. This finding confirms that as the temperature in the Himalayan region increases, it would lead to an initial rise in discharge due to an increase in glacier melt, followed by a drop in runoff and reduction in the glacierized area [53]. A total of ~110 mm of precipitation was recorded during the study period, of which two major precipitation events occurred on 12 July (20 mm) and on 23 September (52 mm) in the form of snow which account for ~66% of total precipitation during the study period (Figure 3d).
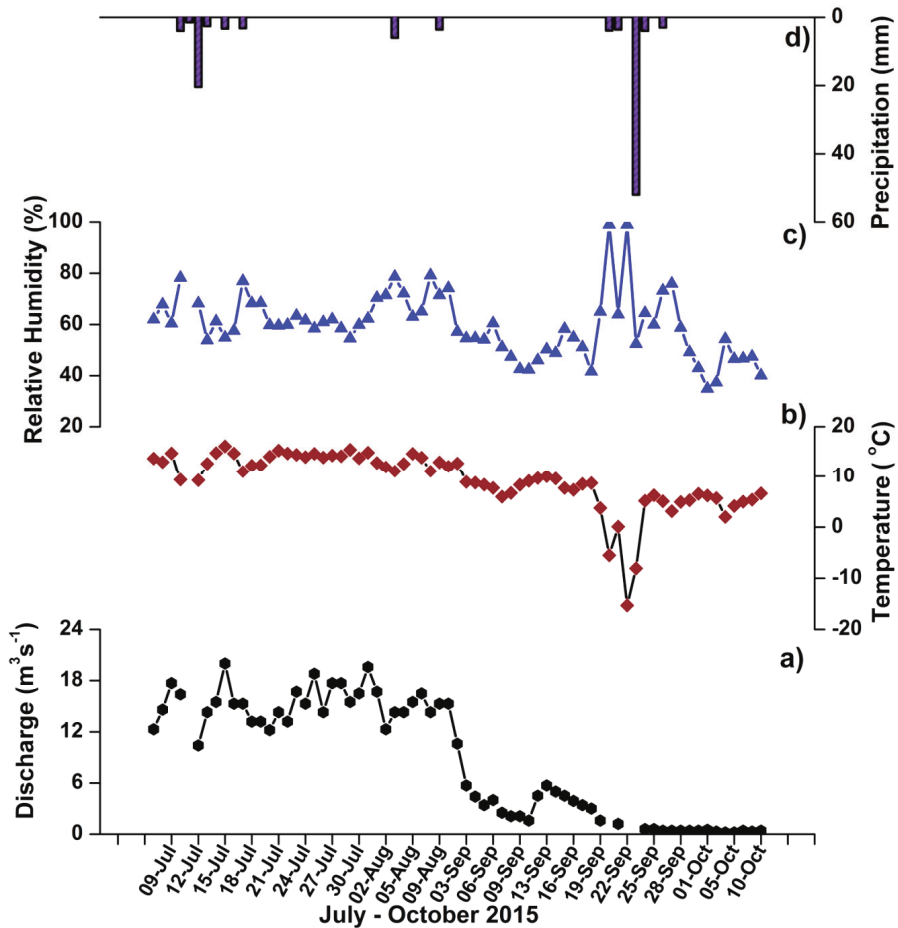
Figure 3. Daily distribution of the observed (**a**) Discharge; (**b**) Daily average temperature; (**c**) daily mean of Relative Humidity (RH%) (**d**) Daily mean precipitation measured during the study period.

4.2. Stable Isotope Characteristics and Its Relationship with Discharge

Details of samples and their isotopic characteristics are mentioned in Table 2 and data provided in supplementary excel sheet. $\delta^{18}O$ and $\delta^{2}H$ measured in rainwater samples varied from $-13.9‰$ to $-5.4‰$ and $-107.2‰$ to $-32.5‰$ with a mean of $-11.2‰$ and $-81.6‰$, respectively. Similarly, $\delta^{18}O$ in rainwater samples collected from the Chhota Shigri Glacier showed a median value of $-11.2‰$ [32]. The fresh snow samples collected at the base camp and hydrological station during the snowfall events, 20–24 September 2015, showed depleted $\delta^{18}O$ values compared to that of the snowpack. Enrichment of $\delta^{18}O$ in snowpack could be the result of isotopic fractionation between the melts and the snowpack. As isotopically-depleted snow starts melting, it leads to the removal of depleted meltwater that results in a heavier residual snowpack [30]. Glacier ice samples showed a narrower range compared to snow samples. $\delta^{18}O$ and $\delta^{2}H$ in ice samples ranged from $-15.7‰$ to $-11.7‰$ (mean $-13.6 \pm 1.2‰$) and $-106.3‰$ to $-73.2‰$ (mean $-91.2 \pm 10.4‰$) respectively. The $\delta^{18}O$ and $\delta^{2}H$ values in stream draining from the Sutri Dhaka Glacier varied from $-15.7‰$ to $-13.3‰$ (mean $-14.4 \pm 0.5‰$) and $-108.9‰$ to $-91.4‰$ (mean $-98.5 \pm 3.8‰$), respectively.

Table 2. δ^{18}O, δ^{2}H and d-excess values of rain, fresh snow, snowpack, glacier ice and meltwater of the Sutri Dhaka Glacier catchment.

Parameter	Rain (n = 9)		Fresh Snow (n = 15)		Snow Pack (n = 8)		Ice (n = 9)		Sutri Dhaka Stream (n = 133)	
	Mean	1 SD	Mean	1 SD	Mean	1 SD	Mean	1 SD	Mean	1 SD
δ^{18}O (‰)	−11.2	3.2	−20.3	0.2	−10.1	0.7	−13.6	1.25	−14.4	0.5
δ^{2}H (‰)	−81.6	26.5	−145.8	1.4	−67.7	5.5	−91.2	10.4	−98.5	3.9
d-excess (‰)	8.1	5.4	17.1	0.7	13.2	2.5	18	1.4	17.1	0.9

The mean d-excess values of snow, ice, meltwater and rainwater are provided in Table 2. The deuterium excess (d-excess) values for all samples range from 0.47‰ to 20.2‰ with a mean of 16.5 ± 2.7‰. Lower d-excess values were observed in rain events, whereas higher values were observed in snowfall events and the snowpack. A similar trend was also reported in precipitation events collected from the Chhota Shigri Glacier during the same period [32]. Glacier ice samples showed the highest d-excess values among all followed by the Sutri Dhaka stream. The higher d-excess (>12‰) of fresh snow, old snow, ice and Sutri Dhaka stream suggest Western Disturbance (WD) as their common moisture source, derived from the Mediterranean regions [19].

4.3. Local Meteoric Water Line (LMWL), d-Excess and Moisture Sources for Precipitation

In an earlier study, a Local Meteoric Water Line (LMWL) plotted based on precipitation samples collected from the Chhota Shigri shows a slope of 7.9 and an intercept of 21.4 [32] (Figure 4). This slope is similar to the Global Meteoric Water Line (GMWL) within their uncertainty (δ^{2}H = 8 $*$ δ^{18}O + 10), suggesting their marine origin, while a higher intercept indicates mixing of air moisture masses derived from different sources. The overall least square regression line or best fit line constructed based on precipitation event samples collected from the Sutri Dhaka Glacier shows that the slope (7.4 ± 0.4) is similar to the Chhota Shigri Glacier with lower intercept (2.0 ± 5.4) (Figure 4). The lower intercept of the Sutri Dhaka Glacier could be because of a smaller number of representative samples for the entire season. Few precipitation events at the Sutri Dhaka Glacier fall close to GMWL, suggesting a contribution of ISM and the effect of sub-cloud evaporation during the precipitation events (Figure 4).
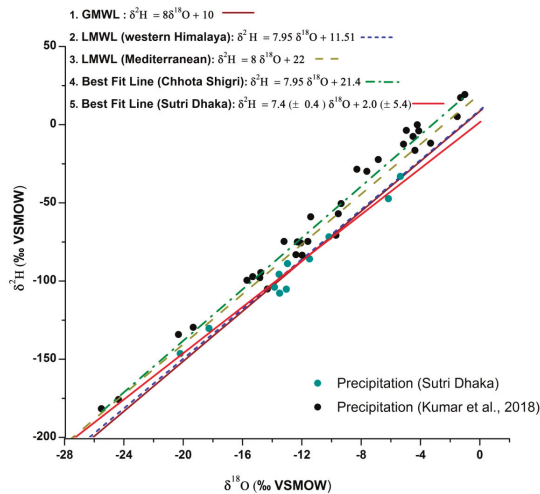

Figure 4. The regression lines in the cross plot (δ^{2}H vs. δ^{18}O) for precipitation samples from the Sutri Dhaka Glacier and Chhota Shigri Glacier are compared with Local Meteoric Water Line (LMWL) of the Western Himalaya, Mediterranean region and Global Meteoric Water Line (GMWL) (Kumar et al., 2018).

δ^2H vs. δ^{18}O plot for fresh snow, snowpack, glacier ice, rain is shown in Figure 5, and the slope and intercept of each regression line are also provided in Table 3. The ice samples collected from the Sutri Dhaka Glacier show a similar slope (8.1 ± 0.4) and intercept (20.3 ± 5.6) similar to the Chhota Shigri and the Mediterranean region. Lower slope (6.5 ± 1.2) and intercept (−1.2 ± 12.3) were reported for the snowpack, indicating the effect of non-equilibrium fractionation leading to isotopic enrichment of the snowpack due to a preferential removal of lighter isotopes in melts during sublimation processes [13,19]. Unlike snowpack, fresh snow samples showed slightly higher slope (7.3 ± 0.2) and intercept of (4.1 ± 5.1), while rainwater showed a slope of (7.7 ± 0.6) and intercept of (6.1 ± 7.1). The Sutri Dhaka stream showed a slope of (7.1 ± 0.2) with an intercept of (5 ± 2.7). The slopes of the regression lines of all components (snow, ice, rain, stream) are similar within their uncertainty, which confirms that they have common moisture sources [20]. However, the intercepts of all components are highly variable, suggesting the effect of secondary isotope fractionation processes during precipitation events and melting processes. The slopes and intercepts of LMWL in the Himalayan region varies significantly, indicating variable sources of precipitation and environmental conditions, such as temperature of condensation, local moisture recycling and amount of sub-cloud evaporation during precipitation (Table 3) [10,54–56].
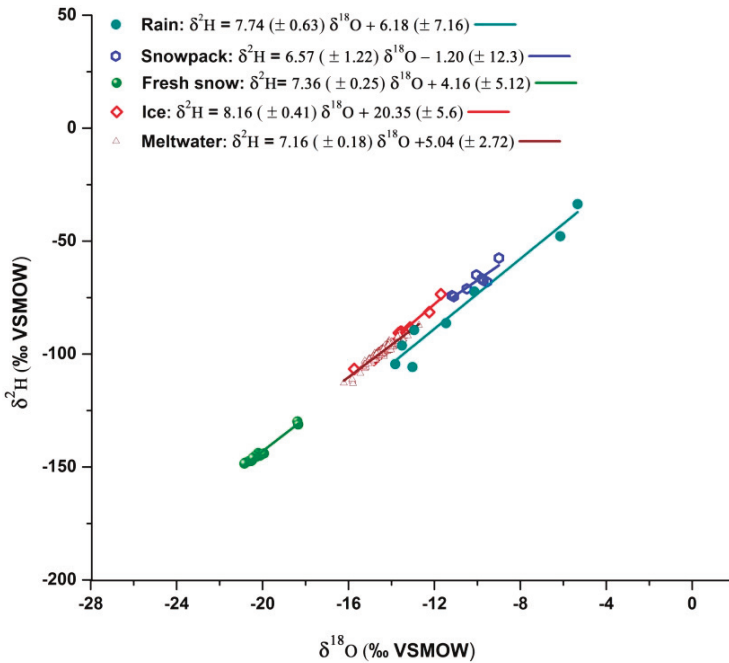

Figure 5. The stable isotope regression plot (δ^2H vs. δ^{18}O) for Rain, Fresh snow, Snowpack, Ice and daily Sutri Dhaka Glacier stream.

Table 3. Compilation of local meteoric water lines (LMWL) of various studies carried out in the Himalayan regions for Rain (R), Fresh Snow (SF), Snowpack/firn (SP), Glacier ice (GI) and meltwater stream or River (SR).

Glacier/Region	Latitude	Longitude	Altitude (m)	LMWL	R^2	n	Reference
Sutri Dhaka Glacier	32°22′49″ N	77°33′05″ E	4500–6200	$\delta^2H = 6.5\ (\pm1.2) * \delta^{18}O -1.2\ (\pm12.3)$ (SP)	0.99	8	Present Study
				$\delta^2H = 7.3\ (\pm0.2) *\delta^{18}O + 4.1\ (\pm5.1)$ (SF)	0.98	17	
				$\delta^2H = 8.1\ (\pm0.4) * \delta^{18}O + 20.3\ (\pm5.6)$ (GI)	0.97	11	
				$\delta^2H = 7.1\ (\pm0.2) * \delta^{18}O + 5.04\ (\pm2.7)$ (SR)	0.94	65	
				$\delta^2H = 7.7\ (\pm0.6) * \delta^{18}O + 6.18\ (\pm7.1)$ (R)	0.95	9	
Chota Shigri Glacier	32°16′48″ N	77°34′ 48″ E	4050–6263	$\delta^2H = 7.8 * \delta^{18}O + 25$ (SP)	0.99	10	[32]
				$\delta^2H = 6.3 * \delta^{18}O + 3.6$ (GI)	0.76	15	
				$\delta^2H = 7.9 * \delta^{18}O + 21.4$ (R)			
Chorabari Glacier	30°46′20.58″ N	79°02′59.381″ E	4400–6200	$\delta^2H = 8.1 * \delta^{18}O + 24.1$(SF)	0.9	45	[16]
				$\delta^2H = 7.7 * \delta^{18}O + 21.2$ (GI)	1	13	
				$\delta^2H = 6.51 * \delta^{18}O - 0.0$ (SR)	0.8	116	
				$\delta^2H = 7.98 * \delta^{18}O + 16.8$ (R)	0.98	35	
QS and Glacier no.12, T.P	39°26.4″ N	96°32.5″ E	4260–5481	$\delta^2H = 8.2* \delta^{18}O + 21.68$ (SP)	0.95		[57]
				$\delta^2H = 7.7 * \delta^{18}O + 15.7$ (GI)	0.83		
				$\delta^2H = 7.8 * \delta^{18}O + 16.8$ (R)	0.95		
Kashmir Drass and Ladakh Zanskar	32°50′–34°18′ N	74°45′–78°20′ E	3250–4345	$\delta^2H = 8.2 * \delta^{18}O + 23.8$ (SR)			[19]
				$\delta^2H = 6.6 * \delta^{18}O - 1$ (SR)			
				$\delta^2H = 9.5 * \delta^{18}O + 38.7$ (GI)			
Jammu and Kashmir	33°20′–34°15′ N	74°30′–75°35′ E	1592–3248	$\delta^2H = 7.6* \delta^{18}O + 11.8$ (R)			[13,14,58]
				$\delta^2H = 7.6 * \delta^{18}O + 15$ (SP)	0.95	39	
				$\delta^2H = 6.7 * \delta^{18}O + 8.1$ (SR)	0.87	155	
Nam Co Basin, T.P	30°39″ N	90°38″ E	4730	$\delta^2H = 8.3 * \delta^{18}O + 7.8$ (SP/GI)	0.98		[59]
				$\delta^2H = 7.6* \delta^{18}O - 2.30$ (SR)	0.99		

The $\delta^{18}O$ values of the precipitation samples collected during the major precipitation events which occurred on 12 July and 20–24 September 2015 show depleted values and higher d-excess (Figure 6a–c).

A significant reduction in discharge after the major precipitation events coincides with temperature drop (Figure 6a). As the fresh snow after major precipitation events melts it also results in depleted $\delta^{18}O$ in stream water with higher d-excess (Figure 6a–c).

Several studies have shown that the higher d-excess (>12‰) in precipitation was generally related to the precipitation sourced from the high evaporation and low humidity regions, such as the Mediterranean, Caspian and Black seas through the western disturbances [19,58]. Monthly back-trajectory analysis of air parcels also reveals that the moisture parcel is primarily derived from the Mediterranean Sea and the Persian Gulf during the winter months due to WDs. Similarly, the moisture sources during the summer months are supplied by WDs with a minor contribution by ISM (Figure 7a). Few studies have also been carried out to decipher moisture sources for precipitation over other parts of the Himalayan regions using d-excess and back trajectory analysis [12,15,16,20,28,59,60]. However, other studies in the lower region of the western Himalayas have reported a stronger influence of ISM with high spatio-temporal variability in the sources for precipitation over the western Himalayan region [12,17,28]. Our event-based back trajectory analysis of the major summer precipitation events shows that the air parcel comprises both ISM and WDs origins (Figure 7b). An extensive study conducted in the western Himalayas found that the precipitation derived from WDs shows a much higher d-excess value (mean 18.9‰) compared to that of ISM (mean 9.4‰) [58]. Considering the higher d-excess (>17‰) in our major precipitation event clearly indicates that they are mainly derived from the WDs. A two-component mixing model using ISM and WDs d-excess values as end members shows that more than 80% of the total precipitation is derived from WDs while the ISM contributes

more than 20%. Since the d-excess values remain constant during phase change at the time of the rainout events, we can confidently deduce that the precipitation source to the major precipitation event is predominantly derived from the WDs. Similarly, a study conducted at a similar duration of our study at the Chhota Shigri Glacier in the Chandra Basin, western Himalayas, also reported higher d-excess values during heavy summer precipitation events, attributing to WDs being the precipitation source [32].
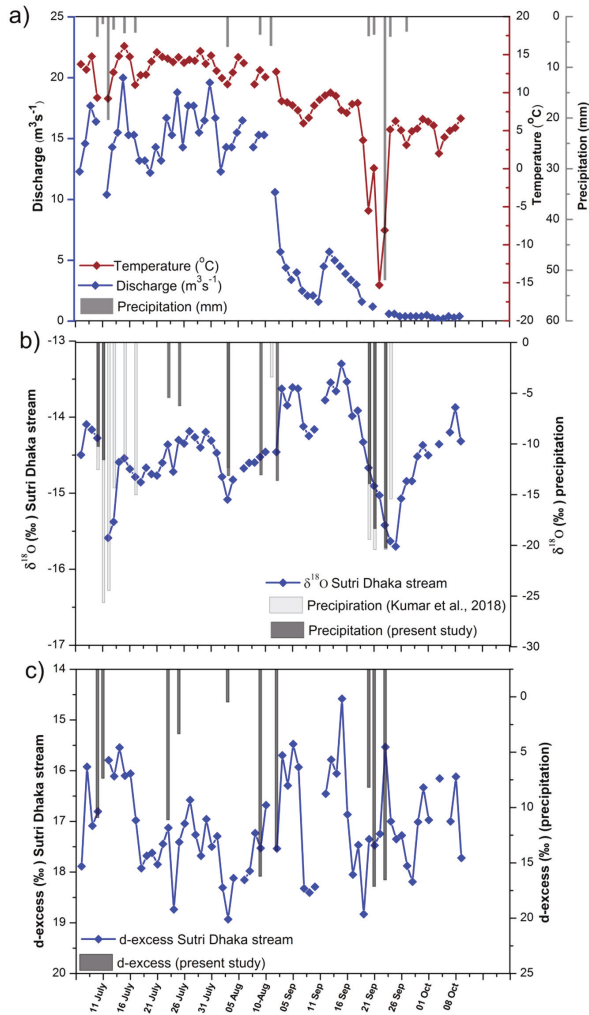
Figure 6. Time series of the measured parameters; (**a**) discharge and precipitation at the study region during the study period along with their associated (**b**) $\delta^{18}O$ ‰ and (**c**) d-excess of the stream water and precipitation at the Sutri Dhaka Glacier (present study), and the Chhota Shigri Glacier (Kumar et al., 2018) Upper Chandra Basin.

A positive correlation ($R^2 = 0.3$, n = 33; $p < 0.05$) was observed between discharge and $\delta^{18}O$ values of the stream water samples during July to mid-August, which was further improved during September and early October ($R^2 = 0.57$, n = 31; $p < 0.05$) (Figure 8). Variable correlations between discharge and $\delta^{18}O$ values suggest that the initial stream water was sourced from both snow as well as

ice-melt waters with variable contributions and as summer progressed, snow contribution got reduced with an increasing contribution from ice-melts to stream discharge. However, it is noteworthy to observe a significant declining trend in discharge and δ^{18}O values after intense precipitation events on 12 July 2015 and 20–24 September 2015 (Figure 8). A significant drop in temperature, glacier melt and discharge indicates that the precipitation on the glacier occurred in the form of snow. Therefore, a major supply of meltwater contributed to the downstream region was supplied by the melting of isotopically-depleted fresh snow, which resulted in depleted meltwater.
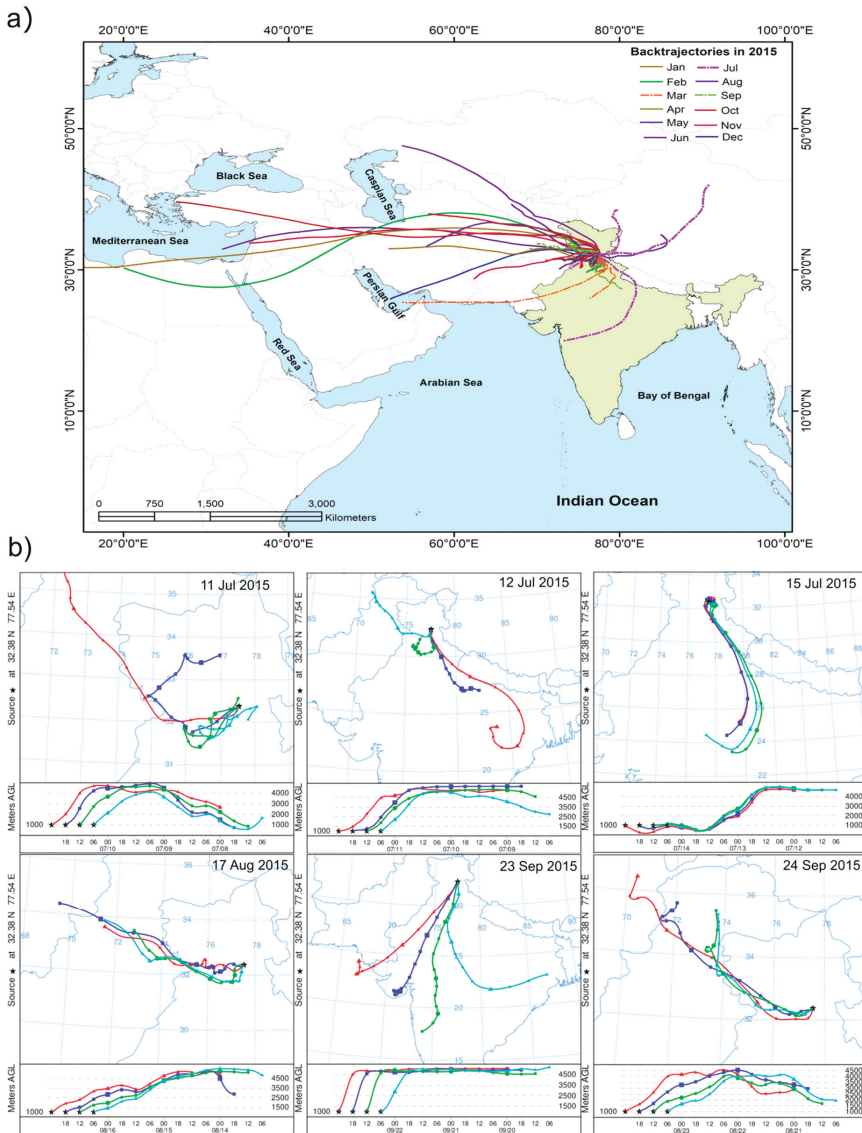
Figure 7. Back trajectory analysis at the study region (**a**) for entire year (January–December 2015) (**b**) for major precipitation events initiated at 1000, 1500 and 2000 m AGL for four days.
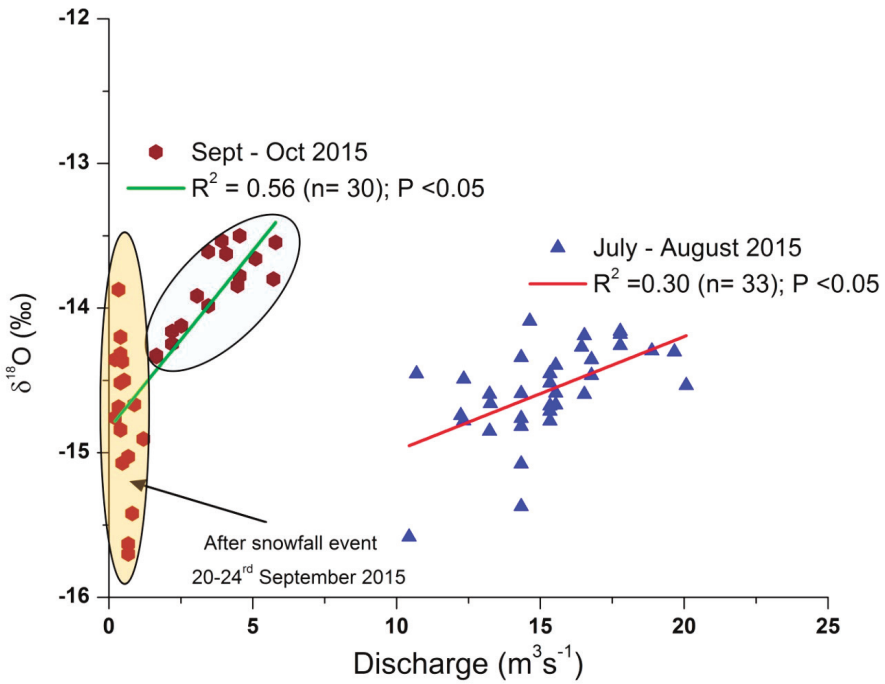
Figure 8. Relationships between $\delta^{18}O$ and stream discharge during the peak ablation period (July and August) and at the end of ablation season (September and October).

4.4. Snow and Ice-Melt Contribution to the Sutri Dhaka Stream

4.4.1. Hydrograph Separation

The hydrological process can be well understood using a mixing plot (d-excess vs. $\delta^{18}O$) [44,45]. Mixing plots in the present study clearly shows that the stable isotope signatures of the Sutri Dhaka stream are more close to the glacier ice-melt end member compared to snowmelt and rainwater (Figure 9). This indicates that the fresh snow on the glacier surface might undergo several stages of post-depositional processes, leading to large isotopic fractionation.

Figure 9. A mixing diagram showing d-excess vs. $\delta^{18}O$ of the mean value of snow, ice and rainwater and daily stream meltwater samples. The arrow indicates the evolution of the fresh snow due to the effect of secondary processes after the precipitation.

A three-component hydrograph separation of the Sutri Dhaka stream revealed that the contribution of ice-melt, snowpack and fresh 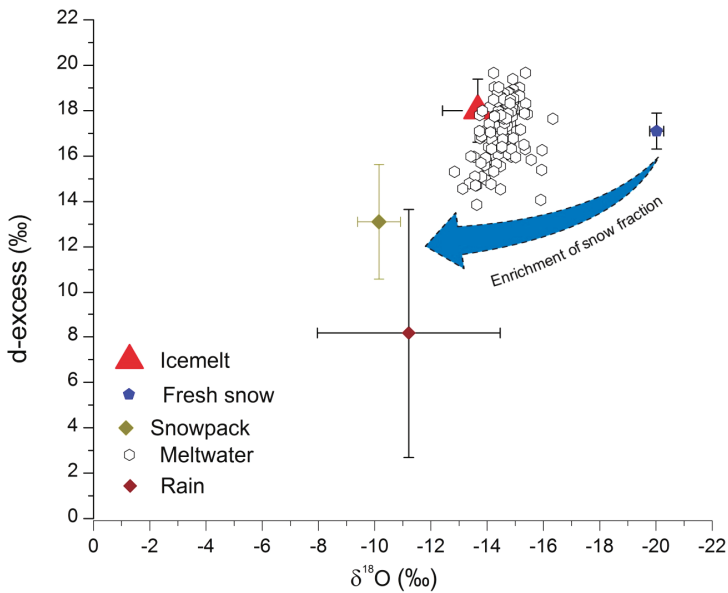snow are 65 ± 14, 15 ± 9 and 20 ± 5%, respectively (Figure 10). Results of hydrograph separation suggest that the ice-melt is the dominant contributor to the Sutri Dhaka stream water during July–October. However, we observed a significant declining trend in ice-melt and an increase in fresh snow, followed by a snowpack contribution to the Sutri Dhaka stream after the major snowfall events on 12 July and 20–24 September 2015. The overall contribution from the snowmelt suggests that they are mainly derived from the isotopically-depleted snow as well as the enriched snowpack. Despite a spike in fresh snow contribution followed by a snowpack, the ice-melt remained a dominant contributor throughout the study period. A significant decline in temperature has been observed after the major snowfall event (20–24 September 2015), which significantly reduces the surface melting. Therefore, the main source of ice-melt during September and October could be from the subglacial ice-melt due to pressure melting [32]. It has been observed that by the end of September the supraglacial melting reduced substantially, and a major contribution to the stream melt water were supplied by the melting of subglacial ice [61].
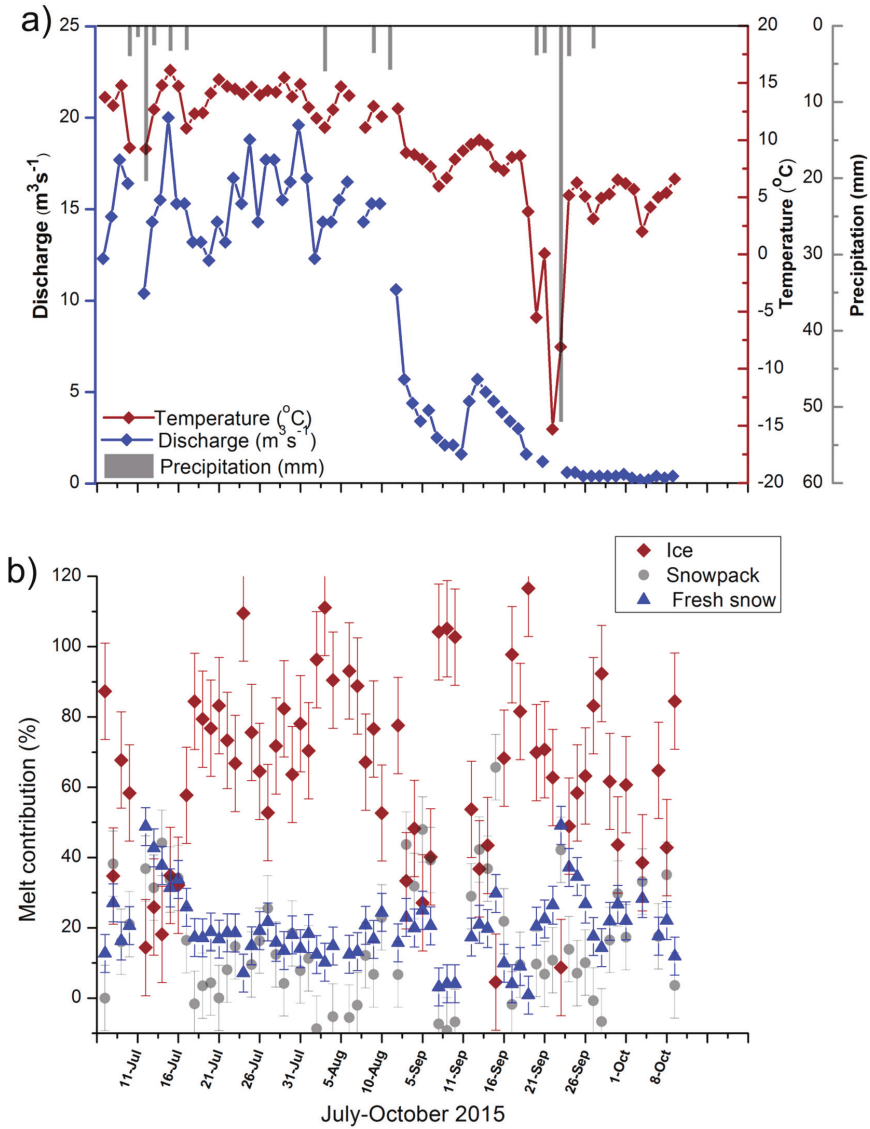
Figure 10. Hydro-meteorological characteristics of the Sutri Dhaka Glacier (**a**) Discharge is compared with temperature and precipitation; (**b**) contribution of ice-melt, snowpack and fresh snow to the Sutri Dhaka stream estimated based on three-component separation.

4.4.2. Specific Ablation of Snow and Ice

To validate our estimates of hydrograph separation based on stable isotope method, we have compared with the field estimates obtained from stake-based ablation and snow accumulation measurements. The estimated winter snow accumulation based on several snow-pit measurements on the glacierized area on 4 July 2015 varied from 0.24 to 1.17 m w.e (meter water equivalent) between the elevation ranges 4500 to 5300 m a.s.l. The total snow accumulation estimated for the glacierized area is $14.0 \pm 2.28 \times 10^6$ m^3 w.e.

As the summer progresses, the accumulated snow starts melting, and by the end of the ablation period most of the area (<5320 m a.s.l) becomes snow-free. At the end of the study period (28 September), estimation of the residual (annual) snow accumulation at ~5300 m a.s.l was $9.04 \pm 1.8 \times 10^6$ m^3 w.e (Figure 11). The depletion of snow line over the glacier surface defines the zero balance area, known as the Equilibrium Line Altitude (ELA). Based on the measurements of stakes installed on the glacier, the ELA observed at the end of the ablation season was at 5320 m a.s.l. To estimate the total snowmelt from 4 July to 28 September (nearly three months), the annual snow accumulation was subtracted from the winter snow accumulation. The difference between the winter accumulation and residual accumulation (Cw-Ca) is $-5.0 \pm 1.0 \times 10^6$ m^3 w.e., which accounts for snowmelt contribution to the stream runoff (Figure 11).
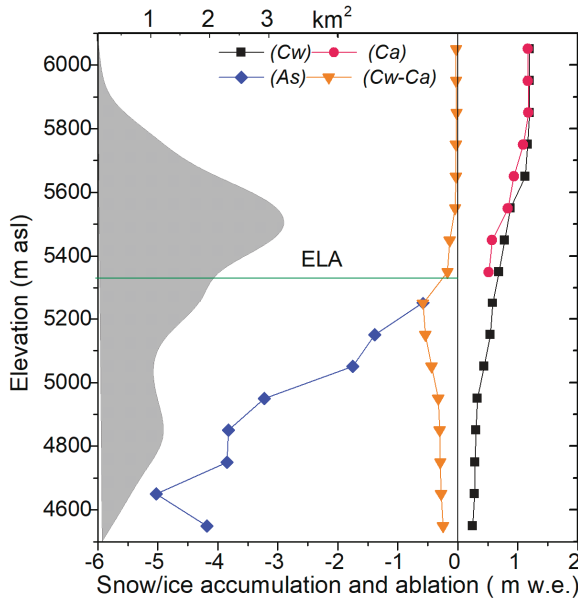

Figure 11. The observed winter snow accumulation (*Cw*), annual/residual snow accumulation (*Ca*), summer ice ablation (*As*) and summer snowmelt (*Cw-Ca*), and the area altitude distribution of Sutri Dhaka Glacier for the period of 5 July–28 September 2015.

A transient snowline on the glacier was estimated using Landsat 8 OLI images and demarcated using ASTER GDEM which was further validated with the ground control points. A transient snowline-snow pit method shows that the snowline position before the study commenced was at an altitude of 4511 (±46) m a.s.l (27 June 2015) (Supplementary Figure S1). As the melting progressed, the snowline reached up to 5601 (±46) m a.s.l (30 August 2015) at peak of ablation season with total snow area loss of 10.41 km^2 and snow volume loss of -5.8×10^6 m^3 w.e (Figure 12). It is noteworthy to observe that the snow ablation estimate using the transient snowline-snow pit method agrees with our field-based snow ablation measurement within the range of uncertainty. As the snow cover melts, the ice becomes exposed, and starts melting with the increase in air temperature. The cumulative summer ice ablation (*As*) for the study period (5 July to 28 September 2015) between the elevation of 4500 to 5300 m a.s.l, yield a total glacier ice-melt of $-20 \pm 4 \times 10^6$ m^3 w.e. Maximum ice ablation was observed at an altitude of 4600–4700 m a.s.l, which was reduced progressively towards higher altitude due to lower air temperature. The total cumulative melt contribution from snow and ice during this period provides an estimate of $-25 \pm 5 \times 10^6$ m^3 w.e (Figure 11). Contributions of snow and ice-melt towards the production of meltwater discharge are approximately 20 ± 4% and 80 ± 16%, respectively.
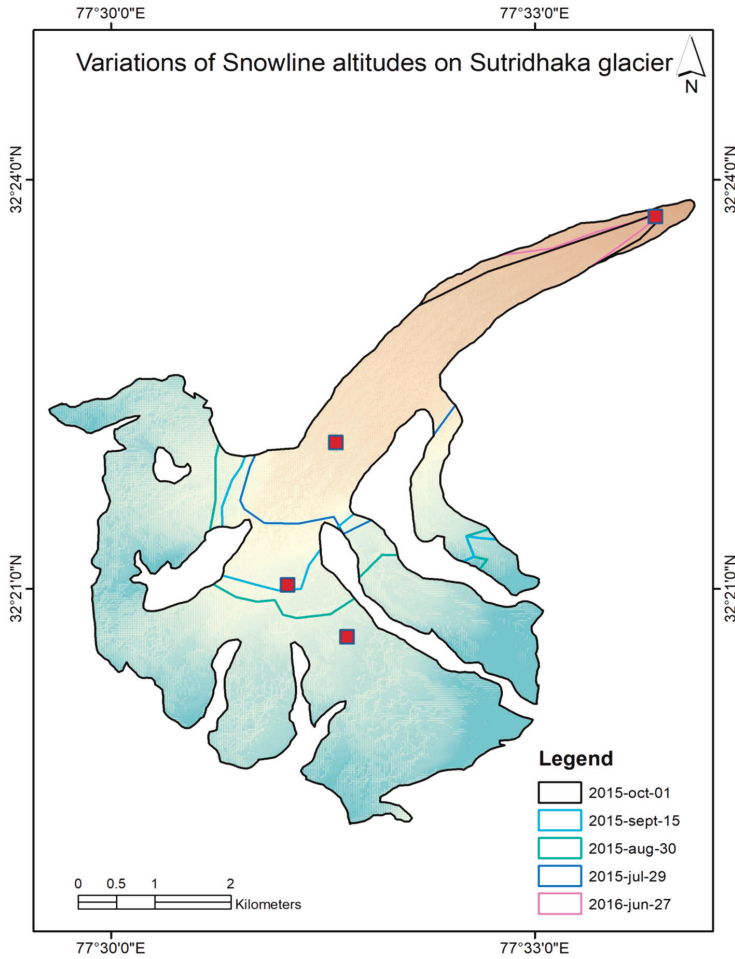
Figure 12. Transient snowline estimated using Landsat 8 OLI images of Sutri Dhaka Glacier and excavated snow pits (brown square) during the study period.

4.4.3. Uncertainty in Hydrograph Separation Estimates

Hydrograph separations and their quantitative assessments using the stable isotope method are often a challenging task due to a large spread on the $\delta^{18}O$ values of the hydrograph components. Stable water isotope compositions of snow and ice vary spatially and temporally, which contributes to uncertainties associated with the estimates of hydrograph components [62,63]. Three-component hydrograph estimates are critically dependent on the end-member values of $\delta^{18}O$ and d-excess and uncertainties associated with them. To better constrain the uncertainty associated with the estimates of hydrograph components based on $\delta^{18}O$ and d-excess, we used a Monte Carlo error propagation method [64,65]. This simulation method was used to solve the Equations (7)–(9) with 50,000 iterations for each stream samples and uncertainty, with a 68% confidence interval (CI) acquired for each mixing fraction. Based on Monte Carlo simulation, the uncertainty in ice-melt, snowpack and fresh snow estimates are 14, 9 and 5%, respectively. The overall uncertainty in each component is shown with error bars (Figure 10).

The accuracy of specific ablation using a network of bamboo stakes and snow pits cannot be evaluated strictly, as some of the random errors in this method are unknown. Uncertainty in this method is mainly derived from glacier area estimates, stake measurements and snow depth and density measurements [66,67]. Based on the field data, uncertainty in glaciological field measurements has been reported to be maximum up to ± 20% [35,65]. Therefore, in the present study, we have considered an error of ± 20% for specific ablation measurements.

Comparison of our hydrograph components estimates-based two independent methods i.e., the field-based ablation measurement and the stable isotope-based hydrograph method, the latter method provides ~15% higher estimates of the snowmelt component. This difference arises due to an unaccounted contribution from the deposited snow over the valley slope of the glacierized area in the field-based method. However, the isotope-based method provides an estimate of an integrated average of snow and ice-melt contributions from the entire basin to the downstream. Therefore, we suggest that for basins in the upper Indus Basin, where the contribution of rainfall and groundwater are minimal, a stable isotope method can be complimentary along with the field-based ablation measurements. Further, the glaciers which are inaccessible for the field measurements, the stable isotope method could add to our ability to evaluate snow /ice-melt contribution from high altitude Himalayan glaciers.

5. Conclusions

The present study provides insights on the moisture sources for the precipitation and hydrograph components of the Sutri Dhaka Glacier basin in the western Himalayas during the peak ablation period in the year 2015. Stable isotope fingerprinting of moisture sources together with back trajectory analysis indicate that the moisture to the study area is predominantly derived from the Mediterranean Sea regions through the Western Disturbances (WDs). However, the major sources for the precipitation during summer are supplied by the ISM as well as WDs. A combination of stable water isotope data and field ablation measurements provide information about the dominant sources of water contributing to the stream runoff of the Sutri Dhaka as well as the major moisture sources for precipitation over the study region. Three-component hydrograph separation of the Sutri Dhaka Glacier based on stable isotope methods shows a dominant contribution of ice-melt (65% ± 14) to the stream discharge, followed by snowpack (15% ± 9) and fresh snow (20 ± 5%). Despite the uncertainties associated with these estimates, the results of isotope hydrograph separation are overall consistent with that of stake-based field measurements; the contribution of ice-melt and snowmelt are 80 ± 16% and 20 ± 4%, respectively. However, the stable isotope method provides relatively more accurate estimates of hydrograph components compared to field-based ablation measurements, as it integrates over the entire catchments in the upstream of the sampling site, whereas the field-based method does not account for part of the snow component in the valley slope. Considering the limited information on the hydrograph components of the Himalayan glaciers, this study will enhance our current knowledge and understanding of hydrological processes in high altitude western Himalayan regions.

References

1. AGRIS. Available online: http://agris.fao.org (accessed on 16 July 2018).
2. Bolch, T.; Kulkarni, A.; Kaab, A.; Huggel, C.; Paul, F.; Cogley, J.G.; Frey, H.; Kargel, J.S.; Fujita, K.; Scheel, M.; et al. The State and Fate of Himalayan Glaciers. *Science* **2012**, *336*, 310–314. [CrossRef] [PubMed]
3. Immerzeel, W.W.; van Beek, L.P.H.; Bierkens, M.F.P. Climate Change Will Affect the Asian Water Towers. *Science* **2010**, *328*, 1382–1385. [CrossRef] [PubMed]
4. Kaser, G.; Grosshauser, M.; Marzeion, B. Contribution potential of glaciers to water availability in different climate regimes. *Proc. Natl. Acad. Sci. USA* **2010**, *107*, 20223–20227. [CrossRef] [PubMed]
5. Milner, A.M.; Khamis, K.; Battin, T.J.; Brittain, J.E.; Barrand, N.E.; Fureder, L.; Cauvy-Fraunie, S.; Gislason, G.M.; Jacobsen, D.; Hannah, D.M.; et al. Glacier shrinkage driving global changes in downstream systems. *Proc. Natl. Acad. Sci. USA* **2017**, *114*, 9770–9778. [CrossRef]
6. Bookhagen, B.; Burbank, D.W. Topography, relief, and TRMM-derived rainfall variations along the Himalaya (vol 33, art no L08405, 2006). *Geophys. Res. Lett.* **2006**, *33*. [CrossRef]
7. Bhambri, R.; Bolch, T. Glacier mapping: A review with special reference to the Indian Himalayas. *Prog. Phys. Geogr.* **2009**, *33*, 672–704. [CrossRef]
8. Casper, J.K. *Global Warming Cycles: Ice Ages and Glacial Retreat*; Infobase Publishing: New York City, NY, USA, 2010.
9. Parry, M.; Parry, M.L.; Canziani, O.; Palutikof, J.; Van der Linden, P.; Hanson, C. *Climate Change 2007-Impacts, Adaptation and Vulnerability: Working Group II Contribution to the Fourth Assessment Report of the IPCC*; Cambridge University Press: Cambridge, MA, USA, 2007; Volume 4.
10. Craig, H. Isotopic Variations in Meteoric Waters. *Science* **1961**, *133*, 1702–1703. [CrossRef]
11. Rahaman, W.; Thamban, M.; Laluraj, C.J.T.H. Twentieth-century sea ice variability in the Weddell Sea and its effect on moisture transport: Evidence from a coastal East Antarctic ice core record. *Holocene* **2016**, *26*, 338–349. [CrossRef]
12. Ahluwalia, R.S.; Rai, S.P.; Jain, S.K.; Kumar, B.; Dobhal, D.P. Assessment of snowmelt runoff modelling and isotope analysis: A case study from the western Himalaya, India. *Ann. Glaciol.* **2013**, *54*, 299–304. [CrossRef]
13. Jeelani, G.; Kumar, U.S.; Kumar, B. Variation of delta O-18 and delta D in precipitation and stream waters across the Kashmir Himalaya (India) to distinguish and estimate the seasonal sources of stream flow. *J. Hydrol.* **2013**, *481*, 157–165. [CrossRef]
14. Jeelani, G.; Shah, R.A.; Fryar, A.E.; Deshpande, R.D.; Mukherjee, A.; Perrin, J. Hydrological processes in glacierized high-altitude basins of the western Himalayas. *Hydrogeol. J.* **2018**, *26*, 615–628. [CrossRef]
15. Jeelani, G.; Shah, R.A.; Jacob, N.; Deshpande, R.D. Estimation of snow and glacier melt contribution to Liddar stream in a mountainous catchment, western Himalaya: An isotopic approach. *Isot. Environ. Health Stud.* **2017**, *53*, 18–35. [CrossRef] [PubMed]
16. Kumar, A.; Tiwari, S.K.; Verma, A.; Gupta, A.K. Tracing isotopic signatures (δD and δ18O) in precipitation and glacier melt over Chorabari Glacier–Hydroclimatic inferences for the Upper Ganga Basin (UGB), Garhwal Himalaya. *J. Hydrol. Reg. Stud.* **2018**, *15*, 68–89. [CrossRef]
17. Laskar, A.H.; Bhattacharya, S.K.; Rao, D.K.; Jani, R.A.; Gandhi, N. Seasonal variation in stable isotope compositions of waters from a Himalayan river: Estimation of glacier melt contribution. *Hydrol. Process.* **2018**, *32*, 3866–3880. [CrossRef]
18. Nijampurkar, V.N.; Rao, D.K. Accumulation and Flow-Rates of Ice On Chhota Shigri Glacier, Central Himalaya, Using Radio Active and Stable Isotopes. *J. Glaciol.* **1992**, *38*, 43–50. [CrossRef]
19. Rai, S.P.; Thayyen, R.J.; Purushothaman, P.; Kumar, B. Isotopic characteristics of cryospheric waters in parts of Western Himalayas, India. *Environ. Earth Sci.* **2016**, *75*, 9. [CrossRef]
20. Verma, A.; Kumar, A.; Gupta, A.K.; Tiwari, S.K.; Bhambri, R.; Naithani, S. Hydroclimatic significance of stable isotopes in precipitation from glaciers of Garhwal Himalaya, Upper Ganga Basin (UGB), India. *Hydrol. Process.* **2018**, *32*, 1874–1893. [CrossRef]
21. Shi, M.; Wang, S.; Argiriou, A.A.; Zhang, M.; Guo, R.; Jiao, R.; Kong, J.; Zhang, Y.; Qiu, X.; Zhou, S. Stable Isotope Composition in Surface Water in the Upper Yellow River in Northwest China. *Water* **2019**, *11*, 967. [CrossRef]

22.   Kurita, N.; Sugimoto, A.; Fujii, Y.; Fukazawa, T.; Makarov, V.N.; Watanabe, O.; Ichiyanagi, K.; Numaguti, A.;
       Yoshida, N. Isotopic composition and origin of snow over Siberia. *J. Geophys. Res. Atmos.* **2005**, *110*.
       [CrossRef]

23.   Suzuki, K.; Konohira, E.; Yamazaki, Y.; Kubota, J.; Ohata, T.; Vuglinsky, V. Transport of organic carbon from
       the Mogot Experimental Watershed in the southern mountainous taiga of eastern Siberia. *Hydrol. Res.* **2006**,
       37, 303–312. [CrossRef]

24.   Owen, L.A.; Bailey, R.M.; Rhodes, E.J.; Mitchell, W.A.; Coxon, P. Style and timing of glaciation in the Lahul
       Himalaya, northern India: A framework for reconstructing late Quaternary palaeoclimatic change in the
       western Himalayas. *J. Quat. Sci.* **1997**, *12*, 83–109. [CrossRef]

25.   Kumar, V.; Singh, P.; Singh, V. Snow and glacier melt contribution in the Beas River at Pandoh Dam, Himachal
       Pradesh, India. *Hydrol. Sci. J.* **2007**, *52*, 376–388. [CrossRef]

26.   Singh, P.; Jain, S.K. Snow and glacier melt in the Satluj River at Bhakra Dam in the western Himalayan region.
       Hydrol. Sci. J. **2002**, *47*, 93–106. [CrossRef]

27.   Singh, P.; Jain, S.K.; Kumar, N. Estimation of snow and glacier-melt contribution to the Chenab River, Western
       Himalaya. *Mt. Res. Dev.* **1997**, *17*, 49–56. [CrossRef]

28.   Maurya, A.S.; Shah, M.; Deshpande, R.D.; Bhardwaj, R.M.; Prasad, A.; Gupta, S.K. Hydrograph separation and
       precipitation source identification using stable water isotopes and conductivity: River Ganga at Himalayan
       foothills. *Hydrol. Process.* **2011**, *25*, 1521–1530. [CrossRef]

29.   Burns, D.A. Stormflow-hydrograph separation based on isotopes: The thrill is gone—What's next? *Hydrol.
       Process.* **2002**, *16*, 1515–1517. [CrossRef]

30.   Unnikrishna, P.V.; McDonnell, J.J.; Kendall, C. Isotope variations in a Sierra Nevada snowpack and their
       relation to meltwater. *J. Hydrol.* **2002**, *260*, 38–57. [CrossRef]

31.   Rai, S.P.; Singh, D.; Jacob, N.; Rawat, Y.S.; Arora, M.; Kumar, B. Identifying contribution of snowmelt and
       glacier melt to the Bhagirathi River (Upper Ganga) near snout of the Gangotri Glacier using environmental
       isotopes. *Catena* **2019**, *173*, 339–351. [CrossRef]

32.   Kumar, N.; Ramanathan, A.; Keesari, T.; Chidambaram, S.; Ranjan, S.; Soheb, M.; Tranter, M. Tracer-based
       estimation of temporal variation of water sources: An insight from supra- and subglacial environments.
       Hydrol. Sci. J. **2018**, *63*, 1717–1732. [CrossRef]

33.   Singh, A.T.; Laluraj, C.M.; Sharma, P.; Patel, L.K.; Thamban, M. Export fluxes of geochemical solutes in the
       meltwater stream of Sutri Dhaka Glacier, Chandra basin, Western Himalaya. *Environ. Monit. Assess.* **2017**,
       189. [CrossRef]

34.   Pratap, B.; Sharma, P.; Patel, L.; Singh, A.T.; Gaddam, V.K.; Oulkar, S.; Thamban, M. Reconciling High Glacier
       Surface Melting in Summer with Air Temperature in the Semi-Arid Zone of Western Himalaya. *Water* **2019**,
       11, 1561. [CrossRef]

35.   Sharma, P.; Patel, L.K.; Ravindra, R.; Singh, A.; Mahalinganathan, K.; Thamban, M. Role of debris cover to
       control specific ablation of adjoining Batal and Sutri Dhaka glaciers in Chandra Basin (Himachal Pradesh)
       during peak ablation season. *J. Earth Syst. Sci.* **2016**, *125*, 459–473. [CrossRef]

36.   Azam, M.F.; Wagnon, P.; Vincent, C.; Ramanathan, A.; Favier, V.; Mandal, A.; Pottakkal, J.G. Processes
       governing the mass balance of Chhota Shigri Glacier (western Himalaya, India) assessed by point-scale
       surface energy balance measurements. *Cryosphere* **2014**, *8*, 2195–2217. [CrossRef]

37.   Pradesh, I. Central Ground Water Board. Available online: http://cgwb.gov.in/District_Profile/HP/Lahul%
       20Spiti.pdf (accessed on 25 October 2019).

38.   Srivastava, P.K.; Han, D.; Rico-Ramirez, M.A.; Islam, T. Sensitivity and uncertainty analysis of mesoscale
       model downscaled hydro-meteorological variables for discharge prediction. *Hydrol. Process.* **2014**, *28*,
       4419–4432. [CrossRef]

39.   Chakraborty, S.; Sinha, N.; Chattopadhyay, R.; Sengupta, S.; Mohan, P.M.; Datye, A. Atmospheric controls on
       the precipitation isotopes over the Andaman Islands, Bay of Bengal. *Sci. Rep.* **2016**, *6*. [CrossRef]

40.   Coplen, T.; De Bièvre, P.; Krouse, H.; Vocke, R., Jr.; Gröning, M.; Rozanski, K. Ratios for light-element isotopes
       standardized for better interlaboratory comparison. *Eos Trans. Am. Geophys. Union* **1996**, *77*, 255. [CrossRef]

41.   Dansgaard, W. Stable isotopes in precipitation. *Tellus* **1964**, *16*, 436–468. [CrossRef]

42.   Taylor, S.; Feng, X.H.; Williams, M.; McNamara, J. How isotopic fractionation of snowmelt affects hydrograph
       separation. *Hydrol. Process.* **2002**, *16*, 3683–3690. [CrossRef]

43. He, Y.; Pang, H.; Theakstone, W.; Zhang, D.; Lu, A.; Song, B.; Yuan, L.; Ning, B. Spatial and temporal variations of oxygen isotopes in snowpacks and glacial runoff in different types of glacial area in western China. *Ann. Glaciol.* **2006**, *43*, 269–274. [CrossRef]

44. Gibson, J.J.; Price, J.S.; Aravena, R.; Fitzgerald, D.F.; Maloney, D. Runoff generation in a hypermaritime bog-forest upland. *Hydrol. Process.* **2000**, *14*, 2711–2730. [CrossRef]

45. Throckmorton, H.M.; Newman, B.D.; Heikoop, J.M.; Perkins, G.B.; Feng, X.; Graham, D.E.; O'Malley, D.; Vesselinov, V.V.; Young, J.; Wullschleger, S.D.; et al. Active layer hydrology in an arctic tundra ecosystem: Quantifying water sources and cycling using water stable isotopes. *Hydrol. Process.* **2016**, *30*, 4972–4986. [CrossRef]

46. Rao, S.; Rao, M.; Ramasastri, K.; Singh, R. A study of sedimentation in Chenab basin in western Himalayas. *Hydrol. Res.* **1997**, *28*, 201–216. [CrossRef]

47. Østrem, G.; Brugman, M. Glacier Mass Balance Measurement Techniques: A Manual for Field and Office Work. Available online: https://wgms.ch/downloads/Oestrem_Brugman_GlacierMassBalanceMeasurements_1991. pdf (accessed on 25 October 2019).

48. Mernild, S.H.; Pelto, M.; Malmros, J.K.; Yde, J.C.; Knudsen, N.T.; Hanna, E. Identification of snow ablation rate, ELA, AAR and net mass balance using transient snowline variations on two Arctic glaciers. *J. Glaciol.* **2013**, *59*, 649–659. [CrossRef]

49. Draxler, R.R.; Rolph, G.D. Hysplit (hybrid single-particle lagrangian integrated trajectory) model access via NOAA ARL ready website. *Silver Spring MD* **2011**, *8*, 26.

50. Stein, A.F.; Draxler, R.R.; Rolph, G.D.; Stunder, B.J.B.; Cohen, M.D.; Ngan, F. Noaa's Hysplit Atmospheric Transport And Dispersion Modeling System. *Bull. Am. Meteorol. Soc.* **2015**, *96*, 2059–2077. [CrossRef]

51. Wallace, J.M.; Hobbs, P.V. *Atmospheric Science: An Introductory Survey*; Elsevier: Amsterdam, The Netherlands, 2006; Volume 92.

52. Wang, Y.; Zhang, X.; Draxler, R.R. TrajStat: GIS-based software that uses various trajectory statistical analysis methods to identify potential sources from long-term air pollution measurement data. *Environ. Model. Softw.* **2009**, *24*, 938–939. [CrossRef]

53. Kraaijenbrink, P.D.A.; Bierkens, M.F.P.; Lutz, A.F.; Immerzeel, W.W. Impact of a global temperature rise of 1.5 degrees Celsius on Asia's glaciers. *Nature* **2017**, *549*, 257–260. [CrossRef]

54. Zhou, S.; Nakawo, M.; Hashimoto, S.; Sakai, A. The effect of refreezing on the isotopic composition of melting snowpack. *Hydrol. Process.* **2008**, *22*, 873–882. [CrossRef]

55. Stichler, W.; Schotterer, U.; Frohlich, K.; Ginot, P.; Kull, C.; Gaggeler, H.; Pouyaud, B. Influence of sublimation on stable isotope records recovered from high-altitude glaciers in the tropical Andes. *J. Geophys. Res. Atmos.* **2001**, *106*, 22613–22620. [CrossRef]

56. Rozanski, K.; Araguás-Araguás, L.; Gonfiantini, R. Isotopic patterns in modern global precipitation. *Clim. Chang. Cont. Isot. Rec.* **1993**, *78*, 1–36.

57. Wu, J.-K.; Ding, Y.-J.; Yang, J.-H.; Liu, S.-W.; Zhou, J.-X.; Qin, X. Spatial variation of stable isotopes in different waters during melt season in the Laohugou Glacial Catchment, Shule River basin. *J. Mt. Sci.* **2016**, *13*, 1453–1463. [CrossRef]

58. Jeelani, G.; Deshpande, R.D.; Shah, R.A.; Hassan, W. Influence of southwest monsoons in the Kashmir Valley, western Himalayas. *Isot. Environ. Health Stud.* **2017**, *53*, 400–412. [CrossRef] [PubMed]

59. Zhou, S.; Wang, Z.; Joswiak, D.R. From precipitation to runoff: Stable isotopic fractionation effect of glacier melting on a catchment scale. *Hydrol. Process.* **2014**, *28*, 3341–3349. [CrossRef]

60. Lone, S.A.; Jeelani, G.; Deshpande, R.D.; Mukherjee, A. Stable isotope (delta O-18 and delta D) dynamics of precipitation in a high altitude Himalayan cold desert and its surroundings in Indus river basin, Ladakh. *Atmos. Res.* **2019**, *221*, 46–57. [CrossRef]

61. Kumar, A.; Gokhale, A.A.; Shukla, T.; Dobhal, D.P. Hydroclimatic influence on particle size distribution of suspended sediments evacuated from debris-covered Chorabari Glacier, upper Mandakini catchment, central Himalaya. *Geomorphology* **2016**, *265*, 45–67. [CrossRef]

62. Khan, A.A.; Pant, N.C.; Sarkar, A.; Tandon, S.K.; Thamban, M.; Mahalinganathan, K. The Himalayan cryosphere: A critical assessment and evaluation of glacial melt fraction in the Bhagirathi basin. *Geosci. Front.* **2017**, *8*, 107–115. [CrossRef]

63. Pfahl, S.; Sodemann, H. What controls deuterium excess in global precipitation? *Clim. Past* **2014**, *10*, 771–781. [CrossRef]

64. Bazemore, D.E.; Eshleman, K.N.; Hollenbeck, K.J. The role of soil water in stormflow generation in a forested headwater catchment: Synthesis of natural tracer and hydrometric evidence. *J. Hydrol.* **1994**, *162*, 47–75. [CrossRef]

65. Genereux, D. Quantifying uncertainty in tracer-based hydrograph separations. *Water Resour. Res.* **1998**, *34*, 915–919. [CrossRef]

66. Funk, M.; Morelli, R.; Stahel, W. Mass balance of Griesgletscher 1961-1994: Different methods of determination. With 10 figures. *Z. Gletsch. Glazialgeol.* **1997**, *33*, 41–56.

67. Jansson, P. Effect of uncertainties in measured variables on the calculated mass balance of Storglaciaren. *Geogr. Ann. Ser. A Phys. Geogr.* **1999**, *81A*, 633–642. [CrossRef]

What Do Plants Leave after Summer on the Ground?—The Effect of Afforested Plants in Arid Environments

César Dionisio Jiménez-Rodríguez [1,2,*], **Miriam Coenders-Gerrits** [1], **Stefan Uhlenbrook** [3] **and Jochen Wenninger** [4]

[1] Department of Water Management, Water Resources Section, Delft University of Technology, 2600 GA Delft, The Netherlands; A.M.J.Coenders@tudelft.nl
[2] Escuela de Ingeniería Forestal, Tecnológico de Costa Rica, P.O. Box 159-7050, Cartago 30101, Costa Rica
[3] UNESCO World Water Assessment Programme, Via dei Ceraioli, 45, 06134 Perugia, PG, Italy; s.uhlenbrook@unesco.org
[4] Water Science and Engineering Department, IHE Delft, 2611 AX Delft, The Netherlands; j.wenninger@un-ihe.org
* Correspondence: cdjimenezcr@gmail.com

Abstract: The implementation of afforestation programs in arid environments in northern China had modified the natural vegetation patterns. This increases the evaporation flux; however, the influence of these new covers on the soil water conditions is poorly understood. This work aims to describe the effect of Willow bushes (*Salix psammophila* C. Wang and Chang Y. Yang) and Willow trees (*Salix matsudana* Koidz.) on the soil water conditions after the summer. Two experimental plots located in the Hailiutu catchment (Shaanxi province, northwest China), and covered with plants of each species, were monitored during Autumn in 2010. The monitoring included the soil moisture, fine root distribution and transpiration fluxes that provided information about water availability, access and use by the plants. Meanwhile, the monitoring of stable water isotopes collected from precipitation, soil water, groundwater and xylem water linked the water paths. The presence of Willow trees and Willow bushes reduce the effect of soil evaporation after summer, increasing the soil moisture respect to bare soil conditions. Also, the presence of soil water with stable water isotope signatures close to groundwater reflect the hydraulic lift process. This is an indication of soil water redistribution carried out by both plant species.

Keywords: stable water isotopes; hydrogen; oxygen; soil water; fine root system

1. Introduction

Continental arid environments are characterized by excessive heat and variable precipitation distributed all over the year, with a tendency to peak during summer months [1–3]. These conditions favoured the presence of a discontinuous vegetation cover characterized by banded and spotted shapes, large size variability and specialized plant species [3–5]. The northern arid lands in China are an example of this type of environment, where the landscape is shaped by eolic erosion due to the high erodability of this soil type and the scarce ground cover protection [6–10]. Consequently, desertification in this region registered a strong growth of barren areas before 1999 [11]. However, after 2005 the plant cover experienced a positive change, reducing the areas affected by desertification thanks to the rehabilitation and afforestation programs established in the region [11,12]. The current implementation of afforestation and agricultural programs modified the landscape cover with additional crop areas. These afforestation practices trigger a series of impacts to the environment due to the inadequate

selection of plant species [13,14]. This increment in vegetation cover reduces the local surface temperature [15] and affects the local evaporation flux due to the increment of plant transpiration which depends mostly on groundwater [16–18].

The evaporation (E) of arid environments is mainly composed of soil evaporation (E_s) and a small proportion of intercepted water by plant surfaces (E_i) and transpiration (E_t) [19–21]. The low precipitation rates underline the importance of soil water and groundwater availability for the plants. Rainfall interception decreases the water infiltration rates of vegetated areas in respect to bare soil conditions in arid and semi-arid regions [22,23]. This is the result of the quick evaporation of the intercepted water on the leaves, branches and stem of the plants [19,21]. The relevance of interception increases considering the precipitation characteristics of the arid and semi–arid regions where the low volume, high intensity, lower and irregular frequency hinder the plant water acquisition [5]. Due to the scarce water resources in these regions the plants are adapted to quickly respond to environmental triggers such as the irregular rains [24]. Thus increases the soil water acquisition by the plants and consequently its transpiration momentarily [25,26].

The plant root system provides anchorage for the plant and an effective water extraction system [27] which is powered by the plant transpiration [28]. This system absorbs the water close to the meristematic region of the root, transporting it through the xylem towards the leaves and using it during photosynthesis [28–30]. However, the presence of young roots in soil layers does not mean effective absorption of water from those zones [31]. Instead, some species are able to absorb water through suberized roots under soft drought or winter conditions [28,30]. As a consequence, the identification of plant water sources is a difficult task that requires the use of tracers.

Determination of water sources for the plants has been successfully done with the stable water isotopes oxygen ($\delta^{18}O$) and hydrogen (δ^2H) [18,27,32–40]. The specific isotopic signatures of soil water is the result of a fractionation process that modifies the isotope composition [41,42], allowing to trace the water paths within the ecosystem [43]. The isotope signature of the absorbed water is not modified by plant uptake until the water reaches the photosynthetic tissues [27,31]. Here, the leaf tissues will become enriched by the escape of lighter isotopes [44]. Although the roots do not modify the soil water during uptake, the isotope signature of xylem water is affected by mixing processes when different water sources are used by the same plant. Barbeta et al. [41] briefly describe a series of analysis tools used for the determination of water sources used by plants. Some of these methods are the Bayesian isotope mixing models such as SIAR [45,46] and MixSIAR [47] or standard linear mixing models such as IsoSource [48,49]. The IsoSource model provides all the feasible combination of water source contributions keeping the mass balance principle. It uses only the isotope signature of the water sources and the xylem water as the final mixture. SIAR and MixSIR models require more complex data sets. These models require the isotope signatures of the sources and mixtures as well as their standard deviations and an enrichment factor. As a result, the models provide the statistical uncertainties and the optimal solution for the analyzed mixture. The IsoSource tool has been used to study sand dunes bushes, corn and cotton plantations, woody species and estuarine vegetation to determine the water sources of those covers [33,34,36,37,39,40]. Thus can provide information of the origin of water within the plant and if this water can be redistributed on the soil profile.

The implementation of afforestation programs in arid environments modify the distribution patterns of local vegetation, influencing the ratio between transpiration and evaporation ($\frac{E_t}{E}$) [50]. These changes together with the usual omission of interception of precipitation [19,21,51], the irregular rains [5] and the large capacity to transpire soil water by arid plants [52]; exert a lot of pressure on the scarce water resources of arid environments. This has been the case with the introduction of Willow trees (*Salix matsudana*) and Willow bushes (*Salix psammophila*) in afforestation programs in the Hailiutu catchment [16–18]. The transpiration of these species increased the demand on the groundwater resource, however its influence on the soil water conditions are poorly understood. This work aims to describe the effect of Willow trees and Willow bushes on the soil water conditions after the summer. The monitoring included the soil moisture, fine root distribution and transpiration fluxes that provided

information about water availability, access and use by the plants. Meanwhile the monitoring of stable water isotopes collected from precipitation, soil water, groundwater and xylem water linked the water fluxes. This information provided an indication of the vegetation influence on the soil water conditions beneath the covers.

2. Materials and Methods
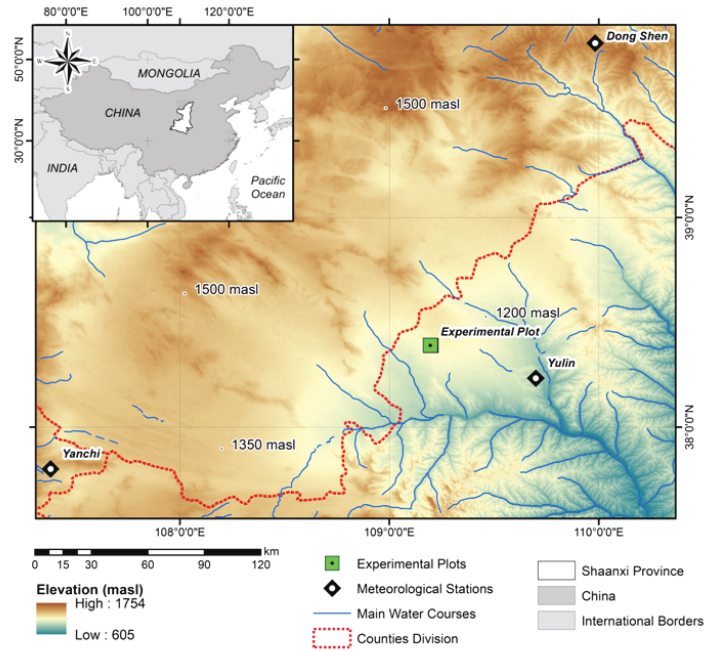
2.1. Study Site

The study site is located within the Hailiutu catchment (area: $2645\,km^2$) in Yulin County; Shaanxi province; Northwest China (Figure 1). This catchment is part of the Maowusu semi-desert, which is characterized by undulating sand dunes over and dominated by a xeric scrubland. The nearest meteorological stations (Dong Shen: 39.833° N–109.983° E; Yanchi: 37.800° N–107.383° E; and Yulin: 38.233° N–109.700° E) described a semi-arid continental climate with a mean annual precipitation of 386.1 mm year^{-1} and a mean annual temperature of 8.6 °C (seasonal range: -17.4 °C to 27.1 °C) based on 12 years of meteorological records (period: 2000–2011). The soil type is classified as Calcaric Arenosols (ARc) with a high concentration of basic cations (Ca^{2+}, Mg^{2+}, K^+ and Na^+) and a pH value over 8.0; with an excessive drainage due to its sandy texture [53]. The study site is composed of two experimental plots (see Appendix A Figure A1) located at 300 m from each other. The first plot is dominated by Willow bushes (*Salix psammophila* C. Wang & Chang Y. Yang) and has an area of 625 m^2 (25 m × 25 m). The second plot covers 81 m^2 (9 m × 9 m) and contains mainly individuals of Willow trees (*Salix matsudana* Koidz.) and Poplar trees (*Populus simonii* Carr.). In both plots soil water, groundwater, plant parameters and soil variables were measured between September and October 2010.
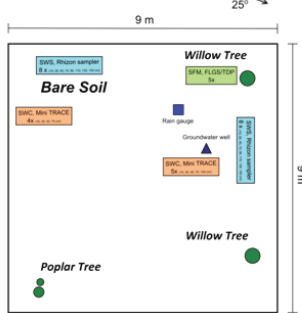
2.2. Hydrologic Data

Meteorological data was retrieved from the stations Dong Shen (1459 m a.s.l.), Yanchi (1356 m a.s.l.) and Yulin (1058 m a.s.l.). The climatic data was downloaded from the National Oceanic and Atmospheric Administration (NOAA) [54]. This data set contains daily values of total precipitation (mm day^{-1}) and daily means for temperature (°C), dewpoint (°C), wind speed (m s^{-1}) and atmospheric pressure (mbar). Due the lack of solar radiation measurements in the selected study period, this variable was estimated according to Allen et al. [55] for missing data. Once all data were determined, the reference evaporation (E_o) in mm day^{-1} was calculated with the FAO Penman–Monteith equation:

$$E_o = \frac{\Delta(R_n - G) + \rho_a C_p \frac{(e_s - e_a)}{r_a}}{\Delta + \gamma\left(1 + \frac{r_s}{r_a}\right)}, \tag{1}$$

where net radiation (R_n) and soil heat flux (G) are expressed in MJ m^{-2} day^{-1}. The vapour pressure deficit of the air ($e_s - e_a$) is based on the saturation vapor pressure (e_s) and actual vapor pressure (e_a) both measured in KPa. Δ is the slope of the vapour-pressure relationship (kPa °C^{-1}), γ is the psychrometric constant (0.054 kPa °C), ρ_a is the air density (1.225 kg m^{-3}) and c_p is the specific heat of the air (1.013 ×10^{-3} MJ kg^{-1} °C^{-1}). The wind speed (m s^{-1}) at 2 m height (u_2) was used to determine the aerodynamic resistance (r_a) and surface resistance (r_s). For daily time steps the soil heat flux is considered to equal 0 MJ m^{-2}day^{-1} due the small daily differences [55].

Figure 1. Geographical location of the experimental site and the meteorological stations Dong Shen, Yanchi and Yulin used during the study period in the Shaanxi province, China. The experimental design of both plots is shown on the bottom of the map.

Soil moisture (θ, m^3 m^{-3}) and groundwater level (h, m) measurements were carried out to describe the soil water dynamics in both sites. Soil moisture measurements were carried out sporadically along the study period. The reference values of soil moisture in sandy soils for permanent wilting point (θ_{WP}), field capacity (θ_{FC}) and saturation point (θ_{SP}) were 0.05 m^3 m^{-3}, 0.1 m^3 m^{-3} and 0.46 m^3 m^{-3}, respectively [56]. Soil moisture was monitored with a Mini-TRASE sensor (type: 6050X3K1B) and the probes were located at 10 cm, 20 cm, 40 cm, 70 cm and 100 cm depth beneath each species. On the Willow bush plot two more depths were monitored: 120 cm and 140 cm. Considering the presence of

bare soil areas within the plots, the soil moisture was also monitored at the same depths as Willow bush. The groundwater monitoring wells were constructed with a manual soil auger thanks to the shallow groundwater level and sandy texture of the soil. The groundwater level was measured on a daily basis from the ground surface as the reference point with a Mini-Diver (type: DI 501) in each plot. Groundwater depth from the surface in both plots oscillates between 136 cm to 164 cm beneath the Willow bush plot and between 150 cm to 172 cm beneath Willow tree plot period between 21 August 2010 to 20 April 2011).

2.3. Water Sampling

Water samples were collected after each rainy day to determine the isotopic signature of the precipitation, groundwater, soil water and xylem water throughout the monitoring period. Soil water samples were taken with a Macro Rhizon SMS Eijkelkamp (length: 9 cm, diameter: 4.5 mm, porous diameter: 0.15 μm, part number: 19.21.SA) soil moisture sampler in both plots. The samples were collected at nine depths (10 cm, 20 cm, 40 cm, 70 cm, 90 cm, 110 cm, 140 cm, 150 cm and 160 cm), while the groundwater sampling depended on the water head elevation during the samplings. Xylem water was collected from an incision done at the twig of each tree; removing the bark, phloem and cambium to prevent the collection of fractionated sap water. The incision location was far from the meristematic region, avoiding the fractionation linked to photosynthesis. Rain water was collected during the events to prevent fractionation by evaporation on an event basis. Each sample was sealed hermetically in 1.5 mL vials and transported to The Netherlands for their analysis. The isotopic composition was determined with a LGR Liquid Water Isotope Analyzer (type: DLT-100) with a precision of $< 0.3\,‰$ for $^{18}O/^{16}O$ and $< 1.0\,‰$ for $^{2}H/^{1}H$ and expressed in respect to the Vienna Standard Mean Ocean Water (VSMOW). The isotopic signature of each sample was expressed in respect to the VSMOW through the following equation [57]:

$$\delta = \left(\frac{R_{\text{sample}}}{R_{\text{standard}}} - 1 \right) \qquad (2)$$

where δ (‰) is the relative isotope composition of ^{18}O and ^{2}H, R_{sample} and R_{standard} are the ratios of heavy to light isotopes ($^{18}O/^{16}O$ or $^{2}H/^{1}H$) of the sample and standard water, respectively.

2.4. Plant Parameters

For each plot the plant densities (plants ha^{-1}), canopy heights (m) and leaf area index (LAI, m^2 m^{-2}) were measured to describe the stand conditions. Transpired water (E_t) was monitored in the Willow shrubs establishing four ring gauges (type: Dynagage Energy Balance sensor, model: SGA3-WS and SGA5-WS) in an individual of Willow bush at 35 cm height; while five probes (type: Thermal Dissipation Probes, model: TDP-50) were installed in an individual of Willow at 1.3 m height. Each probe recorded the data at 10 minute intervals and those were summarized in an hourly and daily time step. Total mobilized water as transpiration was calculated with the product between the sapwood area and flow velocity. Considering the physiognomic differences between both plant species, the sapwood area was estimated accordingly with the plant type. Willow bush is a bush up to 4 m tall with numerous branchlets per plant [58], where most of the xylem within the branchlets is able to transport water. As a consequence, the sapwood area was measured through the average diameter of the measured branchlets. Willow tree is able to grow up to 10 m height with a symmetrical crown with a sole stem [59]. It has a clear differentiation between sapwood and hardwood, allowing to measure directly the sapwood from a tree wood ring obtained from the measured tree. The wood ring area was measured from inked water transported by capillary rise within the active sapwood sections. Sapwood area (A) for the Willow tree was 274.6 cm^2 and the average area for Willow bush was 5.1 cm^2. Transpiration flow for each plant was obtained though the empirical equation developed by Granier [60]:

$$E_t = 3600 \times 0.0119 \times \left(\frac{\partial T_m - \partial T}{\partial T} \right) \times A \times \rho, \qquad (3)$$

where E_t is the transpiration $(g\,h^{-1})$, ∂T is the vertical temperature difference (°C) measured within the plants, ∂T_m is the maximum temperature difference with zero E_t (°C), A is the cross section area (cm^2) and ρ is the water density $(g\,cm^{-3})$.

The fine root system was described through the total root biomass (TRB, $kg\,m^{-3}$) and the root length density (RLD, $cm\,cm^{-3}$). The survey involved the collection of 80 samples of soil per species with an auger of $300\,cm^3$ within a radius of 4.0 m. The sampling procedure was based on eight equidistant points from the stem towards the canopy edge, extracting 10 samples per point until a depth of 150 cm was reached. The samples were sieved to separate the soil from the roots, photographed on a scaled paper and dried up following the procedure proposed by Cornelissen et al. [61] to determine the root length density (RLD, $cm\,cm^{-3}$). The total root biomass was determined by weighing the dry cleaned roots with a digital balance. The total root length (cm) was determined by processing the root images with the use of the GIS free source software (www.gvsig.org). The total root length density was obtained dividing the total root length (cm) by the core volumes (cm^3) [62].

2.5. Data Analysis

Plant differences were determined using an Analysis of Covariance (ANCOVA) with a p_{value} of 0.05. Statistical differences were determined with a Tukey HSD analysis. A Pearson correlation analysis was applied to evaluate the influence of meteorological conditions on plant transpiration. All the statistical analyses are based on normal distributions, so the normality, variance homogeneity and presence of outliers were tested. The plant water source of transpiration was determined using the software IsoSource [48]. This model provides the relative contributions of soil water sources to sap flow in both species, based on the isotopic mass balance principle. Consequently, the isotopic soil water contribution analysis followed the "a posteriori aggregation" method proposed by Phillips et al. [48]. This method allows the aggregation of sources with similar isotopic signatures based on specific characteristics showed by the sources, reducing the number of contributing factors.

3. Results

Total precipitation in 2010 was $401.0\,mm\,year^{-1}$ at the experimental site, registering a slightly wet condition in respect to the regional average of $386.1\,mm\,year^{-1}$. However, this amount of precipitation does not supply the reference evaporation (E_o) of $1339.1\,mm\,year^{-1}$ at this site as a consequence of the irregular rain events (Figure 2). The $938.1\,mm\,year^{-1}$ difference between precipitation and reference evaporation support the Arid Steppe classification due to its annual water deficit [3,5,63,64]. September and October 2010 registered $48.2\,mm\,month^{-1}$ and $40.5\,mm\,month^{-1}$ of precipitation accounting for 12.0% and 10.1% of the annual amount, respectively (see Appendix B Figure A2). The water availability experienced during the study period allowed the presence of soil moisture above the permanent wilting point (θ_{WP}) for sandy soils $(0.05\,m^3\,m^{-3})$ while the field capacity (θ_{FC}) was exceeded only in the deepest layers in both plots (Figure 3). Additionally, soil moisture increases with depth in Willow bush and Willow tree stands, keeping higher values than under bare soil conditions. Soil moisture under both plant species has larger values in respect to bare soil condition until a depth of 100 cm (ANCOVA, F = 37.91, p = 0.0000). Average soil moisture shows the following order: Willow bush (θ: $0.11\,m^3\,m^{-3}$) > Willow tree (θ: $0.10\,m^3\,m^{-3}$) > Bare Soil (θ: $0.08\,m^3\,m^{-3}$).
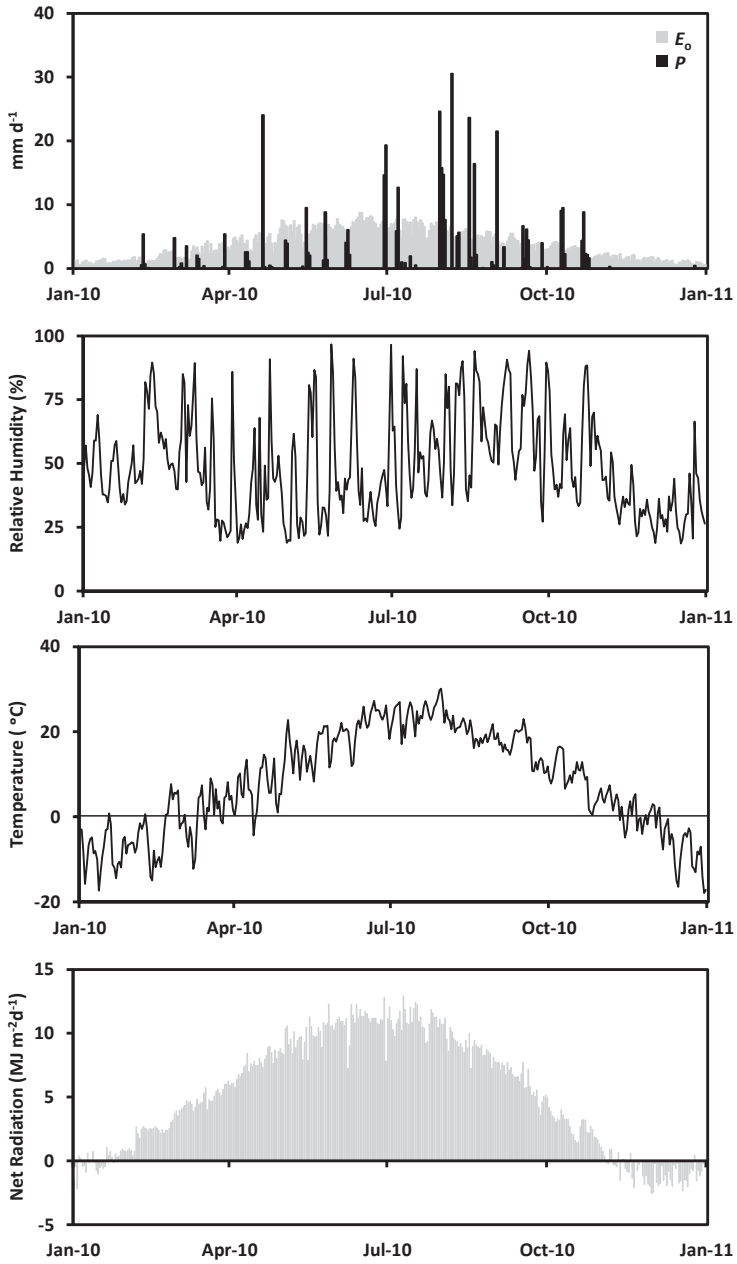
Figure 2. Meteorological conditions registered during 2010 at the research site based on the data of Dong Shen, Yanchi and Yulin meteorological stations.
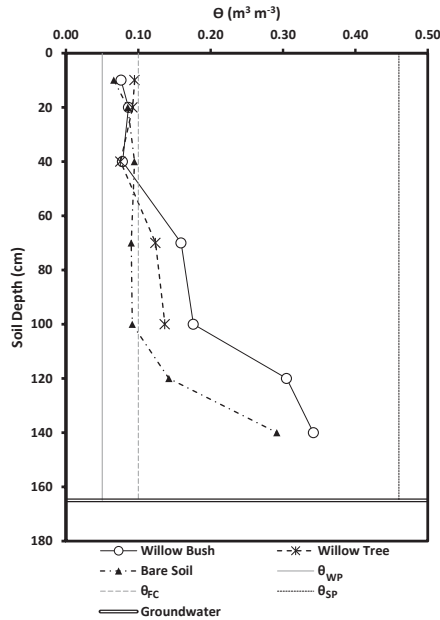
Figure 3. Soil moisture ($m^3\,m^{-3}$) measured in both plots for Willow bush, Willow tree and bare soil conditions during the study period.

Hourly transpiration differs in amount and timing between species. Figure 4 shows the differences along five days where the sap flux for Willow tree is remarkably higher than Willow bush. Willow tree shows a larger capacity to transpire water with peak fluxes averaging 1549.1 $g\,h^{-1}$; whereas Willow bush peaks do not exceed 500 $g\,h^{-1}$ on average. Daily transpiration rates in both species depict a significant decreasing trend (ANCOVA, F = 36.09; n = 87, p = 0.0000) and a statistical difference between total daily rates (ANCOVA, F = 63.05, n = 87, p = 0.0000), where Willow bush transport an average of 4.57 $kg\,day^{-1}$ being three times smaller than Willow tree fluxes (12.82 $kg\,day^{-1}$). In addition, as transpiration is a physiological response to environmental climatic parameters the Pearson correlation analysis ($p < 0.001$) shows a significant positive correlation with temperature (r = 0.47) and net radiation (r = 0.35); while wind speed (r = 0.05) and relative humidity (r = -0.27) are not significant.

Figure 4. Hourly transpiration flow measured in Willow tree and Willow bush plants during the study period.

Rain during the study period has a wide range of isotope signatures (see Appendix C Figure A3). The evaporation front is identifiable at 40 cm depth for Willow and at 20 cm for Willow bush in both isotopes (Figure 5). The isotope signature of groundwater samples (Willow Bush: $\d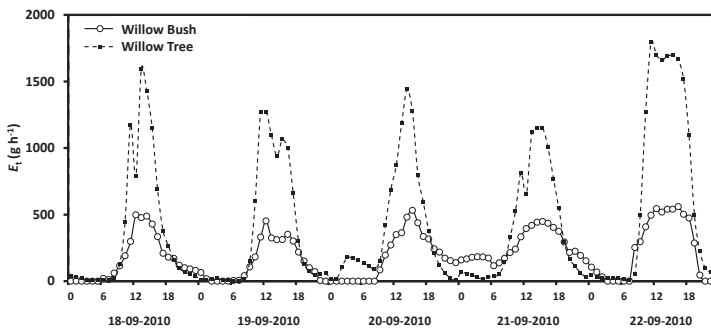elta^{18}$O: $-9.2\,‰$, δ^2H: $-66.1\,‰$ and Willow Tree: δ^{18}O: $-8.59\,‰$, δ^2H: $-60.66\,‰$) lie close to the rain water signature, depicting the effect of local groundwater recharge having a similar signature to local rains. Sap water signature in both species seems to contain fractionated and non-fractionated water. However, both stable isotopes do not show statistical differences between species ($p > 0.05$) as a consequence of the wide variation in isotope signatures. After a preliminary run of the IsoSource the soil water contribution to xylem water from deeper soil layers show a similar proportion in both species. It showed that only the 40 cm and 10 cm soil layers provide a strong contribution in Willow and Willow bush, respectively. Therefore "a posteriori aggregation" [48] was performed, grouping the soil layers according to their similarities between isotopic signatures, evaporation front presence and proximity within the soil profile. The grouping was settled as: 0–30 cm, 30–60 cm, >60 cm; including in the last soil layer the groundwater due its isotopic similarity with the deeper soil waters. The IsoSource output shows all the possible solutions to match the sap water mixture of δ^2H and δ^{18}O (Figure 6). The Willow tree stand shows a well-defined proportion of soil water contributions among the three water sources. The deep water source (>60 cm) contributes, with a proportion lower than 0.08, to the sap water mixture, while the upper soil layers (<30 cm) provides between 0.28 and 0.48 of the mixed water and the intermediate soil layers (30–60 cm) own the higher contribution values from 0.50 to 0.64. The clear differentiation between soil water sources in Willow is not visible for Willow bush. This species shows overlapping contributions of the water sources mainly for the superficial soil layers (0–60 cm), showing the deepest water source a contribution ranging from 0.21 to 0.54 (Figure 6).
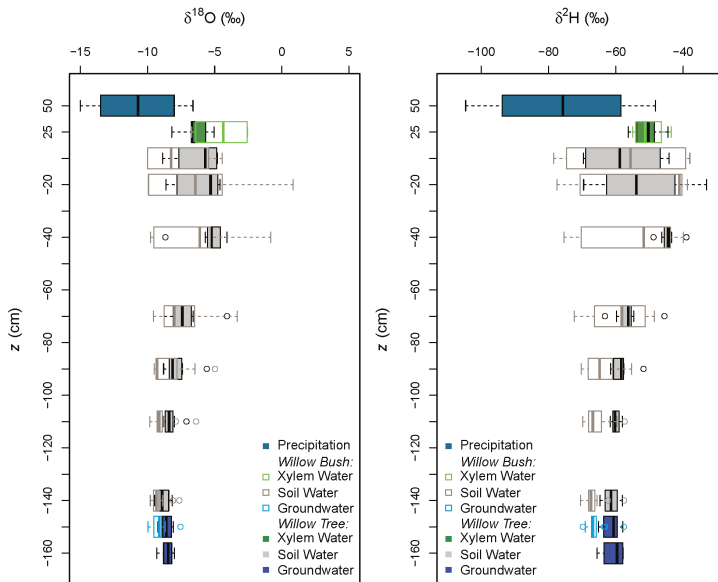

Figure 5. Isotopic profile of the stable water isotopes sampled in both stands during autumn 2010. Each boxplot describes the data set with the median (thick vertical line within the box), the first and third quartiles (edges of the box) and the minimum and maximum values (whiskers).
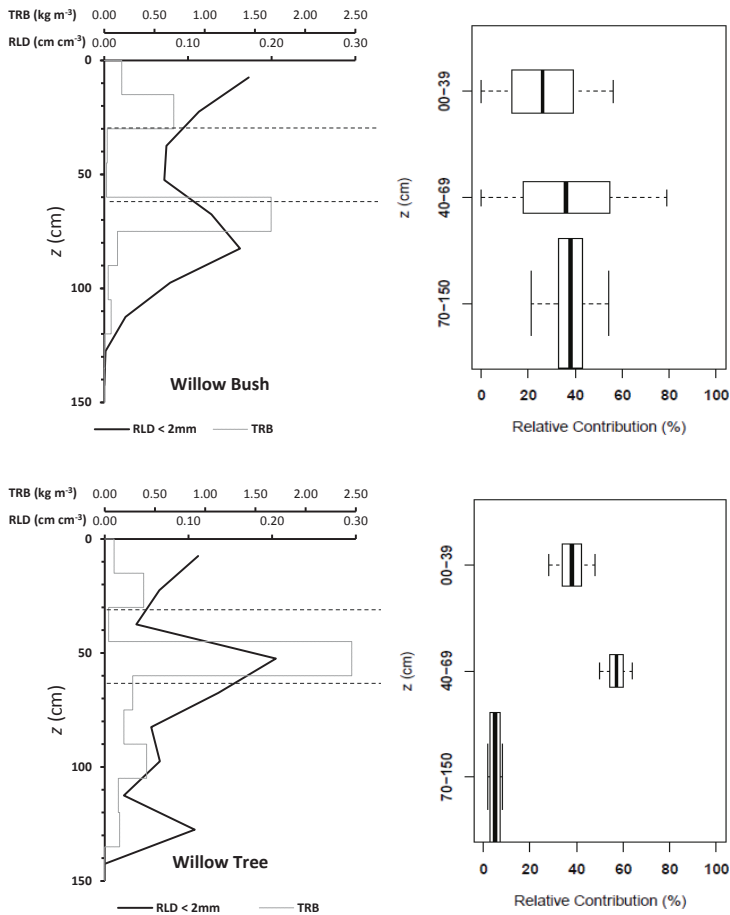
Figure 6. Root length density (RLD) and total root biomass (TRB) distribution along the soil profile and its relation with the relative contribution to sap water mixture of Willow tree and Willow bush based on δ^2H and δ^{18}O isotope signatures per group of soil depth. Each boxplot describes the the median (thick vertical line within the box), the first and third quartiles (edges of the box) and the minimum and maximum values (whiskers). The boxplot height is proportional to the soil depth range.

Plant densities differ between stands, where the Willow bush stand has the higher plant density (900 trees ha^{-1}) with an average height of 2.6 ± 0.6 m. In contrast, the Willow tree stand has a plant density three times smaller (300 trees ha^{-1}) but with higher trees (3.5 ± 0.5 m). However, the LAI is affected by the leaf size and canopy diameter of the individual plants, where Willow bush register a leaf area index of 0.39 m^2 m^{-2} which is twice smaller than Willow tree (0.68 m^2 m^{-2}). Underground stand characteristics also differ between species. Willow trees fix a larger root biomass beneath the 45 cm depth than Willow bush shrubs. Moreover, the root length density distribution shows a bimodal accumulation in Willow bush: at the soil surface (0–30 cm) and at mid depth (55–70 cm). Oppositely, Willow tree has three sections with high RLD values. The first two sections follow the Willow bush pattern, with an additional accumulation bellow 105 cm. The fine root distribution in both species expressed as RLD, provide them a good system for soil water acquisition for the superficial soil layers (Figure 6).

4. Discussion

The main differences in plant size, fine root distribution and water uptake capacity between Willow tree and Willow bush underline the importance of selecting plant species with low water requirements in respect to their biomass for afforestation programs. Willow tree is capable to withdraw up to 12.8 kg day^{-1} of water, extracting more than 90% from soil layers above 60 cm depth. This species is capable to make use of the superficial soil water during the autumn period, even if the groundwater level is shallow. Conversely, Willow bush show lower transpiration rates not higher than 5.0 kg day^{-1} extracted uniformly from the whole soil profile including the groundwater. This extraction pattern shown by Willow bush depicts a more efficient root system acquiring water from different soil water sources due their fine root distribution. During this period, both species extract more than 50% of the water from the upper soil layers, taking advantage of the sporadic autumn rains and residual soil moisture. These results are congruent with the behavior of Willow bush during the growing season (May–July), where Willow bush uses water from both sources—soil and groundwater [18]. On the other hand, the soil water dependency during autumn of Willow trees differ in their summer behavior as documented by Yin et al. [17]. During summer, Willow trees have access to soil and groundwater to maintain their water consumption.

Shallow groundwater levels prevent desiccation processes in scarce rainfall environments, providing a vast water source for adapted plants that use the water economically [65]. Even if both species do not differ in the root amount, their vertical distribution shows different root spots. Willow bush root distribution displays two zones, supporting the hierarchy theory proposed by Schwinning and Sala [66]. The Willow bush can withdraw water from rains as stemflow, while the deeper roots can obtained from a constant source (groundwater in this case). The fine root distribution beneath the Willow tree exemplifies woody patches capacity to use rain water in a short time response [67], as well as the hierarchy theory of Schwinning and Sala [66]. The fine root distribution of Willow tree with three dense regions with RLD higher than 0.1 cm cm^{-3} allow them to use different soil water source depending on soil water availability.

The isotopic values of groundwater are similar to local rain water (see Appendix C Figure A3), depicting a local groundwater recharge documented for the Hailiutu catchment [18]. This is the consequence of the high capacity to infiltrate water by the sandy soils [21]. Consequently, infiltrated water will be available for longer periods because soil water evaporation at soil depths between 10–30 cm can take several weeks in arid environments [24]. The shallow groundwater recharge occurred during the previous growing season due to the high rainfall intensities (>5 mm day^{-1}) between July and September. This phenomenon has also been documented by Li et al. [68] in Taihang (China), reporting a daily groundwater recharge with rains ranging from 3.2 mm day^{-1} to 3.8 mm day^{-1}. This recharge capacity has been registered in the provinces of Shangxi and Inner Mongolia, gattering from 9% to 12% of the long term annual precipitation [22].

Conversely to groundwater, the isotopic composition of the soil water in the unsaturated zone is affected by the interaction between vegetation cover and soil evaporation (see Appendix C Figure A3). Soil evaporation affects the isotopic signature of soil water in the unsaturated zone providing particular signatures at different soil layers [69–72]. Meanwhile the plant cover type reduces the soil evaporation, where lower θ in the top soil layer (0–10 cm) were registered for Willow bushes in comparison to Willow trees. Conversely, the high θ under Willow bush in respect to Willow tree reflects capacity to fix more root biomass below 40 cm depth. This enhanced the infiltration capacity by the presence of a low plant cover with a large alive root system [73,74].

However, the stable isotope signatures of soil water beneath the plant cover differs considerably. Beneath Willow trees, both isotopes depict the theoretical evaporation front. This as a consequence of the evaporation process in the superficial soil layers, enabling the generation of heavy isotope enrichment [67–69,75,76] (see Figure 5). On the other hand, beneath Willow bush only the δ^{18}O profile shows the theoretical evaporation front. The homogeneity of δ^2H beneath Willow bush indicates

a recent redistribution of groundwater along the soil profile, which can be linked to hydraulic lift processes carried out by this bush.

Lower evaporation rates during the study period depict a lower water need for both species, that is visible in the diminution of sap flow rates. Solar radiation and air temperature are the limiting factors for transpiration as it was showed by the p_{values}. The diminution of solar radiation and air temperature in the region are the clear indication of the arrival of autumn [3], which reduces the available energy for the plants to carry out the photosynthesis. Also, the access to the groundwater reservoir allowed the plants to prevent dehydration, reducing the effect of wind speed and relative humidity as triggers of the transpiration process as it happens during summer with both species [17,62]. This reduction in water needs affects the water uptake of Willow tree, which registered a lower contribution of deep soil water sources while the water uptake by superficial roots is more constant. On the other hand, Willow bush shows a high dynamic root system which extracts water from all the available sources indifferently from the upper soil layers and a strong contribution of the deep sources. This contribution is linked to the root distribution, keeping a high root length density in comparison to the Willow tree. The groundwater dependency of Willow bush [18] implies a permanent deep water extraction during summer and autumn, extracting more deep water than Willow trees during the autumn season.

Despite the few rains, water used of both plant species does not reduce the soil water storage on the soil layers above 100 cm. This can be linked to the presence of hydraulic lift, where the root system prevents the soil water depletion on upper soil layers thanks to the redistribution of deeper soil water (in this case, groundwater). The hydraulic lift allows the formation of water pools along the soil profile in water scarce environments [77,78]. This process requires the movement of soil water by the potential difference between roots and the soil [77–80], allowing the diffusion of water through the roots cell membranes. The hydraulic lift had been identified in different plant species such as *Prosopis tamarugo*, *Artemisia tridentata*, *Acer saccharum* and *Madicago sativa* [77].

The hydraulic lifted water has an isotope signature close to the groundwater. It is relocated during night periods [81] and once it is on the superficial soil layers evaporation will happen affecting the isotope signature of soil water [82]. This water relocation is maintained by Willow trees, which despite the larger transpiration rates the soil water is not shortened. Liste and White [78] mention a Willow as a tree with the water redistribution capacity, providing evidence related to the potential of Willow to use groundwater through this process. Other tree species such as *Eucalyptus kochii* has the capacity to redistribute groundwater [79] or use it as an strategy of competition in saline conditions like *Juniperus phoenicea* and *Pistacia lentiscus* [83].

The replacement of bare soil areas with different plant covers none adapted to arid environments, speed up the water use in those regions. Water needs of plants such as the Willow tree (*Salix matsudana*) are high and require a constant water supply [17,59]. On the other hand, the use of plants adapted to arid environments such as the Willow bush (*Salix psammophila*) [58] ensure the success of the afforestation programs without risking the scarce water resources. The plant water use during summer months is the largest of the year, as a consequence of the long light hours in temperate regions [3]. During this time of the year the newly afforested zones extract more water from the soil and groundwater reservoirs. However, the diminution of solar radiation and temperature during autumn reduces the water demand by all the plants. These plants can redistribute part of the groundwater to the upper soil layers, making it available for the periods with no rains. Also, these plants have the capacity to reduce soil evaporation thanks to the shadow effect of their canopy.

5. Conclusions

The presence of Willow trees (*Salix matsudana*) and Willow bushes (*Salix psammophila*) reduced the effect of soil evaporation after summer, allowing a larger soil moisture beneath both species than bare soil conditions. Also, the plant cover allowed the soil moisture below 60 cm depth to be larger than the field capacity for sandy soils. This augment in soil water can be linked to water redistribution thanks to the presence of fine roots along the soil profile and the hydraulic lift carried out by the plants.

This process redistributes groundwater on the spots with larger fine root allocation, enabling the plants to allocate it at night and using it later during day time. Willow trees uses more water for transpiration than willow bushes, this difference in water consumption allowed the Willow bushes to kept a higher soil moisture after summer (θ: $0.11\,\text{m}^3\,\text{m}^{-3}$) followed by Willow trees (θ: $0.10\,\text{m}^3\,\text{m}^{-3}$) and bare soil ($\theta$: $0.08\,\text{m}^3\,\text{m}^{-3}$). The larger transpiration rates of Willow trees respect to Willow bushes do not match with the water source of the xylem water as it is showed by the IsoSource model. This is linked with the hydraulic lift capacity of Willow tree, redistributing groundwater that is quickly affected by evaporation processes. Fine root distribution along the soil profile allowed the water redistribution and later absorption by both plants. This is supported by both species preferences to withdraw water from the upper soil layers. The water use by Willow bush does not show a strong differentiation among water sources. This species is capable of extract soil and ground water with different proportions according to water availability. On the other hand, Willow tree is able to extract soil water and groundwater with specific proportions. The species selection for afforestation programs has to be carried out carefully to not endanger the scarce water resources in arid regions. Thus considering that species such as Willow trees use more water than Willow bushes, despite the diminution in solar radiation and air temperature during autumn.

Appendix A

Figure A1. Photographs of the experimental sites and different sampling procedures carried out in Yulin County; Shaanxi province–China. Picture (**A**): panoramic view of the bush lands dominated by Willow bushes. Picture (**B**): bare soil conditions close to the experimental plots. Picture (**C**): experimental plot with Willow trees. Picture (**D**): Thermal dissipation probe installed in a Willow tree. Picture (**E**): Root sampling within Willow Tree Plot. Picture (**F**): print screen of the fine root measuring procedure.

Appendix B
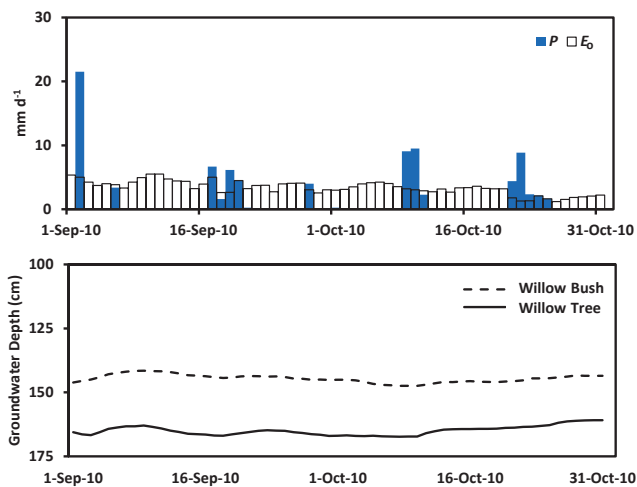
Figure A2. Daily measurements of precipitation, evaporation and groundwater depth during the monitoring period.

Appendix C
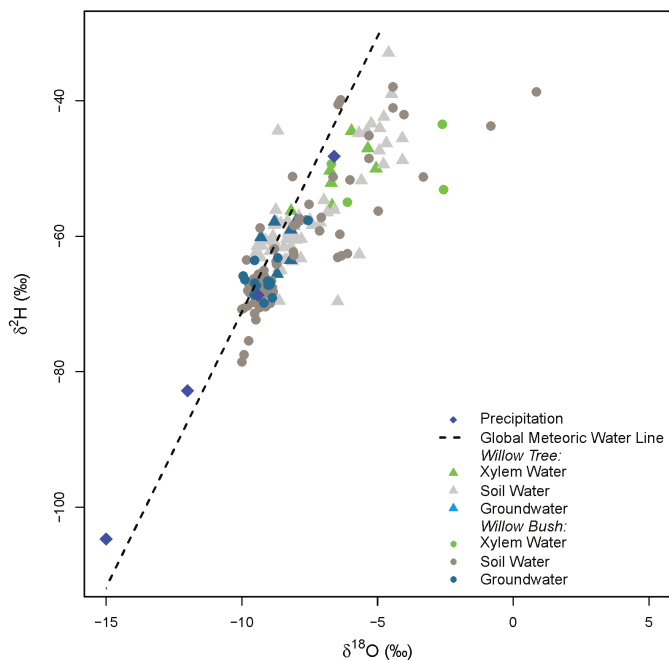
Figure A3. Dual isotope plot of δ^2H and δ^{18}O for the water samples analyzed in the study.

References

1. Abd El-Ghani, M.M.; Huerta-Martínez, F.M.; Hongyan, L.; Qureshi, R. Arid Deserts of the World: Origin, Distribution, and Features. In *Plant Responses to Hyperarid Desert Environments*; Springer International Publishing: Cham, Switzerland, 2017; pp. 1–7. [CrossRef]

2. Salem, B. *Arid Zone Forestry: A Guide for Field Technicians*; Number 20; Food and Agriculture Organization (FAO): Rome, Italy, 1989.

3. Bonan, G. *Ecological Climatology: Concepts and Applications*; Cambridge University Press: Cambridge, UK, 2002.

4. Aguiar, M.R.; Sala, O.E. Patch structure, dynamics and implications for the functioning of arid ecosystems. *Trends Ecol. Evol.* **1999**, *14*, 273–277. [CrossRef]

5. Wainwright, J.; Mulligan, M.; Thornes, J. Plants and water in drylands. In *Eco-Hydrology: Plants and Water in Terrestrial and Aquatic Environments*; Baird, A., Wilby, R., Eds.; Routledge: Abingdon, UK, 1999; pp. 78–126.

6. FAO. *Guidelines for Soil Description*; Food and Agriculture Organization (FAO): Rome, Italy, 2006.

7. Huggett, R. *Fundamentals of Geomorphology*, 2nd ed.; Routledge Fundamentals of Physical Geography: Abingdon, UK, 2007.

8. Summerfield, M. *Global Geomorphology*; Longman: Harlow, UK, 1991.

9. Yang, X.; Zhang, K.; Jia, B.; Ci, L. Desertification assessment in China: An overview. *J. Arid. Environ.* **2005**, *63*, 517–531. [CrossRef]

10. Young, A. *Agroforestry for Soil Conservation*; CAB International: Wallingford, UK, 1989.

11. Han, K.S.; Park, Y.Y.; Yeom, J.M. Detection of change in vegetation in the surrounding Desert areas of Northwest China and Mongolia with multi-temporal satellite images. *Asia-Pac. J. Atmos. Sci.* **2015**, *51*, 173–181. [CrossRef]

12. Song, X.; Wang, T.; Xue, X.; Yan, C.; Li, S. Monitoring and analysis of aeolian desertification dynamics from 1975 to 2010 in the Heihe River Basin, northwestern China. *Environ. Earth Sci.* **2015**, *74*, 3123–3133. [CrossRef]

13. Cao, S.; Tian, T.; Chen, L.; Dong, X.; Yu, X.; Wang, G. Damage Caused to the Environment by Reforestation Policies in Arid and Semi-Arid Areas of China. *AMBIO* **2010**, *39*, 279–283. [CrossRef]

14. Cao, S.; Chen, L.; Shankman, D.; Wang, C.; Wang, X.; Zhang, H. Excessive reliance on afforestation in China's arid and semi-arid regions: Lessons in ecological restoration. *Earth-Sci. Rev.* **2011**, *104*, 240–245. [CrossRef]

15. Peng, S.S.; Piao, S.; Zeng, Z.; Ciais, P.; Zhou, L.; Li, L.Z.X.; Myneni, R.B.; Yin, Y.; Zeng, H. Afforestation in China cools local land surface temperature. *Proc. Natl. Acad. Sci. USA* **2014**, *111*, 2915–2919. [CrossRef]

16. Yang, Z.; Zhou, Y.; Wenninger, J.; Uhlenbrook, S. The causes of flow regime shifts in the semi-arid Hailiutu River, Northwest China. *Hydrol. Earth Syst. Sci.* **2012**, *16*, 87–103. [CrossRef]

17. Yin, L.; Zhou, Y.; Huang, J.; Wenninger, J.; Hou, G.; Zhang, E.; Wang, X.; Dong, J.; Zhang, J.; Uhlenbrook, S. Dynamics of willow tree (Salix matsudana) water use and its response to environmental factors in the semi-arid Hailiutu River catchment, Northwest China. *Environ. Earth Sci.* **2014**, *71*, 4997–5006. [CrossRef]

18. Zhou, Y.; Wenninger, J.; Yang, Z.; Yin, L.; Huang, J.; Hou, L.; Wang, X.; Zhang, D.; Uhlenbrook, S. Groundwater–surface water interactions, vegetation dependencies and implications for water resources management in the semi-arid Hailiutu River catchment, China—A synthesis. *Hydrol. Earth Syst. Sci.* **2013**, *17*, 2435–2447. [CrossRef]

19. Roberts, J. Plants and water in forests and woodlands. In *Eco-Hydrology: Plants and Water in Terrestrial and Aquatic Environments*; Routledge: Abingdon, UK, 1999; pp. 181–236.

20. Savenije, H.H.G. The importance of interception and why we should delete the term evapotranspiration from our vocabulary. *Hydrol. Process.* **2004**, *18*, 1507–1511. [CrossRef]

21. Yaseef, N.R.; Yakir, D.; Rotenberg, E.; Schiller, G.; Cohen, S. Ecohydrology of a semi-arid forest: Partitioning among water balance components and its implications for predicted precipitation changes. *Ecohydrology* **2009**, *3*, 143–154. [CrossRef]

22. Scanlon, B.R.; Keese, K.E.; Flint, A.L.; Flint, L.E.; Gaye, C.B.; Edmunds, W.M.; Simmers, I. Global synthesis of groundwater recharge in semiarid and arid regions. *Hydrol. Process.* **2006**, *20*, 3335–3370. [CrossRef]

23. Zhang, Y.F.; Wang, X.P.; Hu, R.; Pan, Y.X.; Paradeloc, M. Rainfall partitioning into throughfall, stemflow and interception loss by two xerophytic shrubs within a rain-fed re-vegetated desert ecosystem, northwestern China. *J. Hydrol.* **2015**, *527*, 1084–1095. [CrossRef]

24. Noy-Meir, I. Desert Ecosystems: Environment and Producers. *Annu. Rev. Ecol. Syst.* **1973**, *4*, 25–51. [CrossRef]

25. Chesson, P.; Gebauer, R.L.E.; Schwinning, S.; Huntly, N.; Wiegand, K.; Ernest, M.S.K.; Sher, A.; Novoplansky, A.; Weltzin, J.F. Resource pulses, species interactions, and diversity maintenance in arid and semi-arid environments. *Oecologia* **2004**, *141*, 236–253. [CrossRef]

26. Ivans, S.; Hipps, L.; Leffler, A.J.; Ivans, C.Y. Response of Water Vapor and CO_2 Fluxes in Semiarid Lands to Seasonal and Intermittent Precipitation Pulses. *J. Hydrometeorol.* **2006**, *7*, 995–1010. [CrossRef]

27. Ogle, K.; Wolpert, R.L.; Reynolds, J.F. Reconstructing plant root area and water uptake profiles. *Ecology* **2004**, *85*, 1967–1978. [CrossRef]

28. Hopkins, W.G.; Hüner, N.P. *Introduction to Plant Physiology*; Wiley: Hoboken, NJ, USA, 2008.

29. Cardon, Z.G.; Whitbeck, J.L. *The Rhizosphere. An Ecological Perspective*; Elsevier Academic Press: Amsterdam, The Nertherlands, 2007.

30. Curl, E.; Truelove, B. *The Rhizosphere*; Springer: New York, NY, USA, 1986.

31. Dawson, T.E.; Mambelli, S.; Plamboeck, A.H.; Templer, P.H.; Tu, K.P. Stable Isotopes in Plant Ecology. *Annu. Rev. Ecol. Syst.* **2002**, *33*, 507–559. [CrossRef]

32. Evaristo, J.; McDonnell, J.J.; Clemens, J. Plant source water apportionment using stable isotopes: A comparison of simple linear, two-compartment mixing model approaches. *Hydrol. Process.* **2017**, *31*, 3750–3758. [CrossRef]

33. Jia, Z.; Zhu, Y.; Liu, L. Different Water Use Strategies of Juvenile and Adult *Caragana intermedia* Plantations in the Gonghe Basin, Tibet Plateau. *PLoS ONE* **2012**, *7*, e45902. [CrossRef] [PubMed]

34. Nie, Y.P.; Chen, H.S.; Wang, K.l.; Tan, W.; Deng, P.Y.; Yang, J. Seasonal water use patterns of woody species growing on the continuous dolostone outcrops and nearby thin soils in subtropical China. *Plant Soil* **2011**, *341*, 399–412. [CrossRef]

35. Palacio, S.; Montserrat-Martí, G.; Ferrio, J.P. Water use segregation among plants with contrasting root depth and distribution along gypsum hills. *J. Veg. Sci.* **2017**, *28*, 1107–1117. [CrossRef]

36. Rossatto, D.R.; da Silveira Lobo Sternberg, L.; Franco, A.C. The partitioning of water uptake between growth forms in a Neotropical savanna: Do herbs exploit a third water source niche? *Plant Biol.* **2012**, *15*, 84–92. [CrossRef] [PubMed]

37. Swaffer, B.A.; Holland, K.L.; Doody, T.M.; Li, C.; Hutson, J. Water use strategies of two co-occurring tree species in a semi–arid karst environment. *Hydrol. Process.* **2013**, *28*, 2003–2017. [CrossRef]

38. Voltas, J.; Lucabaugh, D.; Chambel, M.R.; Ferrio, J.P. Intraspecific variation in the use of water sources by the circum-Mediterranean conifer Pinus halepensis. *New Phytol.* **2015**, *208*, 1031–1041. [CrossRef] [PubMed]

39. Wang, P.; Song, X.; Han, D.; Zhang, Y.; Liu, X. A study of root water uptake of crops indicated by hydrogen and oxygen stable isotopes: A case in Shanxi Province, China. *Agric. Water Manag.* **2010**, *97*, 475–482. [CrossRef]

40. Wei, L.; Lockington, D.A.; Poh, S.C.; Gasparon, M.; Lovelock, C.E. Water use patterns of estuarine vegetation in a tidal creek system. *Oecologia* **2013**, *172*, 485–494. [CrossRef]

41. Barbeta, A.; Ogée, J.; Peñuelas, J. Stable-Isotope Techniques to Investigate Sources of Plant Water. In *Advances in Plant Ecophysiology Techniques*; Sánchez-Moreiras, A.M., Reigosa, M.J., Eds.; Springer International Publishing: Cham, Switzerland, 2018; pp. 439–456. [CrossRef]

42. Geyh, M. Groundwater. Saturated and unsaturated zone. In *Environmental Isotopes in the Hydrological Cycle: Principles and Applications*; Mook, W., Ed.; UNESCO: Paris, France, 2000; Volume IV.

43. Leibundgut, C.; Seibert, J. 2.09. Tracer Hydrology. In *Treatise on Water Science*; Wilderer, P., Ed.; Elsevier: Amsterdam, The Netherlands, 2011; pp. 215–236.

44. Butt, S.; Ali, M.; Fazil, M.; Latif, Z. Seasonal variations in the isotopic composition of leaf and stem water from an arid region of Southeast Asia. *Hydrol. Sci. J.* **2010**, *55*, 844–848. [CrossRef]

45. Parnell, A.C.; Inger, R.; Bearhop, S.; Jackson, A.L. Source partitioning using stable isotopes: Coping with too much variation. *PLoS ONE* **2010**, *5*, e9672. [CrossRef]

46. Parnell, A.C.; Phillips, D.L.; Bearhop, S.; Semmens, B.X.; Ward, E.J.; Moore, J.W.; Jackson, A.L.; Grey, J.; Kelly, D.J.; Inger, R. Bayesian stable isotope mixing models. *Environmetrics* **2013**, *24*, 387–399. [CrossRef]

47. Moore, J.W.; Semmens, B.X. Incorporating uncertainty and prior information into stable isotope mixing models. *Ecol. Lett.* **2008**, *11*, 470–480. [CrossRef] [PubMed]

48.   Phillips, D.L.; Newsome, S.D.; Gregg, J.W.   Combining sources in stable isotope mixing models: Alternative methods. *Oecologia* **2005**, *144*, 520–527. [CrossRef] [PubMed]

49.   Phillips, D.L.; Gregg, J.W. Source partitioning using stable isotopes: Coping with too many sources. *Oecologia* **2003**, *136*, 261–269. [CrossRef] [PubMed]

50.   Zhu, J.; Sun, D.; Young, M.H.; Caldwell, T.G.; Pan, F.   Shrub spatial organization and partitioning of evaporation and transpiration in arid environments. *Ecohydrology* **2015**, *8*, 1218–1228. [CrossRef]

51.   Walker, B.H.; Langridge, J.L. Modelling plant and soil water dynamics in semi-arid ecosystems with limited site data. *Ecol. Model.* **1996**, *87*, 153–167. [CrossRef]

52.   Schlesinger, W.H.; Fonteyn, P.J.; Marion, G.M.   Soil moisture content and plant transpiration in the Chihuahuan Desert of New Mexico. *J. Arid. Environ.* **1987**, *12*, 119–126. [CrossRef]

53.   IIASA/FAO. *Global Agro-Ecological Zones (GAEZ v3.0)*; IIASA: Laxenburg, Austria; FAO: Rome, Italy, 2012.

54.   NCDC. NNDC Climate Data Online. 2012. Available online: http://www7.ncdc.noaa.gov/CDO/cdoselect. cmd (accessed on 23 January 2012).

55.   Allen, R.G.; Pereira, L.S.; Raes, D.; Smith, M.   *Crop Evapotranspiration-Guidelines for Computing Crop Water Requirements–FAO Irrigation and Drainage Paper 56*; FAO: Rome, Italy, 1998.

56.   Saxton, K.E.; Rawls, W.J. Soil water characteristic estimates by texture and organic matter for hydrologic solutions. *Soil Sci. Soc. Am. J.* **2006**, *70*, 1569–1578. [CrossRef]

57.   Craig, H. Standard for Reporting Concentrations of Deuterium and Oxygen-18 in Natural Waters. *Science* **1961**, *133*, 1833–1834. [CrossRef]

58.   Wang, Z.; Chang, Y. *Salix Psammophila*; Bulletin of Botanical Laboratory of North-Eastern Forestry Institute: Harbin, China, 1980; Volume 9.

59.   Gilman, E.; Watson, G.   *Salix Matsudana 'Tortuosa' Corkscrew Willow*; Fact Sheet ST-577 Environmental Horticulture Department, Florida Cooperative Extension Service, Institute of Food and Agricultural Sciences, University of Florida: Gainesville, FL, USA, 1994.

60.   Granier, A. Une nouvelle méthode pour la mesure du flux de sève brute dans le tronc des arbres. *Ann. Des Sci. For.* **1985**, *42*, 193–200. [CrossRef]

61.   Cornelissen, J.; Lavorel, S.; Garnier, E.; Diaz, S.; Buchmann, N.; Gurvich, D.; Reich, P.; Ter Steege, H.; Morgan, H.; Van Der Heijden, M.; et al. A handbook of protocols for standardised and easy measurement of plant functional traits worldwide. *Aust. J. Bot.* **2003**, *51*, 335–380. [CrossRef]

62.   Huang, J.; Zhou, Y.; Yin, L.; Wenninger, J.; Zhang, J.; Hou, G.; Zhang, E.; Uhlenbrook, S. Climatic controls on sap flow dynamics and used water sources of Salix psammophila in a semi-arid environment in northwest China. *Environ. Earth Sci.* **2015**, *73*, 289–301. [CrossRef]

63.   Kottek, M.; Grieser, J.; Beck, C.; Rudolf, B.; Rubel, F. World map of the Köppen-Geiger climate classification updated. *Meteorol. Z.* **2006**, *15*, 259–263. [CrossRef]

64.   Peel, M.C.; Finlayson, B.L.; Mcmahon, T.A. Updated world map of the Köppen-Geiger climate classification. *Hydrol. Earth Syst. Sci. Discuss.* **2007**, *4*, 439–473. [CrossRef]

65.   Jiang, G.; He, W. Species- and habitat-variability of photosynthesis, transpiration and water use efficiency of different plant species in Maowusu Sand Area. *Acta Bot. Sin.* **1999**, *41*, 1114–1124.

66.   Schwinning, S.; Sala, O.E. Hierarchy of responses to resource pulses in arid and semi-arid ecosystems. *Oecologia* **2004**, *141*, 211–220. [CrossRef]

67.   Midwood, A.; Boutton, T.; Archer, S.; Watts, S. Water use by woody plants on contrasting soils in a savanna parkland: assessment with δ^2H and δ^{18}O. *Plant Soil* **1998**, *205*, 13–24. [CrossRef]

68.   Li, F.; Song, X.; Tang, C.; Liu, C.; Yu, J.; Zhang, W. Tracing infiltration and recharge using stable isotope in Taihang Mt., North China. *Environ. Geol.* **2007**, *53*, 687–696. [CrossRef]

69.   Barnes, C.J.; Allison, G. Tracing of water movement in the unsaturated zone using stable isotopes of hydrogen and oxygen. *J. Hydrol.* **1988**, *100*, 143–176. [CrossRef]

70.   Brunel, J.P.; Walker, G.R.; Kennett-Smith, A.K. Field validation of isotopic procedures for determining sources of water used by plants in a semi-arid environment. *J. Hydrol.* **1995**, *167*, 351–368. [CrossRef]

71.   Rothfuss, Y.; Biron, P.; Braud, I.; Canale, L.; Durand, J.L.; Gaudet, J.P.; Richard, P.; Vauclin, M.; Bariac, T. Partitioning evapotranspiration fluxes into soil evaporation and plant transpiration using water stable isotopes under controlled conditions. *Hydrol. Process.* **2010**, *24*, 3177–3194. [CrossRef]

72.   Schwinning, S.; Ehleringer, J.R. Water use trade-offs and optimal adaptations to pulse-driven arid ecosystems. *J. Ecol.* **2001**, *89*, 464–480. [CrossRef]

73. Basche, A.D.; DeLonge, M.S. Comparing infiltration rates in soils managed with conventional and alternative farming methods: A meta-analysis. *PLoS ONE* **2019**, *14*, e0215702. [CrossRef] [PubMed]

74. Fischer, C.; Tischer, J.; Roscher, C.; Eisenhauer, N.; Ravenek, J.; Gleixner, G.; Attinger, S.; Jensen, B.; de Kroon, H.; Mommer, L.; et al. Plant species diversity affects infiltration capacity in an experimental grassland through changes in soil properties. *Plant Soil* **2015**, *397*, 1–16. [CrossRef]

75. Sutanto, S.J.; Wenninger, J.; Coenders-Gerrits, A.M.J.; Uhlenbrook, S. Partitioning of evaporation into transpiration, soil evaporation and interception: A comparison between isotope measurements and a HYDRUS-1D model. *Hydrol. Earth Syst. Sci.* **2012**, *16*, 2605–2616. [CrossRef]

76. Wenninger, J.; Beza, D.T.; Uhlenbrook, S. Experimental investigations of water fluxes within the soil–vegetation–atmosphere system: Stable isotope mass-balance approach to partition evaporation and transpiration. *Phys. Chem. Earth Parts A/B/C* **2010**, *35*, 565–570. [CrossRef]

77. Horton, J.L.; Hart, S.C. Hydraulic lift: A potentially important ecosystem process. *Trends Ecol. Evol.* **1998**, *13*, 232–235. [CrossRef]

78. Liste, H.H.; White, J.C. Plant hydraulic lift of soil water—Implications for crop production and land restoration. *Plant Soil* **2008**, *313*, 1–17. [CrossRef]

79. Brooksbank, K.; White, D.A.; Veneklaas, E.J.; Carter, J.L. Hydraulic redistribution in Eucalyptus kochii subsp. borealis with variable access to fresh groundwater. *Trees* **2011**, *25*, 735–744. [CrossRef]

80. Niinemets, U. Responses of forest trees to single and multiple environmental stresses from seedlings to mature plants: Past stress history, stress interactions, tolerance and acclimation. *For. Ecol. Manag.* **2010**, *260*, 1623–1639. [CrossRef]

81. Caldwell, M.M.; Dawson, T.E.; Richards, J.H. Hydraulic lift: Consequences of water efflux from the roots of plants. *Oecologia* **1998**, *113*, 151–161. [CrossRef] [PubMed]

82. Dawson, T.E.; Pate, J.S. Seasonal water uptake and movement in root systems of Australian phraeatophytic plants of dimorphic root morphology: A stable isotope investigation. *Oecologia* **1996**, *107*, 13–20. [CrossRef] [PubMed]

83. Armas, C.; Padilla, F.M.; Pugnaire, F.I.; Jackson, R.B. Hydraulic lift and tolerance to salinity of semiarid species: Consequences for species interactions. *Oecologia* **2010**, *162*, 11–21. [CrossRef] [PubMed]

Developing Meteoric Water Lines for Iran Based on Air Masses and Moisture Sources

Mojtaba Heydarizad [1], Ezzat Raeisi [1], Rogert Sorí [2] and Luis Gimeno [2,*

[1]   Department of Geology, Faculty of Sciences, Shiraz University, Shiraz 71946-84695, Iran;
       mojtabaheydarizad@shirazu.ac.ir (M.H.); e_raeisi@yahoo.com (E.R.)

[2]   Environmental Physics Laboratory (EphysLab), Facultad de Ciencias, Universidade de Vigo, 32004 Ourense,
       Spain; rogert.sori@uvigo.es

*   Correspondence: l.gimeno@uvigo.es

Abstract: Iran is a semi-arid to arid country that faces a water shortage crisis. Its weather is also influenced by various air masses and moisture sources. Therefore, applying accurate stable isotope techniques to investigate Iran's precipitation characteristics and developing Iran meteoric water lines (MWLs) as an initial step for future isotope hydrology studies is vitally important. The aim of this study was to determine the MWLs for Iran by considering air masses and dominant moisture sources. The Hybrid Single-Particle Lagrangian Integrated Trajectory (HYSPLIT) model backward analysis was used to determine the trajectories of various air masses in 19 weather stations in Iran and the areas covered by them. δ^{18}O and δ^2H contents were obtained for precipitation events from 32 stations in Iran and four in Iraq. Stable isotope samples were gathered from different sources and analyzed in various laboratories across the world. Three MWLs for north of Iran, south Zagros, and west Zagros, were determined based on the locations of dominant air masses and moisture sources. The proposed MWLs were validated by comparison with fresh karstic spring isotope data across Iran. In addition, Iran main moisture sources MWLs were used to determine dominant moisture sources role in karstic springs and surface water resources recharge.

Keywords: stable isotopes; HYSPLIT model; MWL validation; karstic springs

1. Introduction

Isotope composition of hydrogen (δ^2H) and oxygen (δ^{18}O) of precipitation provides important fingerprint information and allows for the identification of moisture sources for precipitation, evaporated atmospheric moisture conditions, and air mass trajectory patterns [1–7]. The source of the moisture is the most important predictor of the isotope content of precipitation [1,8]. There are numerous numerical models to study moisture sources, but a Hybrid Single-Particle Lagrangian Integrated Trajectory (HYSPLIT) [9] model has been used in numerous stable isotope studies for tracking moisture sources of precipitation [5,10,11]. Some of these studies, such as [11], consider *d*-excess as reliable fingerprints to study moisture sources responsible for precipitation. Moisture released from water bodies with a high sea surface temperature (SST) and a low relative humidity normally show a high *d*-excess (*d*-excess = δ^2H − 8 × δ^{18}O [12]), whereas precipitation originating from water bodies with a low SST and a high relative humidity will normally have a moderate to low *d*-excess [12–14].

Stable isotope technique is a precious method to study water resources characteristics, mainly in semi-arid and arid regions like Iran. To apply the stable isotope technique, it is important to develop MWLs (as an indicator of the local precipitation). For accurate interpretation in water resource studies, stable isotope data in water supply (surface and groundwater resources) should be compared with local precipitation via MWLs. In most stable isotope studies in Iran, the global meteoric water line

(GMWL) and the Eastern Mediterranean MWL (EMMWL) were used. However, some authors have developed local MWLs for certain regions. References [15–24] developed MWLs for Mashhad, Sirjan, Tehran, Zarivar and Marivan, Khersan, western Zagros, Shahrood, Lar National Park, northeast Iran, and North Khorasan Province, respectively. Each of these MWLs is applicable to the region for which it was developed and cannot be used in other parts of Iran because of differences in altitude, latitude, precipitation, and temperature [25,26]. Therefore, there is a need to develop regional Iran MWLs that can be applied to larger areas of the country. These MWLs will solve crucial obstacles regarding stable isotope studies and will be applied in the future isotope hydrology studies in Iran. In addition, to develop an MWL, the statistical approach should also be applied on precipitation isotopes data. In some studies, including [27,28], a statistical approach has been used in developing MWLs.

Developing unique MWLs for Iran is not practical or reliable due to various weather conditions across Iran. Although Shamsi and Kazemi [29] tried to present a unique MWL with a limited number of samples and stations for Iran, their MWL was not reliable due to various climate conditions that govern in different parts of Iran. Therefore, the authors tried to find a way and presented a method to consider moisture sources in developing MWLs. In previous studies [30,31], it has been determined that Iran is under the influence of various air masses with different isotope characteristics. The aim of this study was to determine the sources of precipitation moisture for different regions of Iran using the HYSPLIT model backward trajectories, and also to determine various air masses' dominance zones. Iran MWLs were developed based on various air masses' dominance zones (presented by HYSPLIT) and validated by comparison with fresh karstic springs. Finally, the MWLs for the main Iran moisture sources were developed. These MWLs were used to study the role and contribution of various air masses in karstic springs and surface water recharges across Iran. The application of moisture sources MWLs to study the role and contribution of various moisture sources in karstic springs and surface water resources recharge is a new method.

2. Iran Climatology and Weather Conditions

Iran is known for its diverse topography and climatology. A number of large water bodies border Iran (the Caspian Sea to the north, and the Persian Gulf and Oman Sea to the south). There are also high mountain ranges in Zagros (west and southwest Iran) and Alborz (north of Iran), which surround two large deserts (Dasht-e Lut and Dasht-e Kavir in central Iran). These features influence the climate of Iran, particularly the distribution of precipitation across the country. Average precipitation in Iran is 250 mm/year which varies from less than 100 mm/year in central Iran to higher than 1000 mm/year in the Caspian Sea coastal area [31]. There is a dry period (May to October) and a wet period (November to April) [31,32]. Four air masses including maritime polar (mP), Mediterranean (MedT), continental polar (also called the Siberian high-pressure system, cP), and continental tropical (also known as Sudan, cT) normally influence Iran in the wet period (November to April). However, the maritime tropical (mT) air mass only influences Iran in the dry period (May to October) [25,26]. The cP air mass predominantly supplies moisture from the Caspian Sea, and to a lesser extent from the Black Sea. It enters from the north and influences the north part of Iran. The mP air mass enters Iran from the northwest and mainly affects northwest Iran. The mP air mass predominantly supplies moisture from the Atlantic Ocean and the Black Sea to Iran. MedT is one of the most active air masses and affects almost all parts of Iran. The MedT air mass supplies moisture from the Mediterranean Sea and the Atlantic Ocean, and to a lesser extent the Black Sea. The cP and mP air masses dominantly influence Iran during December, January and February, while the MedT air mass dominantly influences Iran during March and April. The cT air mass affects most parts of Iran (like the MedT air mass) but affects the south most strongly. The cT air mass enters from the south and rarely affects areas outside of Iran. The cT air mass transports a considerable amount of moisture from the Persian Gulf, the Red Sea, and the Arabian Sea. The cT air mass has a crucial role in Iran precipitation during all of the wet period [31]. Precipitation southeast of Iran is predominantly influenced by the mT air mass [25]. The mT air mass supplies moisture from the Arabian Sea and the Indian Ocean to southeast and south

of Iran. Karimi and Farajzadeh [32] calculated air mass trajectories for Iran using 40-year reanalysis datasets provided by the European Center for Medium Range Weather Forecasts, the US National Centers for Environmental Prediction, and the National Center for Atmospheric Research. Numerical models such as HYSPLIT and FLEXible_PARTicle dispersion model (FLEXPART) have been used widely to identify the most important moisture sources and to determine the roles of moisture sources in supplying precipitation to remote regions in several parts of the world including Iran [1,5,10,33–36].

3. Materials and Methods

The dominant air masses and moisture sources for 900 precipitation events (for the period of 2010 to 2016) at 19 meteorological stations were determined using 120-hour backward trajectories. A precipitation event was considered to have occurred when precipitation was > 5 mm/day. These trajectories were obtained using the online version of the HYSPLIT model called READY (Real Time Environmental Application and Display System) [9,37]. HYSPLIT was initially developed by the US National Oceanic and Atmospheric Administration Air Resources Laboratory in 1982 and has been improved markedly since then. The HYSPLIT model can compute simple air parcel trajectories (backwards and forwards) and complex simulations involving dispersion and deposition [37]. The position of an air parcel at a particular time is computed after wind speed, temperature, pressure, and solar radiation data have been input into the HYSPLIT model from the US National Oceanic and Atmospheric Administration "FNL" meteorological database [37].

δ^{18}O and δ^2H data were obtained from 36 precipitation sampling stations. In addition to precipitation, the isotope composition of hydrogen (δ^2H) and oxygen (δ^{18}O) of fresh karstic springs and surface water resources was also studied. All the isotope data were collected from previous publications in academic journals, PhD theses, MSc dissertations, and reports/data from the Global Network of Isotopes in Precipitation (GNIP) stations, the Karst Research Center of Iran, the Iran Regional Water Authorities, and the Iran Water Resources Institute. For event-based determination of stable isotope composition of precipitation, samples were collected in 25 mL polyethylene bottles after each precipitation event and they were sent to the laboratory for analyses. However, for monthly based samples, the procedure presented by the GNIP was used. To avoid and minimize evaporation in monthly samples, these samples were taken in an event-based approach according to the rainwater collected in the rain gauges after each event, and were transferred into a monthly accumulation bottle [38]. These accumulation bottles were sent to the laboratory for further stable isotope analyses. All the samples were analyzed for δ^2H and δ^{18}O (δ (‰) = (R sample /R standard − 1) × 10^3), where R is ^{2}H/H or ^{18}O/^{16}O ratio. The isotopic composition is expressed in δ per mil, and ‰ shows ^{2}H/H and ^{18}O/^{16}O deviation from the reference VSMOW (Vienna Standard Mean Ocean Water). Analysis of the water samples was performed in several laboratories including G.G. HATCH Stable Isotope Laboratory at the University of Ottawa, Canada; Stable Isotope Laboratory at the University of Waterloo, Canada; IAEA laboratories; Federal Institute for Geosciences and Natural Resources in Hannover, Germany; Isotope Science Laboratory at the University of Calgary, Canada; National Research Center for Environment and Health (GSF), Neuherberg, Germany; the Isotope Hydrology Laboratory at Kumamoto University, Kumamoto, Japan, and several other laboratories across the world. Samples were analyzed for isotope composition of hydrogen (δ^2H) and oxygen (δ^{18}O) using isotope ratio mass spectrometer (IRMS) (Thermo Finigan, Bremen, Germany) and Los Gatos Research, Inc. (LGR) (ABB/LGR group, San Jose, CA, USA) instruments. The analytical standard uncertainties for most of the samples were ± 0.1 ‰ and ± 1‰ for δ^{18}O and δ^2H, respectively.

The MWLs for Iran were developed using available isotope data and moisture sources obtained by HYSPLIT model backward trajectories. A linear regression model was used to determine the trend line between $\delta^{18}O$ and δ^2H data and develop MWLs. Linear regression was done in Microsoft Excel with Analysis ToolPack of Microsoft Office (2016) Professional Plus (Microsoft Corporation, Redmond, WA, USA) with License from the University of Vigo [39]. To understand how well the linear regression model fits the data, R-squared (R^2) value was used. The higher R^2 values demonstrate smaller differences between variable data and also show how strongly the variables are correlated with each other. The developed MWLs of Iran were validated using the $\delta^{18}O$ and δ^2H contents of fresh karstic springs across the country. The application of karstic spring as a natural pluviometer has been done previously in several studies such as [40]. In addition to regression models, the Analysis of Covariance test (ANCOVA) was also applied to the precipitation and karstic springs isotope data. An ANCOVA test is just like an ANOVA test, but ANCOVA takes into account the influence of the covariate (a covariate is a variable which has influence on the dependent variable/variables). The ANCOVA test checks the effect of the covariate on the dependent variable/variables. Authors used R programming (R Core team, Vienna, Austria) to calculate the ANCOVA test [41].

4. Results and Discussion

The contributions of different air masses which caused precipitation at 19 weather stations in Iran were determined using the HYSPLIT model backward trajectories. The results are presented in Figure 1. In addition, the main air mass trajectories toward Iran and areas covered by the different air masses are also shown in this figure. Precipitation in large parts of Iran is influenced by several air masses, but in some parts of the country just one or two air masses predominate.
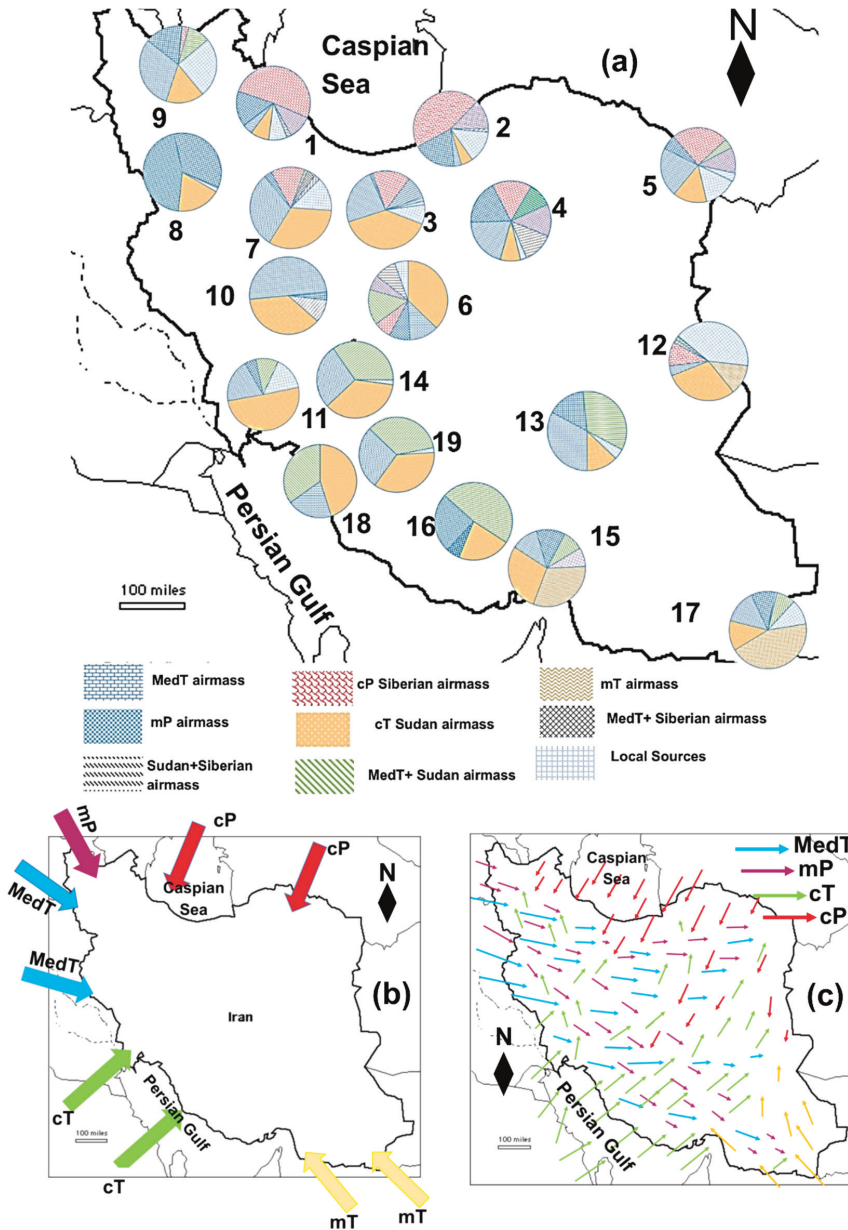
Figure 1. Contributions of different air masses causing precipitation at 19 weather stations in Iran for the period of 2010–2016. (**a**) The dominant air mass trajectories toward Iran. (**b**) The spatial distributions of these air masses across Iran. (**c**) The length of each arrow indicates approximate intensity of the air mass. Station names are as follows: 1 Bandar Anzali, 2 Gorgan, 3 Tehran, 4 Shahrood, 5 Mashhad, 6 Isfahan, 7 Arak, 8 Marivan, 9 Tabriz, 10 Shahrekord, 11 Ahvaz, 12 Zahedan, 13 Sirjan, 14 Samyrom, 15 Bandar Abas, 16 Darab, 17 Chabahar, 18 Bushehr, and 19 Shiraz).

4.1. Developing MWLs for Iran

The mean isotope composition of hydrogen (δ^2H) and oxygen (δ^{18}O) of precipitation as well as *d*-excess, station elevation, precipitation, and air temperature for each station in Iran and Iraq are presented in Supplementary Table S1 [15,16,18,19,21,42–57]. The spatial distribution of the precipitation sampling stations is shown in Figure 2a and karstic springs sampling stations in Figure 2b. These stations were separated into three groups according to air mass dominance zones presented by the HYSPLIT model backward trajectories presented in Figure 1.
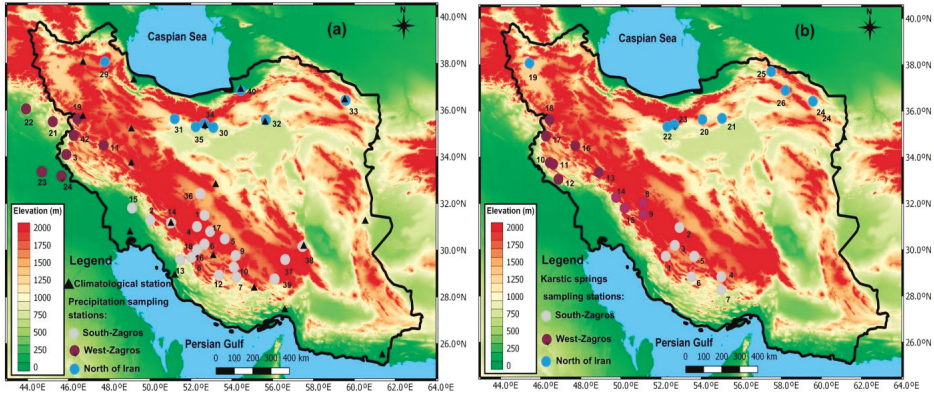

Figure 2. Climatological stations (black triangles) and precipitation sampling sites for isotope composition of hydrogen (δ^2H) and oxygen (δ^{18}O) analysis in North Iran (sky blue circles), West Zagros (brown circles) and South Zagros (gray circles) (**a**). Karstic springs sampling sites for isotope composition of hydrogen (δ^2H) and oxygen (δ^{18}O) analysis in Iran (**b**). The geographic location, boundaries of Iran (black line), and elevation map are derived from the Hydrosheds project [58].

As Iran weather is influenced by various air masses and moisture sources, it has not been possible to develop a single MWL for Iran because the MWL and stable isotopes in precipitation mainly depend on air masses and moisture sources [1,2]. Thus, three MWLs were developed for Iran (one each for Zagros-west, Zagros-south, and north of Iran) according to the various air mass dominance zones across Iran presented in Figure 1. To understand the effect of air mass dominance zones on the developed Iran MWLs, the unique Iran MWL was developed by linear regression model and its R^2 was compared with the R^2 of Iran MWLs developed based on air masses and moisture sources. Results showed that the R^2 values for Iran's unique MWL was lower than the R^2 for Iran MWLs developed based on air masses and moisture sources (Supplementary Table S2). This confirmed that developing MWLs based on air mass and moisture source dominance zones was much more accurate compared to developing a unique MWL for the whole of Iran. The linear regression model was used to develop a trend line between δ^{18}O and δ^2H data and develop MWLs. The proposed Iran MWLs and the relevant equations are shown in Figure 3.

The intercept for the North of Iran MWL (+3.86‰) was markedly lower than the intercept for Zagros-south (14.82‰) and Zagros-west (16.99‰) MWLs, while the North of Iran MWL slope (7.11) was between the slope of Zagros-south (7.06) and Zagros-west (8.12), respectively. The much lower intercept and lower slope of the North of Iran MWL compared to the Zagros region's MWLs was due to various isotope characteristics of moisture sources that influence these regions. The higher slope of the Zagros-west MWL compared to other Iran MWLs and also GMWL δ^2H = (8.17 ± 0.06) δ^{18}O + (10.35 ± 0.65) [59] was due to high relative humidity in this region. This region is covered by high mountains and local jungles with high average annual precipitation and relative humidity (>85%) which is higher than the global average [31]. Furthermore, the average *d*-excess for the north of Iran stations (9.45‰) was considerably lower than the averaged *d*-excess values for the south of

Zagros (18.57‰) and west of Zagros (16.31‰), respectively. This is because the SSTs for the water bodies providing moisture to the Zagros regions (mainly the Mediterranean Sea, the Arabian Sea and the Persian Gulf) are higher during the primary evaporation stage than the SSTs for the water bodies providing moisture to the north of Iran (mainly the Caspian Sea, the Black Sea, and the Atlantic Ocean) [60].
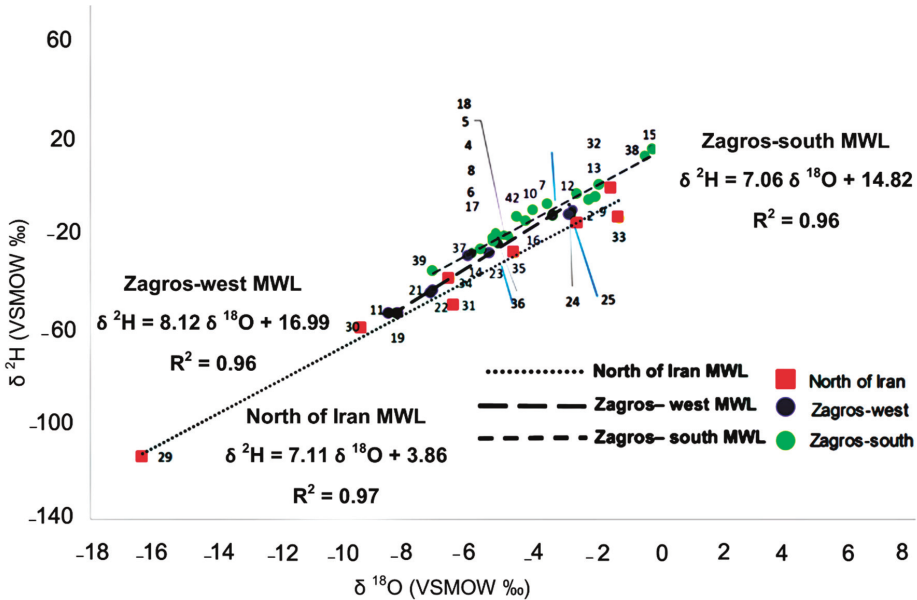

Figure 3. Average δ^2H and δ^{18}O in the sampling station's precipitation, and Iran developed meteoric water lines (MWLs).

In the ANCOVA test on the precipitation samples, air temperature, precipitation amount, and sampling station elevation were considered as covariate variables which influenced the stable isotope content of precipitation. Air mass dominance zones were considered as fixed parameters, while δ^{18}O, δ^2H and d-excess were considered depended variables. After checking the first assumption of the ANCOVA test, only elevation showed $p > 0.05$ and met covariate requirements (Supplementary spreadsheet S1). For the next assumption of the ANCOVA test, the homogeneity of the regression was checked. To check this assumption, air mass dominance zones were considered the fixed factor, elevation was a covariate, and δ^{18}O, δ^2H and d-excess were dependent variables. The p values were >0.05 for all the variables and homogeneity of regression was met (Supplementary spreadsheet S1). Elevation is variable which directly influences the stable isotope content of precipitation in Iran.

To validate the developed Iran MWLs, they were compared with fresh karstic springs across Iran. The δ^{18}O, δ^2H, electrical conductivity (EC), and d-excess values for over 200 karstic freshwater springs are shown in Supplementary Table S3 [17,19,20,43,45,54,61–71]. Evaporation did not markedly affect the selected karstic springs, and the EC of the karstic springs water was < 1000 μS/cm. The isotopic ratio of the karstic springs could therefore be used to check the validity of the MWLs. The proposed MWLs were validated by matching the isotopic ratio of the karstic springs with the MWLs, and the results indicated that the proposed MWLs were appropriate (Figure 4). The linear regression model was applied to trend the karstic springs water line (Supplementary Table S2). Trending lines on karstic springs showed very mild deviation from MWLs which confirmed the very low and negligible evaporation in most of the samples and the reliability of karstic springs for validation of the developed Iran MWLs.

Studying the isotope data in karstic springs using an ANCOVA test demonstrated important results. Authors considered EC as a covariate which influenced the stable isotope content of karstic springs. Authors checked the validity of EC as a covariate and confirmed that this variable met the covariate requirements. Therefore, the first assumption of the ANCOVA test was achieved. Furthermore, the homogeneity of the regression was also tested. Karstic regions of Iran were considered as the fixed parameter, EC as the covariate variable, and $\delta^{18}O$, δ^2H and d-excess as dependent variables (Supplementary spreadsheet S1). The homogeneity of regression was met for all the dependent variables and thus two ANCOVA test assumptions were achieved. EC directly influenced the stable isotope content of karstic springs, and thus choosing the karstic springs with low EC values for validation of MWLs was a wise decision as high EC values (>1000 µS/cm) can influence the stable isotope content of karstic springs.
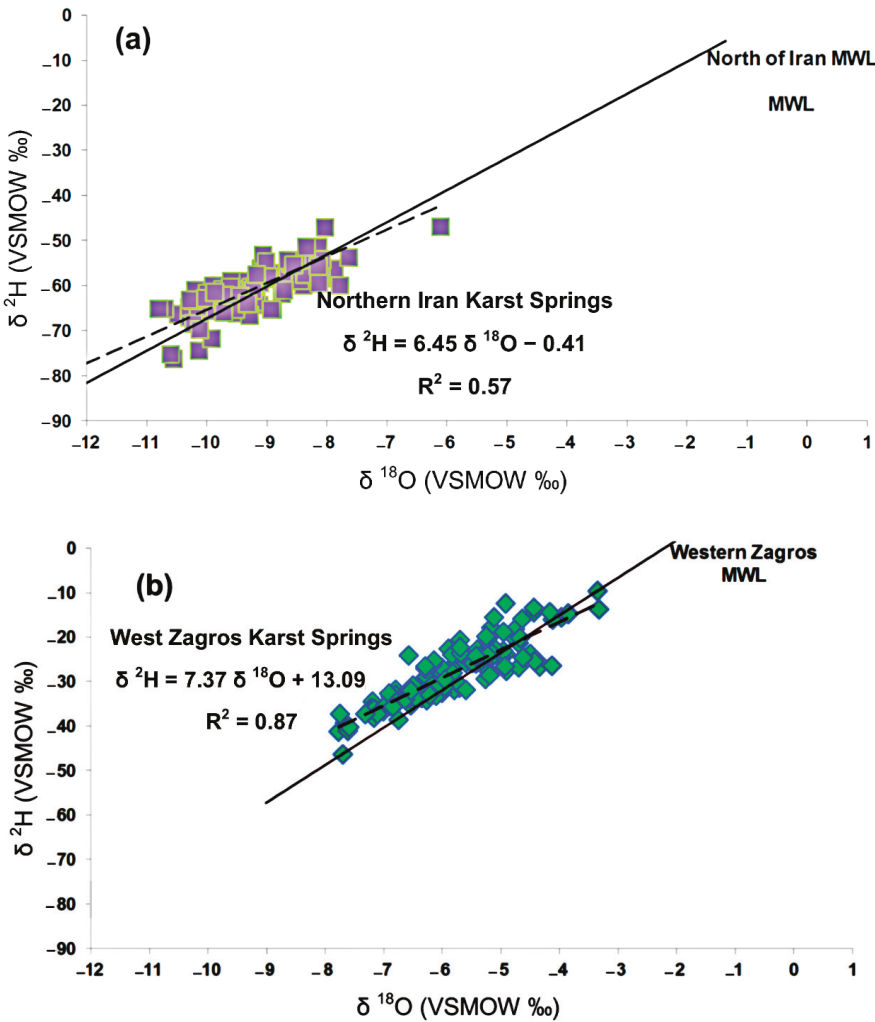
Figure 4. *Cont.*
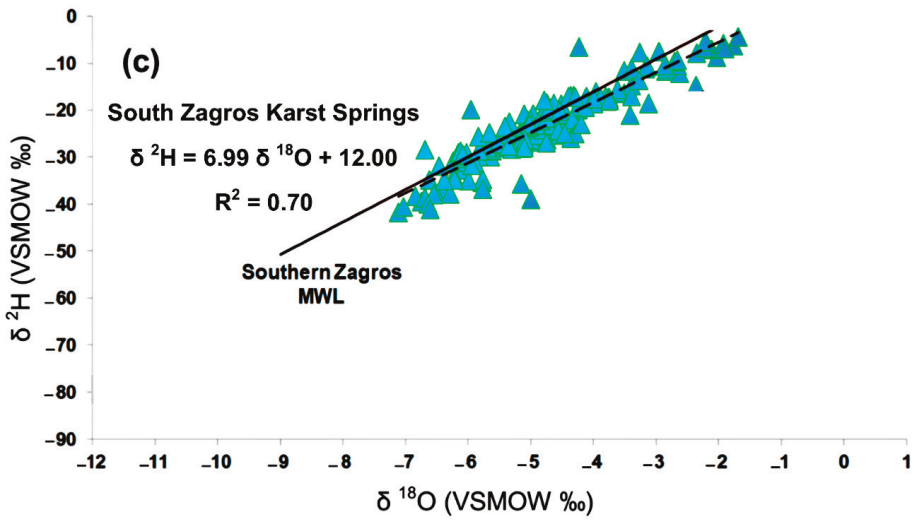
Figure 4. Karstic springs isotope values $\delta^{18}O$ and δ^2H plot on (**a**) North of Iran, (**b**) Zagros-west, and (**c**) Zagros-south MWLs.

The areas covered by the Iran MWLs are shown in Figure 5. No isotope data were available for coastal lowland areas along the Persian Gulf, central Iran, east and southeast Iran. Therefore, MWLs were not developed for these areas. The HYSPLIT model output indicates that the monsoon is the dominant source of precipitation for the southeast of Iran. Karachi (Pakistan) is also influenced by monsoon moisture sources [72], so the Karachi station MWL (KMWL) $\delta^2H = 7.56\ \delta^{18}O + 0.34$ [73] can be used as an alternative MWL for the southeast of Iran. No alternative MWL is available for coastal areas along the Persian Gulf and central Iran.
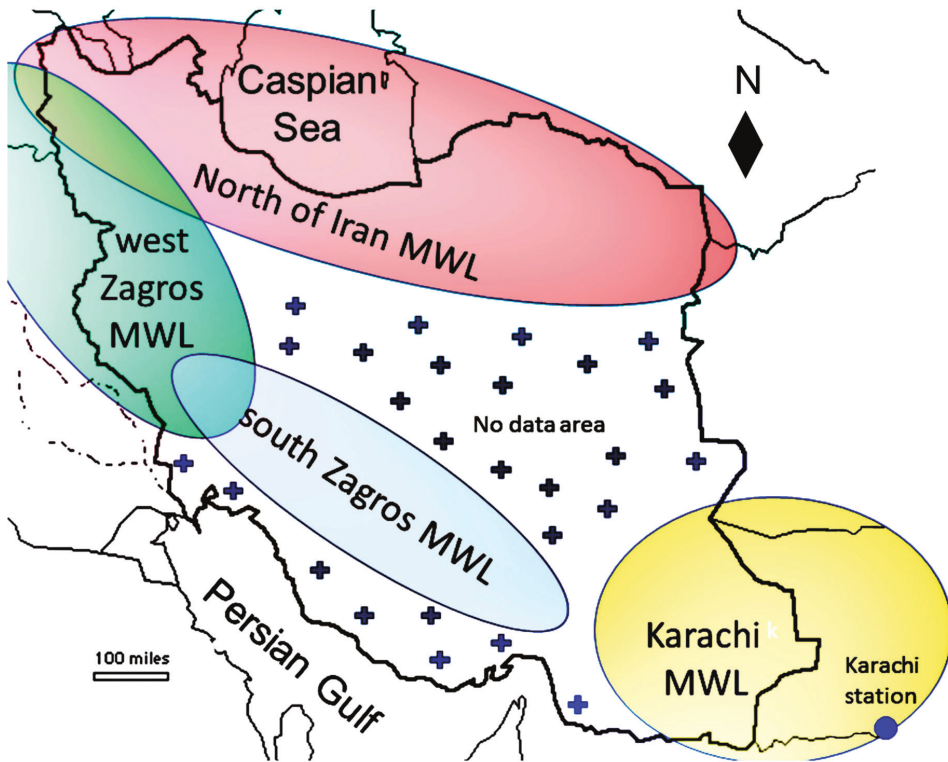
Figure 5. Map of areas covered by Iran MWLs and areas with no suggested MWLs. (The plus signs cover the areas with no suggested MWLs in Iran).

4.2. MWLs for Specific Moisture Sources

The HYSPLIT model output for 161 precipitation events for which isotope data were available (12 of the 32 studied stations in Iran) indicated that moisture predominantly originated from various moisture sources (mainly the Caspian Sea, the Mediterranean Sea, and the Persian Gulf). In previous studies, only the stable isotope characteristics of different moisture sources were determined [1–5,30], but herein an attempt was also made to determine MWLs for the precipitation events originated from the main moisture sources (Figure 6). These MWLs could be used to study the roles and contributions of various moisture sources in surface water and karstic springs recharge in Iran.

Figure 6. MWLs for specific moisture sources from the Caspian Sea (**a**), the Persian Gulf (**b**), and the Mediterranean Sea (**c**), all of which supply precipitation to Iran.

The developed Iran MWLs and dominant moisture sources MWLs are shown in (Table 1). Comparing the slope and intercept of the MWLs demonstrated very valuable results. In the west Zagros region where precipitation is dominantly provided by MedT air mass, the Zagros-west MWL is similar to the Mediterranean Sea MWL in both slope and intercept. However, in the south Zagros region where precipitation is provided dominantly by MedT and cT air masses, Zagros-south MWL slope and intercept values were between the Persian Gulf and the Mediterranean Sea MWLs slope and intercept. In the north of Iran where precipitation is provided mainly by the simultaneous influence of MedT and cP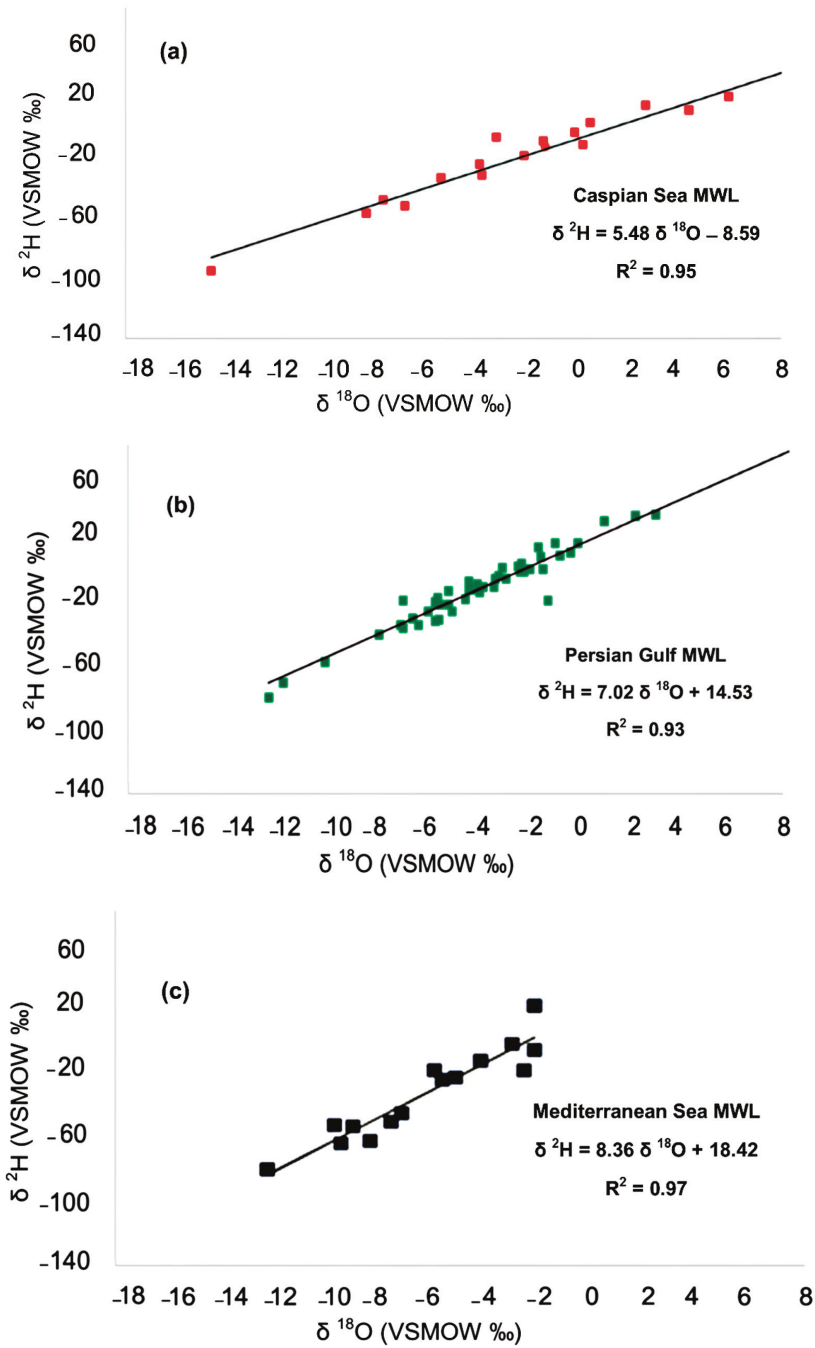 air masses, the North of Iran MWL slope and intercept values were between the Mediterranean and the Caspian Sea MWL slope and intercept values.

Table 1. Regional MWLs for Iran and MWLs for specific moisture sources.

MWL	Slope	Intercept	Dominant Air Masses	Dominant Moisture Sources
Zagros-south	7.06	14.82	MedT & cT	Arabian Sea, Mediterranean Sea, Persian Gulf, and continental sources
Zagros-west	8.12	16.99	MedT, cT, & mP	Mediterranean Sea, Black Sea, Persian Gulf, and continental sources
North of Iran	7.11	3.86	MedT, cT, mP, & cP	Caspian Sea, Mediterranean Sea, Black Sea, Persian Gulf, and continental sources
Karachi MWL (KMWL) for Southeast Iran	7.56	0.34	mT	Indian Ocean and Arabian Sea
Caspian Sea	5.48	−8.59	cP	Caspian Sea
Mediterranean Sea	8.36	18.42	MedT	Mediterranean Sea and Black Sea
Persian Gulf	7.02	14.53	cT	Persian Gulf

4.3. The Role of Various Moisture Sources in Surface Water and Karstic Springs Recharge in Iran

As mentioned earlier, MWLs developed for the dominant Iran moisture sources can be used in the study of moisture source contribution rate in karstic springs and surface water resources recharge. Surface water resources isotope data were collected from three dominant zones in the north of Iran, west Zagros and south Zagros [17,18,20,43,54,57,62,67,68,74–85] and presented in Supplementary Table S4. To study the role of the dominant moisture sources in surface water resources recharge, surface water samples were plotted on the Caspian Sea, the Persian Gulf and the Mediterranean Sea MWLs (Figure 7). Surface water resources in the north of Iran were closely plotted on the Caspian Sea MWL. This demonstrated the considerable role of the Caspian Sea moisture in surface water resources recharge in this region. However, the surface water resources in the south Zagros region were closely plotted on the Persian Gulf MWL. This confirmed that surface water resources in this region were dominantly under the influence of the moisture originating from the Persian Gulf. Some of the surface water resources in the south Zagros region deviated considerably from the Persian Gulf MWL due to huge evaporation effect. These surface water samples (mainly Parishan and Dasht-Arjan lakes) faced huge evaporation from their surfaces (Supplementary Table S4). Finally, plotting surface water resources on the Mediterranean Sea MWL showed that most of the surface water resources in all three dominate regions were plotted closely on this MWL. This confirmed the dominant role of the Mediterranean Sea moisture source in precipitation and surface water resources recharge in all parts of Iran. Some of the surface water resources in the north of Iran (Caspian Sea and Bazangan Lake) and also south Zagros (Parishan and Dasht-Arjan) dominantly deviated from the Mediterranean Sea MWL which was due to an intense evaporation effect on these resources (Supplementary Table S4). A linear regression model was used to develop a water line for surface water resources. The developed surface water isotope lines showed huge decline in both slope and intercept compared to both Iran MWLs and also to karstic springs isotope lines. This was due to the huge evaporation effect on surface water resources in the studied regions (Supplementary Table S4).
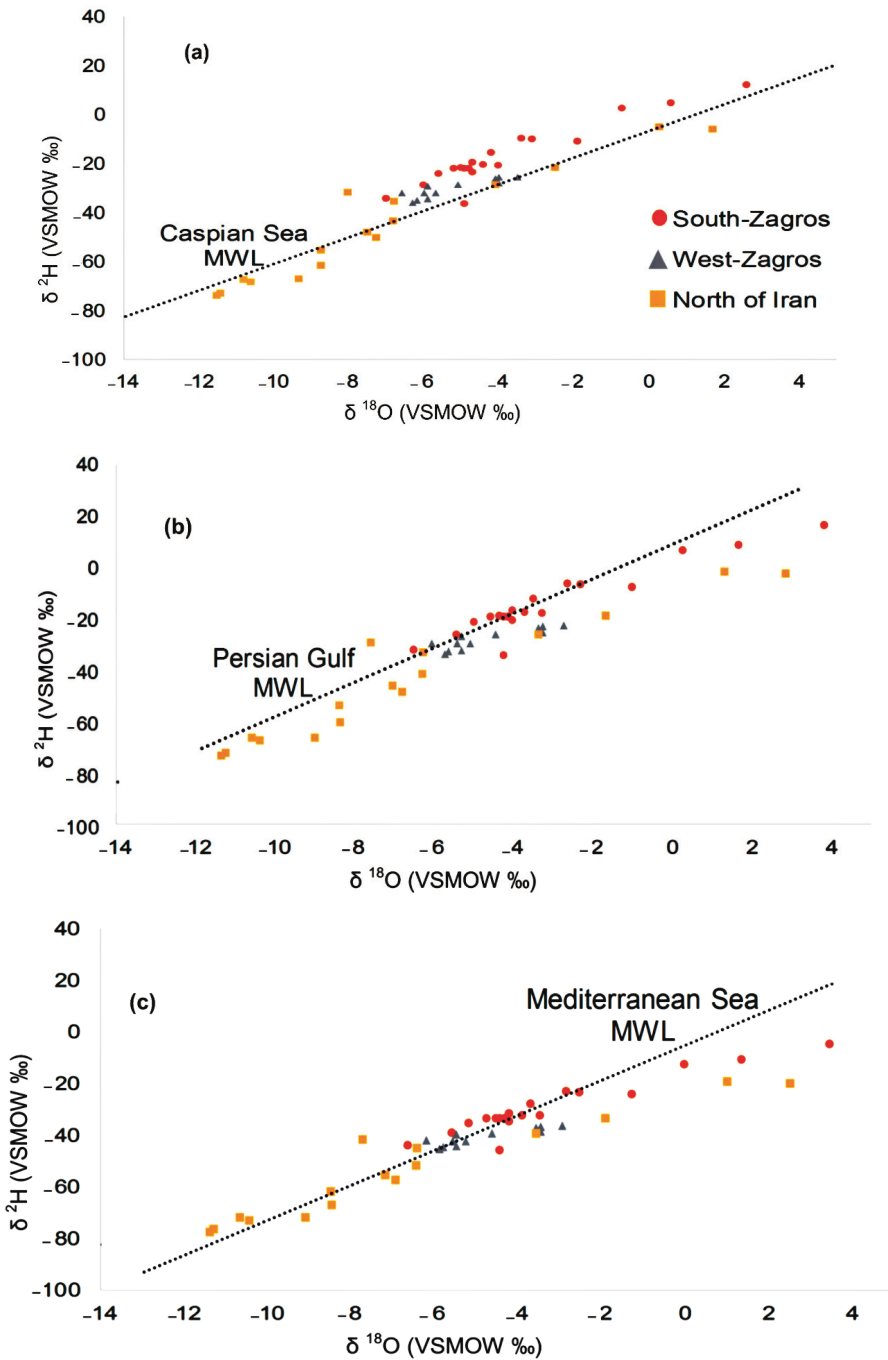
Figure 7. Plotting surface water resources $\delta^{18}O$ and δ^2H on the Caspian Sea (**a**), the Persian Gulf (**b**), and the Mediterranean Sea (**c**) MWLs. (The Mediterranean Sea, the Persian Gulf, and the Caspian Sea MWLs are taken from Figure 6.).

Plotting karstic springs on the dominant moisture sources MWL also demonstrated very valuable results (Figure 8). Karstic springs in the north of Iran were plotted closely on the Caspian Sea and the Mediterranean Sea MWLs. This is due to the fact that the Caspian and Mediterranean seas moisture have a dominant role in karstic springs recharge in the north of Iran. However, karstic springs in the Zagros regions (west and south) were mainly plotted on the Persian Gulf and the Mediterranean Sea MWLs. Karstic springs in the Zagros regions are mainly recharged by the precipitation events originating from these water bodies.
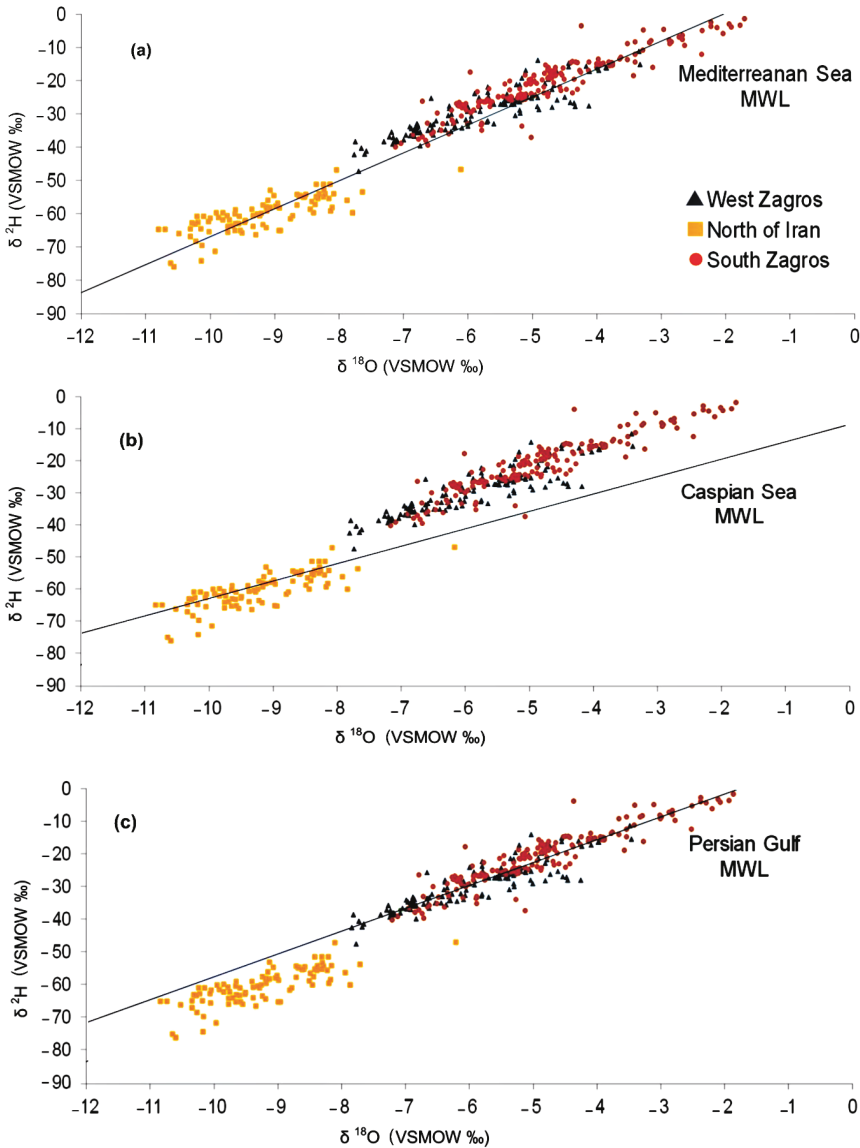
Figure 8. Plotting karstic springs $\delta^{18}O$ and δ^2H across Iran on the Mediterranean Sea (**a**), the Caspian Sea (**b**), and the Persian Gulf (**c**) MWLs. (The Mediterranean Sea, the Persian Gulf, and the Caspian Sea MWLs are taken from Figure 6).

Studying the role of various moisture sources on karstic springs and surface water resources across Iran confirmed that various moisture sources dominantly recharged surface and karstic springs resources across Iran. In the north of Iran, the Caspian and Mediterranean seas influence surface and karstic springs resources, while in the Zagros regions in the west and southwest of Iran, the Persian Gulf and the Mediterranean Sea moisture have a dominant role in surface and karstic springs recharge.

5. Conclusions

Most parts of Iran are influenced by several air masses, but specific air masses are dominant in each part of the country. Thus, a single MWL for Iran is not appropriate. Three MWLs were developed for Iran based on the main moisture sources and air masses which influence this country (Zagros-west, Zagros-south, and North of Iran). The proposed MWLs for Iran were validated by matching karstic spring $\delta^{18}O$ and δ^2H values to the proposed MWLs. The d-excess values were higher for the west and south Zagros regions compared to the north of Iran, because the water bodies supplying moisture to west and south Zagros' precipitation have higher SSTs and lower humidity than those supplying moisture to the north of Iran. Furthermore, MWLs were also developed for the main Iran moisture sources (the Caspian Sea, the Mediterranean Sea, and the Persian Gulf). Plotting karstic springs and surface water resources on the main moisture sources MWLs showed that both karstic springs and surface water samples in the north of Iran were mainly plotted on the Caspian Sea and the Mediterranean Sea MWLs. However, most of the karstic springs and surface water samples were plotted on the Persian Gulf and the Mediterranean Sea MWLs in the south and west Zagros regions. The methods proposed here can be applied in other regions influenced by various air masses and moisture sources.

References

1. Sjostrom, D.J.; Welker, J.M. The influence of air mass source on the seasonal isotopic composition of precipitation, eastern USA. *J. Geochem. Explor.* **2009**, *102*, 103–112. [CrossRef]
2. Birks, J.; EDWARDS, T.W. Atmospheric circulation controls on precipitation isotope—Climate relations in western Canada. *Tellus B Chem. Phys. Meteorol.* **2009**, *61*, 566–576. [CrossRef]
3. Lykoudis, S.P.; Kostopoulou, E.; Argiriou, A.A. Stable isotopic signature of precipitation under various synoptic classifications. *Phys. Chem. Earth Parts A/B/C* **2010**, *35*, 530–535. [CrossRef]
4. Liu, Z.; Bowen, G.J.; Welker, J.M. Atmospheric circulation is reflected in precipitation isotope gradients over the conterminous United States. *J. Geophys. Res. Space Phys.* **2010**, *115*. [CrossRef]

5. Crawford, J.; Hughes, C.E.; Parkes, S.D. Is the isotopic composition of event based precipitation driven by moisture source or synoptic scale weather in the Sydney Basin, Australia? *J. Hydrol.* **2013**, *507*, 213–226. [CrossRef]

6. Kong, Y.; Wang, K.; Li, J.; Pang, Z. Stable Isotopes of Precipitation in China: A Consideration of Moisture Sources. *Water* **2019**, *11*, 1239. [CrossRef]

7. Fan, Y.; Chen, Y.; He, Q.; Li, W.; Wang, Y. Isotopic Characterization of River Waters and Water Source Identification in an Inland River, Central Asia. *Water* **2016**, *8*, 286. [CrossRef]

8. Burnett, A.W.; Mullins, H.T.; Patterson, W.P. Relationship between atmospheric circulation and winter precipitation δ18 O in central New York State. *Geophys. Res. Lett.* **2004**, *31*, 209. [CrossRef]

9. Stein, A.F.; Draxler, R.R.; Rolph, G.D.; Stunder, B.J.B.; Cohen, M.D.; Ngan, F.; Stein, A. NOAA's HYSPLIT Atmospheric Transport and Dispersion Modeling System. *Bull. Am. Meteorol. Soc.* **2015**, *96*, 2059–2077. [CrossRef]

10. Soderberg, K.; Good, S.P.; O'Connor, M.; Wang, L.; Ryan, K.; Caylor, K.K. Using atmospheric trajectories to model the isotopic composition of rainfall in central Kenya. *Ecosphere* **2013**, *4*, 1–18. [CrossRef]

11. Juhlke, T.R.; Meier, C.; Van Geldern, R.; Vanselow, K.A.; Wernicke, J.; Baidulloeva, J.; Barth, J.A.; Weise, S.M. Assessing moisture sources of precipitation in the Western Pamir Mountains (Tajikistan, Central Asia) using deuterium excess. *Tellus B Chem. Phys. Meteorol.* **2019**, *71*, 1–16. [CrossRef]

12. Dansgard, W. Stable isotopes in precipitation. *Tellus* **1964**, *16*, 436–468. [CrossRef]

13. Gat, J.R.; Carmi, I. Evolution of the isotopic composition of atmospheric waters in the Mediterranean Sea area. *J. Geophys. Res. Space Phys.* **1970**, *75*, 3039–3048. [CrossRef]

14. Clark, I.D. *Environmental Isotopes in Hydrogeology*; CRC Press/Lewis Publishers: Boca Raton, FL, USA, 1997; ISBN 1566702496.

15. Mohammadzadeh, H. The Meteoric Relationship for ^{18}O and ^{2}H in Precipitations and Isotopic Compositions of water resources in Mashhad Area (NE Iran). In *The 1st International Applied Geological Congress*; Islamic Azad University—Mashad Branch: Mashhad, Iran, 2010; pp. 555–559.

16. Jahanshahi, R. *Environmental Effects of GoleGohar Iron Ore Mine on Groundwater of the Area*; Shiraz University: Shiraz, Iran, 2013.

17. Heydarizad, M. *Investigation of Hydrochemistry of Karde Dam and its Hydraulically Connection with Downstream Water Resources*; Ferdowsi University of Mashhad: Mashhad, Iran, 2011.

18. Mohammadzadeh, H.; Ebrahimpour, S. Application of stable isotopes and hydrochemistry to investigate sources and quality exchange Zarivar catchment area. *J. Water Soil* **2012**, *26*, 1018–1031.

19. Mohammadi, Z. *Method of Leakage Study at Karst Dam Site, the Zagros Region*; Shiraz University: Shiraz, Iran, 2006.

20. Osati, K.; Koeniger, P.; Salajegheh, A.; Mahdavi, M.; Chapi, K.; Malekian, A. Spatiotemporal patterns of stable isotopes and hydrochemistry in springs and river flow of the upper Karkheh River Basin, Iran. *Isot. Environ. Health Stud.* **2014**, *50*, 169–183. [CrossRef]

21. Kazemi, G.A.; Ichiyanagi, K.; Shimada, J. Isotopic characteristics, chemical composition and salinization of atmospheric precipitation in Shahrood, northeastern Iran. *Environ. Earth Sci.* **2015**, *73*, 361–374. [CrossRef]

22. Shamsi, A.; Karami, G.H.; Hunkeler, D.; Taheri, A. Isotopic and hydrogeochemical evaluation of springs discharging from high-elevation karst aquifers in Lar National Park, northern Iran. *Hydrogeology* **2019**, *27*, 655. [CrossRef]

23. Mohammadzadeh, H.; Heydarizad, M. δ^{18}O and δ^{2}H characteristics of moisture sources and their role in surface water recharge in the north-east of Iran. *Isot. Environ. Health Stud.* **2019**, 1–16. [CrossRef]

24. Bagheri, R.; Bagheri, F.; Karami, G.H.; Jafari, H. Chemo-isotopes (^{18}O & ^{2}H) signatures and HYSPLIT model application: Clues to the atmospheric moisture and air mass origins. *Atmos. Environ.* **2019**, *215*, 116892.

25. Alijani, B. *Iran Climatology*, 5th ed.; Payam Nour Publication: Tehran, Iran, 2000; ISBN 978-964-455-621-0.

26. Heydarizad, M.; Raeisi, E.; Sori, R.; Gimeno, L.; Nieto, R. The Role of Moisture Sources and Climatic Teleconnections in Northeastern and South-Central Iran's Hydro-Climatology. *Water* **2018**, *10*, 1550. [CrossRef]

27. Crawford, J.; Hughes, C.E.; Lykoudis, S. Alternative least squares methods for determining the meteoric water line, demonstrated using GNIP data. *J. Hydrol.* **2014**, *519*, 2331–2340. [CrossRef]

28.   Boschetti, T.; Cifuentes, J.; Iacumin, P.; Selmo, E. Local Meteoric Water Line of Northern Chile (18° S–30° S): An Application of Error-in-Variables Regression to the Oxygen and Hydrogen Stable Isotope Ratio of Precipitation. *Water* **2019**, *11*, 791. [CrossRef]

29.   Shamsi, A.; Kazemi, G.A. A review of research dealing with isotope hydrology in Iran and the first Iranian meteoric water line. *JGeope* **2014**, *4*, 73–86.

30.   Heydarizad, M.; Raeisi, E.; Sori, R.; Gimeno, L. An overview of the atmospheric moisture transport effect on stable isotopes (δ18O, δ 2H) and D excess contents of precipitation in Iran. *Theor. Appl. Clim.* **2019**, *138*, 47–63. [CrossRef]

31.   Heydarizad, M. *Meteoric Water Lines of Iran for Various Precipitation Sources*; Shiraz University: Shiraz, Iran, 2018.

32.   Karimi, M.; Farajzadeh, M. Spatial and Temporal distribution of Iran's precipitation moisture. *J. Geogr. Sci. Stud.* **2011**, *19*, 109–127.

33.   Ciric, D.; Stojanovic, M.; Drumond, A.; Nieto, R.; Gimeno, L. Tracking the Origin of Moisture over the Danube River Basin Using a Lagrangian Approach. *Atmosphere* **2016**, *7*, 162. [CrossRef]

34.   Drumond, A.; Taboada, E.; Nieto, R.; Gimeno, L.; Vicente-Serrano, S.M.; López-Moreno, J.I. A Lagrangian analysis of the present-day sources of moisture for major ice-core sites. *Earth Syst. Dyn.* **2016**, *7*, 549–558. [CrossRef]

35.   Heydarizad, M.; Raeisi, E.; Sori, R.; Gimeno, L. The Identification of Iran's Moisture Sources Using a Lagrangian Particle Dispersion Model. *Atmosphere* **2018**, *9*, 408. [CrossRef]

36.   Nieto, R.; Gimeno, L.; Gallego, D.; Trigo, R. Contributions to the moisture budget of airmasses over Iceland. *Meteorol. Z.* **2007**, *16*, 37–44. [CrossRef]

37.   NOAA. Available online: https://www.esrl.noaa.gov (accessed on 20 October 2019).

38.   IAEA/GNIP. *Precipitation Sampling Guide*; International Atomic Energy Agency (IAEA): Vienna, Austria, 2014.

39.   *Microsoft Office (2016) Professional PLus Microsoft Excel 2016*; Microsoft corporation: Redmond, WA, USA; Available online: https://www.office.com/ (accessed on 10 November 2019).

40.   Minissale, A.; Vaselli, O. Karst springs as "natural" pluviometers: Constraints on the isotopic composition of rainfall in the Apennines of central Italy. *Appl. Geochem.* **2011**, *26*, 838–852. [CrossRef]

41.   R core Team. *R: A Language and Environment for Statistical Computing*; R Foundation for Statistical Computing: Vienna, Austria, 2018; Available online: https://www.R-project.org/ (accessed on 10 November 2019).

42.   Faroughi, A. *Characterizing Isotopic Signature of Precipitation in Fars Province, Iran*; Shiraz University: Shiraz, Iran, 2008.

43.   Zarei, H.; Akhondali, A.M.; Mohammadzadeh, H.; Radmanesh, F.; Laudon, H. Runoff generation processes during the wet-up phase in a semi-arid basin in Iran. *Hydrol. Earth Syst. Sci. Discuss.* **2014**, *11*, 3787–3810. [CrossRef]

44.   Karimi, H. Investigating the Oxygen-18 and Deuterium Isotope Composition of Precipitations in Western Zagros. In Proceedings of the 1st National Conference on Application of Stable Isotopes, Mashhad, Iran, 8 May 2013.

45.   Rezaei, M.; Karimi, H.; Jokar, B. Studies of Kazeroon-Persian Gulf karstic basins. *Karst Res. Cent. Iran* **1998**, *2*, 75–120.

46.   Ghazban, F. Geological and geochemical investigation of Damavand geothermal prospect, central Alborz mountain, northern Iran. *Geotherm. Resour. Counc. Trans.* **2000**, *24*, 229–234.

47.   Nickghoujag, Y.; Mohammadzadeh, H.; Naseri, H.R. The application of stable isotopes (^{18}O and ^{2}H) to determine the role of surface water in shallow groundwater resources in Gorgan rood basin. In Proceedings of the Second National Conference on Application of Stable Isotopes, Mashhad, Iran, 11 May 2016.

48.   Feyzi, D. *Traceing Studies in Roudball Dam Site*; Iran Regional Water Authorities: Shiraz, Iran, 1998.

49.   Saadati, H.; Sharifi, F.; Mahdavi, M.; Ahmadi, H.; Mohseni, M. Determining origin of groundwater recharge resources, drought and wet periods by isotopic tracers in Hashtgerd plain. *Manag. J. Range Water Shed* **2009**, *62*, 49–63.

50.   Khademi, H.; Mermut, A.; Krouse, H. Isotopic composition of gypsum hydration water in selected landforms from central Iran. *Chem. Geol.* **1997**, *138*, 245–255. [CrossRef]

51.   Mohammadzadeh, H.; Eskandari, E.; Najafi, M. Studying the stable isotope content of precipitation in Paveh region. In Proceedings of the Second National Conference on Application of Stable Isotopes, Mashhad, Iran, 11 May 2016.

52. Farpoor, M.; Khademi, H.; Eghbal, M.; Krouse, H. Mode of gypsum deposition in southeastern Iranian soils as revealed by isotopic composition of crystallization water. *Geoderma* **2004**, *121*, 233–242. [CrossRef]

53. Parizi, H.S.; Samani, N. Environmental Isotope Investigation of Groundwater in the Sarcheshmeh Copper Mine Area, Iran. *Mine Water Environ.* **2014**, *33*, 97–109. [CrossRef]

54. Kalantari, N.; Mohamadi Behzad, H. Investigation source of recharge to Sabzab and Bibi Talkhon karstic springes by application of ^{18}O and ^{2}H stable isotopes. In Proceedings of the 1st National Conference on Application of Stable Isotopes, Mashhad, Iran, 8 May 2013.

55. Ali, K.K.; Al-Kubaisi, Q.Y.; Al-Paruany, K.B. Isotopic study of water resources in a semi-arid region, western Iraq. *Environ. Earth Sci.* **2015**, *74*, 1671–1686. [CrossRef]

56. IAEA/GNIP Global Network of Isotopes in Precipitation (GNIP). Available online: https://www.iaea.org/servises/networks/gnip. (accessed on 8 November 2019).

57. Porkhial, S.; Ghomshei, M.M.; Yousefi, P. Stable Isotope and Elemental Chemistry of Mt. Sabalan Geothermal Field, Ardebil Province of North West Iran. In Proceedings of the World Geothermal Congress, Bali, Indonesia, 25–30 April 2010.

58. Lehner, B.; Verdin, K.; Jarvis, A. New Global Hydrography Derived From Spaceborne Elevation Data. *Eos* **2008**, *89*, 93. [CrossRef]

59. Rozanski, K.; Araguas-Araguas, L.; Gonfiantini, R. Isotopic patterns in modem global precipitation. In *Climate Change in Continental Isotopic Records*; Swart, P.K., Lohmann, K.C., Mckenzie, J., Savin, S., Eds.; Geophysical Monograph Series; American Geophysical Union: Washington, DC, USA, 1993; pp. 1–36. ISBN 9781118664025.

60. Kalnay, E.; Kanamitsu, M.; Kistler, R.; Collins, W.; Deaven, D.; Gandin, L.; Iredell, M.; Saha, S.; White, G.; Woollen, J.; et al. The NCEP/NCAR 40-Year Reanalysis Project. *Bull. Am. Meteorol. Soc.* **1996**, *77*, 437–471. [CrossRef]

61. Asari, A. *Source of Salinity at the Plunge of Gar and Barm Firooz Karstic Anticlines*; Shiraz University: Shiraz, Iran, 2011.

62. Bagheri Sheshdeh, R. *Leakage Potential in Seymareh Dam Site*; Shiraz University: Shiraz, Iran, 2007.

63. Masjedi, M.; Jahani, H.; Khalaj Amir hosseini, Y.; Hatami, F.; Kooh Pour, E. *Tracer Studies in Seymareh Dam Site in Ilam Province*; Iran Water Resources Institute: Tehran, Iran, 1995.

64. Rafighdoust, Y.; Eckstein, Y.; Harami, R.M.; Gharaie, M.H.M.; Griffith, E.M.; Mahboubi, A. Isotopic analysis, hydrogeochemistry and geothermometry of Tang-Bijar oilfield springs, Zagros region, Iran. *Geothermics* **2015**, *55*, 24–30. [CrossRef]

65. Ahmadipour, M. reza Karst springs of Alashtar, Iran. *Acta Carsolog.* **2003**, *32*, 244–254.

66. Chitsazan, M.; Vardanjani, H.K.; Karimi, H.; Charchi, A. A comparison between karst development in two main zones of Iran: Case study—Keyno anticline (Zagros Range) and Shotori anticline (Central Iran). *Arab. J. Geosci.* **2015**, *8*, 10833–10844. [CrossRef]

67. Khalaj Amirhosseini, Y. Application of isotopes and dye tracing methods in hydrology (case study: Havasan dam construction). In Proceedings of the An International Symposium of Isotopes in Hydrology, Marine Ecosystems and Climate Change Studies, Monaco-Ville, Monaco, 27 March–1 April 2011.

68. Mohammadzadeh, H.; Heydarizad, M. Investigating geochemistry and the stable isotope (δ^{18}O & δ^{2}H) composition of Karde Carbonate Lake water (NE Iran). In Proceedings of the 22th Goldschmidt Conference, Monteral, QC, Canada, 24–29 June 2012; p. 2123.

69. Faezi, N. *Hydrogeology and Vulnerability Assessment of Ghaleh Dokhtar Spring Catchment Area*; Shiraz University: Shiraz, Iran, 2015.

70. Mohammadzadeh, H.; Kazemi, M. Geofluids Assessment of the Ayub and Shafa Hot Springs in Kopet-Dagh Zone (NE Iran): An Isotopic Geochemistry Approach. *Geofluids* **2017**, *2017*, 1–11. [CrossRef]

71. Karimi, H.; Raeisi, E.; Bakalowicz, M. Characterising the main karst aquifers of the Alvand basin, northwest of Zagros, Iran, by a hydrological approach. *Hydrogeol. J.* **2005**, *13*, 787–799. [CrossRef]

72. Araguás-Araguás, L.; Froehlich, K.; Rozanski, K. Stable isotope composition of precipitation over southeast Asia. *J. Geophys. Res. Space Phys.* **1998**, *103*, 28721–28742. [CrossRef]

73. Mashiatullah, A.; Qureshi, R.; Tasneem, M.; Javed, T.; Gaye, C.; Ahmad, E.; Ahmad, N. Isotope hydrochemical investigation of saline intrusion in the coastal aquifer of Karachi, Pakistan. *Radioact. Environ.* **2006**, *8*, 382–393.

74. Niroomand, M.H.; Pakzad, M. *Studies of Bakhtegan Karstic Water Resources*; Karst Research Center of Iran: Shiraz, Iran, 1997.

75. Zarei, H.; Damough, N.A. Determination the recharge zones of Karstic springs downstram of Karoun3 dam reservoir. In *The Fifth Engineering Geology and Enviromental Geology Meeings*; Engineering Geology Assossiation: Tehran, Iran, 2007.

76. Mirnejad, H.; Sisakht, V.; Mohammadzadeh, H.; Amini, A.H.; Rostron, B.J.; Haghparast, G. Major, minor element chemistry and oxygen and hydrogen isotopic compositions of Marun oil-field brines, SW Iran: Source history and economic potential. *Geol. J.* **2011**, *46*, 1–9. [CrossRef]

77. Ehghahi, M. *Traceing Studies of Doupulan Tapeh Karstic Region*; Iran Regional Water Authorities: Tehran, Iran, 1990.

78. Pakzad, M. *Tracer Studies in Mirza Shirazi (Kovar) Dam Site in Fars Province*; Iran Water Research Institute: Tehran, Iran, 1993.

79. Rezaei, M.; Karami, H.; Jokar, B. *Studies of Hajiabad Karstic Water Resources*; Karst Research Center of Iran: Shiraz, Iran, 2000.

80. Rezaei, M.; Krimi, H.; Jokar, B. *Semi Detail Studies of Kazeroun and Persian Gulf Karstic Mega Basin*; Karst Research Center of Iran: Shiraz, Iran, 1998.

81. Mohammadzadeh, H. ^{18}O, ^{2}H, and ^{13}C isotopic compositions of water in Torogh and Kardeh dams, Mashhad. In Proceedings of the Joint European Stable Isotope User Meeting—JESIUM, Presqu'ile de Giens, France, 31 August–5 September 2008.

82. Pakzad, M. *Isotopic Studies of Karstic Resources in Kashaf Rood Basin in Khorasan Province*; Iran Water Resources Institute: Tehran, Iran, 2000.

83. Mohammadzadeh, H.; Robin, M.; Khanehbad, M. An Investigating of the origin and the groundwater discharge to Bazangan Lake, Eastern Kopet-Dagh Basin-Iran, using geochemistry and stable isotopes approaches. *Geochmica Cosmochim. Acta* **2008**, *72*, A641.

84. Lar dam consulting bureau. *Tracing Studies in Lar Dam Site*; Iran Water Resources Institute: Tehran, Iran, 1983.

85. Mousavi Shalmani, M.A.; Lakzian, A.; Khorasani, A.; Feiziasl, V.; Mahmoudi, A.; Pourmohammad, N. Use of Multiple Linear Regression Method for Modelling Seasonal Changes in Stable Isotopes of ^{18}O and ^{2}H in 30 Pouns in Gilan Province. *J. Water Soil* **2014**, *28*, 239–252.

Long-Term Isotope Records of Precipitation in Zagreb, Croatia

Ines Krajcar Bronić [1,*], Jadranka Barešić [1], Damir Borković [1], Andreja Sironić [1], Ivanka Lovrenčić Mikelić [1] and Polona Vreča [2]

[1] Laboratory for Low-level Radioactivities, Division of Experimental Physics, Ruđer Bošković Institute, 10000 Zagreb, Croatia; jbaresic@irb.hr (J.B.); damir.borkovic@irb.hr (D.B.); asironic@irb.hr (A.S.); ivanka.lovrencic@irb.hr (I.L.M.)

[2] Department of Environmental Sciences, Jožef Stefan Institute, 1000 Ljubljana, Slovenia; polona.vreca@ijs.si

* Correspondence: krajcar@irb.hr

Abstract: The isotope composition of precipitation has been monitored in monthly precipitation at Zagreb, Croatia, since 1976. Here, we present a statistical analysis of available long-term isotope data (^{3}H activity concentration, δ^2H, δ^{18}O, and deuterium excess) and compare them to basic meteorological data. The aim was to see whether isotope composition reflected observed climate changes in Zagreb: a significant increase in the annual air temperature and larger variations in the precipitation amount. Annual mean δ^{18}O and δ^2H values showed an increase of 0.017‰ and 0.14‰ per year, respectively, with larger differences in monthly mean values in the first half of the year than in the second half. Mean annual d-excess remained constant over the whole long-term period, with a tendency for monthly mean d-excess values to decrease in the first half of the year and increase in the second half due to the influence of air masses originating from the eastern Mediterranean. Changes in the stable isotope composition of precipitation thus resembled changes in the temperature, the circulation pattern of air masses, and the precipitation regime. A local meteoric water line was obtained using different regression methods, which did not result in significant differences between nonweighted and precipitation-weighted slope and intercept values. Deviations from the Global Meteoric Water Line GMWL (lower slopes and intercepts) were observed in two recent periods and could be explained by changes in climate parameters. The temperature gradient of δ^{18}O was 0.33‰/°C. The tritium activity concentrations in precipitation showed slight decreases during the last two decades, and the mean A in the most recent period, 2012–2018, was 7.6 ± 0.8 Tritium Units (TU).

1. Introduction

Water, especially groundwater, has become an invaluable natural resource, and the availability of freshwater is one of the greatest issues facing mankind today [1]. A consistent and careful assessment and management of water resources is crucial for their sustainable development. This can be performed by various methodologies, among which isotope methods using environmental (stable and radioactive) and artificial radioactive isotopes have proven to be effective tools for solving many critical hydrological problems and processes [2–9]. In many cases, isotope techniques have provided information that could not be obtained through any other conventional means [10–12].

Isotopes that are constituent elements of a water molecule are of special interest as perfect candidates for water tracers: hydrogen (^{1}H, ^{2}H, ^{3}H) and oxygen (^{16}O, ^{17}O, ^{18}O) isotopes. Among these, only ^{3}H is a radioactive isotope, while the others are stable isotopes.

Precipitation presents an input to groundwater, and therefore knowledge on the isotope composition of precipitation is a prerequisite for groundwater studies. Temporal and spatial patterns of isotopes in precipitation (expressed as δ^2H and $\delta^{18}O$ values and the tritium activity concentration, A) have been observed since the 1950s and have contributed to hydrological and hydrogeological research [13–16], climate and paleoclimate studies [4,15,17–22], and ecological research [23–25]; further, precipitation isotope mapping has been widely implemented during recent decades [25,26].

The International Atomic Energy Agency (IAEA) and the World Meteorological Organization (WMO) have recognized the importance of the isotopic composition of precipitation on a global scale. A program involving the worldwide monitoring of the isotopic composition of monthly precipitation (called the Global Network of Isotopes in Precipitation (GNIP)) was therefore established in 1961. The objective of the network was a systematic collection of data on the isotopic composition of precipitation across the globe to determine temporal and spatial variations of isotopes in precipitation. Isotopic data include the tritium activity concentration, A (expressed in tritium units, TU), and stable isotopes of hydrogen and oxygen isotopes (δ^2H and $\delta^{18}O$ values), as well as climatological data (mean monthly temperature, monthly precipitation amount, and atmospheric water vapor pressure) [27]. The collected records have enabled the establishment of seasonal variations and various correlations among the data. Seasonal variations in $\delta^{18}O$ and δ^2H values of precipitation and their weighted mean annual values have remained fairly constant from year to year at a given location as long as the annual range and sequence of climatic conditions did not change significantly from year to year.

However, in recent years, we have become aware of climatic changes that have caused an increase in global temperature and changes in the precipitation pattern, as well as severe and extreme weather events (droughts, heavy storms, and temperature records). The recent increase in global temperature has exceeded the natural variabilities during the Holocene [28]. The planet's average surface temperature has risen about 1 °C (between 0.8 °C and 1.2 °C [29]) since the late 19th century, a change driven largely by increased carbon dioxide and other human-made emissions into the atmosphere. Most of the warming has occurred in the past 35 years, with 16 of the 17 warmest years on record occurring since 2001. The 10 hottest years ever recorded have all occurred since 1998 [30]. The hottest years on record globally have been the last five (2014–2018), with 2016 being the hottest year [31], and eight months in 2016 (from January through September, except for June) were the warmest on record for those respective months. October, November, and December of 2016 were the second warmest of those months on record: in all three cases, behind records set in 2015. Correlations between the precipitation isotope ratios recorded in the GNIP and meteorological quantities may provide additional evidence of recent climate change that appears to have manifested globally as well as evidence of the local weather situation. To find such evidence, one should have sufficiently long records of both climate data and the isotopic composition of precipitation.

Monitoring of the isotope composition of monthly precipitation at a station in Zagreb (Croatia) has been performed since 1976 (tritium activity concentration, A) and since 1980 (stable isotope ratios of hydrogen ($^2H/^1H$) and oxygen ($^{18}O/^{16}O$)). Isotope data up to 2003 are available in the GNIP database [27]. This work presents details on the history of monitoring the isotope composition of precipitation in Zagreb, Croatia, for the period 1976–2018. Such series of isotope data are rather scarce in Europe [27], and the present time series analysis can be a first step toward a more detailed comparison of data reported for sites with similar long-term records, such as Vienna (Austria), Krakow (Poland), and Ljubljana (Slovenia), in order to obtain a wider spatial and temporal pattern of the isotope composition of precipitation. Statistical analyses of isotope (δ^2H, $\delta^{18}O$, deuterium excess, and tritium activity concentration) and basic meteorological data (temperature and precipitation amount) were performed. The complete 43-year-long record was divided into subperiods in order to better investigate climatological and isotope-in-precipitation changes. Subperiods should be neither too long nor too short, so we arbitrarily chose four almost equally long subperiods: 1976–1985, 1986–1995, 1996–2006, and 2007–2018.

In the following section, we introduce the notation (δ^2H, δ^{18}O) used for stable isotope composition as well as the concepts of meteoric water lines and deuterium excess. We describe the behavior of tritium activity concentration in the atmosphere and give a brief description of measurement techniques that have changed during the studied period. An overview of sampling locations of monthly precipitation in Croatia and climate characteristics of the area are presented, which will help in discussing the data from Zagreb. In Section 3, we show the results of the monthly data, while in Section 4, we present a discussion of the statistical analyses of the annual data and average values in the subperiods, the observed temporal trends, and various correlations among the data. We discuss how the observed temperature and precipitation amount changes were recorded in the isotopic composition of precipitation in Zagreb.

2. Materials and Methods

2.1. Stable Isotopes of Hydrogen and Oxygen

The isotopic composition of water constituents depends on isotope fractionation caused by phase transfers of water masses (evaporation/precipitation), which depend on the area of water origin (latitude, altitude, continent or maritime, climate region) and the precipitation amount [2,4,32–34]. Therefore, the isotopic composition of precipitation of different origins and seasons provides for the application of stable water isotopes as tracers of the hydrological cycle.

The results are reported as δ-values per mill (‰) relative to the standard [4,35–38]:

$$\delta_{S/R} = \frac{R_{\text{Sample}}}{R_{\text{Reference}}} - 1. \tag{1}$$

Here, R_{Sample} and $R_{\text{Reference}}$ stand for the isotope ratio ($R = {}^2\text{H}/{}^1\text{H}$ and $R = {}^{18}\text{O}/{}^{16}\text{O}$) in the sample and the reference material (standard), respectively. Standard mean ocean water, SMOW, has been proposed as a (virtual) standard for reporting measured values [39]. SMOW is an arbitrary mean value based on the Epstein–Mayeda oxygen scale obtained from deep ocean water, since it does not interact with the atmosphere and has a stable isotopic composition [40], and it is defined in terms of an actual water reference standard, the NBS-1 (National Bureau of Standards, USA). In 1968, the IAEA established an international standard, the Vienna SMOW (VSMOW), which has been replaced by the VSMOW2 [38,41].

The δ^2H and δ^{18}O isotopic compositions of meteoric waters (precipitation and atmospheric water vapor) are strongly correlated. If δ^2H is plotted versus δ^{18}O, the data cluster along a straight line is

$$\delta^2\text{H} = 8.0 \cdot \delta^{18}\text{O} + 10. \tag{2}$$

The relation in Equation (2) is referred to as the global meteoric water line (GMWL) [2,39,42]. It describes the general relation between δ^2H and δ^{18}O on a global scale reasonably well. However, the intercept is higher for precipitation originating from the Mediterranean area [2,4,43–45], while the slope does not change, as in the case of the eastern Mediterranean meteoric water line, δ^2H = 8 δ^{18}O + 22 [43]. This example shows that for applications in hydrogeological studies, regional local meteoric water lines (LMWLs), either long-term or for certain shorter periods, can be more appropriate. Generally, an LMWL has the form δ^2H = a δ^{18}O + b, where a is the slope and b is the intercept. LMWLs can differ from the GMWL in terms of both the slope and intercept values, depending on the conditions for forming a local water source [1,4,46,47]. There are different ways of calculating a- and b-values. Traditionally, the ordinary least squares regression (OLSR) is used, and more recently, the reduced major axis regression (RMA) and the major axis least squares regression (MA, sometimes also called the orthogonal regression) [48,49] have been applied. The precipitation-weighted OLSR approach (PWLSR) was introduced to reduce the impact of small precipitation events that are hydrogeologically not

significant [49]. Similarly, precipitation-weighted RMA and MA, i.e., PWRMA and PWMA, regressions have been applied to data from the GNIP database, with at least 36 monthly datapoints available [48].

Deuterium excess (d-excess, or d) is defined as [2]

$$d = \delta^2H - 8\,\delta^{18}O, \tag{3}$$

which can be related to the meteorological conditions in the source region from which the water vapor is obtained [1,4,35,43,46]; therefore, it can be used to identify vapor source regions, and it is often considered to be the most useful parameter in characterizing vapor origin [43]. Winter precipitation originating from the Mediterranean Sea is characterized by distinctly higher d-excess values ($d > 18‰$) than is precipitation coming from the Atlantic ($d \sim 10‰$), reflecting the specific source conditions during water vapor formation. Increased deuterium excess in precipitation can also arise from a significant addition of re-evaporated moisture from continental basins to water vapor traveling inland [1,4,27,35,44–46,50,51].

2.2. Tritium

Tritium (^{3}H) is a natural cosmogenic isotope of hydrogen that is formed in the upper atmosphere through reactions of thermal neutrons with ^{14}N. It oxidizes to tritiated water, H^{3}HO, and thus enters the natural water cycle. The half-life of ^{3}H is 12.32 years [52], and it decays to ^{3}He by emitting beta particles with a maximal energy of 18.6 keV.

Tritium is also an anthropogenically produced isotope, and it can be differentiated as "bomb-produced" tritium and technogenic tritium. Massive injections of ^{3}H from weapons tests in the 1950s and 1960s, mostly in the Northern Hemisphere, caused an almost 100-fold increase in the tritium activity concentration in precipitation [1], known as the bomb peak. The highest concentration of tritium, about 6000 TU (1 TU = 0.118 Bq/l), was observed in 1963 in precipitation at continental stations in the Northern Hemisphere [1,27,53], while at maritime stations, the maximal values were lower (about 2000 TU). The data at the marine stations were systematically lower than at the continental stations because moisture evaporated from the ocean has a low ^{3}H activity concentration due to the long residence time of water in the ocean. After the cessation of atmospheric nuclear weapons tests, a gradual decrease in ^{3}H activity concentration at all stations in both hemispheres was observed due to natural decay and the washout of tritium into the oceans and groundwater. The levels of tritium have declined globally and regionally, approaching the natural pre-bomb level. The pre-bomb natural tritium activity concentration is assumed to be about 1 TU in oceanic regions, about 10 TU in inland areas, about 5 TU in central Europe [1], and about 5 TU on average globally [54]. Monitoring of the tritium level in precipitation at several short-distance stations showed that there was no significant systematic discrepancy between them [1]. The "anthropogenically modified natural distributions" present now are "new natural global" environmental levels.

Technogenic tritium is produced in various industries, such as nuclear power plants, nuclear reactors, future fusion reactors, fuel reprocessing plants, heavy water production facilities, medical diagnostics, radiopharmaceuticals, luminous paints, sign illumination, self-luminous aircraft, airport runway lights, luminous dials, and gauges and wrist watches [55–58]. Technogenic tritium causes deviations from the "anthropogenically modified natural tritium distribution" at a local or regional level.

The seasonal and spatial distribution of tritium activity concentration in precipitation around the globe has been found to be dominated by the annual stratosphere–troposphere exchange at high latitudes in early spring, in combination with latitudinal and continental effects [1]. The latitude effect is described as the highest ^{3}H activity concentrations observed between the 30th and 60th parallel, with values lower by a factor of approximately five at low-latitude and tropical stations.

It should be noted that the seasonal variations in ^{3}H activity concentration in precipitation do not have the same origin as the seasonal variations in δ^2H and δ^{18}O: variations in ^{3}H are caused by the exchange between the stratosphere and the troposphere and are not caused or influenced by the

temperature, while the local seasonal variations in δ^2H and $\delta^{18}O$ show a close relation with the local temperature [1,2,4,47].

2.3. Sampling Sites and Climate

There are three main climate types prevailing in Croatia: continental, maritime, and mountain. Such a climate distribution is determined by the geographical position of Croatia in the northern midlatitudes and the corresponding weather processes. Croatia is a relatively small country (56,594 km^2) positioned between the Pannonian Plain and the Adriatic Sea and has a large orographic variety. Therefore, the most important climate modifiers are the Adriatic Sea in the southwest, the mountain chain Dinarides in the central part, and openness to the Pannonian plain in the northeast [59]. Accordingly, most of Croatia has a temperate rainy climate (Köppen code Cxx [60,61]). For example, the Zagreb climate zone is described as Cfb: a temperate climate without a dry season and with a warm summer. The highest mountain areas have a cold snow and forest climate (Köppen code Dxx). The complete designation of climates for particular sampling sites is presented in Table S1 (Supplementary Materials). A comparison of the 30-year period 1981–2010 to the standard climatological period, 1961–1990, showed a significant increase in the mean annual temperature at all 20 studied stations in Croatia, with stronger warming at the continental stations than along the coast and with the largest changes in the summer [59]. It was also noted that both minimal and maximal temperatures increased by larger amplitudes inland compared to along the coast. The precipitation pattern has also changed, but differently in different parts of Croatia: an increase in the precipitation amount has been observed inland, with a statistically significant increase in autumn [59]. The observed climate changes (temperature increase and the precipitation regime) have resulted in changes in climate classes for some stations. The stations with isotope-in-precipitation data for which the climate class changed are Dubrovnik and Zadar (from Cfa to Csa) and Puntijarka on Mt. Medvednica, near Zagreb (from Dfb to Cfb) (Table S1).

A long-term isotopes-in-precipitation record (1976–2018) exists in Croatia only for the Zagreb station [27,47,62] (although microlocations have changed, as will be explained later). Data for some other stations with shorter monitoring periods were obtained during various individual projects (location numbers 1 to 12, Figure 1) [18,47,62–68]. Details on sampling sites are presented in Table S1. Some projects have also included monitoring at stations in Slovenia (location numbers 13 to 15, Figure 1), e.g., in Ljubljana [47,62,69–71], Portorož, and Kozina [47,72,73].

Precipitation monthly composite samples for the Zagreb station were collected at the Ruđer Bošković Institute (RBI, 45.817° N, 15.967°, 165 m a.s.l.) from 1976 until 1995. In 1994 and 1995, higher ^3H activity concentrations were measured due to experimental research in the nearby department in which technogenic tritium was used [74,75], while there was no influence on stable isotope data. As a consequence of local tritium contamination, a new location for precipitation sampling had to be found. During 1995 and 1996, precipitation samples were additionally collected at Puntijarka, on Mt. Medvednica (45.917° N, 15.95°, 988 m a.s.l.), 15 km north of the city of Zagreb [62], and at the Zagreb–Grič site at the Croatian Meteorological and Hydrological Service (45.814° N, 15.972° E, 157 m a.s.l.) in the center of Zagreb (in 1996). ^3H activity concentrations in precipitation at the stations Zagreb–Grič and Puntijarka in 1996 were almost identical, 10.7 ± 4.0 TU and 10.4 ± 6.0 TU, respectively [62]. For the analyses in this paper, the Zagreb–RBI data for tritium activity concentration were used for up to 1993, data from Puntijarka were taken as representative for Zagreb in 1995, and for 1996 and on, data from Zagreb–Grič were used. Tritium data exist for 1994, but they will not be discussed here because they present technogenic (local) tritium. Data for the stable isotope composition of Zagreb precipitation are not available for the 2007–2009 period and for 2011.

Daily rain events were collected in Zagreb for the period from October 2002 to March 2003, and the obtained stable isotope composition was compared to the monthly $\delta^{18}O$ and δ^2H data [76].
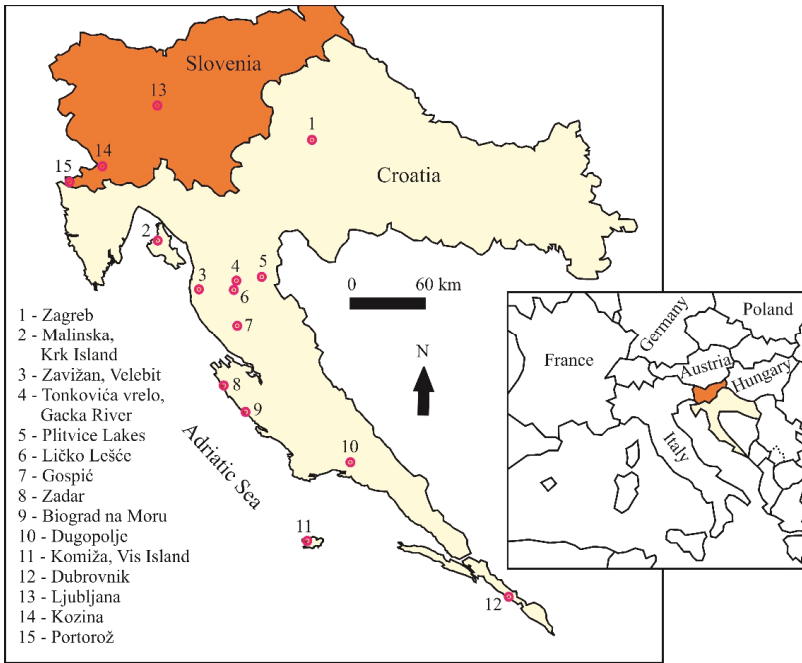
Figure 1. Map of stations with isotope-in-precipitation data in Croatia (locations 1–12) and in Slovenia (locations 13–15). Details on stations are in Table S1.

2.4. Meteorological Data

The meteorological data consisted of monthly precipitation amount and average monthly air temperature. Data were obtained on request from the Croatian Meteorological and Hydrological Service (CMHS). Meteorological records for Zagreb, Croatia, exist for the period since 1862 and have been analyzed by CMHS for the usual climatological periods [77]. Here, we used data from only the 1976–2018 period, for which we had records of the isotope composition of precipitation. Minimal and maximal monthly values within a year were identified, and the mean annual values of temperature and the total annual precipitation amount were determined.

2.5. Measurement of δ^2H and $\delta^{18}O$

The stable isotope composition of the precipitation samples for the period 1980–2003 was measured on a Varian MAT 250 dual inlet isotope ratio mass spectrometer (IRMS) at the Jožef Stefan Institute in Ljubljana [49,69,70,73]. The isotopic composition of hydrogen (δ^2H) was determined by means of the H_2 generated by the reduction of water over hot zinc (up to 1998) [69], and later over hot chromium [78]. The oxygen isotopic composition ($\delta^{18}O$) was measured by means of the water–CO_2 equilibration technique [40]. All measurements were carried out together with laboratory standards that were calibrated periodically against international standards, as recommended by the IAEA. The measurement precision of duplicates was better than ±0.1‰ for $\delta^{18}O$ and ±1‰ for δ^2H. The stable isotope composition of the precipitation sampled between 2004 and 2006 was determined at SILab (Stable Isotope Laboratory at the Physics Department, School of Medicine, University of Rijeka, Rijeka, Croatia). An HDO Equilibration Unit (ISO Cal) attached to the dual inlet port of a DeltaPlusXP (Thermo Finnigan) IRMS was used [68,79]. The $\delta^{18}O$ and the δ^2H were obtained from CO_2 and H_2 gas, respectively, after equilibration with a 4-ml water sample. The measurement reproducibility of duplicates was better than ±0.1‰ for $\delta^{18}O$ and ±1‰ for δ^2H. The stable isotope composition

of precipitation from 2010 and on was analyzed with a Liquid Water Isotope Analyzer (LWIA-24d, Los Gatos Research) at the Institute for Geochemical Research, the Hungarian Academy of Sciences, Budapest, Hungary. The uncertainty of the measurements was reported to be ±0.2‰ for $\delta^{18}O$ and ±0.6‰ for δ^2H [66]. The stable isotope composition of Zagreb's precipitation for the 2012–2018 period was determined at the Laboratory for Spectroscopy of the Faculty of Mining, Geology, and Petroleum Engineering, University of Zagreb, with a Liquid Water Isotope Analyzer (LWIA-45-EP, Los Gatos Research). Data were analyzed by the Laboratory Information Management System (LIMS) [80]. The measurement precision of duplicates was ±0.1‰ for $\delta^{18}O$ and ±0.3‰ for δ^2H.

2.6. Measurement of Tritium Activity Concentration

Tritium activity concentration (A) in all monthly samples was determined at the Ruđer Bošković Institute in Zagreb. The results are expressed in tritium units (1 TU = 0.118 Bq l^{-1}) [1] since the same units are used by the IAEA–WMO/GNIP database [27]. A tritium unit represents one ^3H atom in 10^{18} atoms of hydrogen. The gas proportional counting technique (GPC) was used up to 2009 [81–83]. Methane (CH_4) was used as a counting gas in a multiwire proportional counter. It was obtained through the reaction of water (50 ml) with aluminum carbide at 150 °C [81]. The counting energy window was set to energies between 1 keV and 10 keV to obtain the best figure of merit. Gas quality control was performed by simultaneously monitoring the count rate above the tritium channel, i.e., above 20 keV [82]. The detection limit was 2.5 TU, and the measurement uncertainty was between 2 and 5 TU, depending on the activity concentration. In 2008, a technique of liquid scintillation counting of electrolytically enriched samples (LSC-EE) was introduced, and between 2008 and 2009, GPC and LSC-EE techniques were used [83,84]. Since 2010, samples have been measured using the LSC-EE technique only [71,83–86].

The electrolytic enrichment system at the RBI was produced by the AGH University of Science and Technology, Krakow, Poland [87,88]. It consists of 20 cells 500 ml in volume (stainless steel anodes and mild steel cathodes). Each sample was distilled before electrolysis, as the required conductivity is <50 μS/cm. An enrichment run contained 15 unknown samples, 3 spike waters (water of known tritium activity concentration, 500–600 TU) used for monitoring the electrolysis performances and the calculation of enrichment factor, and 2 tritium-free samples used for system control. The enrichment procedure at RBI took 1420 Ah distributed over 8 days. Enriched samples were distilled again after electrolysis, with 6–8 g of PbCl$_2$ added to each sample. The scintillation cocktails for measurement in LSC were prepared by 8 ml of sample and 12 ml of scintillator Ultima Gold LLT in high-density low-diffusion polyethylene vials. Measurements were performed by an ultra-low-level liquid scintillation counter, the Quantulus 1220, in 10 cycles of 50 min each. Each measurement run consisted of 24 scintillation cocktails: 20 enriched samples, 1 nonenriched spike sample, 1 international standard, and 2 nonenriched background samples. On the basis of the initial and final mass of water in cells and the individual count rates of the spike water before and after enrichment, the enrichment factor E was calculated [86,87]. The average 10-year E value of the system was 26 ± 2. The detection limit obtained by the LSC-EE technique was around 0.5 TU, and the measurement uncertainty was between 0.5 and 3 TU [71,83–86].

2.7. Data Evaluation

Mean $\delta^{18}O$, δ^2H, and d-excess values, weighted by precipitation amount, were calculated from all monthly data and then summed over all collected samples per month and per year. Thus, the monthly mean values for a specific month over a certain period were obtained, as were the annual mean values. The number of datapoints per year for all years (Table 1) fulfilled the requirement for the calculation of annual mean values, i.e., the lowest number of monthly isotope datapoints per year was 9, while at least 7 monthly samples were required [89]. All years with an incomplete number of monthly samples, however, met the requirement that the available isotope data comprise more than 70% of the total precipitation amount collected per year (Table 1) [89].

Table 1. Mean annual temperature *T*, ranges of monthly temperatures within a year, annual precipitation amount *P*, weighted mean (w.m.) annual δ^{18}O, δ^2H, *d*-excess (*d*), and the mean annual tritium activity concentration *A* in precipitation at Zagreb, 1976–2018. Here, *n*: number of monthly datapoints; %*P*: percentage of precipitation if different from 100%, comprised by δ^{18}O, δ^2H, and *d*-excess data; TU: tritium unit. Bold font: the lowest and highest values in a series.

Year	T (°C) Mean	T (°C) Range	P (mm)	δ^{18}O (‰) w.m.	n, %P	δ^2H (‰) w.m.	n, %P	d (‰) w.m.	n, %P	A (TU) Mean
1976	10.6	1.3–21.4	908	–	–	–	–	–	–	**100.5**
1977	11.4	0.2–20.1	1014	–	–	–	–	–	–	79.4
1978	9.8	0.8–**18.9**	758	–	–	–	–	–	–	73.8
1979	11.0	−1.1–20.9	792	–	–	–	–	–	–	36.8
1980	**9.6**	−1.5–20.0	931	−8.92	12	−62.65	12	8.86	12	39.5
1981	11.6	−0.8–21.2	871	−9.44	12	−67.32	12	8.20	12	38.3
1982	11.7	−0.9–22.2	805	−8.31	10, 97	−59.21	10, 97	7.27	10, 97	25.1
1983	12.1	0.7–23.8	755	−9.07	12	−65.22	12	7.35	12	25.8
1984	10.9	1.3–19.9	897	−9.25	12	−64.24	12	9.75	12	20.6
1985	11.0	−**3.4**–22.0	800	−9.12	12	−66.85	12	8.84	12	18.4
1986	11.1	−2.1–21.8	786	−8.96	12	−64.45	12	7.20	12	19.3
1987	11.4	−1.8–23.2	816	−9.21	12	−64.64	12	9.04	12	23.2
1988	11.9	2.6–23.3	749	−7.29	10, 81	−55.17	11, 86	6.90	10, 81	17.8
1989	12.0	0.1–21.8	957	−6.54	11, 95	−43.23	11, 89	8.46	10, 84	23.2
1990	12.5	1.1–22.2	694	−7.81	12	−56.12	12	6.44	12	16.1
1991	11.4	0.2–23.0	787	−8.37	12	−61.94	12	5.06	12	14.5
1992	13.0	2.3–**25.8**	808	−8.96	11, 99	−63.54	11, 99	8.11	11, 99	11.1
1993	12.1	2.3–22.3	928	−8.48	10, 97	−58.22	10, 97	9.65	10, 97	17.3
1994	13.2	3.3–23.9	962	−7.20	12	−48.02	12	9.59	12	–
1995	12.0	1.8–23.8	962	−9.15	11, 99	−62.49	11, 99	**10.74**	11, 99	11.9
1996	11.0	−0.3–21.1	959	−8.30	12	−52.46	10, 90	6.79	10, 90	10.5
1997	12.2	−0.3–21.7	723	−8.02	11, 92	−56.33	11, 92	7.85	11, 92	9.7
1998	12.4	−1.5–22.5	1000	−6.87	10, 93	−47.38	10, 81	7.21	10, 81	9.1
1999	12.5	1.7–22.4	997	−8.55	12	−64.53	12	3.89	12	8.8
2000	13.8	−0.2–24.4	725	−**5.54**	10, 85	−**39.68**	9, 81	**2.28**	9, 81	9.2
2001	12.7	−0.7–23.6	813	−7.97	12	−56.68	12	7.10	12	9.5
2002	13.2	2.2–22.5	1064	−8.21	12	−56.03	12	9.65	12	8.6
2003	12.9	−0.1–**25.8**	623	−7.74	10, 95	−55.29	12	9.56	10, 95	7.3
2004	12.0	0.8–21.7	993	−8.12	12	−60.99	12	8.41	12	**5.4**
2005	11.7	−0.1–22.1	988	−9.22	12	−64.38	12	9.40	12	9.7
2006	12.7	−0.1–24.6	754	−8.23	12	−58.10	12	7.76	12	8.5
2007	13.6	1.4–23.8	896	–	–	–	–	–	–	9.5
2008	13.4	3.8–22.8	769	–	–	–	–	–	–	9.1
2009	13.4	0.0–23.6	795	–	–	–	–	–	–	9.5
2010	12.2	0.3–24.1	1155	−**9.67**	12	−**68.6**	12	8.76	12	7.9
2011	13.2	2.9–24.3	**521**	–	–	–	–	–	–	9.4
2012	13.7	−0.2–25.4	813	−6.33	9, 77	−45.22	9, 77	5.41	9, 77	6.7
2013	12.9	2.4–24.5	1092	−8.77	9, 94	−61.82	9, 94	8.37	9, 94	8.5
2014	13.8	**5.4**–22.4	**1234**	−7.69	12	−53.64	12	7.90	12	7.4
2015	13.7	3.6–25.4	824	−7.81	10, 92	−55.35	10, 92	7.16	10, 92	7.9
2016	13.1	1.0–24.2	854	−8.54	11, 99	−61.00	11, 99	7.30	11, 99	7.3
2017	13.6	−2.3–25.0	889	−7.44	11, 95	−50.40	11, 95	9.14	11, 95	6.8
2018	14.1	0.9–25.0	827	−9.27	12	−63.85	12	10.33	12	8.7

Correlations between various datapoints were obtained as ordinary least squares regressions, and the Pearson's coefficient *r* is given, as are the number of data pairs *n* and the *p*-value describing the statistical significance of the correlations. Data taken from the literature usually have the adjacent r^2 value reported.

In the special case of correlations between δ^2H and δ^{18}O (i.e., for LMWLs), different methods were applied: an ordinary least squares regression (OLSR), a reduced major axis regression (RMA), and a major axis least squares regression (MA) [48,49,89]. In addition, we calculated precipitation-weighted regressions (PWLSR, PWRMA, and PWMA) [48,49], which took into account the precipitation amount

in a particular month. The local meteoric water lines are defined as LMWL$_{OLSF}$, LMWL$_{RMA}$, LMWL$_{MA}$, LMWL$_{PWLSR}$, LMWL$_{PWRMA}$, and LMWL$_{PWMA}$. While OLSR regressions were found by commercially available software (MS Excel), for other regressions we used Local Meteoric Water Line Freeware [90]. The software also calculated an average of the root mean square sum of squared errors ($rmSSE_{av}$), which is a relative error that allows for a comparison of different methods: the closer the value of $rmSSE_{av}$ is to 1.0, the better the regression method for that set of data [48].

Deuterium excess d was calculated from paired monthly data according to Equation (3). Some precipitation samples showed very low (highly negative; in our case, the lowest value was −13‰) d-excess values. This can be caused by improper sampling (e.g., the precipitation stayed for the whole month in a sample collector), by evaporation due to a low amount of precipitation and/or high temperatures, or by the evaporation/sublimation of raindrops falling in a dry atmosphere [50,51,71].

3. Results

Data on monthly temperatures, monthly precipitation amount, and the tritium activity concentration of precipitation at Zagreb for the 1976–2018 period, as well as the stable isotope composition of monthly precipitation ($\delta^{18}O$, δ^2H, d-excess) for the 1980–2018 period, are shown in Table S2 (Supplementary Materials).

3.1. Meteorological Data

Minimal monthly (mean air) temperatures at Zagreb for the 1976–2018 period ranged from −3.4 °C (in 1985) to 5.4 °C (in 2014) (Figure 2a). They were measured in January (in 21 cases, or 49%), February (12 cases, or 27.9%), and December (9 cases, or 20.9%), and only once, in 1988, was the coldest month November. The highest monthly temperatures, in a range from 18.9 °C (1978) to 25.8 °C (1992, 2003) were measured in 26 out of 43 years (60.5%) in July, 15 times (35%) in August, and only in 2 cases in June (1979 and 1996).
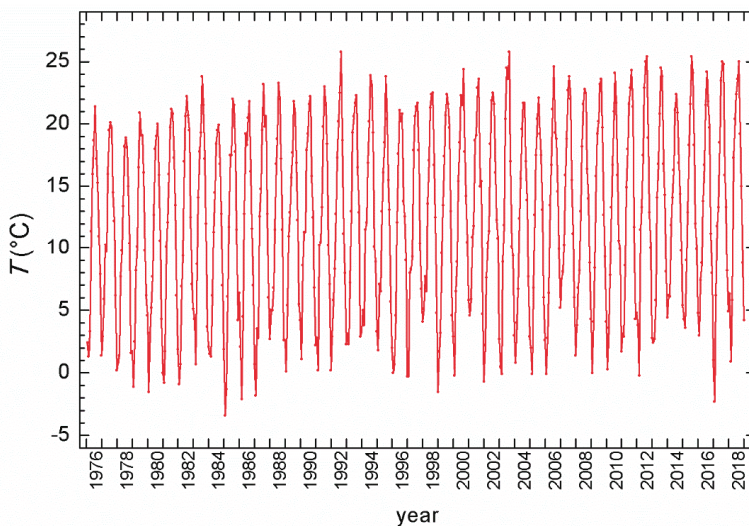
(a)

Figure 2. Cont.
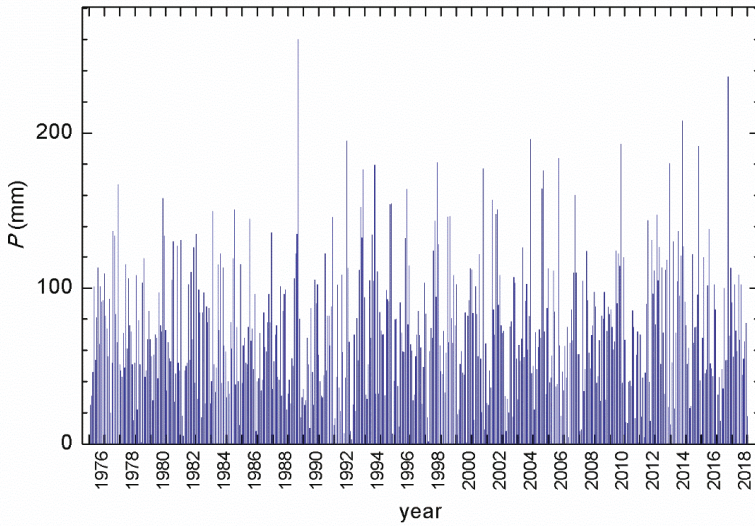
(**b**)

Figure 2. (**a**) Mean monthly air temperatures; (**b**) monthly precipitation amount. Data from station Zagreb–Grič for the 1976–2018 period. Data obtained from the Croatian Meteorological and Hydrological Service (CMHS).

Mean annual temperatures, together with yearly minimal and maximal monthly temperatures and the total yearly amount of precipitation at Zagreb for the 1976–2018 period, are shown in Table 1. Mean annual temperatures ranged from 9.6 °C in 1980 to 14.1 °C in 2018.

The annual precipitation amount ranged from 521 mm (2011) to 1234 mm (2014) (Table 1), while the maximal monthly precipitation amount occurred in August 1989 (260 mm), followed by 236 mm in September 2017 and 208 mm in September 2014. In all other months, the monthly amount of precipitation was below 200 mm (Figure 2b).

3.2. Stable Isotopes

Monthly $\delta^{18}O$ values in precipitation at Zagreb ranged from −17.6‰ (January 2005) to −0.5‰ in June 1998 (Figure 3). Similarly, the lowest δ^2H = −133.1‰ (January 2005) and the highest δ^2H = −11.4‰ (June 1998) were determined in the same months (Figure S1, Supplementary Materials).

The lowest weighted mean annual values were observed in 2010 ($\delta^{18}O$ = −9.7‰, δ^2H = −68.0‰) and the highest in 2000 ($\delta^{18}O$ = −5.54‰, δ^2H = −39.68‰) (Table 1). The number of monthly isotope datapoints (*n*) available in each year as well as the percentage of annual precipitation amount (%*P*) comprised by the isotope data during the *n* months (Table 1) satisfied the requirements for the calculation of mean annual values [89]. For 15 years out of 39 (with the available stable isotope data), the number of monthly samples was less than 12, but it was never less than 9, and the available isotope data comprised at least 77% of annual precipitation in these years.
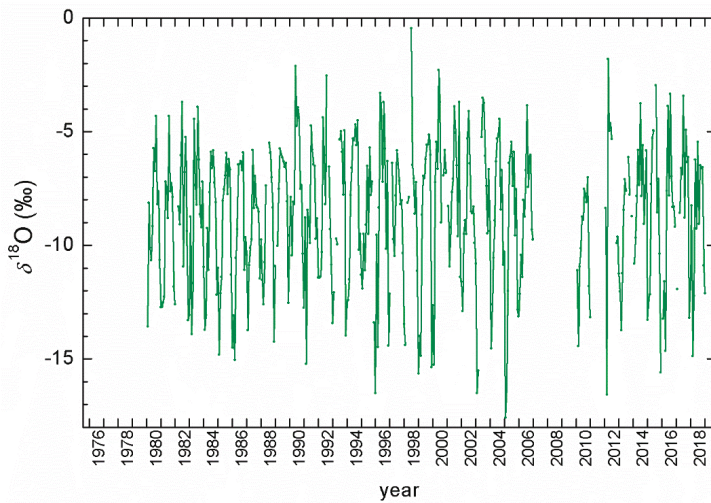
Figure 3. Monthly $\delta^{18}O$ in precipitation at Zagreb, 1980–2018 period.

Monthly values of deuterium excess (Figure 4, Table S2) ranged from −6.9‰ in May 2000 to 22.5‰ in October 1994, with 110 mm rain, probably from the Mediterranean. It should be noted here that for six months of the entire studied period, the monthly d-excess values were lower than −7‰, i.e., they were more than three standard deviations lower than the overall mean d-excess value and were therefore deleted from the record and further analysis. Three out of six cases were caused by the evaporation of small monthly precipitation amounts (11 mm in March 1996, 22 mm in February 2000, and 2 mm in December 2016), and the other three (January 1996, June 1998, and July 2012) were probably from the evaporation/sublimation of raindrops. Mean annual d-excess values ranged between 2.28‰ and 10.74‰ in 2000 and 1995, respectively (Table 1).
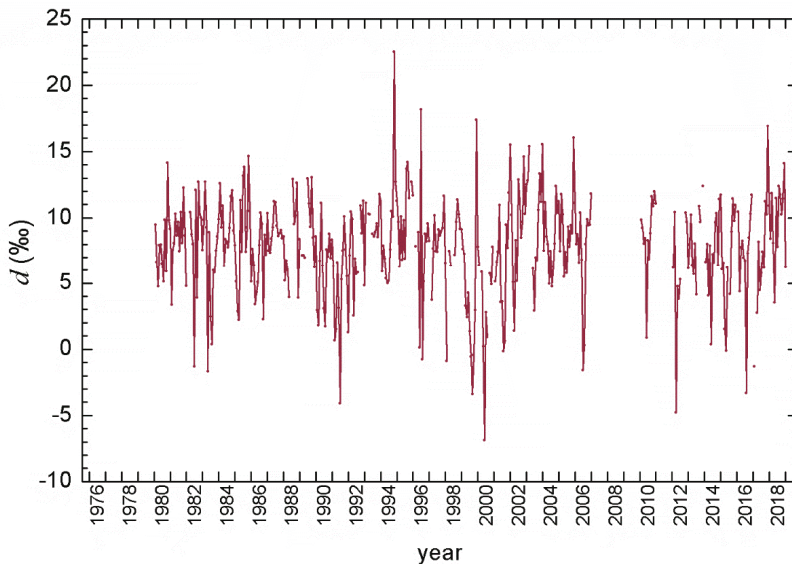

Figure 4. Monthly deuterium excess values for precipitation at Zagreb, 1980–2018.

3.3. Tritium Activity Concentration in Precipitation at Zagreb

The complete record of tritium activity concentration (A) in precipitation for Zagreb, 1976–2018 (Figure 5), exhibited a pattern typical of continental stations of the Northern Hemisphere. Seasonal variations were superposed on the basic decreasing trend of mean annual values until approximately 1996. The maximal monthly ^{3}H activity concentration at the Zagreb station was observed between May and July, mostly in June. A secondary maximum was also observed three times in January and February. The lowest ^{3}H activity concentrations were almost uniformly distributed from October to February, with a slightly more frequent occurrence in December.
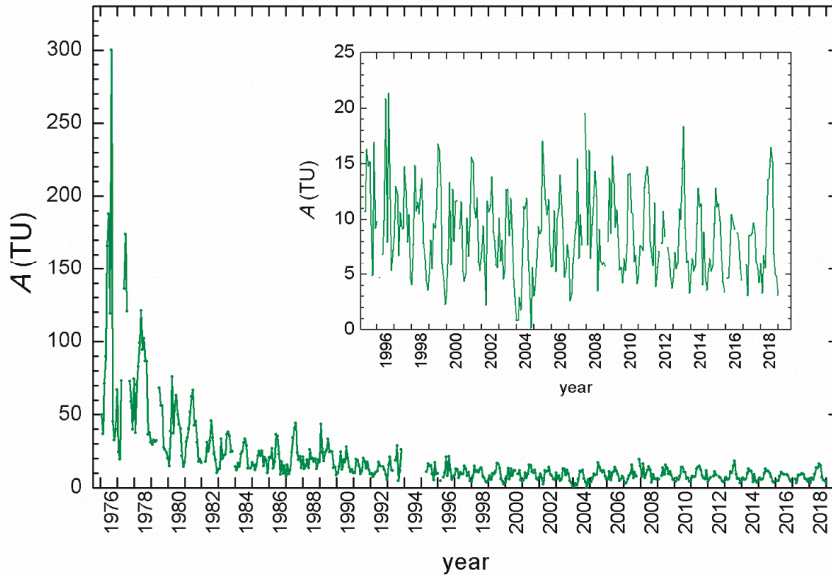

Figure 5. Complete record of monthly tritium activity concentration (A) in precipitation at Zagreb, 1976–2018. Insert: for the 1995–2018 period.

Data recorded from 1995 to 2018 (insert in Figure 5) showed an almost constant mean annual ^{3}H activity concentration ranging between 5.4 TU (in 2004) and 13.5 TU (in 1995), with a mean value of 8.5 ± 1.2 TU. Seasonal variations remained observable, with winter activities close to the natural pre-bomb ^{3}H activity concentrations (≤5 TU) and summer values up to 21 TU [91,92].

4. Discussion

4.1. Trends in Meteorological Parameters

The annual precipitation amount P at Zagreb for the 1976–2018 period (Figure 6) showed a slight increase (1.4 ± 1.7 mm/y, $r = 0.13$, $p = 0.4$), as did the maximal monthly values within a year (0.7 ± 0.5 mm/y, $r = 0.23$, $p = 0.14$), while the minimal monthly values within a year, including no-rain months, showed a slight decrease ($-0.1 ± 0.1$ mm/y, $r = -0.13$, $p = 0.41$). However, the trends (statistically not significant) were not the most prominent characteristics of the data. Higher dispersion/fluctuations from the mean value for the whole period, 1976–2018 (867 ± 138 mm), were obvious (Figure 6). In the period 1976–2000, practically all values lay within ±1 standard deviation (±1 σ), while later on there were some years with deviations from the mean over ±2 σ. The mean values of the precipitation amount in the subperiods (1980–1985, 1986–1995, 1996–2006, and 2012–2018) for which isotope data were available showed larger fluctuations in the precipitation amount in more recent periods (Table 2).
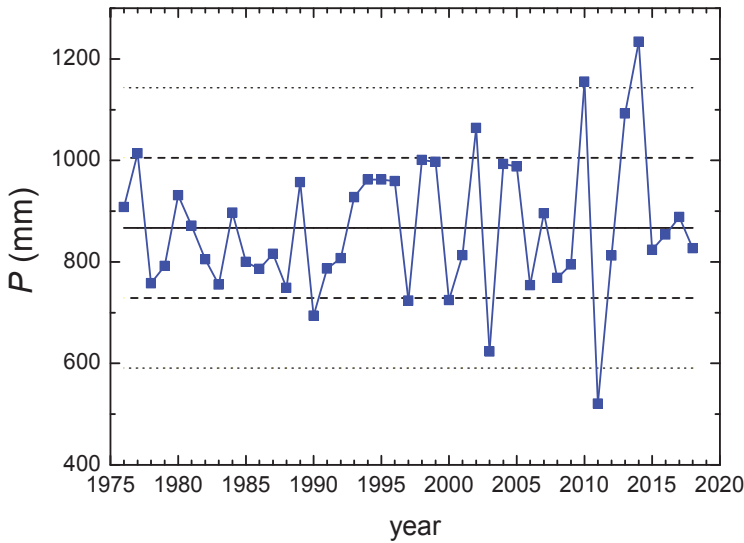
Figure 6. Annual precipitation amount *P* in Zagreb, 1976–2018 period. Solid line: the mean value for the whole period; dashed lines: ±1σ; dotted lines: ±2σ.

Table 2. Comparison of mean values of meteorological parameters (*T*, *P*) and isotopic data ($\delta^{18}O$, δ^2H, and *d*-excess) for different periods.

Period	T (°C)	P (mm)	$\delta^{18}O_{w.m.}$ (‰)	$\delta^2H_{w.m.}$ (‰)	$d_{w.m.}$ (‰)
1980–1985	11.2 ± 0.9	843 ± 67	−9.0 ± 0.4	−64.2 ± 3.0	8.4 ± 0.9
1986–1995	12.1 ± 0.7	845 ± 98	−8.2 ± 0.9	−57.8 ± 7.3	8.1 ± 1.7
1996–2006	12.5 ± 0.8	876 ± 150	−7.9 ± 1.0	−55.6 ± 7.2	7.3 ± 2.3
2012–2018	13.5 ± 0.4	933 ± 164	−8.0 ± 1.0	−55.9 ± 6.8	7.9 ± 1.6

Mean annual temperature and the minimal and maximal monthly temperature within a year (Figure 7) showed a significant increase at a 95% confidence level (*p* < 0.05) (a mean value of 0.071 ± 0.008 °C per year (*r* = 0.82), a minimal value of 0.05 ± 0.08 °C/year (*r* = 0.33), and a maximal value of 0.09 ± 0.02 °C per year (*r* = 0.69)). Since both the minimal and maximal monthly temperatures increased, but with different gradients, the result was that the increase in the amplitudes of the air temperatures (0.04 ± 0.03 °C per year, *r* = 0.26, *p* = 0.09) was significant at a 90% significance level (Figure 7).

It is also interesting to look at the monthly mean *P* and *T* values at the Zagreb station averaged for each month over a certain period (Figure 8) and calculated for four subperiods. The monthly amount of precipitation was relatively uniformly distributed throughout the year. However, the average values in January–April and in December were lower (<61 mm) than in May–November (>70 mm). The month with the highest average precipitation was September, with 97 mm. September was also the only month showing a constant increase in the amount of precipitation over the studied periods. Monthly precipitation for the period 1976–1996 (i.e., the first two periods from Figure 8a) also showed lower precipitation (<60 mm) for January to April. However, maximum precipitation amounts were observed in June (94 mm) and August (91 mm) [62]. Such a shift in the precipitation regime is in accordance with observations of climate changes in Croatia [59].
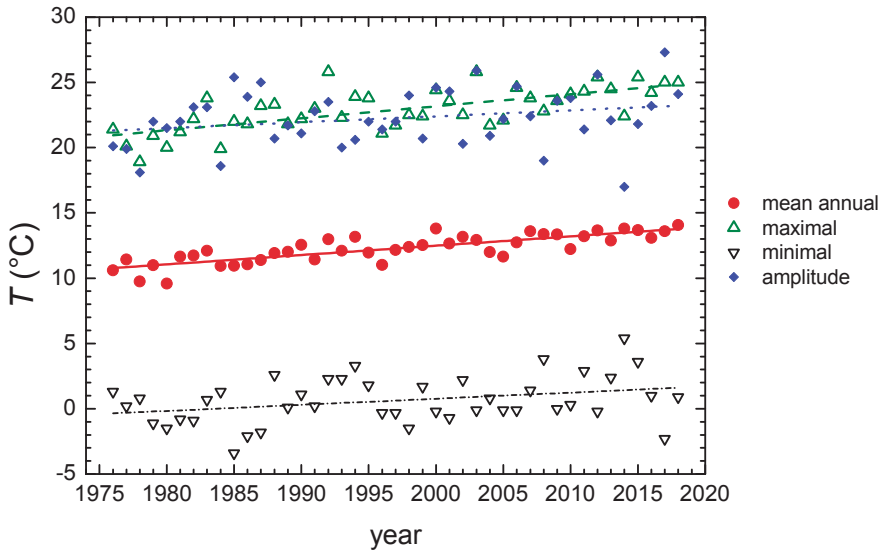
Figure 7. Mean annual temperature, minimaland maximal monthly temperatures within a year, and the temperature amplitudes in Zagreb, 1976–2018 period. Trend lines for each dataset are shown in the same color.

Mean monthly temperatures (Figure 8b) for all months in the 1976–1985 period were lower than in the most recent period, 2007–2018. The difference ranged from 1.1 °C in October and December to 3.5 °C in August and 3.6 °C in April. This observation once more corroborates observations of constant recent temperature increases that are more pronounced in the spring–summer periods [59].

4.2. Trends in Stable Isotope Data

Both the arithmetic mean annual values ($\delta^{18}O_a$, δ^2H_a, d_a) and the weighted mean annual values by amount of precipitation ($\delta^{18}O_{w.m.}$, $\delta^2H_{w.m.}$, $d_{w.m.}$) were calculated (Table S3). Due to the relatively homogeneous distribution of the annual precipitation amount (Figure 8a), there was no significant difference between the two types of annual means; in fact, a very good correlation was obtained, and here we present an example of the $\delta^{18}O$ values:

$$\delta^{18}O_{w.m.} = (1.006 \pm 0.16)\,\delta^{18}O_a + (0.48 \pm 1.4),\ n = 34,\ r = 0.73. \tag{4}$$

Changes in the weighted mean annual values of $\delta^{18}O$, δ^2H, and d-excess in the studied 1980–2018 period are shown in Figure 9 together with their respective trends. The $\delta^{18}O$ and δ^2H values exhibited increases, with an increase rate of 0.017‰ ± 0.014‰ per year ($r = 0.21$, $p = 0.23$) for $\delta^{18}O$ and 0.14‰ ± 0.11‰ per year ($r = 0.23$, $p = 0.19$) for δ^2H. The annual mean d-excess remained constant (slope ≈ 0). The corresponding weighted mean values for the periods 1980–2006 (as well as for the shorter subperiods) and 2012–2018 are shown in Table 2. Both the $\delta^{18}O$ and δ^2H values were higher in the more recent period, 2012–2018, than from 1980 to 2006. We observed a similar trend earlier: the mean $\delta^{18}O$ in the 2001–2003 period (−8.3‰) was more positive than the long-term mean $\delta^{18}O$ (−8.8‰) [76]. However, it was noticed (Table 2) that the values in the 1996–2006 and 2012–2018 periods were practically the same, although the temperature differed in these periods.
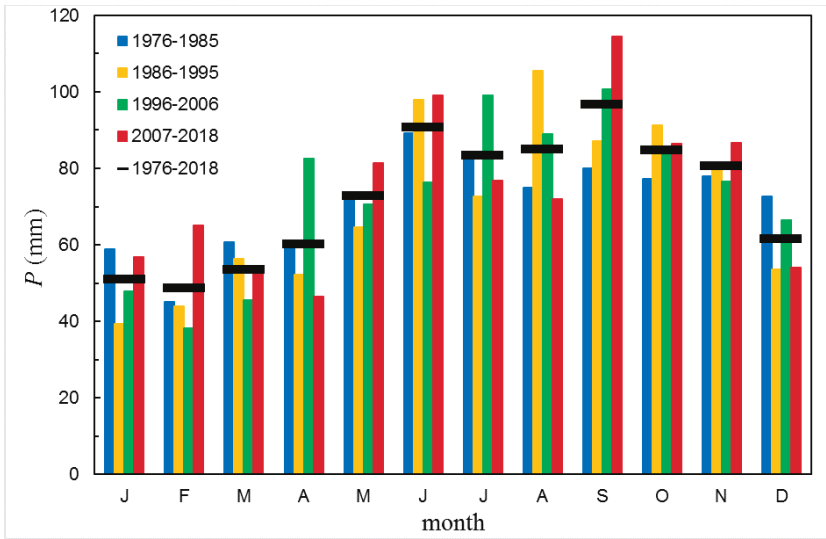
(**a**)
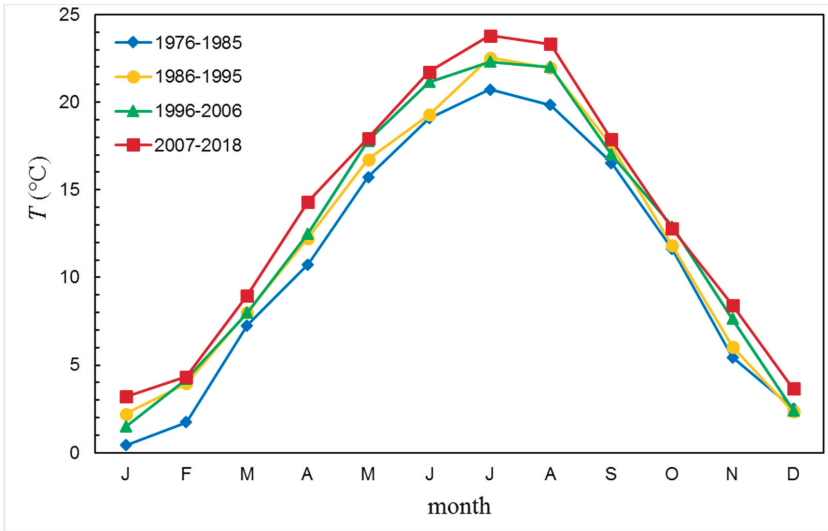
(**b**)

Figure 8. (**a**) Monthly mean precipitation amounts for the four subperiods and the average value for the whole period; (**b**) monthly mean air temperature for the subperiods.
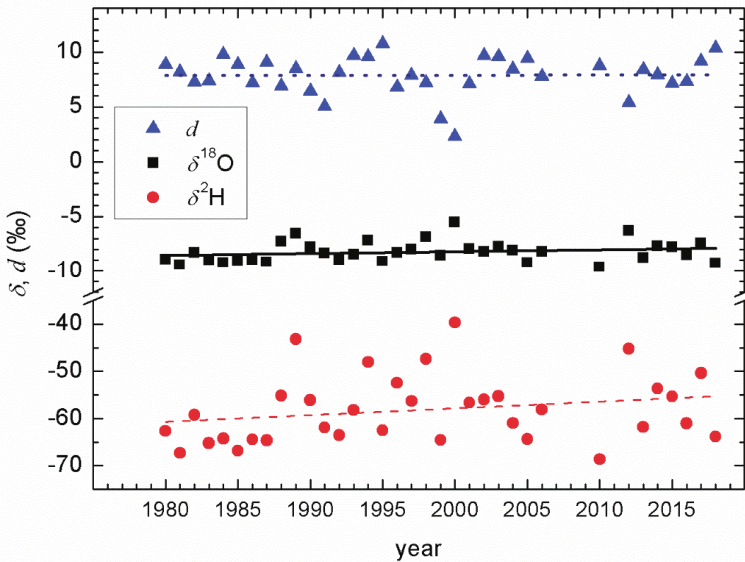
Figure 9. Temporal changes of weighted mean annual $\delta^{18}O$, δ^2H, and d-excess values.

To investigate which months contributed most to the changes in the mean annual values of $\delta^{18}O$ and δ^2H, we calculated the monthly mean $\delta^{18}O$ values in the four subperiods (Figure 10). The most pronounced differences were observed in the first half of the year, with higher values in the 2012–2018 period than in earlier years in January, March, and April, while in February, the most recent $\delta^{18}O$ and δ^2H were the lowest. The differences in the second half of the year were not large. This is behavior similar to that described earlier for the monthly mean temperature (Figure 8b). However, while the summer temperatures (June, July, and August) were the highest in the most recent period, the $\delta^{18}O$ and δ^2H were not.
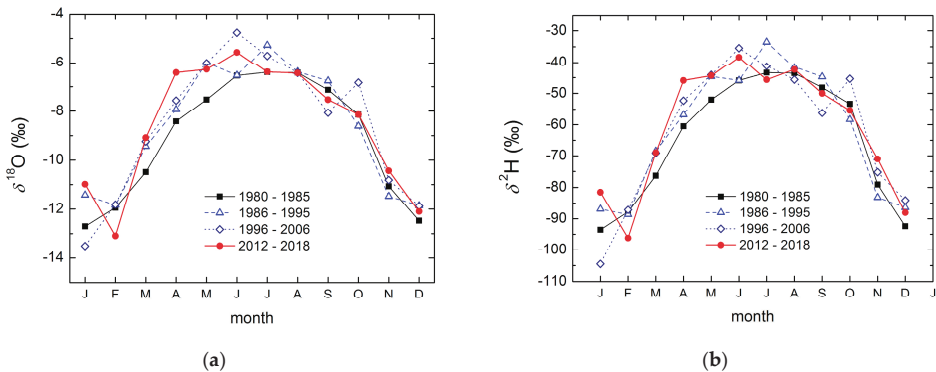
Figure 10. (**a**) Monthly mean values of $\delta^{18}O$ in the four subperiods; (**b**) monthly mean values of δ^2H in the four subperiods.

No significant correlation was observed between $\delta^{18}O$ and P. This was expected for the midlatitude continental station of Zagreb, which had an expressed seasonality in temperature (Figure 8b) and $\delta^{18}O$ values (Figure 10a) and a lack of clear seasonality in precipitation amount (Figure 8a) [4]. No amount effect was observed or reported for stations in Croatia and Slovenia [17,47,62,70–73].

4.3. Deuterium Excess

In previous analyses [47,76], it was demonstrated that the deuterium excess values for Zagreb's precipitation were higher in autumn than in the spring. The same occurred in this study using monthly mean values of *d*-excess for the four periods, 1980–1985, 1986–1995, 1995–2006, and 2012–2018 (Figure 11). In all periods, values from January to June (<8‰) were lower than those in the second half of the year (>8‰). While in the first half, there was a slight decrease in the newer periods (7.6 ± 0.6‰ in 1980–1985 to 6.0 ± 1.6‰ in 2012–2018), the *d*-excess values in the second half of the year showed an increasing trend. Such an interplay of decreases and increases of the monthly mean values eventually resulted in no change in the mean annual *d*-excess values over the whole studied period, as was shown earlier (Figure 9, Table 2). The higher *d*-excess in autumn (Figure 11) indicates a higher influence of the Mediterranean air masses in these months. It is interesting to note the shift of the autumn peak in the *d*-excess value from October (in 1980–1985) to November in the 2012–2018 period. Such behavior resembled the changes in the monthly precipitation amount in autumn (Figure 8a). November was the only month in which a significant increase in *d*-excess in the whole period was observed, with a rate/slope of 0.14‰ ± 0.04‰ per year ($n = 35$, $r = 0.54$, $p < 0.05$).
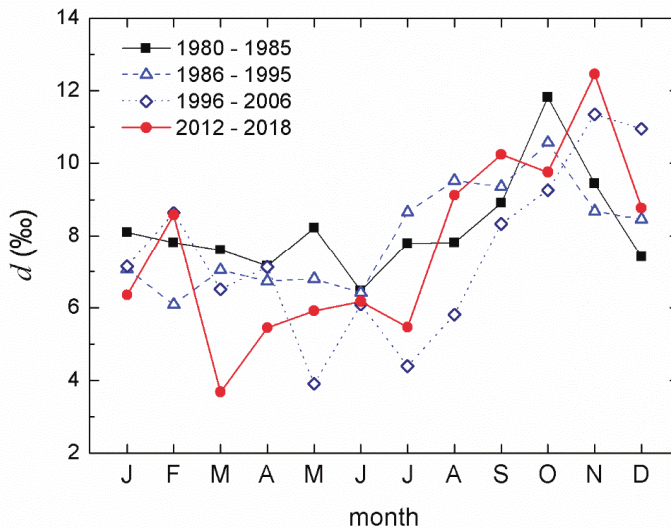
Figure 11. Monthly mean values of *d*-excess in the four subperiods.

A similar pattern of monthly *d*-excess distribution was also observed for all other Croatian stations (Figure 1, Table S1) [27,47]. The mean *d*-excess value depended on the location and altitude of the station, but in all cases, higher *d*-excess monthly values were observed in autumn–winter precipitation, usually from September to December [47]. The lowest mean monthly *d*-excess values were observed in summer months. At the South Adriatic stations (Komiža, Dubrovnik), the distribution of the precipitation amount had higher seasonality (a low amount in summer and high in winter) than it did in Zagreb, and the *d*-excess values in summer months (from May to August) were lower than 8‰, which is indicative of secondary evaporation of raindrops falling in a warm and dry atmosphere [47,50,51].

The very striking behavior of *d*-excess in March of the 2012–2018 period (Figure 11) can be explained as follows. During this period, the precipitation amount in March (57%) in four out of seven months was below 23 mm, resulting in *d*-excess values between −4.8‰ (2012, $P = 4$ mm) and 4.1‰ (2014, $P = 22$ mm), which was fully in accordance with observations from the station in Ljubljana [71] d < 5‰) and corresponded with months with low precipitation. These *d*-excess values were low, but were still within 3σ of the mean value, and therefore they were not excluded from the analyses. When

these lower *d*-excess values were excluded from the mean *d*-values for March from 2012 to 2018, the mean *d*-excess for 2012–2018 became 7.4‰, which was not different from other periods. In contrast, in the 1980–2006 period, the total number of months with precipitation below 23 mm was only two (i.e., the occurrence of low precipitation in March was only 8%), and both *d*-excess values were excluded from the analyses. This observation also corroborated observed changes in the seasonal distribution of precipitation at continental stations in Croatia [59].

4.4. Trends in Tritium Activity Concentration

The seasonal variations in the tritium activity concentration in precipitation at Zagreb for the period from 1976 to 1993 were superposed onto a generally decreasing trend (Figure 5) that could be approximated by an exponential decay curve with a half-life of about 6 years, in accordance with the estimated residence time of tritiated water vapor in the lower stratosphere (of the order of a few years) [1]. The same pattern for the tritium-in-precipitation regime (maxima from June to July and minima in winter) was observed in other continental stations (Figure 1): Ljubljana [47,70,71], Plitvice Lakes [65,67], and Gacka [68]. The ratio of the maximum to minimum value for Zagreb precipitation up to 1996 ranged from 2.2 to 5.7 without a significant trend [62], similarly to other Northern Hemisphere stations (between 2.5 and 6 [1]). The ratio was similar in the 1996–2018 period, between 2.3 and 5.3 in most cases, and was higher only in years with tritium activity concentrations close to the GPC detection limit.

The decrease in mean annual tritium activity concentration values continued after 1996 (Figure 5 insert, Figure 12), but to a much lesser extent of 0.08 TU per year, resulting in mean values of 8.8 ± 1.4 TU in 1996–2006 and 7.6 ± 0.8 TU in 2012–2018. The mean values for the station Ljubljana were 9.1 TU and 8.3 TU during 1998–2010 and 2007–2010, respectively [71], showing the same trend.
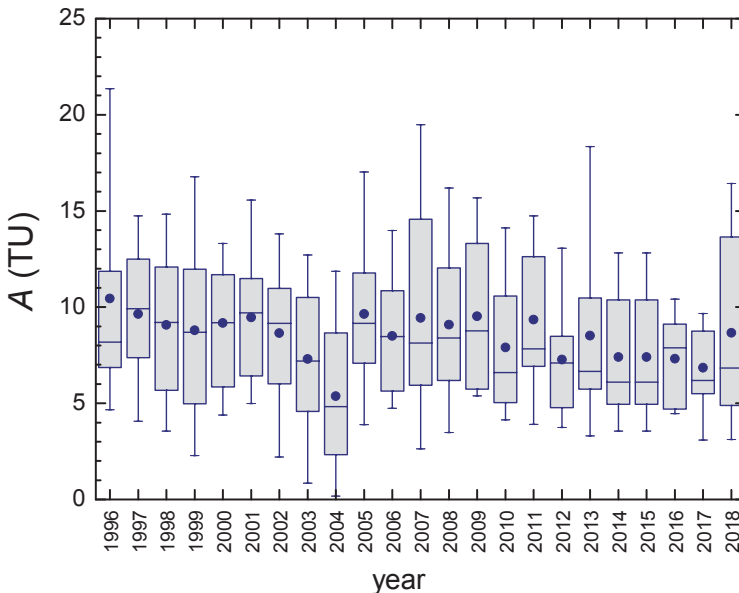
Figure 12. Tritium activity concentration in precipitation at Zagreb during the period 1996–2018. The boxplot shows the median value and the percentile range 25%–75% in a shadowed box, — shows the percentile range 5%–95%, and the average value is shown by the symbol ●.

Bomb-produced tritium in precipitation until about 1995 prevented studies on whether the natural production of tritium was influenced by variations in solar activities. The modulation of cosmogenic

tritium production by an 11-year solar cycle has been recently shown in precipitation at several stations worldwide [93]. Local maxima in the tritium activity concentration in precipitation were observed simultaneously with maxima in neutron flux (minima in sunspot numbers). Our data (Figure 12) also showed local maxima in mean annual values and larger variability in 1996, 2007, and 2018 in accordance with the observations presented in Reference [93].

4.5. Local Meteoric Water Line

The slopes (*a*) and intercepts (*b*) of LMWLs were obtained using different regression methods (Table 3). The whole 1980–2018 period was taken, as were individual subperiods, and the present values were compared to the available data on LMWLs for Zagreb precipitation from different earlier periods (obtained using different regression methods). The slopes and intercepts determined using different regression methods increased from the OLSR to the RMA and MA (in the whole period, as well as in the subperiods (Table 3)), as was also observed for most continental stations [48]. The same was also valid for precipitation-weighted regressions. No difference was observed between the corresponding nonweighted and weighted types of regression, as was expected from the rather homogeneous distribution of the monthly precipitation amount. If the $rmSSE_{av}$ value was taken into account, all values were close to 1 (closer to 1 for RMA and PWRMA over the whole long-term period). In subperiod 1980–1985, PWMA represented the LMWL equally as well as PWRMA and RMA did; in subperiods 1986–1995 and 1996–2006, the best fits were obtained by RMA and PWMA; and in the most recent subperiods, the best fits were obtained by RMA and PWLSR (Table 3). It may be concluded that the local meteoric water line for Zagreb was best described by the nonweighted RMA regression method (Figure 13):

$$\delta^2 H_{RMA,all} = (7.74 \pm 0.06)\, \delta^{18}O + (5.6 \pm 0.6),\ n = 389. \tag{5}$$
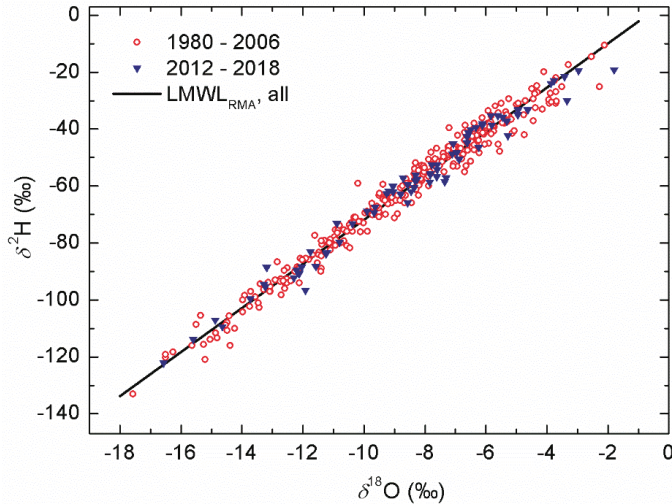
Figure 13. Local meteoric water line (LMWL) for Zagreb precipitation. Data from two periods are shown by different symbols. The fitted line is expressed by Equation (5).

A closer look at previously published LMWLs points to the difference in data up to 1996, with slope and intercept values close to 8 [27,62], while in 2001–2003, the slope was lower (7.3 + 0.2) and the intercept much lower (2.8 + 1.8) [47]. A similar conclusion was obtained from the present calculations (Table 3): all regression methods resulted in a slope close to 8 and an intercept in the range 7.3 to 9.3 in the subperiods 1980–1985 and 1986–1995. However, the slope values ranged from 7.4 to 7.8 and the

intercept values from 2.6 to 6.3 in the subperiods 1996–2006 and 2012–2018. This difference can be explained by increases in temperature, especially in the summer months, and higher variability in the precipitation amount, which both led to more precipitation with lower d-excess, i.e., below the LMWL, as can be seen from Figure 13.

Table 3. Slopes (a) and intercepts (b) of the local meteoric water line (LMWL) for Zagreb in different periods and obtained using different regression methods. OLSR: ordinary least squares regression; RMA: reduced major axis regression; MA: major axis least squares regression; PWLSR, PWRMA, and PWMA: precipitation-weighted respective regressions; n: number of datapoints included; r and r^2: regression coefficients; $rmSSE_{av}$: average of the root mean square sum of squared errors [48].

Period	Method	a	b	n	r or r^2	Ref.
1980–1996	OLSR	7.9 ± 0.1	7.9 ± 0.1	194	$r = 0.985$	[62]
1980–1995 Zagreb	OLSR	7.91 ± 0.09	7.33 ± 0.83	182	$r^2 = 0.98$	[27]
	RMA	8.00 ± 0.09	8.13 ± 0.83	182	$r^2 = 0.98$	
	PWLSR	7.88 ± 0.09	7.52 ± 0.82	182	$r^2 = 0.95$	
1996–2003 Zagreb–Grič	OLSR	7.32 ± 0.17	0.68 ± 1.57	89	$r^2 = 0.95$	[27]
	RMA	7.50 ± 0.17	2.16 ± 1.55	89	$r^2 = 0.95$	
	PWLSR	7.22 ± 0.16	0.50 ± 1.39	89	$r^2 = 0.96$	
1980–2003	OLSR	7.8 ± 0.1	5.7 ± 0.8	271	$r = 0.98$	[47]
2001–2003	OLSR	7.3 ± 0.2	2.8 + 1.8	37	$r = 0.99$	[47]
					$rmSSE_{av}$	
1980–2018	OLSR	7.65 ± 0.06	4.79 ± 0.55	389	1.0047	This work
	RMA	7.74 ± 0.06	5.57 ± 0.55	389	1.0019	
	MA	7.83 ± 0.06	6.36 ± 0.56	389	1.0047	
	PWLSR	7.64 ± 0.06	5.24 ± 0.54	389	1.0060	
	PWRMA	7.73 ± 0.06	6.00 ± 0.54	389	1.0019	
	PWMA	7.82 ± 0.06	6.76 ± 0.55	389	1.0035	
1980–1985	OLSR	7.92 ± 0.14	7.45 ± 1.35	70	1.0044	This work
	RMA	8.00 ± 0.14	8.23 ± 1.33	70	1.0018	
	MA	8.09 ± 0.14	9.00 ± 1.36	70	1.0044	
	PWLSR	7.87 ± 0.14	7.26 ± 1.36	70	1.0075	
	PWRMA	7.96 ± 0.14	8.07 ± 1.36	70	1.0018	
	PWMA	8.05 ± 0.15	8.86 ± 1.38	70	1.0018	
1986–1995	OLSR	7.94 ± 0.11	7.46 ± 1.03	112	1.0045	This work
	RMA	8.03 ± 0.11	8.22 ± 1.02	112	1.0018	
	MA	8.11 ± 0.11	8.96 ± 1.04	112	1.0044	
	PWLSR	7.90 ± 0.12	7.73 ± 1.03	112	1.0093	
	PWRMA	7.99 ± 0.12	8.51 ± 1.03	112	1.0024	
	PWMA	8.08 ± 0.12	9.28 ± 1.04	112	1.0016	
1996–2006	OLSR	7.43 ± 0.11	2.59 ± 0.97	121	1.0048	This work
	RMA	7.52 ± 0.10	3.35 ± 0.96	121	1.0019	
	MA	7.60 ± 0.11	4.08 ± 0.98	121	1.0047	
	PWLSR	7.38 ± 0.11	2.68 ± 0.95	121	1.0095	
	PWRMA	7.47 ± 0.11	3.44 ± 0.95	121	1.0024	
	PWMA	7.56 ± 0.11	4.19 ± 0.96	121	1.0018	
2012–2018	OLSR	7.52 ± 0.13	3.56 ± 1.17	74	1.0043	This work
	RMA	7.60 ± 0.13	4.24 ± 1.16	74	1.0017	
	MA	7.68 ± 0.13	4.90 ± 1.19	74	1.0043	
	PWLSR	7.61 ± 0.12	5.16 ± 1.09	74	1.0008	
	PWRMA	7.68 ± 0.12	5.74 ± 1.09	74	1.0029	
	PWMA	7.75 ± 0.12	6.32 ± 1.10	74	1.0084	

4.6. Temperature Dependence of $\delta^{18}O$

The relation between all values of the mean monthly air temperature T and the monthly $\delta^{18}O$ values (Figure 14) can be described as

$$\delta^{18}O = (0.331 \pm 0.013) \, T - (12.8 \pm 0.2), \; n = 394, \; r = 0.795. \tag{6}$$

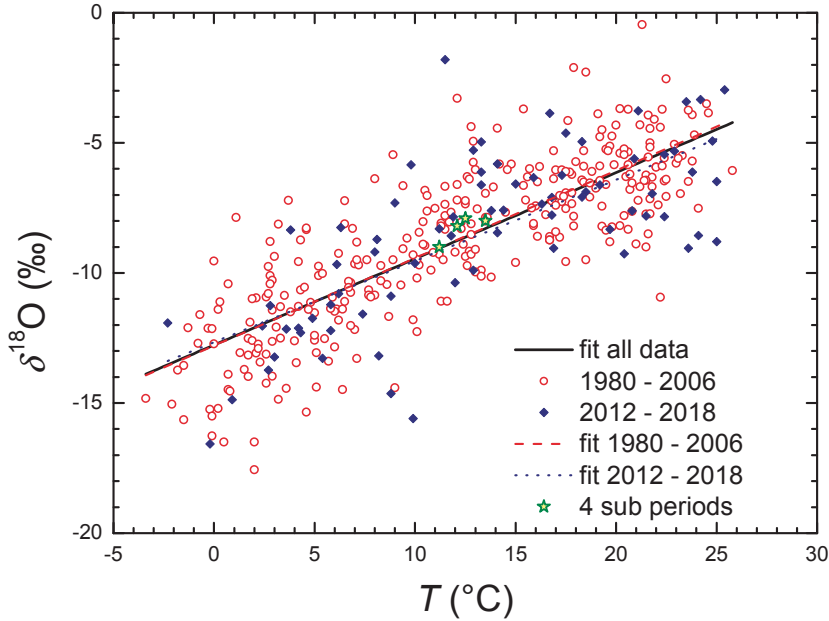**Figure 14.** Temperature dependence of $\delta^{18}O$ in monthly precipitation at the Zagreb station during different periods. Regression lines are represented by Equations (6) and (8). The mean values in the subperiods (stars) are taken from Table 2.

When data for the periods 1980–2006 and 2012–2018 were separated, the two relations were

$$\delta^{18}O_{1980\text{-}2006} = (0.336 \pm 0.013) \, T - (12.8 \pm 0.2), \; n = 320, \; r = 0.814, \tag{7}$$

$$\delta^{18}O_{2012\text{-}2018} = (0.312 \pm 0.036) \, T - (12.7 \pm 0.5), \; n = 74, \; r = 0.718. \tag{8}$$

Although Equations (7) and (8) indicate a slight change in the temperature coefficient, the difference is comparable to the statistical uncertainties in the *a*-values, and therefore it can be concluded that there was no change in the relation $\delta^{18}O$ versus T in the recent period compared to the older one. The two lines (Equations (7) and (8)) are practically indistinguishable (Figure 14). The new relation for the complete set of long-term data for Zagreb (Equation (6)) was not different (i.e., it is within uncertainties) from the same relation for the data for the 1980–1996 period ($\delta^{18}O = (0.325 \pm 0.016) \, T - (12.6 \pm 0.2)$, $r = 0.83$, $n = 183$) [62]. The slopes in Equations (7) and (8) were also comparable to the slope of 0.31‰ per °C, which was determined from long-term data from midlatitude stations in the Northern Hemisphere [4].

5. Conclusions

A 43-year-long record of data on the isotope composition of precipitation ($\delta^{18}O$, δ^2H, *d*-excess, and the tritium activity concentration A), together with meteorological data (air temperature, precipitation

amount) at a continental station in Zagreb, Croatia, was studied, divided into four almost equally long subperiods. However, due to some missing data on stable isotope composition, the first (1980–1985) and the last (2012–2018) subperiods were shorter than the two subperiods in between (1986–1996, 1996–2006).

A constant increase in mean annual temperature was observed at a rate of 0.07 °C per year. An increase in monthly mean temperature was observed in all months in 2012–2018 when compared to earlier subperiods, with larger differences in the spring–summer than in autumn. The most striking feature of the annual precipitation amount was larger variations in the last two subperiods compared to earlier. A shift of the month with the highest precipitation amount was observed, from June and August to September.

Annual mean $\delta^{18}O$ and δ^2H values in the whole long-term period showed an increase of 0.017‰ per year and 0.14‰ per year, respectively. When monthly mean values in different subperiods were compared, larger differences were observed in the first half of the year than in the second one. Both of these changes in the stable isotope composition resembled observed changes in air temperature.

Although mean annual d-excess remained constant over the whole long-term period, there was a tendency for a decrease in the d-excess value in the first half of the year and an increase in the second half due to the influence of air masses originating from the eastern Mediterranean. Together with a shift in the maximal monthly mean value from October to November and a significant increase in d-excess in November, these observations point to changes in the precipitation regime and circulation pattern of air masses during the most recent period.

Different regression methods for the calculation of the local meteoric water line for Zagreb gave very similar values for the slope and intercept, with a slight preference for the RMA method and with no difference between nonweighted and precipitation-weighted values. In addition, no significant difference in both LMWLs and the temperature dependence of $\delta^{18}O$ values was observed between the most recent period (2012–2018) and the earlier period (1980–2006). The observed temperature gradient of 0.33‰ per °C was comparable to that of other similar stations.

The tritium activity concentration in precipitation in Zagreb between 1976 and 1994 exhibited pronounced seasonal variations superposed on a generally decreasing trend with a half-life of about 6 years, which is typical for continental stations of the Northern Hemisphere. Since 1996, the mean annual A values have been almost constant, and the mean A value during the 2012–2018 period was 7.6 ± 0.8 TU. The tritium activity concentration in precipitation with no bomb-peak influence is worth further monitoring because of possible local contamination with technogenic tritium and also to enable studies of the solar cycle influence on the production of cosmogenic tritium.

The present analysis of long-term data on the isotope composition of precipitation may be useful for future comparisons to some other long-term records in nearby countries to obtain better knowledge on spatial and temporal variations across the wider region. It can also be a good basis for a comparison to some short-term records at other stations in Croatia. Last but not least, this analysis shows that climate changes are reflected in isotope compositions of precipitation, which means that further monitoring at stations with long-term records could be useful in studying the impact of climate changes on the environment, especially on water resources.

participated in discussions and reviewed the manuscript. All authors have read and agreed to the published version of the manuscript.

List of Abbreviations

CMHS	Croatian Meteorological and Hydrological Service
GMWL	Global meteoric water line
GNIP	Global Network of Isotopes in Precipitation
GPC	Gas proportional counting
IAEA	International Atomic Energy Agency
IRMS	Isotope ratio mass spectrometry
LMWL	Local meteoric water line
LSC-EE	Liquid scintillation counting with electrolytic enrichment
MA	Major axis least squares regression
OLSR	Ordinary least squares regression
PWLSR	Precipitation-weighted OLSR
PWMA	Precipitation-weighted MA
PWRMA	Precipitation-weighted RMA
RBI	Ruđer Bošković Institute
RMA	Reduced major axis regression
rmSSEav	Average of the root mean square sum of squared errors
SMOW	Standard mean ocean water
TU	Tritium unit
WMO	World Meteorological Organization

References

1. Mook, W.G. *Environmental Isotopes in the Hydrological Cycle, Principles and Applications, Volumes I, IV and V*; Technical Documents in Hydrology No. 39; IAEA-UNESCO: Paris, France, 2001.
2. Dansgaard, W. Stable isotopes in precipitation. *Tellus* **1964**, *16*, 436–468. [CrossRef]
3. Maloszewski, P.; Zuber, A. Principles and practice of calibration and validation mathematical models for the interpretation of environmental tracer data in aquifers. *Adv. Water Resour.* **1993**, *16*, 173–190. [CrossRef]
4. Rozanski, K.; Araguás-Araguás, L.; Gonfiantini, R. Isotopic patterns in modern global precipitation. *Geophys. Monogr.* **1993**, *78*, 1–36. [CrossRef]
5. Rozanski, K.; Araguás-Araguás, L. Spatial and temporal variability of stable isotope composition of precipitation over the South American continent. *Bull. Inst. Fr. Études Andin.* **1995**, *24*, 379–390.
6. Adomako, D.; Gibrilla, A.; Maloszewski, P.; Ganyaglo, S.Y.; Rai, S.P. Tracing stable isotopes (δ^2H and δ^{18}O) from meteoric water to groundwater in the Densu River basin of Ghana. *Environ. Monit. Assess.* **2015**, *187*, 1–15. [CrossRef]
7. Vrzel, J.; Kip Solomon, D.; Blažeka, Ž.; Ogrinc, N. The study of the interactions between groundwater and Sava River water in the Ljubljansko polje aquifer system (Slovenia). *J. Hydrol.* **2018**, *556*, 384–396. [CrossRef]
8. Parlov, J.; Kovač, Z.; Nakić, Z.; Barešić, J. Using Water Stable Isotopes for Identifying Groundwater Recharge Sources of the Unconfined Alluvial Zagreb Aquifer (Croatia). *Water* **2019**, *11*, 2177. [CrossRef]
9. Kong, Y.; Wang, K.; Li, J.; Pang, Z. Stable Isotopes of Precipitation in China: A Consideration of Moisture Sources. *Water* **2019**, *11*, 1239. [CrossRef]
10. Rao, S.M. Injected radiotracer techniques in hydrology. *Proc. Indian Acad. Sci.* **1984**, *99*, 319–335.
11. Clark, I.; Fritz, P. *Environmental Isotopes in Hydrogeology*; Lewis Publ.: Boca Raton, FL, USA, 1997; p. 328.
12. Kendall, C.; McDonnell, J.J. *Isotope Tracers in Catchment Hydrology*; Elsevier Science: Amsterdam, The Netherlands, 1998; p. 840.
13. Mayr, C.; Langhamer, L.; Wissel, H.; Meier, W.; Sauter, T.; Laprida, C.; Massaferro, J.; Försterra, G.; Lücke, A. Atmospheric controls on hydrogen and oxygen isotope composition of meteoric and surface waters in Patagonia. *Hydrol. Earth Syst. Sci.* **2018**. [CrossRef]
14. Burnik Šturm, M.; Ganbaatar, O.; Voigt, C.C.; Kaczenskya, P. First field-based observations of δ^2H and δ^{18}O values of event-based precipitation, rivers and other water bodies in the Dzungarian Gobi, SW Mongolia. *Isot. Environ. Health Stud.* **2017**, *53*, 157–171. [CrossRef] [PubMed]
15. Lawrence, J.R.; White, J.R.C. The Elusive Climate Signal in the Isotopic Composition of Precipitation Stable Isotope Geochemistry: A Tribute to Samuel Epstein. In *Stable Isotope Geochemistry: A Tribute to Samuel Epstein*; Taylor, H.P., O'Neil, J.R., Jr., Kaplan, I.R., Eds.; Special Publication No.3; The Geochemical Society: Washington, DC, USA, 1991.
16. Gat, J.R. Some classical concepts of isotope hydrology. In *Isotopes in the Water Cycle: Past, Present and Future of a Developing Science*; Aggarwal, P.K., Gat, J.R., Fröhlich, K., Eds.; Springer: Dordrecht, The Netherlands, 2005; pp. 127–137.
17. Krklec, K.; Domínguez-Villar, D.; Lojen, S. The impact of moisture sources on the oxygen isotope composition of precipitation at a continental site in central Europe. *J. Hydrol.* **2018**, *561*, 810–821. [CrossRef]
18. Horvatinčić, N.; Krajcar Bronić, I.; Barešić, J.; Obelić, B.; Vidič, S. Tritium and stable isotope distribution in the atmosphere at the coastal region of Croatia. In *Isotopic Composition of Precipitation in the Mediterranean Basin in Relation to Air Circulation Patterns and Climate, IAEA-TECDOC-1453*; Gourcy, L., Ed.; IAEA: Vienna, Austria, 2005; pp. 37–50.
19. Giustini, F.; Brilli, M.; Patera, A. Mapping oxygen stable isotopes of precipitation in Italy. *J. Hydrol. Reg. Stud.* **2016**, *8*, 162–181. [CrossRef]
20. Longinelli, A.; Anglesio, E.; Flora, O.; Iacumin, P.; Selmo, E. Isotopic composition of precipitation in Northern Italy: Reverse effect of anomalous climatic events. *J. Hydrol.* **2006**, *329*, 471–476. [CrossRef]
21. Rozanski, K.L.; Gonfiantini, R. Isotopes in climatological studies: Environmental isotopes are helping us understand the world's climate. *IAEA Bull.* **1990**, *4*, 9–15.
22. Marchetti, D.W.; Marchetti, S.B. Stable isotope compositions of precipitation from Gunnison, Colorado 2007–2016: Implications for the climatology of a high-elevation valley. *Heliyon* **2019**, *5*, e02120. [CrossRef]

23. Ehleringer, J.R.; Cerling, T.E.; West, J.B.; Podlesak, D.W.; Chesson, L.A.; Bowen, G.J. Spatial considerations of stable isotope analyses in environmental forensics. In *Issues in Environmental Science and Technology*; Hester, R.E., Harrison, R.M., Eds.; Royal Society of Chemistry Publishing: Cambridge, UK, 2008; Volume 26, pp. 36–53. [CrossRef]

24. Bowen, G.J.; Wassenaar, L.I.; Hobson, K.A. Global application of stable hydrogen and oxygen isotopes to wildlife forensics. *Oecologia* **2005**, *143*, 337–348. [CrossRef]

25. West, A.G.; February, E.C.; Bowen, G.J. Spatial analysis of hydrogen and oxygen stable isotopes ("isoscapes") in ground water and tap water across South Africa. *J. Geochem. Explor.* **2014**, *145*, 213–222. [CrossRef]

26. Terzer, S.; Wassenaar, L.I.; Araguás-Araguás, L.J.; Aggarwal, P.K. Global isoscapes for δ^{18}O and δ^{2}H in precipitation: Improved prediction using regionalized climatic regression models. *Hydrol. Earth Syst. Sci.* **2013**, *17*, 4713–4728. [CrossRef]

27. IAEA/WMO. Global Network of Isotopes in Precipitation. The GNIP Database. Available online: https://nucleus.iaea.org/wiser (accessed on 22 November 2019).

28. Lewis, S.L.; Maslin, M.A. Defining the Anthropocene. *Nature* **2015**, *519*, 171–180. [CrossRef]

29. IPCC. The Intergovernmental Panel on Climate Change. Available online: https://www.ipcc.ch/sr15/ (accessed on 26 November 2019).

30. Climate Central. Available online: https://www.climatecentral.org/gallery/graphics/the-10-hottest-global-years-on-record (accessed on 22 November 2019).

31. NASA. Available online: https://www.nasa.gov/press-release/nasa-noaa-data-show-2016-warmest-year-on-record-globally (accessed on 22 November 2019).

32. Craig, H. Isotope variations in meteoric waters. *Science* **1961**, *133*, 1702–1703. [CrossRef] [PubMed]

33. Gat, J.R. Oxygen and hydrogen isotopes in the hydrologic cycle. *Annu. Rev. Earth Planet Sci.* **1996**, *24*, 225–262. [CrossRef]

34. Gat, R.J.; Mook, W.G.; Meijer, A.J. Atmospheric water. In *Environmental Isotopes in the Hydrological Cycle—rinciples and Applications*; Mook, W.G., Ed.; Technical Documents in Hydrology; IAEA: Vienna, Austria, 2001; No. 39; Volume 2, p. 113.

35. IAEA. *Stable Isotope Hydrology: Deuterium and Oxygen-18 in Water Cycle*; Gat, J.R., Gonfiantini, R., Eds.; Technical Reports Series 210; IAEA: Vienna, Austria, 1981; p. 339.

36. Coplen, T.B. New guidelines for the reporting of stable hydrogen, carbon, and oxygen isotope ratio data. *Geochim. Cosmochim. Acta* **1996**, *60*, 3359. [CrossRef]

37. Coplen, T.B.; Bohlke, J.K.; De Bievre, P.; Ding, T.; Holden, N.E.; Hopple, J.A.; Krouse, H.R.; Lamberty, A.; Peiser, P.S.; Revesz, K.; et al. Isotope-abundance variations of selected elements (IUPAC Technical Report). *Pure Appl. Chem.* **2002**, *74*, 1987–2017. [CrossRef]

38. Dunn, P.J.H.; Carter, J.F. (Eds.) *Good Practice Guide for Isotope Ratio Mass Spectrometry*, 2nd ed.; FIRMS: Bristol, UK, 2018; p. 84. ISBN 978-0-948926-33-4. Available online: http://www.forensic-isotopes.org/gpg.html (accessed on 26 November 2019).

39. Craig, H. Standard for Reporting Concentrations of Deuterium and Oxygen-18 in Natural Waters. *Science* **1961**, *133*, 1833–1834. [CrossRef]

40. Epstein, S.; Mayeda, T.K. Variations of ^{18}O content of waters from natural sources. *Geochim. Cosmochim. Acta* **1953**, *4*, 213–224. [CrossRef]

41. Brand, W.A.; Coplen, T.B.; Vogl, J.; Rosner, M.; Prohaska, T. Assessment of International Reference Materials for Isotope-Ratio Analysis (IUPAC Technical Report). *Pure Appl. Chem.* **2014**, *86*, 425–467. [CrossRef]

42. Dansgaard, W. The isotope composition of natural waters. *Medd. Grønland* **1961**, *165*, 120.

43. Gat, J.R.; Carmi, I. Evolution of the Isotopic Composition of Atmospheric Waters in the Mediterranean Sea Area. *J. Geophys. Res.* **1970**, *75*, 3039–3048. [CrossRef]

44. Cruz-San, J.; Araguas-Araguas, L.; Rozanski, K.; Benavente, J.; Cardenal, J.; Hidalgo, M.C.; Garcia-Lopez, S.; Martinez-Garrido, J.C.; Moral, F.; Olias, M. Sources of precipitation over South-Eastern Spain and groundwater recharge—An isotopic study. *Tellus B* **1992**, *44*, 226–236. [CrossRef]

45. IAEA. *Isotopic Composition of Precipitation in the Mediterranean Basin in Relation to Air Circulation Patterns and Climate: Final Report of a Coordinated Research Project 2000–2004*; IAEA-TECDOC-1453; IAEA: Vienna, Austria, 2005.

46. Gat, J.R.; Shemesh, A.; Tziperman, E.; Hecht, A.; Georgopoulos, D.; Basturk, O. The stable isotope composition of waters of the eastern Mediterranean Sea. *J. Geophys. Res.* **1996**, *101*, 6441–6451. [CrossRef]

47. Vreča, P.; Krajcar Bronić, I.; Horvatinčić, N.; Barešić, J. Isotopic characteristics of precipitation in Slovenia and Croatia: Comparisom of continental and maritime stations. *J. Hydrol.* **2006**, *330*, 457–469. [CrossRef]

48. Crawford, J.; Hughes, C.E.; Lykoudis, S. Alternative least squares methods for determining the meteoric water line, demonstrated using GNIP data. *J. Hydrol.* **2014**, *519*, 2331–2340. [CrossRef]

49. Hughes, C.E.; Crawford, J. A new precipitation weighted method for determining the meteoric water line for hydrological applications demonstrated using Australian and global GNIP data. *J. Hydrol.* **2012**, *464*, 344–351. [CrossRef]

50. Araguás-Araguás, L.; Fröhlich, K.; Rozanski, K. Deuterium and oxygen-18 isotope composition of precipitation and atmospheric moisture. *Hydrol. Process.* **2000**, *14*, 1341–1355. [CrossRef]

51. Peng, H.; Mayer, B.; Harris, S.; Krouse, H.R. A 10-yr record of stable isotope ratios of hydrogen and oxygen in precipitation at Calgary, Alberta, Canada. *Tellus B* **2004**, *56*, 147–159. [CrossRef]

52. Lucas, L.; Unterweger, M.P. Comprehensive review and critical evaluation of the half-life of tritium. *J. Res. Natl. Inst. Stand. Technol.* **2000**, *105*, 541–549. [CrossRef]

53. Nikolov, J.; Krajcar Bronić, I.; Todorović, N.; Stojković, I.; Barešić, J.; Petrović-Pantić, T. Tritium in water—Hydrology and health implications. In *Tritium—Advances in Research and Applications*; Janković, M.M., Ed.; NOVA Science Publishers: New York, NY, USA, 2018; pp. 157–213.

54. Tadros, C.V.; Hughes, C.E.; Crawford, J.; Hollins, S.E.; Chisari, R. Tritium in Australian precipitation: A 50 year record. *J. Hydrol.* **2014**, *513*, 262–273. [CrossRef]

55. Rozanski, K.; Gonfiantini, R.; Araguas-Araguas, L. Tritium in the global atmosphere: Distribution patterns and recent trends. *J. Phys. G Nucl. Part. Phys.* **1991**, *17*, 523–536. [CrossRef]

56. Galeriu, D.; Melintescu, A.; Beresford, N.A.; Crout, N.M.J.; Takeda, H. 14C and tritium dynamics in wild mammals: A metabolic model. *Radioprotection* **2005**, *40*, S351–S357. [CrossRef]

57. Hebert, D. Technogenic Tritium in Central European Precipitations. *Isot. Environ. Health Stud.* **1990**, *26*, 592–595. [CrossRef]

58. UN; ILO; WHO. *Selected Radionuclides—Environmental Health Criteria 25*; WHO: Geneva, Switzerland, 1983; ISBN 92-4-154085-0.

59. Nimac, I.; Perčec Tadić, M. New 1981–2010 climatological normals for Croatia and comparison to previous 1961–1990 and 1971–2000 normals. In Proceedings of the GeoMLA Conference, Belgrade, Serbia, 21–24 June 2016; University of Belgrade—Faculty of Civil Engineering: Belgrade, Serbia, 2016; pp. 79–85.

60. Köppen, W. Das geographische System der Klimate. In *Handbuch der Klimatologie*; Köppen, W., Geiger, G., Eds.; Gebrüder Borntraeger: Berlin, Germany, 1936; pp. 1–44.

61. Peel, M.C.; Finlyanson, B.L.; McMahon, T.A. Updated world map of the Köppen-Geiger climate classification. *Hydrol. Earth Syst. Sci.* **2007**, *11*, 1633–1644. [CrossRef]

62. Krajcar Bronić, I.; Horvatinčić, N.; Obelić, B. Two decades of environmental isotope records in Croatia: Reconstruction of the past and prediction of future levels. *Radiocarbon* **1998**, *40*, 399–416. [CrossRef]

63. Krajcar Bronić, I.; Vreča, P.; Horvatinčić, N.; Barešić, J.; Obelić, B. Distribution of hydrogen, oxygen and carbon isotopes in the atmosphere of Croatia and Slovenia. *Arch. Ind. Hyg. Toxicol.* **2006**, *57*, 23–29.

64. Krajcar Bronić, I.; Horvatinčić, N.; Barešić, J.; Obelić, B.; Vreča, P. Widening the Radiation Protection World, Tritium distribution in precipitation over Croatia and Slovenia. In Proceedings of the 11th International Congress of the International Radiation Protection Association, Madrid, Spain, 23–28 May 2004; IRPA: Madrid, Spain, 2014. ISBN 84-87078-05-2.

65. Horvatinčić, N.; Kapelj, S.; Sironić, A.; Krajcar Bronić, I.; Kapelj, J.; Marković, T. Investigation of water resources and water protection in the karst area of Croatia using isotopic and geochemical analyses. In Proceedings of the Advances in Isotope Hydrology and its Role in Sustainable Water Resources Management (IHS-2007), Vienna, Austria, 21–25 May 2007; IAEA: Vienna, Austria, 2007; Volume 2, pp. 295–304, ISBN 978-92-0-110207-2.

66. Horvatinčić, N.; Barešić, J.; Krajcar Bronić, I.; Karman, K.; Forisz, I.; Obelić, B. Study of the bank filtered groundwater system of the Sava River at Zagreb (Croatia) using isotope analyses. *Cent. Eur. Geol.* **2011**, *54*, 121–127. [CrossRef]

67. Babinka, S.; Obelić, B.; Krajcar Bronić, I.; Horvatinčić, N.; Barešić, J.; Kapelj, S.; Suckow, A. MRT of water from springs of the Plitvice Lakes and Una River area. In *Book of Abstracts IAEA-CN-151, Proceedings of the IAEA IHS International Symposium on Advances in Isotope Hydrology and its Role in Sustainable Water Resources Management, Vienna, Austria, 21–25 May 2007*; IAEA: Vienna, Austria, 2007; p. 45.

68. Mandić, M.; Bojić, D.; Roller-Lutz, Z.; Lutz, H.O.; Krajcar Bronić, I. Note on the spring region of Gacka River (Croatia). *Isot. Environ. Health Stud.* **2008**, *44*, 201–208. [CrossRef]

69. Pezdič, J. *Izotopi in Geokemijski Procesi*; Naravoslovnotehniška Fakulteta, Oddelek za Geologijo: Ljubljana, Slovenia, 1999; p. 269.

70. Vreča, P.; Krajcar Bronić, I.; Leis, A.; Brenčič, M. Isotopic composition of precipitation in Ljubljana (Slovenia). *Geologija* **2008**, *51*, 169–180. [CrossRef]

71. Vreča, P.; Krajcar Bronić, I.; Leis, A.; Demšar, M. Isotopic composition of precipitation at the station Ljubljana (Reaktor), Slovenia—Period 2007–2010. *Geologija* **2014**, *57*, 217–230. [CrossRef]

72. Vreča, P.; Krajcar Bronić, I.; Leis, A. Isotopic composition of precipitation in Portorož (Slovenia). *Geologija* **2011**, *54*, 129–138. [CrossRef]

73. Vreča, P.; Malenšek, N. Slovenian Network of Isotopes in precipitation (SLONIP)—A review of activities in the period 1981–2015. *Geologija* **2016**, *59*, 67–84. [CrossRef]

74. Horvatinčić, N.; Krajcar Bronić, I.; Obelić, B.; Bistrović, R. Long-time atmospheric tritium record in Croatia. *Acta Geol. Hung.* **1996**, *39*, 81–84.

75. Horvatinčić, N.; Krajcar Bronić, I. ^{14}C and ^{3}H as indicators of the environmental contamination. *RMZ Mater. Geoenviron.* **1998**, *45*, 56–60.

76. Barešić, J.; Horvatinčić, N.; Krajcar Bronić, I.; Obelić, B.; Vreča, P. Stable isotope composition of daily and monthly precipitation in Zagreb. *Isot. Environ. Health Stud.* **2006**, *42*, 239–249. [CrossRef] [PubMed]

77. Zaninović, K.; Gajić-Čapka, M.; Perčec Tadić, M.; Vučetić, M.; Milković, J.; Bajić, A.; Cindrić, K.; Cvitan, L.; Katušin, Z.; Kaučić, D.; et al. *Klimatski Atlas Hrvatske/Climate Atlas of Croatia 1961–1990, 1971–2000*; Državni Hidrometeorološki Zavod: Zagreb, Croatia, 2008.

78. Gehre, M.; Hoefling, R.; Kowski, P.; Strauch, G. Sample preparation device for quantitative hydrogen isotope analysis using chromium metal. *Anal. Chem.* **1996**, *68*, 4414–4417. [CrossRef]

79. Surić, M.; Roller-Lutz, Z.; Mandić, M.; Krajcar Bronić, I.; Juračić, M. Modern C, O, and H isotope composition of speleothem and dripwater from Modrič Cave, eastern Adriatic coast (Croatia). *Int. J. Speleol.* **2010**, *39*, 91–97. [CrossRef]

80. Coplen, T.B.; Wassenaar, L.I. LIMS for Lasers for achieving long-term accuracy and precision of δ^2H, δ^{17}O, and δ^{18}O of waters using laser absorption spectrometry. *Rapid Commun. Mass Spectrom.* **2015**, *29*, 2122–2130. [CrossRef]

81. Horvatinčić, N. Radiocarbon and tritium measurements in water samples and application of isotopic analyses in hydrology. *Fizika* **1980**, *12*, 201–218.

82. Krajcar Bronić, I.; Obelić, B.; Srdoč, D. The simultaneous measurement of tritium activity and background count rate in a proportional counter by the Povinec method: Three years experience at the Rudjer Bošković Institute. *Nucl. Instrum. Methods Phys. Res. B* **1986**, *17*, 498–500. [CrossRef]

83. Barešić, J.; Horvatinčić, N.; Krajcar Bronić, I.; Obelić, B. Comparison of two techniques for low-level tritium measurement—Gas proportional and liquid scintillation counting. In Proceedings of the Third European IRPA Congress, Helsinki, Finland, 14–18 June 2010; IRPA: Helsinki, Finland, 2010; pp. 1988–1992.

84. Barešić, J.; Krajcar Bronić, I.; Horvatinčić, N.; Obelić, B.; Sironić, A.; Kožar-Logar, J. Tritium activity measurement of water samples using liquid scintillation counter and electrolytical enrichment. In Proceedings of the 8th Symposium of the Croatian Radiation Protection Association, Krk, Croatia, 13–15 April 2011; Krajcar Bronić, I., Kopjar, N., Milić, M., Branica, G., Eds.; HDZZ: Zagreb, Croatia, 2011; pp. 461–467.

85. Krajcar Bronić, I.; Barešić, J.; Sironić, A.; Horvatinčić, N. Stability analysis of systems for preparation and measurement of ^{3}H and ^{14}C (Analiza stabilnosti sustava za pripremu i mjerenje ^{3}H i ^{14}C, in Croatian with English Abstract). In Proceedings of the 9th Symposium of the Croatian Radiation Protection Association, Krk, Croatia, 10–12 April 2013; Knežević, Ž., Majer, M., Krajcar Bronić, I., Eds.; CRPA: Zagreb, Croatia, 2013; pp. 495–501.

86. Stojković, I.; Todorović, N.; Nikolov, J.; Krajcar Bronić, I.; Barešić, J.; Kozmidic Luburić, U. Methodology of tritium determination in aqueous samples by Liquid Scintillation Counting techniques. In *Tritium—Advances in Research and Applications*; Janković, M.M., Ed.; NOVA Science Publishers: New York, NY, USA, 2018; pp. 99–156.

87. Rozanski, K.; Gröning, M. Tritium assay in water samples using electrolytic enrichment and liquid scintillation spectrometry. In *Quantifying Uncertainty in Nuclear Analytical Measurements IAEA-TECDOC-1401*; IAEA: Vienna, Austria, 2004; pp. 195–217.

88. Gröning, M.; Auer, R.; Brummer, D.; Jaklitsch, M.; Sambandam, C.; Tanwee, A.; Tatzber, H. Increasing the performance of tritium analysis by electrolytic enrichment. *Isot. Environ. Health Stud.* **2009**, *45*, 118–125. [CrossRef]

89. IAEA. *Statistical Treatment of Environmental Isotopes in Precipitation*; Technical Report Series 331; IAEA: Vienna, Austria, 1992; p. 781.

90. Australian Nuclear Science and Technology Organisation (ANSTO). Local Meteoric Water Line Freeware. 2012. Available online: https://openscience.ansto.gov.au/collection/879 (accessed on 28 November 2019).

91. Barešić, J.; Štrok, M.; Svetek, B.; Vreča, P.; Krajcar Bronić, I. Activity concentration of tritium (^{3}H) in precipitation—Long-term investigations performed in Croatia and Slovenia. In Proceedings of the Sixth International Conference on Radiation and Applications in Various Fields of Research, Ohrid, North Macedonia, 18–22 June 2018; Ristić, G., Ed.; RAD Association: Niš, Serbia, 2018; p. 186.

92. Krajcar Bronić, I. Environmental ^{14}C and ^{3}H levels in Croatia. In *Book of Abstracts, ENVIRA2017, Proceedings of the 4th International Conference on Environmental Radioactivity: Radionuclides as Tracers of Environmental Processes, Vilnius, Litva, 29 May–2 June 2017*; Lujaniene, L., Povinec, P., Eds.; ENVIRA: Vilnius, Litva, 2017; p. 152.

93. Palcsu, L.; Morgenstern, U.; Sültenfuss, J.; Koltai, G.; László, E.; Temovski, M.; Major, Z.; Nagy, J.T.; Papp, L.; Varlam, C.; et al. Modulation of Cosmogenic Tritium in Meteoric Precipitation by the 11-year Cycle of Solar Magnetic Field Activity. *Sci. Rep.* **2018**, *8*, 12813. [CrossRef]

Characteristics of Water Isotopes and Water Source Identification During the Wet Season in Naqu River Basin, Qinghai–Tibet Plateau

Xi Chen [1], Guoli Wang [1], Fuqiang Wang [2,3,*], Denghua Yan [4] and Heng Zhao [2,3]

[1] School of Hydraulic Engineering, Dalian University of Technology, Dalian 116024, China; chenxi218@mail.dlut.edu.cn (X.C.); wanggl@dlut.edu.cn (G.W.)

[2] Department of Water Conservancy Engineering, North China University of Water Resources and Electric Power, Zhengzhou 450046, China; zhaoheng@ncwu.edu.cn

[3] Collaborative Innovation Center of Water Resources Efficient Utilization and Support Engineering, Zhengzhou 450046, China

[4] Water Resources Department, China Institute of Water Resources and Hydropower Research, Beijing 100038, China; yandh@iwhr.com

* Correspondence: wangfuqiang@ncwu.edu.cn;

Abstract: Climate change is affecting the discharge of headstreams from mountainous areas on the Qinghai–Tibet Plateau. To constrain future changes in discharge, it is important to understand the present-day formation mechanism and components of runoff in the basin. Here we explore the sources of runoff and spatial variations in discharge through measurements of δ^2H and $\delta^{18}O$ in the Naqu River, at the source of the Nu River, on the Qinghai–Tibet plateau, during the month of August from 2016 to 2018. We established thirteen sampling sites on the main stream and tributaries, and collected 39 samples from the river. We examined all the water samples and analyzed them for isotopes. We find a significant spatial variation trend based on one-way analysis of variance (ANOVA) ($p < 0.05$) between Main stream-2 and tributaries. The local meteoric water-line (LMWL) can be described as: $\delta^2H = 7.9\delta^{18}O + 6.29$. Isotopic evaporative fractionation in water and mixing of different water sources are responsible for the spatial difference in isotopic values between Main stream-2 and tributaries. Based on isotopic hydrograph separation, the proportion of snowmelt in runoff components ranges from 15% to 47%, and the proportion of rainwater ranges from 3% to 35%. Thus, the main components of runoff in the Naqu River are snowmelt and groundwater.

Keywords: stable isotopes; spatial variations; hydrograph separation; Naqu River basin; Qinghai–Tibet Plateau

1. Introduction

The gradual trend of global warming will affect the discharge of headstreams to plateau rivers, including on the Qinghai–Tibet Plateau [1–4]. Therefore, it is important to explore the formation mechanism and identify the components of runoff on the Qinghai–Tibet Plateau [5,6].

The Naqu River basin is sensitive to environmental change due to its high altitude. Studying its water cycle is not straightforward due to the lack of hydrological data and harsh natural conditions. Meanwhile, little is known about the water source contribution and the mechanism of the runoff. To constrain future changes in discharge, it is important to understand the present-day formation mechanism and components of runoff in the basin.

There are many methods to identify runoff components [7–13]. Recent studies have shown that hydrograph separation based on stable isotopes is an effective way to study the runoff mechanism [14–16]. In general, river components can be divided into precipitation, groundwater,

soil water, and snowmelt based on isotope hydrological separation [17–25]. For example, based on the isotopic values of river waters, significant spatial and temporal variations of the Xijiang River were investigated [26]; Kong et al. found that the snowmelt water accounted for more than 57% of runoff of the Kumalak River [1], and more than 53% during the wet season [6]. Based on isotopes and geochemical tracers, streams in plateau regions are mainly replenished by snowmelt and groundwater [27–38]. There has been relatively little research on the composition and mechanism of water sources on the Qinghai–Tibet Plateau. The advantages of isotope techniques in the hydrologic cycle are obvious and water samples can be obtained easily in the plateau region due to the lack of hydrological and meteorological data [18].

In this study, we analyze the spatial variation of isotopes in the runoff and compute the proportions of runoff components in the month of August based on hydrograph separation. We hope that the research results of this paper will provide a relevant theoretical basis for the formation mechanism of runoff on the Qinghai–Tibet Plateau.

2. Study Areas

The Naqu River basin is the source of the Nu River in southwest China (Figure 1). The Naqu River has several main tributaries, such as the Najinqu, Sangqu, Bazongqu, Mumuqu, Chengqu, Zongqungqu, Mugequ, and Gongqu Rivers. There are many seasonal streams and mountain streams flowing into the Naqu River. The average annual temperature in this area is -0.6 °C. The drainage area of the Naqu River basin is 16,350 km^2, at a high altitude of 4600 m above sea level [39].

Annual precipitation is 531 mm. From May to October, precipitation accounts for about 82% of the total annual rainfall, with less precipitation from November to April. Although there is not a significant amount of snowfall throughout the whole year, snowmelt has a strong replenishment effect on the runoff in the flood season. The climate is affected by Indian Ocean southwest monsoon in summer. The water vapor of precipitation comes from water vapor that evaporated under wetter conditions. This is consistent with summer southwest monsoon precipitation in the region coming directly from the Bay of Bengal. The d-excess value in the precipitation directly from the Bay of Bengal is lower due to the high relative humidity of the sea surface [37–42]. For this reason, the precipitation is coincident with the annual peak of snowmelt during the wet season. And they become the main components of runoff in the Naqu River basin.
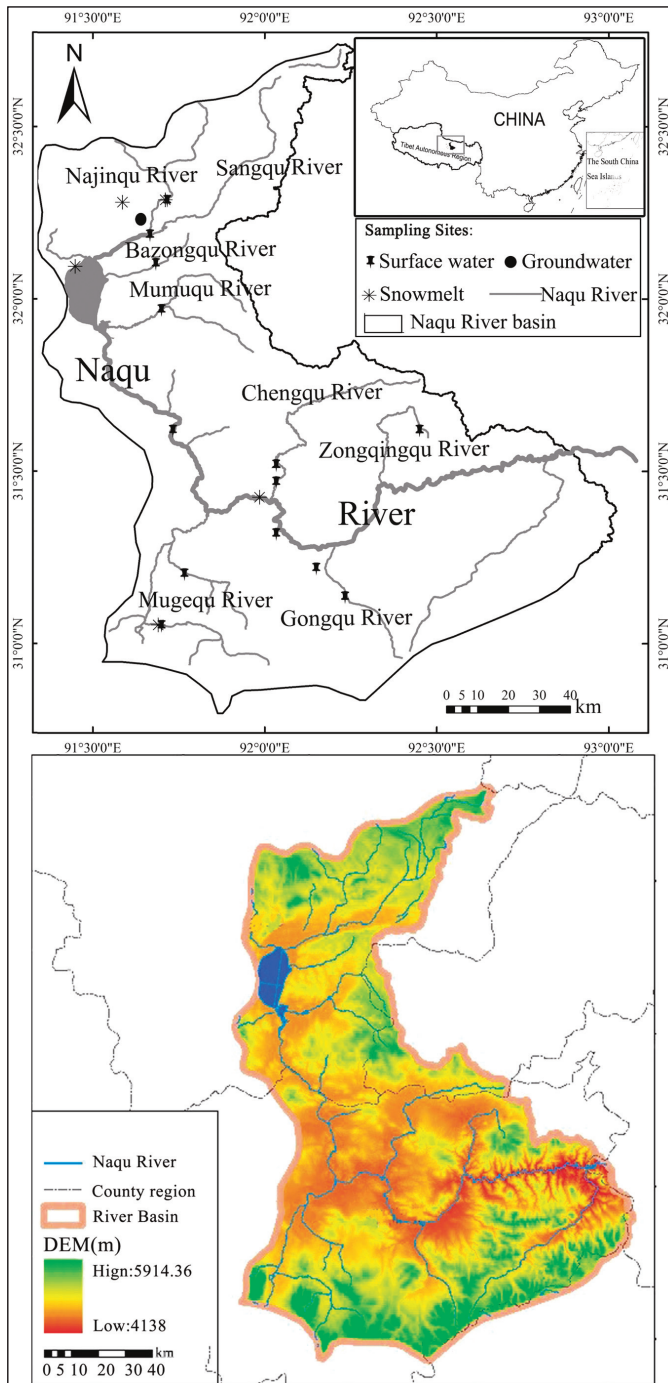
Figure 1. Research area and geographic location.

3. Materials and Methods

3.1. Field Sampling

We installed thirteen sampling sites on the main stream and tributaries of the Naqu River, with the sampling sites of Main stream-1 and Main stream-2 along the main channel, and Najinqu, Sangqu, Bazongqu, Mumuqu, Chengqu, Zongqungqu, Mugequ, and Gongqu on eight tributaries (Figure 1). We collected a total of 39 samples from the river in the month of August from 2016 to 2018.

In general, water samples included 39 runoff samples, two groundwater samples, two rain samples, and five snowmelt samples during the wet season from 2016 to 2018. We collected two rain samples on 13 August 2018.

3.2. Measurement

$\delta^{18}O$ and $\delta^{2}H$ analysis: Wavelength-scanned cavity ring down spectroscopy (WS-CRDS) (Picarro L1115-I, Picarro, Santa Clara, CA, USA) was used to measure water isotope composition, which were corrected using the Vienna Standard Mean Ocean Water (VSMOW, $\delta^{2}H = 0‰$, $\delta^{18}O = 0‰$) and Standard Light Antarctic Precipitation ($\delta^{2}H = -428‰$, $\delta^{18}O = -55.5‰$). The analytical precision was generally 0.5‰ for $\delta^{2}H$ and 0.1‰ for $\delta^{18}O$ [39]. The $\delta^{18}O$ and $\delta^{2}H$ values are expressed as follows:

$$\delta^{2}H_{\text{V-SMOW}} = \left(\frac{^{2}H/^{1}H_{sample}}{^{2}H/^{1}H_{standard}} - 1 \right) \times 1000 (‰) \tag{1}$$

$$\delta^{18}O_{\text{V-SMOW}} = \left(\frac{^{18}O/^{16}O_{sample}}{^{18}O/^{16}O_{standard}} - 1 \right) \times 1000 (‰) \tag{2}$$

EC analysis: Electrical conductivity (EC) was measured in situ with a conductivity meter. EC was measured concurrently with stream sampling using a standard conductivity cell (WTW Cond 340iTM). The standard conductivity cell was calibrated to correct for water temperature to 25 °C.

D-excess calculation: The deuterium excess (d-excess) was used to measure the isotopic variability [19] and is defined as:

$$\text{d-excess} = \delta^{2}H - 8 \times \delta^{18}O \tag{3}$$

3.3. Data Analysis

We explored the spatial characteristics of the isotopes based on one-way analysis of variance (ANOVA) by using SPSS 17.0. Isotopic contents in water bodies of different main stream tributaries are expressed by box plot. ArcGIS of ESRI is applied to display spatial features of the Naqu River basin based on inverse distance weighting (IDW).

We analyzed samples for the two tracers collected from snowmelt, rain, stream water, and groundwater. Respecting the water and tracer mass conservation, electrical conductivity was measured in situ with a conductivity meter. The percentage of different components in the total runoff was determined using isotope hydrologic separation. If we suppose the objective percentage of n components are evaluated based on n parts and $n-1$ measuring factors $t_1, t_2, \cdots, t_{n-1}$, there are n linear mixing equations. These are defined as follows:

$$Q_T = Q_1 + Q_2 + \cdots + Q_n \tag{4}$$

$$C_T^{t_i} Q_T = C_1^{t_i} Q_1 + C_2^{t_i} Q_2 + \cdots + C_n^{t_i} Q_n \tag{5}$$

where Q_T is the total flow of the river; $Q_1, Q_2, \cdots, Q_n$ represent the flows of different water sources of runoff, and $C_1^{t_1}, C_2^{t_2}, \cdots, C_i^{t_i}$ represent the concentrations of relevant observed tracer t_i.

When the runoff contains only two sources of water, the percentages of different components of the runoff can be expressed as follows:

$$Q_1/Q_s = (C_2 - C_s)/(C_2 - C_1) \tag{6}$$

$$Q_2/Q_s = (C_s - C_1)/(C_2 - C_1) \tag{7}$$

where Q is the runoff of each component, C is the concentrations of relevant observed tracer, and s is the total flow.

When the runoff contains only three sources of water, groundwater, snowmelt, and precipitation are the main components of runoff in August in the Naqu River basin. Hydrograph separation is used to calculate the various composition of the runoff based on two tracers (δ^2H and EC). Supposing the river flow is a function of snowmelt, groundwater, and precipitation, then the three-component sources model can be defined as follows:

$$f_p + f_g + f_m = 1 \tag{8}$$

$$f_p Q_p + f_g Q_g + f_m Q_m = Q_r \tag{9}$$

$$f_p E_p + f_g E_g + f_m E_m = E_r \tag{10}$$

where f_p, f_g, f_m represent the shares of the individual components in the total runoff, and Q and E represent the concentrations of tracers.

4. Results

4.1. Spatial Characteristics of $\delta^{18}O$ and $\delta^2 H$

In August 2017, δ^{18}O values of runoff vary from −15.6‰ to −10.5‰ with a mean of −15.49‰. The δ^{18}O values of snowmelt water range from −15.0‰ and −7.6‰ with an average of −11.4‰. The δ^{18}O values of runoff vary from −15.49‰ to −14.27‰ (Table 1). For groundwater, the δ^{18}O values are relatively stable, ranging from −19.03‰ to −17.66‰, which indicated that the surrounding environment had little influence on groundwater and the recharge source of groundwater was relatively stable (Table 1).

Table 1. Oxygen isotope composition of different types of water in the Naqu River basin.

Water type		2016.8	2017.8	2018.8
Stream water	Sample number	13	13	13
	Mean of δ^{18}O (‰)	−14.27	−15.49	−14.83

Water type		2016–2018
Snowmelt water	Sample number	5
	Mean of δ^{18}O (‰)	−11.37
Groundwater	Sample number	2
	Mean of δ^{18}O (‰)	−18.51
Rain	Sample number	2
	Mean of δ^{18}O (‰)	−18.35

The results of elevation effect analysis on the collected rivers (Table 2) show that the isotopes in runoff do not change with elevation (Figure 2). All values are plotted against altitude. We hypothesize that the water body experienced intense evaporative fractionation due to the slow river flow rate in the Naqu River basin.

Table 2. Average values of δ^2H and $\delta^{18}O$ of main streams and tributaries.

Location	Sampling Sites	Sample Number	$\delta^{18}O$ (‰)	δ^2H (‰)	Longtitude (E)	Latitude (N)	Altitude (m a.s.l.)
Main stream−1	4	3	−15.68	−118.58	92°02′38.7″	31°19′52″	4451
Main stream−2	8	3	−15.48	−116.32	91°44′17.7″	31°37′15.2″	4551
Bazongqu	9	3	−16.88	−124.93	91°42′51.9″	31°58′40.2″	4622
Chengqu	3	3	−16.37	−124.20	92°03′34.9″	31°29′44.7″	4503
	13	3	−17.03	−127.50	92°02′19.3″	31°31′39.5″	4519
Gongqu	5	3	−15.83	−119.46	92°09′30.5″	31°13′32.5″	4498
	6	3	−16.21	−121.16	92°14′23.2″	31°08′21.8″	4578
Mugequ	2	3	−15.17	−113.81	91°41′23.3″	31°3′17.9″	4681
	14	3	−15.26	−115.65	91°46′33.3″	31°11′56″	4591
Mumuqu	10	3	−14.97	−113.63	91°41′23.4″	32°06′5.1″	4712
Najinqu	12	3	−14.81	−111.99	91°42′38.5″	32°22′30.3″	4771
Sangqu	11	3	−14.57	−111.32	91°40′44.3″	32°11′22″	4626
Zongqingqu	7	3	−13.18	−103.02	92°25′42.2″	31°41′12.6″	4567
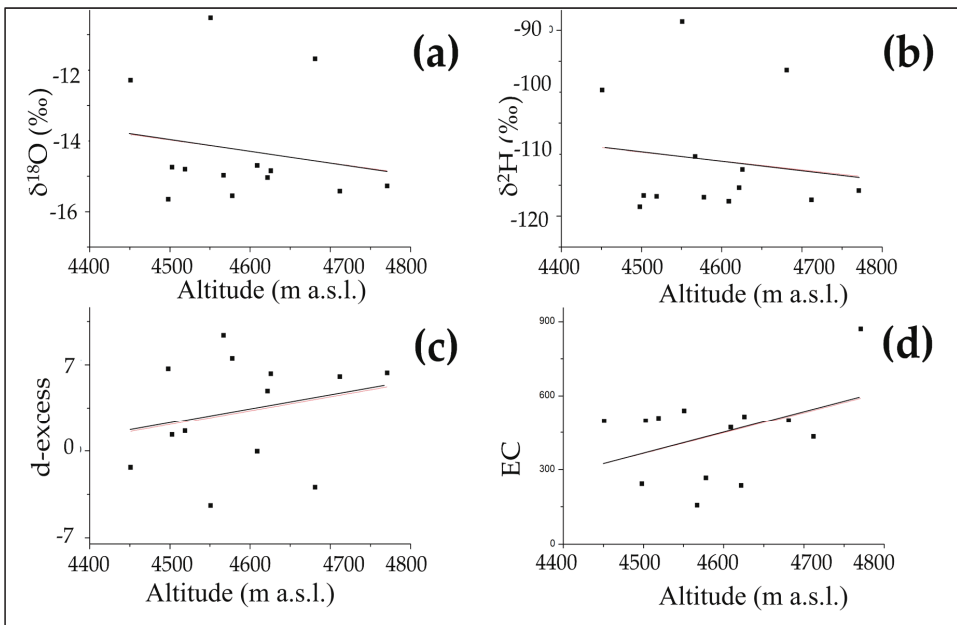
Figure 2. (**a**) $\delta^{18}O$ altitude, (**b**) δ^2H altitude, (**c**) d-excess altitude, and (**d**) electrical conductivity (EC) altitude relationship.

$\delta^{18}O$ and δ^2H values are shown in box plots for all the sampling sites (Figure 3).

Our analysis showed a significant spatial trend based on one-way ANOVA ($p < 0.05$) at 13 sampling sites between Main stream-2 and tributaries (Najinqu, Sangqu, Bazongqu, Mumuqu, Chengqu, Zongqungqu, Mugequ, and Gongqu). We speculate that isotopic evaporative fractionation in water and mixing of different water sources are the reasons for the spatial difference in isotopic values between Main stream-2 and tributaries.
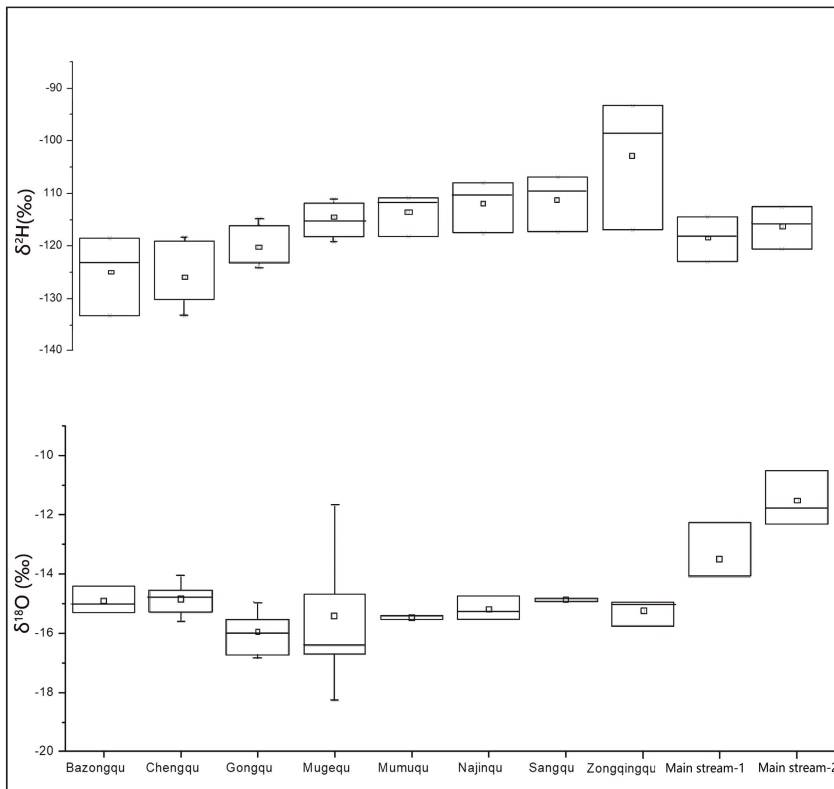
Figure 3. Box plots for δ^2H and δ^{18}O of runoff.

4.2. Isotopic Characterization of River

Craig [12] found that stable isotope ratios of δ^{18}O and δ^2H in precipitation correlate at a global scale in a linear relationship known as the global meteoric water line (GMWL). A linear relationship between δ^{18}O and δ^2H was established for average local meteoric waters as the local meteoric water line (LMWL). Important information about the water sources of precipitation can be revealed based on the deviation between LMWL and GMWL. By the location characteristics of different water samples, the water sources of rivers and the isotopic evaporative fractionation can be analyzed. In this paper, the LMWL of Lhasa region is adopted to replace the LMWL of the Naqu River basin. The LMWL can be described as: δ^2H = 7.9δ^{18}O + 6.29 [43]. Compared to the LMWL, some sets of isotopic data with high δ^{18}O values are below the LMWL, which signifies the effect of intensive evaporation processes.

By comparing different water samples with the LMWL, the water sources of the river and the isotopic evaporative fractionation can be analyzed. Most of the river sampling sites are close to LMWL (δ^2H = 7.9δ^{18}O + 6.29) (Figure 4). At the same time, many samples are close to each other, indicating that the water sources of these tributaries are relatively similar. The river water line is δ^2H = 5.75δ^{18}O − 27.98. The groundwater and snowmelt samples are distributed around the river samples, indicating that the water is originated from local rainfall and runoff is recharged by groundwater, snowmelt, and precipitation.
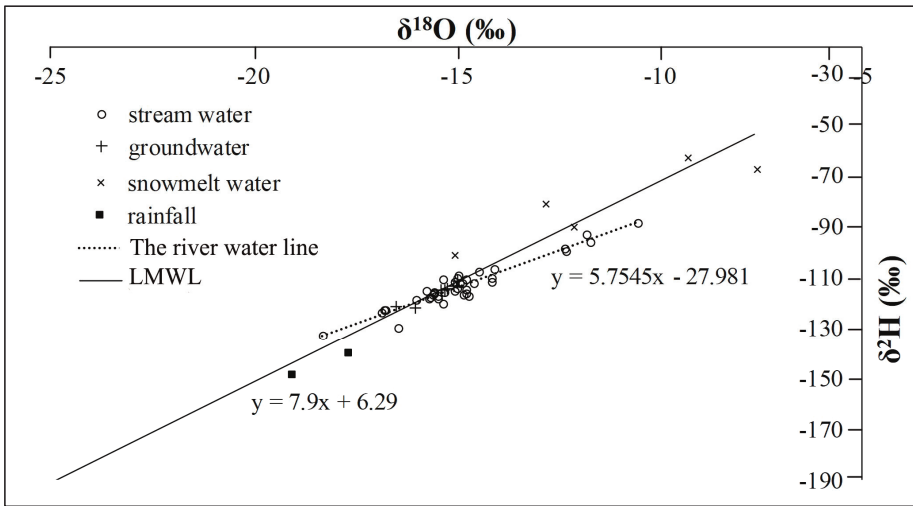
Figure 4. Plot of δ^2H versus $\delta^{18}O$ for different water sources.

The isotopic values of river water samples are closer to groundwater than those of snowmelt, indicating the frequent interaction between groundwater and runoff (Figure 4). Meanwhile, the slope and intercept are both smaller than that of LMWL, indicating that the water body in the Naqu River basin have experienced an obvious evaporation process.

The isotopes of snowmelt in winter appear to be the most enriched compared with other water sources, which is due to evaporation. When the snow begins to melt, the influence of evaporative fractionation increases, and the content of heavy isotopes in the meltwater increases.

4.3. Hydrograph Separation

Based on the formulas provided above, we calculated the contributions of rain, groundwater, and snowmelt by isotopic hydrograph separation in 2018 (Table 3, Figure 5). The proportion of snowmelt in runoff components ranges from 15% to 47%, and the proportion of rainwater ranges from 3% to 35%. The main components of runoff in the Naqu River are snowmelt and groundwater.

Table 3. Contribution of different water sources (^2H, ‰; EC, ms/cm).

Tributary	Mean Elevation	River Water		Snowmelt		Groundwater		Rainfall		Contribution (%)		
	(m a.s.l.)	D	EC	D	EC	D	EC	D	EC	Snowmelt	Groundwater	Rainfall
Bazongqu	4622	−112	0.21	−87	0.12	−122	0.50	−144	0.01	45%	30%	24%
Chengqu	4519	−115	0.31	−87	0.12	−122	0.50	−144	0.01	29%	56%	16%
Gongqu	4578	−119	0.22	−87	0.12	−122	0.50	−144	0.01	29%	36%	35%
Mugequ	4609	−121	0.31	−87	0.12	−122	0.50	−144	0.01	18%	58%	24%
Mumuqu	4712	−117	0.43	−87	0.12	−122	0.50	−144	0.01	15%	82%	3%
Najinqu	4771	−114	0.21	−87	0.12	−122	0.50	−144	0.01	40%	32%	29%
Sangqu	4626	−112	0.21	−87	0.12	−122	0.50	−144	0.01	45%	30%	25%
Zongqingqu	4567	−113	0.17	−87	0.12	−122	0.50	−144	0.01	46%	23%	31%
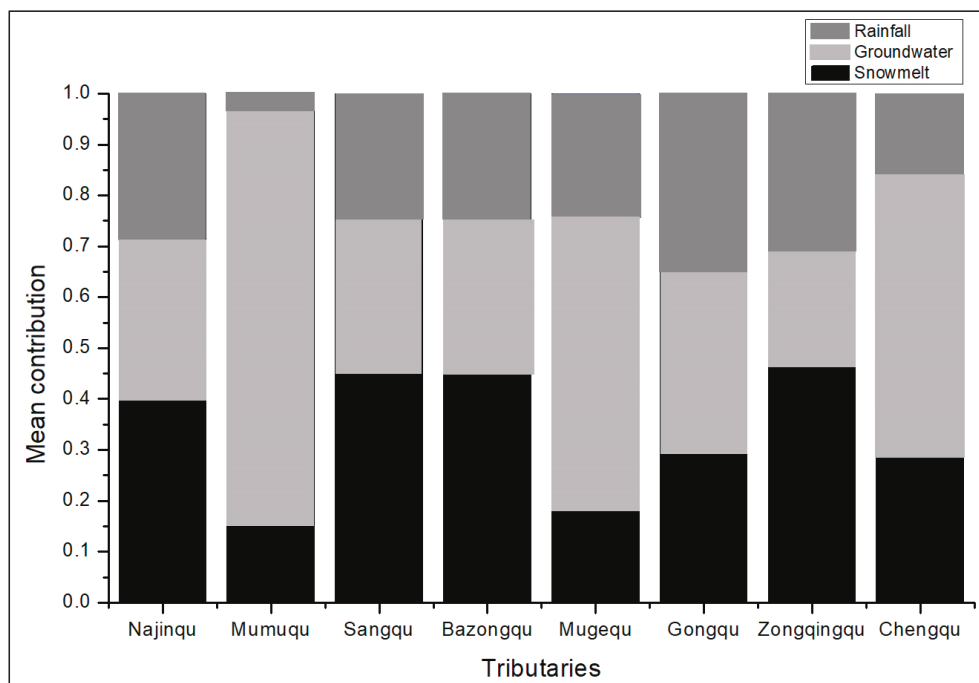
Figure 5. Contribution of different water sources.

5. Discussion

5.1. Analysis of Spatial Variations of $\delta^2 H$ and $\delta^{18}O$ Values of the River

Our analysis showed an insignificant spatial trend of either $\delta^2 H$ or $\delta^{18}O$ among tributaries Najinqu, Sangqu, Bazongqu, Mumuqu, Chengqu, Zongqungqu, Mugequ, and Gongqu in August. However, there is a significant spatial variation trend based on one-way ANOVA between Main stream-2 and tributaries (Najinqu, Sangqu, Bazongqu, Mumuqu, Chengqu, Zongqungqu, Mugequ, and Gongqu) (Figure 3). Although elevation effects play an important role in isotopic variation in large topographic area, there was no obvious elevation effects between Main stream-2 and tributaries (Figure 2). Surface and groundwater samples are often below the LMWL and GMWL under intense evaporative fractionation and low humidity. In the Naqu River, some water samples deviate from the LMWL, and the waters experience intense evaporative fractionation due to the slow river flow rate.

For groundwater, the $\delta^{18}O$ values were relatively stable, ranging from −19.03‰ to −17.66‰, indicating that the surrounding environment has little influence on groundwater and the recharge source of groundwater is relatively stable (Table 1)., The groundwater was recharged by old water stored in the basin previously.

5.2. Estimation of Different Water Sources Contribution to the River Flow

Based on the analysis of runoff components, runoff of the Naqu River can be divided into three water sources by isotopic hydrograph separation: Groundwater, rain, and snowmelt. The calculation results show that snowmelt of most tributaries contributed more than 30% to the runoff, while the proportion of rain ranges from 3% to 35% in the Naqu River basin. The results of hydrologic separation show that during the wet season, the river sources are mainly meltwater, and groundwater, with groundwater accounting for the largest proportion (more than 50%). Groundwater and snowmelt

account for a greater proportion of runoff composition in the Naqu River basin. Such results are different from the runoff data collected at the hydrological station (Figure 6). In the past, we believed that the changing trend of runoff was completely controlled by precipitation. We speculate that the main components of runoff are snowmelt water and groundwater, while rain affects the change of runoff in the Naqu River.
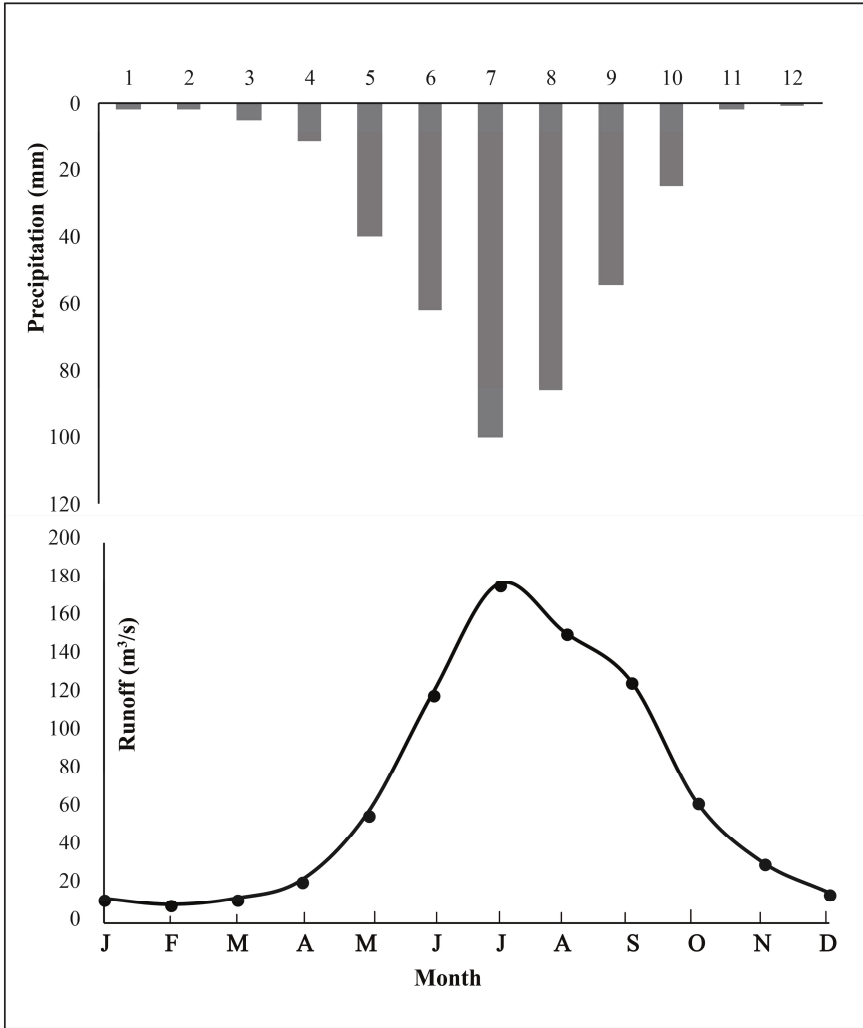
Figure 6. Monthly variations of precipitation and runoff in the Naqu River basin.

As shown in Figure 7, the contributions of groundwater of Mumuqu, Mugequ, and Chengqu are bigger than those of other tributaries. The contributions of snowmelt of Najinqu, Sangqu, Bazongqu, and Zongqingqu Rivers are bigger than those of other tributaries. We speculate that this phenomenon is related to the elevation characteristics of the Naqu River basin (Figure 1). At lower altitudes to the south, the recharge of groundwater in the river is stronger. The loose structure of the rocks, large areas of grassland, and abundant melt-water make the area relatively permeable. At higher altitudes in the north and east, the recharge of snowmelt to the river is stronger. The results of elevation effect

analysis on the collected samples of the main stream and tributaries showed that isotopes in runoff do not change with elevation. There is a certain correlation between runoff composition and elevation, particularly related to the proportion of groundwater and snowmelt. Groundwater contributes more to the river in the central and western regions. Spatially, in the Naqu River, meltwater contributes more than 30% to runoff in the north, east, and south. Our results show that the groundwater and snowmelt water have different dominant effects on runoff composition from the upper to the lower reaches in the Naqu River. And the results can be referred to for near-future assessments of changes in discharge in the basin.
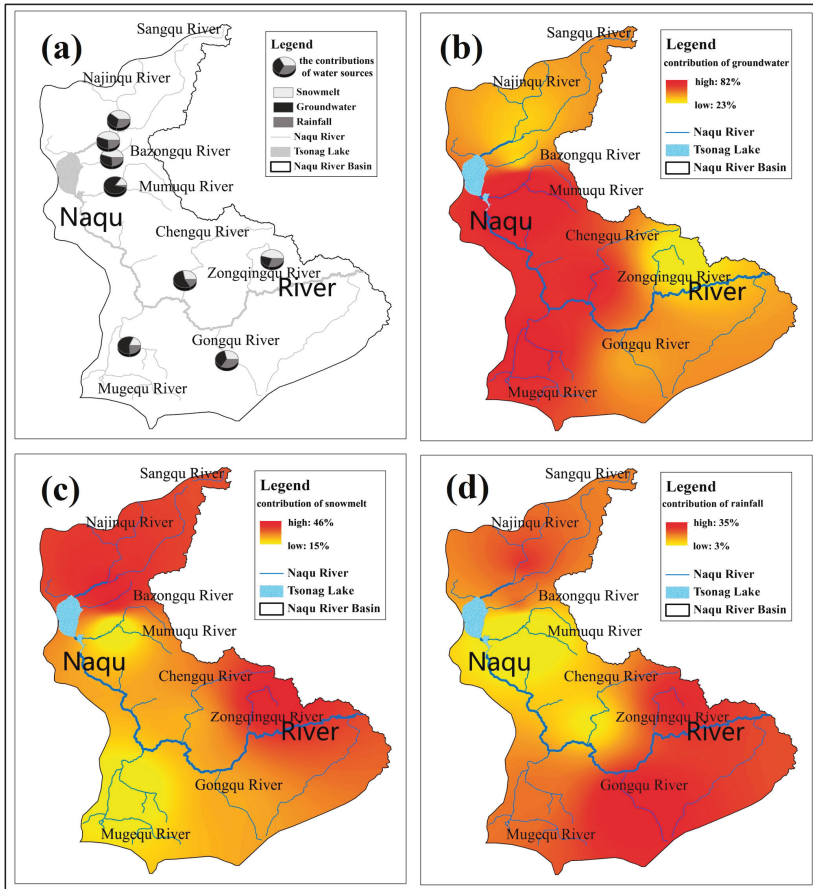
Figure 7. Spatial variation of contributions of numerous water sources in the Naqu River basin: (**a**) numerous water sources (**b**) groundwater, (**c**) snowmelt, and (**d**) rainfall.

6. Conclusions

We analyze the spatial variations of δ^2H and δ^{18}O with influencing factors and the sources of runoff in August, 2016–2018, for the Naqu River at the source of the Nu River on the Qinghai–Tibet. Our analysis showed an insignificant spatial trend of either δ^2H or δ^{18}O values among the tributaries Najinqu, Sangqu, Bazongqu, Mumuqu, Chengqu, Zongqungqu, Mugequ, and Gongqu in August. However, there is a significant spatial variation trend based on one-way ANOVA at 13 sampling sites between Main stream-2 and tributaries (Najinqu, Sangqu, Bazongqu, Mumuqu, Chengqu, Zongqungqu,

Mugequ, and Gongqu). Isotopic evaporative fractionation in water and mixing of different water sources are the reasons for the spatial difference of isotopic values between Main stream-2 and tributaries. Runoff of the Naqu River can be divided into three water sources: Groundwater, rainwater, and snowmelt. The proportion of snowmelt in runoff components ranges from 15% to 47%, and the proportion of rainwater ranges from 3% to 35%. Thus, the main components of runoff are snowmelt and groundwater, while rain affects the change of runoff.

Author Contributions: X.C. and F.W. conceived, designed, and drafted the manuscript; X.C., G.W., D.Y. and H.Z. planned and designed the methodology; X.C. revised the manuscript; F.W. guided and supervised the whole process; and all authors read and approved the final manuscript.

References

1. Kong, Y.; Pang, Z. Evaluating the sensitivity of glacier rivers to climate change based on hydrograph separation of discharge. *J. Hydrol.* **2012**, *434*, 121–129. [CrossRef]

2. Wang, X.; Li, Z.; Ross, E.; Tayier, R.; Zhou, P. Characteristics of water isotopes and hydrograph separation during the spring flood period in Yushugou River basin, Eastern Tianshans, China. *J. Earth Syst. Sci.* **2015**, *124*, 115–124. [CrossRef]

3. Wang, Z.; Zhou, C.; Guan, B.; Deng, Z.; Zhi, Y.; Liu, Y.; Xu, C.; Fang, S.; Xu, Z.; Yang, H. The Headwater Loss of the Western Plateau Exacerbates China's Long Thirst. *AMBIO* **2006**, *35*, 271. [PubMed]

4. Zhou, J.; Wu, J.; Liu, S.; Zeng, G.; Qin, J.; Wang, X.; Zhao, Q. Hydrograph Separation in the Headwaters of the Shule River Basin: Combining Water Chemistry and Stable Isotopes. *Adv. Meteorol.* **2015**, *2015*, 1–10. [CrossRef]

5. Barthold, F.K.; Wu, J.K.; Vaché, K.B.; Schneider, K.; Frede, H.G.; Breuer, L.; Tetzlaff, D.; Carey, S.K.; Laudon, H.; Mcguire, K. Identification of geographic runoff sources in a data sparse region: Hydrological processes and the limitations of tracer-based approaches. *Hydrol. Process.* **2010**, *24*, 2313–2327. [CrossRef]

6. Pu, T.; He, Y.; Zhu, G.; Zhang, N.; Du, J.; Wang, C. Characteristics of water stable isotopes and hydrograph separation in Baishui catchment during the wet season in Mt.Yulong region, south western China. *Hydrol. Process.* **2013**, *27*, 3641–3648. [CrossRef]

7. Buttle, J.M. Isotope hydrograph separations and rapid delivery of pre-event water from drainage basins. *Progr. Phys. Geogr.* **1994**, *18*, 16–41. [CrossRef]

8. Liu, Y.; Fan, N.; An, S.; Bai, X.; Liu, F.; Xu, Z.; Wang, Z.; Liu, S. Characteristics of water isotopes and hydrograph separation during the wet season in the Heishui River, China. *J. Hydrol.* **2008**, *353*, 314–321. [CrossRef]

9. Sun, C.; Chen, Y.; Li, W.; Li, X.; Yang, Y. Isotopic time series partitioning of streamflow components under regional climate change in the Urumqi River, northwest China. *Hydrol. Sci. J.* **2016**, *61*, 1443–1459.

10. Wu, H.; Zhang, X.; Li, X.; Li, G.; Huang, Y. Seasonal variations of deuterium and oxygen-18 isotopes and their response to moisture source for precipitation events in the subtropical monsoon region. *Hydrol. Process.* **2015**, *29*, 90–102. [CrossRef]

11. James, C. Hydrogeological Conceptual Model of Groundwater from Carbonate Aquifers Using Environmental Isotopes (^{18}O, ^{2}H) and Chemical Tracers: A Case Study in Southern Latium Region, Central Italy. *J. Water Resour. Prot.* **2012**, *4*, 695–716.

12. Craig, H. Isotopic variations in meteoric waters. *Science* **1961**, *133*, 1702–1703. [CrossRef] [PubMed]

13. Longinelli, A.; Selmo, E. Isotopic composition of precipitation in Italy: A first overall map. *J. Hydrol.* **2003**, *270*, 75–88.

14. Gibson, J.J.; Edwards, T.W.D.; Birks, S.J.; St Amour, N.A.; Buhay, W.M.; McEachern, P.; Wolfe, B.B.; Peters, D.L. Progress in isotope tracer hydrology in Canada. *Hydrol. Process.* **2005**, *19*, 303–327. [CrossRef]

15. Rank, D.; Wyhlidal, S.; Schott, K.; Weigand, S.; Oblin, A. Temporal and spatial distribution of isotopes in river water in Central Europe: 50 years experience with the Austrian network of isotopes in rivers. *Isot. Environ. Health Stud.* **2018**, *54*, 115–136. [CrossRef]

16. Zhang, W.; Cheng, B.; Hu, Z.; An, S.; Xu, Z.; Zhao, Y.; Cui, J.; Xu, Q. Using stable isotopes to determine the water sources in alpine ecosystems on the east Qinghai-Tibet plateau, China. *Hydrol. Process.* **2010**, *24*, 3270–3280. [CrossRef]

17. Kendall, C.; Coplen, T.B. Distribution of oxygen-18 and deuterium in river waters across the United States. *Hydrol. Process.* **2001**, *15*, 1363–1393. [CrossRef]

18. Liu, W.; Chen, S.; Xiang, Q.; Baumann, F.; Scholten, T.; Zhou, Z.; Sun, W.; Zhang, T.; Ren, J.; Qin, D. Storage, patterns, and control of soil organic carbon and nitrogen in the northeastern margin of the Qinghai–Tibetan Plateau. *Environ. Res. Lett.* **2012**, *7*, 35401–35412. [CrossRef]

19. Dansgaard, W. Stable isotopes in precipitation. *Tellus* **1964**, *16*, 436–468. [CrossRef]

20. Price, R.M.; Swart, P.K.; Willoughby, H.E. Seasonal and spatial variation in the stable isotopic composition (δ^{18}O and δ^2H) of precipitation in south Florida. *J. Hydrol.* **2008**, *358*, 193–205. [CrossRef]

21. Song, X.; Kayane, I.; Tanaka, T.; Shimada, J. A study of the ground cycle in Sri Lanka using stable isotopes. *Hydrol. Process.* **2015**, *13*, 1479–1496. [CrossRef]

22. Harrington, G.A.; Cook, P.G.; Herczeg, A.L. Spatial and temporal variability of ground water recharge in central Australia: A tracer approach. *Groundwater* **2010**, *40*, 518–527. [CrossRef] [PubMed]

23. He, Y.; Theakstone, W.H.; Yao, T.; Shi, Y. The isotopic record at an alpine glacier and its implications for local climatic changes and isotopic homogenization processes. *J. Glaciol.* **2017**, *47*, 147–151.

24. Fan, Z.; Ma, Y. Some Issues about the Exploitation and the Rational Utilization of Water Resources in the Arid Areas. *Arid Zone Res.* **2000**, *17*, 6–11.

25. Xu, Q. Application of Environmental Isotopes in Water Cycle of Forest Ecosystem. *World For. Res.* **2008**, *21*, 11–15.

26. Han, G.; Lv, P.; Tang, Y.; Song, Z. Spatial and temporal variation of H and O isotopic compositions of the Xijiang River system, Southwest China. *Isot. Environ. Health Stud.* **2018**, *54*, 137–146. [CrossRef] [PubMed]

27. Qu, S.; Wang, Y.; Zhou, M.; Liu, H.; Shi, P.; Yu, Z.; Xiang, L. Temporal ^{18}O and deuterium variations in hydrologic components of a small watershed during a typhoon event. *Isot. Environ. Health Stud.* **2017**, *53*, 172–183. [CrossRef]

28. Yang, Y.; Xiao, H.; Qin, Z.; Zou, S. Hydrogen and oxygen isotopic records in monthly scales variations of hydrological characteristics in the different landscape zones of alpine cold regions. *J. Hydrol.* **2013**, *499*, 124–131. [CrossRef]

29. Meredith, K.T.; Hollins, S.E.; Hughes, C.E.; Cendón, D.I.; Chisari, R.; Griffiths, A.; Crawford, J. Evaporation and concentration gradients created by episodic river recharge in a semi-arid zone aquifer: Insights from Cl$^-$, δ^{18}O, δ^2H, and ^{3}H. *J. Hydrol.* **2015**, *529*, 1070–1078. [CrossRef]

30. Biggs, T.W.; Lai, C.T.; Chandan, P.; Lee, R.M.; Messina, A.; Lesher, R.S.; Khatoon, N. Evaporative fractions and elevation effects on stable isotopes of high elevation lakes and streams in arid western Himalaya. *J. Hydrol.* **2015**, *522*, 239–249. [CrossRef]

31. Edirisinghe, E.A.; Pitawala, H.M.; Dharmagunawardhane, H.A.; Wijayawardane, R.L. Spatial and temporal variation in the stable isotope composition (δ^{18}O and δ^2H) of rain across the tropical island of Sri Lanka. *Isot. Environ. Health Stud.* **2017**, *53*, 628–645. [CrossRef] [PubMed]

32. Wassenaar, L.I.; Athanasopoulos, P.; Hendry, M.J. Isotope hydrology of precipitation, surface and ground waters in the Okanagan Valley, British Columbia, Canada. *J. Hydrol.* **2011**, *411*, 37–48. [CrossRef]

33. Sánchez-Murillo, R.; Esquivel-Hernández, G.; Sáenz-Rosales, O.; Piedra-Marín, G.; Fonseca-Sánchez, A.; Madrigal-Solís, H.; Ulloa-Chaverri, F.; Rojas-Jiménez, L.D.; Vargas-Víquez, J.A. Isotopic composition in precipitation and groundwater in the northern mountainous region of the Central Valley of Costa Rica. *Isot. Environ. Health Stud.* **2016**, *53*, 1–17. [CrossRef] [PubMed]

34. Jin, L.; Siegel, D.I.; Lautz, L.K.; Lu, Z. Identifying streamflow sources during spring snowmelt using water chemistry and isotopic composition in semi-arid mountain streams. *J. Hydrol.* **2012**, *470*, 289–301. [CrossRef]

35. Rock, L.; Mayer, B. Isotope hydrology of the Oldman River basin, southern Alberta, Canada. *Hydrol. Process.* **2010**, *21*, 3301–3315. [CrossRef]

36. Pinder, G.F.; Jones, J.F. Determination of the Ground-Water Component of Peak Discharge from the Chemistry of Total Runoff. *Water Resour. Res.* **1969**, *5*, 438–445. [CrossRef]

37. Aggarwal, P.K. Isotope hydrology at the International Atomic Energy Agency. *Hydrol. Process.* **2002**, *16*, 2257–2259. [CrossRef]

38. Christophersen, N.; Hooper, R.P. Multivariate Analysis of Stream Water Chemical Data: The Use of Principal Component Analysis for the End-Member Mixing Problem. *Water Resour. Res.* **1992**, *28*, 99–107. [CrossRef]

39. Chen, X.; Wang, G.; Wang, F. Classification of Stable Isotopes and Identification of Water Replenishment in the Naqu River Basin, Qinghai-Tibet Plateau. *Water* **2019**, *11*, 46. [CrossRef]

40. Vespasiano, G.; Apollaro, C.; De Rosa, R.; Muto, F.; Larosa, S.; Fiebig, J.; Mulch, A.; Marini, L. The Small Spring Method (SSM) for the definition of stable isotope-elevation relationships in Northern Calabria (Southern Italy). *Appl. Geochem.* **2015**, *63*, 333–346. [CrossRef]

41. Vespasiano, G.; Apollaro, C.; Muto, F.; Dotsika, E.; De Rosa, R.; Marini, L. Chemical and isotopic characteristics of the warm and cold waters of the Luigiane Spa near Guardia Piemontese (Calabria, Italy) in a complex faulted geological framework. *Appl. Geochem.* **2014**, *41*, 73–88. [CrossRef]

42. Apollaro, C.; Dotsika, E.; Marini, L.; Barca, D.; Bloise, A.; De Rosa, R.; Doveri, M.; Lelli, M.; Muto, F. Chemical and isotopic characterization of the thermo mineral water of Terme Sibarite springs (Northern Calabria, Italy). *Geochem. J.* **2012**, *46*, 117–129. [CrossRef]

43. Li-De, T.; Shan-Dong, Y.; Wei-Zhen, S.; Stievenard, M.; Jouzel, J. Relationship between δ^2H and $\delta^{18}O$ and water vapour circulation in the precipitation of the qinghai-tibet plateau. *Sci. Sin. Terrae* **2001**, *31*, 214–220.

Stable Isotopes of Water and Nitrate for the Identification of Groundwater Flowpaths: A Review

Hyejung Jung [1], Dong-Chan Koh [2], Yun S. Kim [3], Sung-Wook Jeen [4] and Jeonghoon Lee [1,*]

[1] Department of Science Education, Ewha Womans University, Seoul 03760, Korea; hyejeong.chung@gmail.com

[2] Groundwater Department, Geologic Environment Division, Korea Institute of Geoscience and Mineral Resources, Daejeon 34132, Korea; chankoh@kigam.re.kr

[3] Water Quality Research Center, K-Water Convergence Institute, Daejeon 34350, Korea; yunskim@kwater.or.kr

[4] Department of Earth and Environmental Sciences & The Earth and Environmental Science System Research Center, Jeonbuk National University, Jeonju 54896, Korea; sjeen@jbnu.ac.kr

* Correspondence: jeonghoon.lee@ewha.ac.kr;

Abstract: Nitrate contamination in stream water and groundwater is a serious environmental problem that arises in areas of high agricultural activities or high population density. It is therefore important to identify the source and flowpath of nitrate in water bodies. In recent decades, the dual isotope analysis (δ^{15}N and δ^{18}O) of nitrate has been widely applied to track contamination sources by taking advantage of the difference in nitrogen and oxygen isotope ratios for different sources. However, transformation processes of nitrogen compounds can change the isotopic composition of nitrate due to the various redox processes in the environment, which often makes it difficult to identify contaminant sources. To compensate for this, the stable water isotope of the H_2O itself can be used to interpret the complex hydrological and hydrochemical processes for the movement of nitrate contaminants. Therefore, the present study aims at understanding the fundamental background of stable water and nitrate isotope analysis, including isotope fractionation, analytical methods such as nitrate concentration from samples, instrumentation, and the typical ranges of δ^{15}N and δ^{18}O from various nitrate sources. In addition, we discuss hydrograph separation using the oxygen and hydrogen isotopes of water in combination with the nitrogen and oxygen isotopes of nitrate to understand the relative contributions of precipitation and groundwater to stream water. This study will assist in understanding the groundwater flowpaths as well as tracking the sources of nitrate contamination using the stable isotope analysis in combination with nitrate and water.

Keywords: groundwater; isotope hydrology; stable water isotopes; stable nitrate isotopes

1. Introduction

Identifying groundwater flowpaths can provide important information regarding the movements of water itself and of contaminants therein via interaction with surface water. For example, contaminants can be discharged directly into the stream water but, if they are recharged into groundwater that then passes indirectly into stream water, the groundwater can contribute significantly to the water quality of the stream [1]. In particular, since nitrate is highly mobile and primarily originates from nonpoint source pollution, it is distributed across a wide area through various groundwater flowpaths and it can be difficult to trace the source [2]. In order to effectively control the spread of contaminants, and to clean up the contaminated stream water, it is therefore important to understand the flowpath of groundwater [3].

While concentration-based chemical analyses such as total nitrogen (TN), total phosphorus (TP), total organic carbon (TOC), biochemical oxygen demand (BOD), and chemical oxygen demand (COD)

have traditionally been used to effectively trace mixed contamination, this approach does not easily track contaminant movement and physical processes [4]. By contrast, stable isotope analysis is an effective tool for identifying sources, inferring processes, and determining the contributions of various inputs [5]. In particular, stable water isotopes ($\delta^{18}O$ and δD) are affected by meteorological processes that provide a characteristic fingerprint of their origin, which is essential for investigating the source of groundwater [6]. The stable isotopes of nitrogen and oxygen in nitrate ($\delta^{15}N$ and $\delta^{18}O$) are also fundamental to identifying the sources of nitrate contamination because the isotopic values are distinct from source to source [7].

While the stable water isotopes have been used as tracers in hydrograph separation studies since the pioneering work of Craig [8], the stable nitrate isotopes have been used to identify nitrate sources since nitrate contaminants became an environmental issue in the 1970s. Even now, nitrate is a very common groundwater pollutant, imposing a serious threat to drinking water supplies and contributing to eutrophication of surface waters [9–11]. Nitrate is the dominant nitrogen species in groundwater, which may be derived from soil organic nitrogen, synthetic fertilizer, livestock waste, sewage effluent, and atmospheric precipitation [11]. In some areas, atmospheric deposition of anthropogenic nitrogen exceeds ecosystem nutrient demand and the influence of atmospheric deposition on nitrogen export has not been well-documented for short-term discharge events such as rainfall and snowmelt [12].

Isotopic hydrograph separation using stable isotopes in water and nitrate provides a useful tool for determining the water flowpath and the source of nitrates. This approach has been widely used to understand the proportion of different water sources contributing to stream water, which can be used to infer the flowpath and residence time [13–16]. In particular, distinguishing between nitrate sources such as direct atmospheric deposition or biological assimilation and release in the soil zone may reveal the flowpath of groundwater into stream or river water [12]. Hence, the isotopic analysis of nitrogen and oxygen in nitrates (the dual isotopic technique) has been used to identify the source of nitrate in many studies. For example, Böttcher et al. [17] determined the sources of nitrate in groundwater downgradient from an agricultural area and Durka et al. [18] later determined the sources of nitrate in an undisturbed watershed in Bavaria, Germany. The dual isotope approach can be used to determine the source of nitrate in stream water because of the distinct isotopic signature of nitrate sources such as event water (rainfall or snowmelt), soil water, and groundwater.

To study the hydrograph separation of stable water isotopes, it is important to understand how precipitation infiltrates into soil water or recharges into groundwater and is subsequently released into stream water. To this end, studies on stable water isotopes in the atmospheric source must first be conducted in order to form a basis for understanding and predicting the movement of contaminants in the groundwater flowpath [16]. For the past 40 years, many studies have been conducted using the hydrograph separation technique through stable water isotopes or conservative chemical tracers to investigate the movement of water components such as groundwater, rainfall, snowmelt, and soil water in the stream water [16,19–26]. In particular, Ladouche et al. [20] investigated the streamflow components using hydrograph separation with stable water isotopes, major chemical parameters, and dissolved organic carbon (DOC). Dahlke et al. [22] used the value of the stable oxygen isotope ($\delta^{18}O$) of water to indicate that the majority of storm runoff was dominated by pre-event water in the 30% glaciated sub-arctic catchment of Tarfala, northern Sweden. Later, Rahman et al. [24] conducted an end-member mixing analysis to describe the daily variation of runoff components in the Alpine watershed, and Kim et al. [16] used chemical and isotopic tracers to identify the impact of the pre-event water component of a granitic watershed with a thin soil layer.

Isotope hydrology involves measuring the stable isotopic compositions of precipitation, stream water, and groundwater samples, then interpreting these measurements in order to quantify or conceptualize the groundwater flowpath and velocity profile along with hydrogeochemical and biogeochemical reactions. With more conventional hydrogeological and hydrogeochemical data, such as information on lithology, meteorology, and solute concentrations, isotopic approaches have been helpful in identifying water movement among various reservoirs, e.g., evapotranspiration,

groundwater recharge, discharge, and runoff [12,15,27–31]. The present paper is focused on isotope hydrology reviews dealing with methodological advances and their limitations and lessons drawn from decades of research. This review is motivated by the importance of understanding the groundwater flowpath to rivers and/or streams via analysis of isotopes in water and nitrates. After briefly introducing the systematic processes affecting the oxygen and hydrogen isotopes from precipitation to groundwater and the nitrogen and oxygen isotopes of nitrates, the review goes on to examine the commonly applied isotopic technique of hydrograph separation using stable water isotopes. Hence, this study will help to understand the groundwater flowpath and the tracking of nitrate contamination to its source using the stable isotope analysis of nitrate and water.

2. Hydrograph Separation

Hydrograph separation is the separation of streamflow components into two or more different components that contribute to the stream in a small catchment area or watershed. For example, isotopic hydrograph separation using isotopic tracers was first proposed by Dincer et al. [32], was developed by Sklash and Farvolden [19], and has been evaluated in many studies [33]. The isotopic hydrograph separation technique is based on the assumption that two components contribute to the stream after the precipitation occurs, namely: (1) The runoff caused by the rainwater (new water) and (2) the groundwater (old water). To separate the stream water discharge into rainwater and groundwater components, a two-component mixing model was used. The following mass balance equations introduced by Sklash and Farvolden [19] can be used:

$$Q_t = Q_r + Q_g \tag{1}$$

$$C_t Q_t = C_r Q_r + C_g Q_g \tag{2}$$

$$x = \frac{C_t - C_g}{C_r - C_g} \tag{3}$$

where Q indicates the discharge of each component, C is the concentration of an observed tracer or an isotopic composition, the subscripts t, r, and g indicate total discharge, rainwater, and groundwater, respectively, and x_r is the ratio of stream water contributed by rainwater ($x_r = \frac{Q_r}{Q_t}$).

The following four assumptions underlie the application of these mass balance equations: (1) There is a significant difference between the concentration of tracers in groundwater and rainwater; (2) the concentrations or isotopic compositions of the tracers for groundwater and rainwater are constant in space and time; (3) for two-component hydrograph separation, the concentrations of each tracer are equivalent in groundwater and vadose water, or else the contribution of vadose water is negligible; and (4) surface storage contributes minimally during the runoff. If these assumptions are valid, then two-component hydrograph separation can be used to determine the amounts of stream water contributed by rainwater and groundwater. Otherwise, hydrograph separation of three or more components should be carried out. For example, if the amount of vadose water in the saturation zone is not negligible and must be taken into account, then hydrograph separation of the three components of runoff, soil water, and groundwater should be used. In two-component systems, soil water can be interpreted as runoff or groundwater, depending on the geological characteristics. When considering the soil water among the factors contributing to the stream water after rainfall or snowmelt, hydrograph separation of the three components (soil water, rain or snowmelt, and groundwater) should be used. Hydrograph separation of the three components is basically expressed in the form of a three-way linear system of equations, which can be interpreted as follows:

$$Q_t = Q_r + Q_g + Q_s \tag{4}$$

$$C_t = C_t \frac{Q_r}{Q_t} + C_g \frac{Q_g}{Q_t} + C_s \frac{Q_s}{Q_t} \tag{5}$$

$$I_t = I_t \frac{Q_r}{Q_t} + I_g \frac{Q_g}{Q_t} + I_s \frac{Q_s}{Q_t} \tag{6}$$

where Q indicates the discharge of each component, C is the concentration of an observed tracer, I is the isotopic composition of each component, and the subscripts t, r, g, and s indicate the total discharge, rainwater, groundwater, and soil water, respectively. Since solutions for more than three components are difficult to obtain, matrix operation has been applied to the Equations (4)–(6) in the present work as follows:

$$A = \begin{bmatrix} 1 & 1 & 1 \\ C_r & C_g & C_s \\ I_r & I_g & I_s \end{bmatrix}, X = \begin{bmatrix} \frac{Q_r}{Q_t} \\ \frac{Q_g}{Q_t} \\ \frac{Q_s}{Q_t} \end{bmatrix}, B = \begin{bmatrix} 1 \\ C_t \\ I_t \end{bmatrix}. \tag{7}$$

$$AX = B, \ X = A^{-1}B \tag{8}$$

A system of linear equations is introduced that enables a three-component hydrograph separation using both isotopic and chemical compositions. MATLAB can be used to solve the matrix. These are mathematically underdetermined systems of n equations in n + 1 unknowns for which there is no unique solution. However, even with n isotope systems and >n + 1 sources, recently published studies introduce software (IsoSource model) that calculates multiple source proportions using mass balance conservation requirements. The IsoSource model, based on the principle of stable isotope mass conservation, can be used to partition contaminant sources in wastewater [34–36].

According to the second assumption mentioned above, there should be no temporal or spatial variation in the isotopic compositions of groundwater and rainwater (i.e., no isotopic fractionation), which would otherwise lead to deviation. Thus, if the isotopic composition of rain and groundwater changes over time, a systematic error in the fraction of rainwater contributing to the stream will arise. This systematic error can be determined using Gaussian error propagation [37,38]. The isotope composition of groundwater (old water) is known to be relatively constant. However, rain or snowmelt (new water) is subject to much greater isotopic fractionation, so hydrograph separation using the mean isotope value generates errors. The uncertainty of new water generated from isotopic fractionation can be calculated according to the following equation [38]:

$$\Delta x_r = -\frac{x_r}{C_r - C_g} \Delta c_r \tag{9}$$

where Δx_r is the systematic error when new water (rain or snowmelt) contributes to the stream, and Δc_r is the error in c_r. This is the variation in the tracer concentration or the ratio of stable isotopes in the rain (new water). Therefore, according to Equation (9), the error generated when considering the effect of new water on the stream is inversely proportional to the difference of the tracer concentration between new and old water, and directly proportional to the actual contribution of new water (x_r) to the stream water and the tracer concentration of the new water over time (Δc_r).

3. Stable Water Isotopes

Water evaporates from the ocean and moves into the continents, cools and condenses to form clouds, then falls to the surface as precipitation (rain or snow). In turn, the precipitated water (stream water, groundwater, and runoff) is evaporated again and recycled. As shown in Figure 1, during the transition from ocean to continent, the isotopic composition is changed through the processes of evaporation and rainout within the hydrologic cycle based on the isotope data from Hoefs [39] and Coplen et al. [40]. When water undergoes a change of physical phase, the water molecules containing heavier isotopes (H^2HO and $H_2^{18}O$) are preferentially concentrated in the more condensed phase (i.e., liquid rather than vapor, and solid rather than liquid), while molecules containing the lighter isotope ($H_2^{16}O$) are concentrated in the remaining phase [41]. Consequently, the rainout process causes continual fractionation of heavy isotopes into the precipitation (Rayleigh-like distillation) such that

the residual vapor becomes progressively more depleted in heavy isotopes [42]. Hence, subsequent precipitations will be depleted in heavy isotopes compared to previous precipitations originating from the same atmospheric water vapor [43]. Moreover, since the isotope composition of water varies among the components of the water cycle, isotope measurement makes it possible to identify the source of water masses and determine their interrelationships [42]. In particular, because stream water has a complicated relationship between rainfall (new water) and groundwater (old water), isotope composition is a useful tool for determining mixing patterns and relative contribution rates via hydrograph separation [26,38].
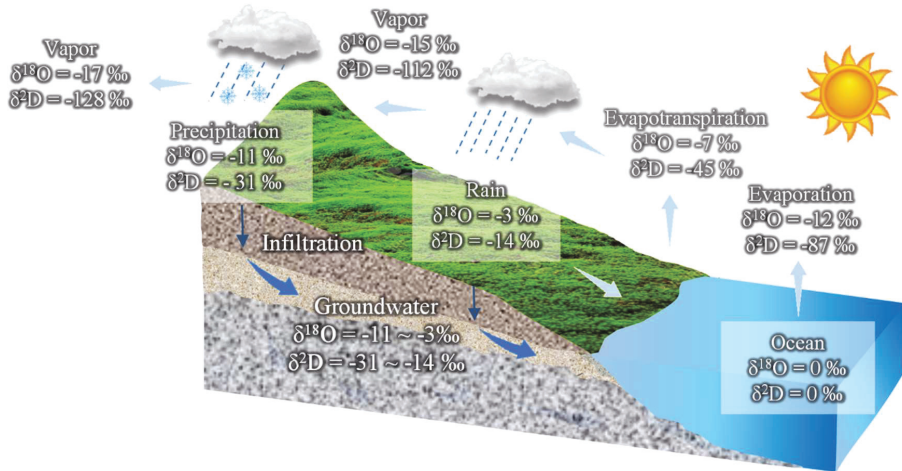
Figure 1. The diagram of isotopic composition change of atmospheric water vapor showing the processes of evaporation and rainout as the air mass proceeds from an ocean to a continent (based on Hoefs [39]; Coplen et al. [40]).

3.1. Isotopes in Precipitation

Unlike other tracers, stable water isotopes are added naturally on the scale of the watershed by precipitation (rain or snowmelt events) and, upon entering the watershed, undergo transport according to the natural movement of the body of water through the watershed. Since the stable isotope compositions of the water only change via the above-mentioned mixing and fractionation processes during evaporation and condensation, these environmental isotopes (supplied by meteoric processes) can be used to trace and identify the different air and water masses contributing precipitation to the watershed [43]. Moreover, since precipitation is a major source of water in the hydrological cycle, an understanding of the processes that control the spatial and temporal isotopic composition distributions of precipitation is essential [43].

In general, the fractionation processes of the stable hydrogen and oxygen isotopes are similar; hence, their behavior in the hydrological cycle is also similar [44]. This similarity causes covariance between the stable hydrogen and oxygen isotope concentrations found in most meteoric water, as first observed by Friedman [45]. This covariance can be explained by the following relationship, which was defined by Craig [8]:

$$\delta^2 H = 8\ \delta^{18}O + 10 \tag{10}$$

This linear relationship, termed the meteoric water line (MWL), provides a convenient reference for understanding and tracing the origins of water [43]. In particular, an MWL with an intercept of 10 and a slope of 8 has been defined as the global meteoric water line (GMWL). The GMWL may be explained by the condensation of water vapor under conditions close to equilibrium, producing the

slope of 8 [46]. The slope is related to the ratio of the fractionation coefficients and to factors relating to whether the water entering the soil, groundwater, and lakes has experienced evaporation [31,47]. Typically, the evaporation of soil or lake water results in a slope of less than 8 (generally between 4 and 7) for the local meteoric water line [46].

In a plot of Equation (10), the y-intercept is termed the deuterium excess (or d-excess). According to Dansgaard [46] this is defined by the deviation of isotopic equilibrium during evaporation from sourced precipitation and is related to the relative humidity parameter of the vapor source for evaporation. Dansgaard [46] recognized four parameters that determine this depletion in isotope values, namely: Altitude, distance from the shore, latitude, and quantity. Since the affected factors differ regionally, the d-excess is useful for identifying moisture source regions [31,48–50]. More recently, Lee et al. [38] reviewed the results of previous studies on how the fractionation of stable water isotopes significantly differs depending upon the region. In the New Hampshire area of the United States, for example, the difference of stable oxygen isotopic value is 2 to 3‰ [33] and the stable hydrogen isotopic value is 10 to 12‰ [31], while the isotopic values in Incheon, Korea, are 20‰ for oxygen and approximately 60‰ for hydrogen, and in Jeju Island, Korea, the respective isotopic values of oxygen and hydrogen are 7 to 8‰ and 50 to 60‰.

The isotopic compositions of precipitation are dependent upon several factors, including those of its vapor source (typically from nearby oceanic regions) along with the processes of precipitation formation and air mass trajectory (i.e., the influence of vapor source and rainout processes along the pathway of the air mass) [43]. Most of these factors are related to isotopic fractionation through diffusion during physical phase changes such as evaporation, sublimation, condensation, and melting [43]. Further details relating to isotopic fractionation will be discussed in the following sections.

3.2. Isotopic Evolution of Snow

Snowmelt is the largest contributor to groundwater recharge in Alpine environments [51]. Since snow dynamics are highly variable in space and time, an understanding of the hydrological responses of snowmelt contributing to the watershed is crucial for water-resource management [52]. While the isotopic composition of the snowpack profile generally represents the distinct isotopic composition of individual precipitation events, the signal in the snow layers provided by these individual events is attenuated by isotopic exchange, snowpack metamorphism and surface sublimation [53]. The isotopic composition of snowmelt generated from a snowpack results from two major processes, namely: (1) Sublimation and molecular exchange between vapor and the snowpack, and (2) meltwater infiltration and exchange with snow and meltwater within the snowpack [31,33,54,55].

With respect to the first process, Moser and Stichler [56] indicated that the isotopic fractionation associated with sublimation of snow surfaces behaves similarly to that of evaporating water, although Cooper [53] pointed out an exception when the well-mixed conditions of a water body are not present in the snowpack. In the second process, the meltwater is initially depleted in heavy isotopes relative to the remaining snowpack and then becomes gradually enriched in heavy isotopes as the melting proceeds [15,33,54]. This isotopic evolution results from isotopic exchange between liquid water and ice as the liquid water percolates down the snowpack [15,33,54]. Consequently, since the isotopic compositions of snowmelt are generally not the same as those of the bulk snow, hydrograph separations based on the isotope composition of the bulk snow will be erroneous [57]. Since snowmelt is a significant component of groundwater and surface runoff in temperate areas, an understanding of the isotopic evolution of a snowpack is crucial to both climatic and hydrological studies.

Studies of artificial and natural snowpack have demonstrated that complex changes in isotopic compositions can be expected to occur between accumulation and melting [58,59]. The isotopic composition of the upper snow layers is significantly altered by sublimation and exchange with atmospheric water vapor. Enrichment in $\delta^{18}O$ and δ^2H in the snowpack as a result of evaporation is a predictable outcome [60], and theoretical fractionation models developed for evaporation from well-mixed water bodies [61]) are reasonably successful at predicting the effects of simple evaporation

once they are modified to account for the less than well-mixed conditions of the natural snowpack. However, isotopic change in the snowpack is more complicated than simple surface evaporation, and is dependent on variable conditions such as soil temperature, soil moisture, relative humidity, air temperature, vegetation cover, and the period of time for which the snowpack is present on the ground. Mast et al. [62] showed that although most of the water in Andrews Creek was new water from snowmelt (based on hydrograph separation using $\delta^{18}O$), much of that water had been transported along subsurface flowpaths prior to reaching the stream, and substantial interaction had occurred with soil or soil-like materials (based on hydrograph separation using dissolved silica). The highest nitrate concentrations in the springs and streams have been found to arise from a combination of the microbial cycle and flushing of nitrates and nitrates directly from rain or snowmelt [12].

3.3. Stable Water Isotope Measurements

The stable isotope composition of water is mainly determined by isotope ratio mass spectrometry (IRMS) [63]. This technique measures the relative isotope ratios of molecular compounds by analyzing mass differences [64]. A spectrum of masses is produced by generating a beam of charged molecules (usually by thermal ionization of gaseous samples) then bending the beam in a magnetic field [6]. In general, stable isotope analysis of water using IRMS requires chemical pretreatment [64]. For example, oxygen isotopes require ion-exchange between H_2O and CO_2 via bicarbonate reactions, and hydrogen isotopes require reduction with metals such as uranium, zinc, platinum and chromium [45,65–70]. Consequently, the oxygen isotope composition is analyzed as CO_2 and the hydrogen isotope composition is analyzed as H_2 [6]. The first dual-inlet mass spectrometer was developed by Alfred Nier in the late 1940s. However, the classical off-line procedures for sample preparation are time consuming and analytical precision depends on the skill of the investigator [6]. These considerations led to the modification of the classic dual inlet technique to create the continuous-flow isotope ratio mass spectrometer in which a trace amount of the gas to be analyzed is delivered in a stream of helium carrier gas [39].

Recently, isotope ratio infrared spectroscopy (IRIS) has been developed to analyze stable water isotopes using laser-based techniques [64]. This technique examines the characteristics of water absorption in the near-infrared wavelength region due to vibration–rotation transitions, which depend upon the ^{18}O and ^2H substitution of H_2O gas molecules [71]. Since these molecular motions are directly related to the proportion of isotopes, the isotope ratio can be measured [72]. The IRIS technique is sub-divided into off-axis integrated cavity output spectroscopy (OA-ICOS) and wavelength-scanned cavity ring-down spectroscopy (WS-CRDS) [64]. Compared to conventional IRMS, the IRIS technique has the advantages of simple preparation and operation, comparative portability for application in the field, and applicability with relatively small amounts of water samples (ppb, ppt) [73–77]. However, the presence of dissolved organic molecules with O−H bonds has the disadvantage of degrading analytical performance due to spectral interferences between the dissolved organics and water molecules [78].

4. Stable Nitrate Isotopes

4.1. Pretreatment Method for Nitrate Isotope Analysis

Dual isotope analysis of nitrates ($\delta^{15}N$ and $\delta^{18}O$) can be a powerful tool for identifying nitrate sources and nitrate cycling mechanisms in stream water because the different sources have isotopically distinct $\delta^{15}N$ and $\delta^{18}O$ compositions [79,80]. Over the past few decades, several pretreatment methods have been developed to concentrate dissolved nitrates for dual isotope analysis. Until recently, almost all nitrates for both $\delta^{15}N$ and $\delta^{18}O$ analysis were prepared using modifications of the silver nitrate method, in which samples are concentrated on anion exchange resins, eluted, and purified to produce $AgNO_3$ [80,81]. The $AgNO_3$ obtained from freeze drying is mixed with a catalyst composed of CuO/Cu wire/CaO and heated to 850 °C in a sealed reactor to generate N_2 gas for $\delta^{15}N$ analysis by IRMS. Meanwhile, $\delta^{18}O$ is analyzed by mixing $AgNO_3$ with graphite (spectroscopic analysis grade) to obtain

CO gas by pyrolysis or CO_2 gas by complete combustion. The combined techniques have been successfully used and published in studies from Alpine, agricultural, and urban environments [3,82]. The ion exchange method described above has the advantages of easy transport and storage, direct applicability in the field, and minimal isotope fractionation of nitrate during ion exchange. However, disadvantages of the ion exchange method include the long time and large cost of sample preparation, and interference due to the presence of other anions (Cl^-, SO_4^{2-}) in the sample. In addition, a relatively large amount of sample is required for precise analysis.

Another nitrate pretreatment method is denitrification by inoculation with a pure culture of denitrifying bacteria that lack the enzyme to reduce nitrate beyond N_2O [83,84]. The gas is then analyzed by IRMS. Microbial denitrification provides a saving in time and cost of sample preparation compared to the silver nitrate method and requires a small amount of sample. Nevertheless, this method involves a long time for culturing the microorganisms and the activity of the microorganisms is affected by toxic substances (antibiotics, heavy metals, pesticides, etc.) in the sample. Moreover, the presence of NO_2^- may distort the composition of the N_2O gas. In order to solve these problems, an advanced method of chemically reducing nitrate to N_2O gas was described by McIlvin and Altabet [85]. In this technique, nitrate (NO_3^-) is converted to nitrite (NO_2^-) using cadmium reduction and then to nitrous oxide (N_2O) using a 1:1 azide and acetic acid solution. The N_2O gas is analyzed in the same manner as in the microbial denitrification method. This chemical reduction method can significantly reduce the time and cost required for sample preparation and requires a small amount of sample for analysis. In addition, unlike microbial denitrification, it is not affected by toxic substances contained in the sample. However, there is a risk of exposure to dangerous chemicals (cadmium, sodium azide) during the sample pretreatment, and inaccurate data can be obtained due to the NO_2^- in the sample, as with microbial denitrification.

More recently, besides IRMS, measurements of $\delta^{15}N$ and $\delta^{18}O$ from the headspace N_2O gas are analyzed in a N_2O triple isotope analyzer (N_2OIA-23e-EP Model 914-0060; Los Gatos Research, Mountain View, CA, USA) using laser absorption spectroscopy after N_2O produced by conversion of NO_3^- by earlier mentioned pretreatment [86,87]. The instrument measures N_2O concentrations (0.3–20 ppm), and $\delta^{15}N_\alpha$, $\delta^{15}N_\beta$, $\delta^{15}N_{bulk}$, $\delta^{17}O$, $\delta^{18}O$, and H_2O values in air to precisions of 0.03 ppb for N_2O, less than ±1‰(SEM) for N and less than ±2‰ (SEM) for O isotopes over 300 s of measurement integration [86]. However, the laser spectrometry technique is lower precision and accuracy than IRMS technique (less than 0.2‰ for $\delta^{15}N$-NO_3^-, 0.5‰ for $\delta^{18}O$-NO_3^-) [88].

4.2. Identification of Contaminant Source Using Nitrate Isotopes

As previously mentioned, the analyzed nitrate $\delta^{15}N$ and $\delta^{18}O$ isotope ratios provide distinct values for each contaminant source. The value of $\delta^{15}N$ in atmospheric NO_3^- is usually in the range of −15‰ to +15‰ [9,89]. This large range is due to complex chemical reactions of nitrates or related compounds in the atmosphere, seasons, meteorological conditions, types of anthropogenic inputs, proximity to pollution sources, distance from the ocean, etc. [90]. Synthetic nitrogen fertilizers have $\delta^{15}N$ values in the range of −4‰ to +4‰ [79] and the $\delta^{15}N$ value of nitrogen in the soil ranges from −2‰ to +5‰. However, manure and sewage can be more enriched in ^{15}N due to volatilization of ^{15}N-depleted ammonia, and oxidation of much of the residual waste may result in high $\delta^{15}N$ of nitrate [79]. By this process, the $\delta^{15}N$ value becomes significant with a range of +10‰ to +20‰ [91,92]. Hence, the $\delta^{15}N$ is an important indicator of nitrates in the atmosphere, fertilizers, soil, manure and sewage. However, the identification of nitrogen sources and cycles using $\delta^{15}N$ values alone is limited because the ranges of values from precipitation, soil, fertilizer, manure, and sewage show substantial overlap (Figure 2). The analysis is therefore used in combination with $\delta^{18}O$, another indicator for identifying and separating sources of nitrates, in order to reduce the uncertainty of nitrogen isotopes in the identification [3,18,79,93–96].
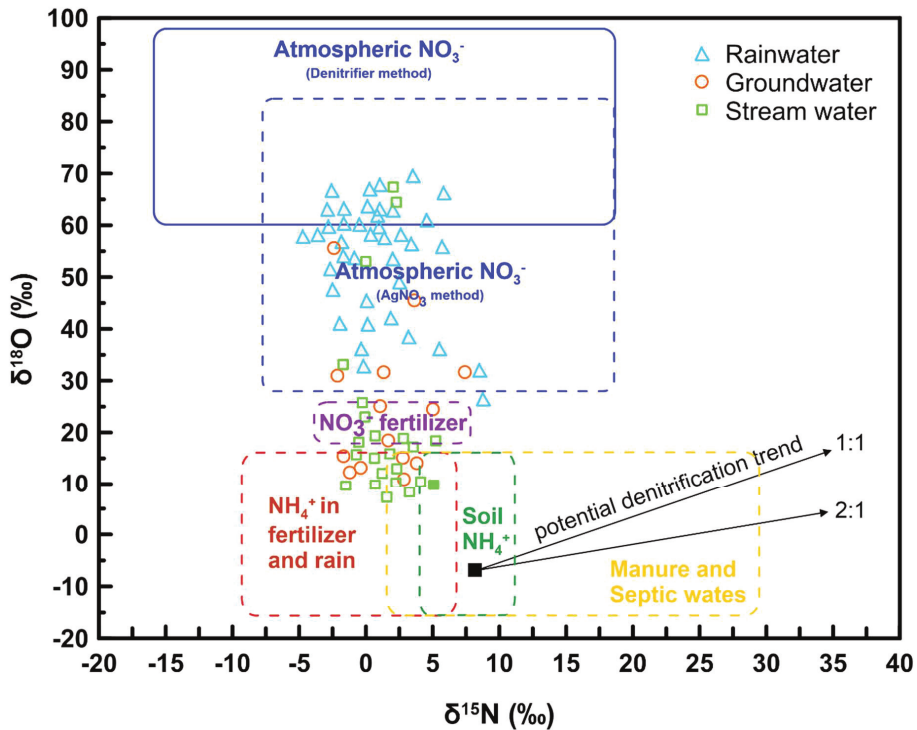
Figure 2. A plot of the $\delta^{15}N$ and $\delta^{18}O$ values of nitrate from various N sources. The nitrate in stream samples (green squares) was largely derived from groundwater sources. This diagram was modified from Kendall et al. [96] and data from Kendall et al. [79].

The conventional theory asserts that one oxygen atom of newly generated nitrate in soil is derived from dissolved atmospheric oxygen (O_2) and the other two oxygen atoms are from the surrounding water bodies [12,18,79,94,97–100]. If these oxygens are included without any fractionation, and the $\delta^{18}O$ values of water and atmospheric sources are known, the $\delta^{18}O$ value of microbial nitrate can be calculated as follows:

$$\delta^{18}O_{NO_3} = 2/3\ \delta^{18}O_{H_2O} + 1/3\ \delta^{18}O_{O_2} \tag{11}$$

While the $\delta^{18}O$ values of atmospheric-derived nitrates are usually high, between +20‰ and +70‰ [101], the $\delta^{18}O$ values of synthetic nitrate fertilizer are 22 ± 3‰; those of soil nitrogen transformed from ammonium via nitrification are between −10 and +10‰; and those of manure and sewage are below 15‰ [79]. As such, nitrate shows distinct isotopic composition of nitrogen and oxygen for each contaminant source, which is useful for contaminant source identification. In addition to identifying contaminant source, it can also be used to identify the contribution of contaminant sources using previously mentioned hydrograph separation.

However, the $\delta^{15}N$ and $\delta^{18}O$ values of nitrate are altered by isotopic fractionation due to mineralization, absorption/desorption, nitrification, denitrification, volatilization, assimilation (uptake), and leaching from the soil zone [3]. Common microbial organisms preferentially use the lighter isotopes (^{14}N and ^{16}O) over the heavier (^{15}N and ^{18}O), so that the microbial products are isotopically depleted and the residual nitrates are enriched in ^{15}N and ^{18}O [3]. For example, when microbial organisms convert nitrate to nitrogen gases N_2O (denitrification), the formed nitrogen gases are lighter than the remaining nitrates (low $\delta^{15}N$ and $\delta^{18}O$). Therefore, denitrification causes increases in the $\delta^{15}N$

and $\delta^{18}O$ values of the residual nitrates, and the enrichment ratios of $\delta^{15}N$ and $\delta^{18}O$ are positively correlated by a factor of between 1.3:1 and 2.1:1 [2,17,79,101–104]. This indicates that, even if isotope fractionation by denitrification occurs, the initial isotope composition can be estimated by knowing the enrichment factor [105].

4.3. Movements of Nitrate from Surface to Stream

After reaching the ground, precipitation moves from the surface to the stream, which gradually alters the water isotope composition [42]. These processes typically involve two flow pathways, which are direct and indirect. The direct pathway is the runoff of surface water from rainfall or melting snowpack into the stream water, while the indirect pathway is the vertical movement of dissolved nitrate through the soil profile into the groundwater, after which the groundwater can be flushed out and contribute to the stream water [16,38]. In these processes, the potential sources of nitrates in stream water are atmospheric via rainfall and snowmelt [3], mineralization of soils under snowpacks [106], groundwater [107–109], nitrification [3,12,93], or a combination of these [110]. As mentioned previously, the $\delta^{18}O$ values of nitrates from atmospheric sources differ significantly from those of groundwater nitrates originating from nitrification in the soil. Thus, if rainfall and surface water run off directly to the stream, the $\delta^{18}O$ value of nitrate is similar to that of the atmospheric source. However, if precipitation is infiltrated into the soil layer and then recharged to groundwater and released into the stream water, the isotope composition of the stream water is similar to that of the groundwater or soil water. As shown in Figure 2, if the isotopic composition of rainwater and groundwater is determined, the typical isotope values of nitrogen and oxygen can be used to identify the source of stream water and the relative contribution rate.

Many previous studies have shown that groundwater (old water) via indirect pathways is the dominant source for stream water (Table 1). By examining the $\delta^{15}N$ and $\delta^{18}O$ values of nitrate, Kendall et al. [3] concluded that the main source of nitrates in stream water is groundwater, and that a direct contribution of atmospheric-derived nitrate from the snowpack to the stream is a relatively minor source. Ohte et al. [111] studied the nitrate sources of a headwater stream at the Sleepers River Research Watershed in Vermont, USA, during snowmelt using the $\delta^{18}O$ values of nitrate with precipitation, soil water, and groundwater as the three end members. The results indicated that, as the groundwater was recharged by meltwater and precipitation during snowmelt, the input to the groundwater gradually increased to eventually make it the dominant source of nitrate. As shown in Figure 3, Piatek et al. [109] analyzed $\delta^{15}N$ and $\delta^{18}O$ values of nitrate in the stream and compared them to those of snow and groundwater in the Arbutus Watershed of New York State, NY, USA, to indicate that stream water, atmospherically-derived solutions, and groundwater had overlapping nitrate $\delta^{15}N$ values. However, while the $\delta^{18}O$ values of nitrates displayed similar ranges in stream water and groundwater, these values were significantly lower than those of atmospheric solutions. In addition to these studies, Barnes et al. [112] demonstrated a seasonal variation in the rate of nitrate contribution from atmospheric sources and calculated that, on average, 1–3% of the summer and 10–18% of the winter/spring exported stream NO_3^- is derived from direct atmospheric deposits. Such information is important to the development of efficient and successful abatement strategies that may include ecosystem management, controls on NO_x emissions and possible correlations of nitrogen exports with climate change [109]. Moreover, $\delta^{15}N$ and $\delta^{18}O$ values of nitrate are useful for identifying the source of nitrate and flowpath process using hydrograph separation because they have distinct isotope values for each source (precipitation, groundwater, soil, etc.).
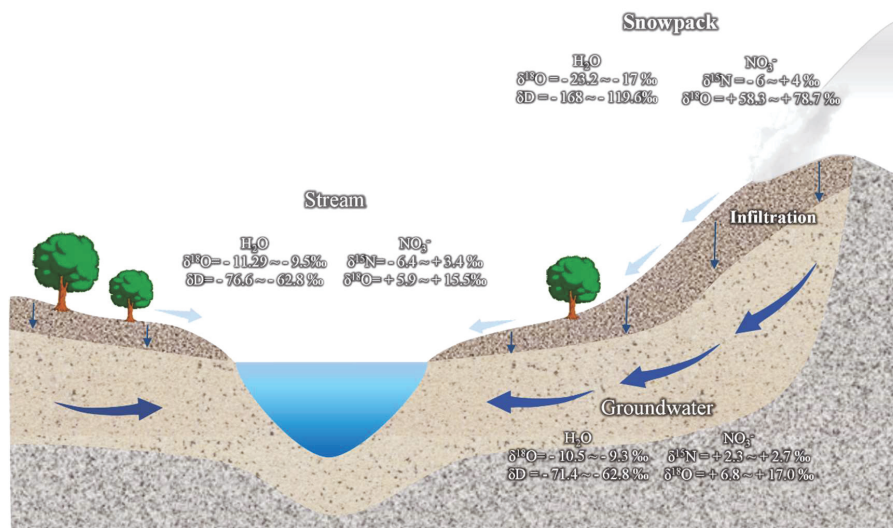
Figure 3. Isotopic compositions of water and nitrate in snowpack, groundwater, stream (data from Kendall [79]; Piatek et al. [109]).

Table 1. Summary of studies that account for more than two different end-members in hydrograph separation using nitrate isotopic tracer.

Location	End-Member ($\delta^{15}N$-NO_3^-, $\delta^{18}O$-NO_3^-)	Groundwater (Nitrified Sources) Fraction in Stream Water	Reference
Bavaria, Germany	Atmospheric; Nitrification	84–70%	[18]
Catskill Mountains, New York State, USA; Rocky Mountain National Park, Colorado, USA; Danville, Vermont, USA	Snowmelt; Nitrification	Nitrified sources dominant	[3]
Turkey Lakes watershed, Ontario, Canada	Atmospheric; Nitrification	70%	[113]
Catskill Mountains, New York, USA	Precipitation; Snowmelt; Soil water	Soil water dominant	[93]
Loch Vale watershed, Colorado, USA	Nitrification	>75%	[12]
Sleepers River Research Watershed, Vermont, USA	Precipitation; Groundwater; Soil water	Groundwater dominant	[111]
New Hampshire, USA	Precipitation; Nitrification	55–100%	[94]
Arbutus Watershed, New York State, USA	Wet deposition; Groundwater	Groundwater dominant during late winter/early spring	[109]
Green Mountains, Vermont, USA	Precipitation; Soil water	Soil water dominant during snowmelt periods	[114]
Connecticut and Massachusetts, USA	Microbially produced; Atmospheric deposition	Summer 97–99% Winter/Spring 82–90%	[112]
Pennsylvania, USA	Atmospheric sources; Microbial soil nitrification	67%	[115]

Table 1. *Cont.*

Location	End-Member (δ^{15}N-NO$_3^-$, δ^{18}O-NO$_3^-$)	Groundwater (Nitrified Sources) Fraction in Stream Water	Reference
Hubbard Brook Experimental Forest, New Hampshire, USA	Precipitation; Nitrification	66–71% during summer rainfall event	[116]
NMR above-ground streams, Pittsburgh, USA	Atmospheric; Sewage (δ^{15}N: 0‰ to +20‰; δ^{18}O: −15‰ to +15‰)	<66% sewage-derived	[117]
Savannah River, South Carolina, USA	Throughfall; Trench (soil) water; Groundwater	Groundwater predominant	[118]
Savannah River, South Carolina, USA	Atmospheric; Groundwater	Watershed B: 72% Watershed R and C: 90%	[119]

4.4. Implications of the Flowpath of Water and Nitrates

The stable isotope of nitrate (δ^{15}N and δ^{18}O) can be used to trace the nitrate sources in water bodies because nitrate contaminants usually have distinct isotope compositions [7]. In order to increase the reliability of contaminant tracking, there is a need for a multilateral investigation of precipitation, land-use type and area utilization rates, synthetic fertilizers, animal wastes, the presence of point sources (septic tanks and landfills), and the presence of sewer systems. In addition, hydrogeological data such as groundwater flow rate and direction, aquifer geometry, matrix characteristics, nitrate concentrations, electrical conductivity (EC), redox potential (Eh), and dissolved oxygen (DO) can be used to assess variations in the level of contaminants as well as for tracking contaminant sources.

While isotope analysis is a useful tool for tracking nitrate contaminants, isotope fractionation by nitrification, denitrification, and the presence of multiple contaminants continue to make this difficult. Hence, the use of water stable isotope analysis in combination with the isotopic composition of nitrates may improve the reliability of source identification.

5. Summary and Perspectives

Nitrate contamination of stream water has become an environmental problem of global concern [101]. To identify the nitrate source is an effective approach to controlling discharge and emissions of nitrate contamination of stream water. In recent decades, dual nitrate isotope analysis (δ^{15}N and δ^{18}O) has been used as a useful tool for identifying the source and flowpath of nitrate contaminants in water bodies. We have tried to demonstrate in this paper an understanding of the identification water sources and flowpaths process, and the proportion of various sources contributing to stream water via water and nitrate stable isotope technique. However, the application of this method has some limitations due to the multiple nitrogen sources and the influence of isotopic fractionation [101]. In details, nitrates are subjected to multiple physical, chemical, and biological fractionation processes during transport from the original nitrate source to water bodies, and these reactions are influenced by such factors as land-use types, climate, and hydrogeological conditions. Besides, the stable isotope values of nitrate vary according to country or region due to the various regional conditions. To enable the quick and accurate analysis of nitrogen contaminant sources for water bodies, it is therefore suggested that data on the stable isotope values of nitrate from various contaminant sources should be collected in order to establish a global and regional isotope database. For identifying the contaminant sources and tracing the flowpath, it is therefore of great significance to study the influencing factors and transformation processes of nitrates.

More recently, quantification of the relative contributions of nitrate can be improved if other isotope (B, Sr, S, C, Li, U) or chemical tracers [96]. The isotopic signature of boron (δ^{11}B) in association with the nitrates has been demonstrated [120–125]. Strontium and sulphate isotopes give additional information on the sources of contaminant [126,127]. In particular, combined use of boron isotopes with nitrate (δ^{15}N and δ^{18}O) can be a useful tool for nitrate source contributions [120–122,127–129]. Moreover, different nitrate sources can show distinct δ^{11}B values and different processes control the

isotopic composition of boron and nitrate [120,127]. Moreover, stable isotopes of dissolved nitrates indicate the absence of denitrification, while the coupled use of boron isotopes evidences, even in rural areas, a contribution from septic effluents [130]. Therefore, the combined use of $\delta^{15}N_{NO3}$, $\delta^{18}O_{NO3}$, and $\delta^{11}B$ is an effective approach to the differentiation of complex NO_3^- sources, assuming that these compounds co-migrate in many environments [7,120,121]. In natural waters, the boron isotopic composition is controlled by the aquifer matrix; the anthropogenic source may be a variable of $\delta^{11}B$ [130]. For example, detergents obtained from evaporites, manure, fertilizers, and organic wastes have high concentrations of boron and distinct $\delta^{11}B$ values [122,128,130–134].

Likewise, there are many effective multi-isotopic toolboxes for identifying the flowpath and the contaminant source of nitrate. In particular, we discuss hydrograph separation using the oxygen and hydrogen isotopes of water in combination with the nitrogen and oxygen isotopes of nitrate to understand the relative contributions of precipitation and groundwater to stream water. While transformation processes of nitrogen compounds can change the isotopic composition of nitrate due to the various redox processes in the environment, the use of the stable water isotopes of the H_2O itself can be used to interpret the multiple hydrological and hydrochemical processes for the movement of nitrate contaminants. Therefore, this study will assist in understanding the groundwater flowpaths as well as tracking the sources of nitrate contamination using the stable isotope analysis in combination with nitrate and water. This suggests that source and process information relating to groundwater and nitrates should be made part of the decision-making process in order to better understand and effectively manage the hydrological and nitrogen cycles.

Author Contributions: H.J. was responsible for the implementation of the reference collection, processing and writing of the manuscript. D.-C.K. provided constructive comments and funding. Y.S.K. and S.-W.J. provided constructive comments for this manuscript. J.L. was responsible for the designing and analyzing of the work. All authors have read and agreed to the published version of the manuscript.

References

1. Modica, E.; Buxton, H.T.; Plummer, L.N. Evaluating the source and residence times of groundwater seepage to streams, New Jersey Coastal Plain. *Water Resour. Res.* **1998**, *34*, 2797–2810. [CrossRef]
2. Kaushal, S.S.; Groffman, P.M.; Brand, L.E.; Elliott, E.M.; Shields, C.A.; Kendall, C. Tracking Nonpoint Source Nitrogen Pollution in Human-Impacted Watersheds. *Environ. Sci. Technol.* **2011**, *45*, 8225–8232. [CrossRef] [PubMed]
3. Kendall, C.; Campbell, D.H.; Burns, D.A.; Shanley, J.B.; Silva, S.R.; Chang, C.C.Y. Tracing sources of nitrate in snowmelt runoff using the oxygen and nitrogen isotopic compositions of nitrate. In *Biogeochemistry of Seasonally Snow-Covered Catchments*; Tonnessen, K., Williams, M., Tranter, M., Eds.; IAHS Publication: Boulder, CO, USA, 1995; pp. 339–347.
4. Alimi, H.; Ertel, T.; Schug, B. Fingerprinting of hydrocarbon fuel contaminants: Literature review. *Environ. Forensics* **2003**, *4*, 25–38. [CrossRef]
5. McGuire, K.; McDonnell, J.J. Stable isotope tracers in watershed hydrology. In *Stable Isotopes in Ecology and Environmental Science*, 2st ed.; Michener, R., Lajtha, K., Eds.; Wiley/Blackwell: Malden, MA, USA, 2007; pp. 334–540.
6. Clark, I.D.; Fritz, P. *Environmental Isotopes in Hydrogeology*, 2st ed.; CRC Press: New York, NY, USA, 1997; pp. 13–168.
7. Xue, D.; Botte, J.; De Baets, B.; Accoe, F.; Nestler, A.; Taylor, P.; Van Cleemput, O.; Berglund, M.; Boeckx, P. Present limitations and future prospects of stable isotope methods for nitrate source identification in surface and groundwater. *Water Res.* **2009**, *43*, 1159–1170. [CrossRef]

8. Craig, H. Isotopic Variations in Meteoric Waters. *Science* **1961**, *133*, 1702–1703. [CrossRef]

9. Heaton, T.H.E. Isotopic studies of nitrogen pollution in the hydrosphere and atmosphere: A review. *Chem. Geol. (Isot. Geosci. Sect.)* **1986**, *59*, 87–102. [CrossRef]

10. Smith, V.H.; Tilman, G.D.; Nekola, J.C. Eutrophication: Impacts of excess nutrient inputs on freshwater, marine, and terrestrial ecosystems. *Environ. Pollut.* **1999**, *100*, 179–196. [CrossRef]

11. Liu, C.Q.; Li, S.L.; Lang, Y.C.; Xiao, H.Y. Using δ^{15}N- and δ^{18}O-Values to Identify Nitrate Sources in Karst Ground Water, Guiyang, Southwest China. *Environ. Sci. Technol.* **2006**, *40*, 6928–6933. [CrossRef]

12. Campbell, D.H.; Kendall, C.; Chang, C.C.Y.; Silva, S.R. Pathways for nitrate release from an alpine watershed: Determination using d^{15}N and d^{18}O. *Water Resour. Res.* **2002**, *38*, 1052. [CrossRef]

13. Buttle, J.M.; Sami, K. Recharge processes during snowmelt: An isotopic and hydrometric investigation. *Hydrol. Process.* **1990**, *4*, 343–360. [CrossRef]

14. Wels, C.; Cornett, R.J.; Lazerte, B.D. Hydrograph separation: A comparison of geochemical and isotopic tracers. *J. Hydrol.* **1991**, *122*, 253–274. [CrossRef]

15. Taylor, S.; Feng, X.; Williams, M.; McNamara, J. How isotopic fractionation of snowmelt affects hydrograph separation. *Hydrol. Process.* **2002**, *16*, 3683–3690. [CrossRef]

16. Kim, H.; Cho, S.H.; Lee, D.; Jung, Y.Y.; Kim, Y.H.; Koh, D.C.; Lee, J. Influence of pre-event water on streamflow in a granitic watershed using hydrograph separation. *Environ. Earth Sci.* **2017**, *76*, 82. [CrossRef]

17. Böttcher, J.; Strebel, O.; Voerkelius, S.; Schmidt, H.L. Using isotope fractionation of nitrate-nitrogen and nitrate-oxygen for evaluation of microbial denitrification in a sandy aquifer. *J. Hydrol.* **1990**, *114*, 413–424. [CrossRef]

18. Durka, W.; Schulze, E.D.; Gebauer, G.; Voerkeliust, S. Effects of forest decline on uptake and leaching of deposited nitrate determined from ^{15}N and ^{18}O measurements. *Nature* **1994**, *372*, 765–767. [CrossRef]

19. Sklash, M.G.; Farvorden, R.N. The role of groundwater in storm runoff. *J. Hydrol.* **1979**, *43*, 45–65. [CrossRef]

20. Ladouche, B.; Probst, A.; Viville, D.; Idir, S.; Baqué, D.; Loubet, M.; Probst, J.; Bariac, T. Hydrograph separation using isotopic, chemical and hydrological approaches (Strengbach Catchment, France). *J. Hydrol.* **2001**, *242*, 255–274. [CrossRef]

21. Pu, T.; He, Y.; Zhu, G.; Zhang, N.; Du, J.; Wang, C. Characteristics of water stable isotopes and hydrograph separation in Baishui catchment during the wet season in Mt. Yulong region, south western China. *Hydrol. Process.* **2013**, *27*, 3641–3648. [CrossRef]

22. Dahlke, H.E.; Lyon, S.W.; Jansson, P.; Karlin, T.; Rosqvist, G. Isotopic investigation of runoff generation in a glacierized catchment in northern Sweden. *Hydrol. Process.* **2014**, *28*, 11383–11398. [CrossRef]

23. Li, Z.; Feng, Q.; Jianguo, L.; Yanhui, P.; Tingting, W.; Liu, L.; Guo, X.; Gao, Y.; Jia, B.; Guo, R. Environmental significance and hydrochemical processes at a cold alpine basin in the Qilian Mountains. *Environ. Earth Sci.* **2015**, *73*, 4043–4052. [CrossRef]

24. Rahman, K.; Besacier-Monbertrand, A.L.; Castella, E.; Lods-Crozet, B.; Ilg, C.; Beguin, O. Quantification of the daily dynamics of streamflow components in a small alpine watershed in Switzerland using end member mixing analysis. *Environ. Earth Sci.* **2015**, *74*, 4927–4937. [CrossRef]

25. Semenov, M.Y.; Zimnik, E.A. A three-component hydrograph separation based on relationship between organic and inorganic component concentrations: A case study in Eastern Siberia, Russia. *Environ. Earth Sci.* **2015**, *73*, 611–620. [CrossRef]

26. Lee, J.; Lee, H.J.; Ham, J.Y.; Kim, H. Chemical separation of the discharge generated by artificial rain-on-snow experiments in a snowpack. *J. Geol. Soc. Korea* **2016**, *52*, 113–120. [CrossRef]

27. Unnikrishna, P.V.; McDonnell, J.J.; Kendall, C. Isotope variations in a Sierra Nevada snowpack and their relation to meltwater. *J. Hydrol.* **2002**, *260*, 38–57. [CrossRef]

28. Laudon, H.; Hemond, H.F.; Krouse, R.; Bishop, K.H. Oxygen 18 fractionation during snowmelt: Implications for spring flood hydrograph separation. *Water Resour. Res.* **2002**, *38*, 1258. [CrossRef]

29. Worden, J.; Noone, D.; Bowman, K. Importance of rain evaporation and conti-nental convection in the tropical water cycle. *Nature* **2007**, *445*, 528–532. [CrossRef] [PubMed]

30. Yuan, F.; Miyamoto, S. Characteristics of oxygen-18 and deuterium compositionin waters from the Pecos River in America Southwest. *Chem. Geol.* **2008**, *255*, 220–230. [CrossRef]

31. Lee, J.; Feng, X.; Faiia, A.M.; Posmentier, E.S.; Kirchner, J.W.; Osterhuber, R.; Taylor, S. Isotopic evolution of a seasonal snowcover and its melt by isotopic exchange between liquid water and ice. *Chem. Geol.* **2010**, *270*, 126–134. [CrossRef]

32. Dincer, T.; Payne, B.R.; Florkowski, T.; Marthinec, J.; Tongiorgi, E. Snowmelt runoff from measurements of tritium and oxygen-18. *Water Resour. Res.* **1970**, *6*, 110–124. [CrossRef]

33. Taylor, S.; Feng, X.; Kirchner, J.W.; Osterhuber, R.; Klaue, B.; Renshaw, C.E. Isotopic evolution of a seasonal snowpack and its melt. *Water Resour. Res.* **2001**, *37*, 759–769. [CrossRef]

34. Phillips, D.L.; Gregg, J.W. Source partitioning using stable isotopes: Coping with too many sources. *Oecologia* **2003**, *136*, 261–269. [CrossRef] [PubMed]

35. Benstead, J.P.; March, J.G.; Fry, B.; Ewel, K.C.; Pringle, C.M. Testing isosource: Stable isotope analysis of a tropical fishery with diverse organic matter sources. *Ecology* **2006**, *87*, 326–333. [CrossRef]

36. Meng, Z.; Yang, Y.; Qin, Z.; Huang, L. Evaluating Temporal and Spatial Variation in Nitrogen Sources along the Lower Reach of Fenhe River (Shanxi Province, China) Using Stable Isotope and Hydrochemical Tracers. *Water* **2018**, *10*, 231. [CrossRef]

37. Genereux, D. Quantifying uncertainty in tracer-based hydrograph separation. *Water Resour. Res.* **1998**, *34*, 915–919. [CrossRef]

38. Lee, J.; Koh, D.C.; Choo, M.K. Influences of Fractionation of Stable Isotopic Composition of Rain and Snowmelt on Isotopic Hydrograph Separation. *J. Korean Earth Sci. Soc.* **2014**, *35*, 97–103. [CrossRef]

39. Hoefs, J. *Stable Isotope Geochemistry*, 4th ed.; Springer: Berlin, Germany, 1997.

40. Coplen, T.B.; Herczeg, A.L.; Barnes, C. Isotope engineering: Using stable isotopes of the water molecule to solve practical problems. In *Environmental Tracers in Subsurface Hydrology*; Cook, P.G., Herczeg, A.L., Eds.; Kluwer Academic Publishers: Boston, MA, USA, 2000.

41. Ingraham, N.L. Isotopic variation in precipitation. In *Isotope Tracers in Catchment Hydrology*; Kendall, C., McDonnell, J.J., Eds.; Elsevier: Amsterdam, The Netherlands, 1998; pp. 87–118.

42. Gat, J.R. Oxygen and Hydrogen Isotopes in the Hydrologic Cycle. *Annu. Rev. Earth Planet. Sci.* **1996**, *24*, 225–262. [CrossRef]

43. McGuire, K.; McDonnell, J.J. Stable isotope tracers in watershed hydrology. In *Stable Isotopes in Ecology and Environmental Science*, 2st ed.; Michener, R., Lajtha, K., Eds.; Wiley/Blackwell: Malden, MA, USA, 2007; pp. 334–540.

44. Ingraham, N.L.; Zukosky, K.; Kreamer, D.K. Application of Stable Isotopes to Identify Problems in Large-Scale Water Transfer in Grand Canyon National Park. *Environ. Sci. Technol.* **2001**, *35*, 1299–1302. [CrossRef]

45. Friedman, I. Deuterium content of natural waters and other substances. *Geochim. Cosmochim. Acta* **1953**, *4*, 89–103. [CrossRef]

46. Dansgaard, W. Stable isotopes in precipitation. *Tellus* **1964**, *16*, 436–468. [CrossRef]

47. Blasch, K.W.; Bryson, J.R. Distinguishing Sources of Ground Water Recharge by Using δ^2H and δ^{18}O. *Groundwater* **2007**, *45*, 294–308. [CrossRef]

48. Merlivat, L.; Jouzel, J. Global climatic interpretation of the deuterium–oxygen 18 relationship for precipitation. *J. Geophys. Res.* **1979**, *84*, 5029–5033. [CrossRef]

49. Johnsen, S.J.; Dansgaard, W.; White, J.W.C. The origin of Arctic precipitation under present and glacier conditions. *Tellus* **1989**, *41*, 452–468. [CrossRef]

50. Feng, X.; Faiia, A.M.; Posmentier, E.S. Seasonality of isotopes in precipitation: A global perspective. *J. Geophys. Res.* **2009**, *114*, D08116. [CrossRef]

51. Koeniger, P.; Hubbart, J.A.; Link, T.; Marshall, J.D. Isotopic variation of snow cover and streamflow in response to changes in canopy structure in a snow-dominated mountain catchment. *Hydrol. Process.* **2008**, *22*, 557–566. [CrossRef]

52. Lundquist, J.D.; Cayan, D.R. Seasonal and spatial patterns in diurnal cycles in streamflow in the western united states. *J. Hydrometeorol.* **2002**, *3*, 591–603. [CrossRef]

53. Cooper, L.W. Isotopic fractionation in snow cover. In *Isotope Tracers in Catchment Hydrology*; Kendall, C., McDonnell, J.J., Eds.; Elsevier: Amsterdam, The Netherlands, 1998; pp. 119–136.

54. Lee, J.; Feng, X.; Posmentier, E.S.; Faiia, A.M.; Taylor, S. Stable isotopic exchange rate constant between snow and liquid water. *Chem. Geol.* **2009**, *260*, 57–62. [CrossRef]

55. Lee, J. A review on stable isotopic variations of a seasonal snowpack and meltwater. *J. Geol. Soc. Korea* **2014**, *50*, 671–679. [CrossRef]

56. Moser, H.; Stichler, W. Use of environmental isotope methods as a reconnaissance tool in groundwater exploration near San Antonio de Pichincha, Ecuador. *Water Resour. Res.* **1975**, *11*, 501–505. [CrossRef]

57.   Talyor, S.; Feng, X.; Kirchner, J.W.; Osterhuber, R.; Klaue, B.; Renshaw, C.E. Isotopic evolution of a seasonal snowpack and its melt. *Water Resour. Res.* **2001**, *37*, 759–769. [CrossRef]

58.   Sommerfield, R.A.; Judy, C.; Friedman, I. Isotopic changes during the formation of depth hoar in experimental snowpacks. In *Stable Isotope Geochemistry: A Tribute to Sam Epstein*; Taylor, H.P., O'Neil, J.R., Kaplan, I.R., Eds.; The Geochemical Society: San Antonio, TX, USA, 1991; pp. 205–210.

59.   Friedman, I.; Benson, C.; Gleason, J. Isotopic changes during snow metamorphism. In *Stable Isotope Geochemistry: A Tribute to Sam Epstein*; Taylor, H.P., O'Neil, J.R., Kaplan, I.R., Eds.; The Geochemical Society: San Antonio, TX, USA, 1991; pp. 211–221.

60.   Rodhe, A. Spring flood: Meltwater or groundwater? *Nord. Hydrol.* **1981**, *12*, 21–30. [CrossRef]

61.   Craig, H.; Gordon, L.I. Deuterium and oxygen-18 variations in the ocean and the marine atmosphere. In *Proceedings of the Conference on Stable Isotopes in Oceanographic Studies and Paleotemperatures. Spoleto, Italy*; Tongiorgi, E., Ed.; Consiglio nazionale delle richerche, Laboratorio de geologia nucleare: Pisa, Italy, 1965; pp. 9–130.

62.   Mast, M.A.; Kendall, C.; Campbell, D.H.; Clow, D.W.; Back, J. Determination of hydrologic pathways in an alpine-subalpine basin using isotopic and chemical tracers. In *Biogeochemistry of Seasonally Snow Covered Catchments*; IAHS Publ. 228; Tonnessen, K., Williams, M., Trantner, M., Eds.; IAHS Publication: Boulder, CO, USA, 1995; pp. 263–270.

63.   Kendall, C.; Coldwell, E.A. Fundamentals of Isotope Geochemistry. In *Isotope Tracers in Catchment Hydrology*; Kendall, C., McDonnell, J.J., Eds.; Elsevier: Amsterdam, The Netherlands, 1998; pp. 51–86.

64.   Jung, Y.Y.; Koh, D.C.; Ko, K.S.; Lee, J. Applications of Isotope Ratio Infrared Spectroscopy (IRIS) to Analysis of Stable Isotopic Compositions of Liquid Water. *Econ. Environ. Geol.* **2013**, *46*, 495–508. [CrossRef]

65.   Bigeleisen, J.; Perlman, M.J.; Prosser, H. Conversion of hydrogenic materials for hydrogen to isotopic analysis. *Anal. Chem.* **1952**, *24*, 1356–1357. [CrossRef]

66.   Epstein, S.; Mayada, T.K. Variations of O-18 content of waters from natural sources. *Geochim. Cosmochim. Ac.* **1953**, *4*, 213–224. [CrossRef]

67.   Horita, J. Hydrogen isotope analysis of natural waters using an H_2-water equilibration method: A special implication to brines. *Chem. Geol.* **1988**, *72*, 89–94. [CrossRef]

68.   Gehre, M.; Höfling, R.; Kowski, P.; Strauch, G. Sample preparation device for quantitative hydrogen isotope analysis using chromium metal. *Anal. Chem.* **1996**, *68*, 4414–4417. [CrossRef]

69.   Coplen, T.B.; Wildman, J.D.; Chen, J. Improvements in the gaseous hydrogen-water equilibration technique for hydrogen isotope-ratio analysis. *Anal. Chem.* **1991**, *63*, 910–912. [CrossRef]

70.   Socki, R.A.; Romanek, C.S.; Gibson, E.K. Online technique for measuring stable oxygen and hydrogen isotopes from microliter quantities of water. *Anal. Chem.* **1999**, *71*, 2250–2253. [CrossRef]

71.   Kerstel, E. *Handbook of Stable Isotope Analytical Techniques*, 1st ed.; Elsevier Science: Amsterdam, The Netherlands, 2004; pp. 759–787.

72.   Berden, G.; Peeters, R.; Meijer, G. Cavity ringdown spectroscopy: Exerimental schemes and applications. *Int. Rev. Phys. Chem.* **2000**, *19*, 565–607. [CrossRef]

73.   Wassenaar, L.I.; Hendry, M.J.; Chostner, V.L.; Lis, G.P. High resolution pore water $\delta^2 H$ and $\delta^{18}O$ measurements by H_2O(liquid)-H_2O(vapor) equilibration laser spectroscopy. *Environ. Sci. Technol.* **2008**, *42*, 9262–9267. [CrossRef]

74.   Berman, E.S.F.; Gupta, M.; Gabrielli, C.; Garland, T.; McDonnell, J.J. High-frequency field deployable isotope analyzer for hydrological applications. *Water Resour. Res.* **2009**, *45*, W10201. [CrossRef]

75.   Gupta, P.; Noone, D.; Galewsky, J.; Sweeney, C.; Vaughn, B.H. Demonstration of high-precision continuous measurements of water vapor isotopologues in laboratory and remote field deployments using wavelength-scanned cavity ring-down spectroscopy (WS-CRDS) technology. *Rapid Commun. Mass Spectrom.* **2009**, *23*, 2534–2542. [CrossRef] [PubMed]

76.   Hendry, M.J.; Wassenaar, L.I. Inferring heterogeneity in aquitards using high-resolution δD and $\delta^{18}O$ profiles. *Ground Water* **2009**, *47*, 639–645. [CrossRef] [PubMed]

77.   Penna, D.; Stenni, B.; Sanda, M.; Wrede, S.; Bogaard, T.A.; Gobbi, A.; Borga, M.; Fischer, B.M.C.; Bonazza, M.; Charova, Z. On the reproducibility and repeatability of laser absorption spectroscopy measurements for $\delta^2 H$ and $\delta^{18}O$ isotopic analysis. *Hydrol. Earth Syst. Sci. Discuss.* **2010**, *14*, 1551–1566. [CrossRef]

78.   Brand, W.A.; Geilmann, H.; Crosson, E.R.; Rella, C.W. Cavity ring-down spectroscopy versus hightemperature conversion isotope ratio mass spectrometry: A case study on δ^2H and δ^{18}O of pure water samples and alcohol/water mixture. *Rapid Commun. Mass Spectrom.* **2009**, *23*, 1879–1884. [CrossRef]

79.   Kendall, C. Tracing nitrogen sources and cycling in catchments. In *Isotope Tracers in Catchment Hydrology*; Kendall, C., McDonnell, J.J., Eds.; Elsevier: Amsterdam, The Netherlands, 1998; pp. 519–576.

80.   Silva, S.; Kendall, C.; Wilkison, D.; Ziegler, A.; Chang, C.C.; Avanzino, R. A new method for collection of nitrate from fresh water and the analysis of nitrogen and oxygen isotope ratios. *J. Hydrol.* **2000**, *228*, 22–36. [CrossRef]

81.   Chang, C.C.Y.; Langston, J.; Riggs, M.; Campbell, D.H.; Silva, S.R.; Kendall, C. Amethod for nitrate collection for δ^{15}N and δ^{18}O analysis from waters with low nitrate concentrations. *Can. J. Fish. Aquat. Sci.* **1999**, *56*, 1856–1864. [CrossRef]

82.   Wassenaar, L.I. Evaluation of the origin and fate of nitrate in the Abbotsford Aquifer using the isotopes of ^{15}N and ^{18}O in NO_3^-. *Appl. Geochem.* **1995**, *10*, 391–405. [CrossRef]

83.   Sigman, D.M.; Casciotti, K.L.; Andreani, M.; Barford, C.; Galanter, M.; Böhlke, J.K. A Bacterial Method for the Nitrogen Isotopic Analysis of Nitrate in Seawater and Freshwater. *Anal. Chem.* **2001**, *73*, 4145–4153. [CrossRef]

84.   Casciotti, K.L.; Sigman, D.M.; Galanter Hastings, M.; Böhlke, J.K.; Hilkert, A. Measurement of the Oxygen Isotopic Composition of Nitrate in Seawater and Freshwater Using the Denitrifier Method. *Anal. Chem.* **2002**, *74*, 4905–4912. [CrossRef]

85.   McIlvin, M.R.; Altabet, M.A. Chemical Conversion of Nitrate and Nitrite to Nitrous Oxide for Nitrogen and Oxygen Isotopic Analysis in Freshwater and Seawater. *Anal. Chem.* **2005**, *77*, 5589–5595. [CrossRef]

86.   Wassenaar, L.I.; Douence, C.; Altabet, M.; Aggarwal, P. N and O isotope (δ^{15}N$_\alpha$, δ^{15}N$_\beta$, δ^{18}O, δ^{17}O) analyses of dissolved NO_3^- and NO_2^- by the Cd-azide reduction method and N_2O laser spectrometry. *Rapid Commun. Mass Spectrom* **2018**, *32*, 184–194. [CrossRef] [PubMed]

87.   Soto, D.X.; Koehler, G.; Wassenaar, L.I.; Hobson, K.A. Spatio-temporal variation of nitrate sources to Lake Winnipeg using N and O isotope (δ^{15}N, δ^{18}O) analyses. *Sci. Total Environ.* **2019**, *647*, 486–493. [CrossRef] [PubMed]

88.   Liu, X.Y.; Koba, K.; Koyama, L.A.; Hobbie, S.E.; Weiss, M.S.; Inagaki, Y.; Shaver, G.R.; Giblin, A.E.; Hobara, S.; Nadelhoffer, K.J. Nitrate is an important nitrogen source for Arctic tundra plants. *Proc. Natl. Acad. Sci. USA* **2018**, *115*, 3398–3403. [CrossRef] [PubMed]

89.   Hoering, T. The isotopic composition of the ammonia and the nitrate ion in rain *Geochim. Cosmochim. Ac.* **1957**, *12*, 97–102. [CrossRef]

90.   Hübner, H.; Fritz, P.; Fontes, J.-C. *Handbook of Environmental Isotope Geochemistry: The Terrestrial Environment*; Elsevier: Amsterdam, The Netherlands, 1986; Volume 2, pp. 361–425.

91.   Kreitler, C.W. *Determining the Source of Nitrate in Ground Water by Nitrogen Isotope Studies*; Report 83; Bureau of Economics and Geology, University of Texas: Austin, TX, USA, 1975; p. 57.

92.   Kreitler, C.W. Nitrogen-isotope ratio studies or soil and ground-water nitrate from alluvial fan aquifers in Texas. *J. Hydrol.* **1979**, *42*, 147–170. [CrossRef]

93.   Burns, D.A.; Kendall, C. Analysis of δ^{15}N and δ^{18}O to differentiate NO_3^- sources in runoff at two watersheds in the Catskill Mountains of New York. *Water Resour. Res.* **2002**, *38*, WR000292. [CrossRef]

94.   Pardo, L.H.; Kendall, C.; Pett-Ridge, J.; Chang, C.C.Y. Evaluating the source of streamwater nitrate using δ^{15}N and δ^{18}O in nitrate in two watersheds in New Hampshire, USA. *Hydrol Process.* **2004**, *18*, 2699–2712. [CrossRef]

95.   Savard, M.M.; Somers, G.; Smirnoff, A.; Paradis, D.; van Bochove, E.; Liao, S. Nitrate isotopes unveil distinct seasonal N-sources and the critical role of crop residues in groundwater contamination. *J. Hydrol.* **2010**, *381*, 134–141. [CrossRef]

96.   Kendall, C.; Elliott, E.M.; Wankel, S.D. Tracing anthropogenic inputs of nitrogen to ecosystems. In *Stable Isotopes in Ecology and Environmental Science*, 2st ed.; Michener, R., Lajtha, K., Eds.; Wiley/Blackwell: Malden, MA, USA, 2007; pp. 375–449.

97.   Andersson, K.K.; Hooper, A.B. $O_2$and H_2O and each the source of one O in NO_2 produced from NH_3 by *Nitrosomonas*: ^{15}N evidence. *FEBS Lett.* **1983**, *164*, 236–240. [CrossRef]

98.   Kumar, S.; Nicholas, D.J.D.; Williams, E.H. Definitive ^{15}N NMR evidence that water serves as a source of 'O' during nitrite oxidation by *Nitrobacter agilis*. *FEBS Lett.* **1983**, *152*, 71–74. [CrossRef]

99. Hollocher, T.C. Source of the oxygen atoms of nitrate in the oxidation of nitrite by *Nitrobacter agilis*: Evidence against a P–O–N anhydride mechanism in oxidative phosphorylation. *Arch. Biochem. Biophys.* **1984**, *233*, 721–727. [CrossRef]

100. Voerkelius, S. Isotopendiskriminierungen bei der Nitrifikation und Denitrifikation: Grundlagen und Anwendungen der Herkunfts-Zuordnung von Nitrat und Disickstoffmonoxid. Ph.D. Thesis, Technische University at Munchen, München, Germany, 1990.

101. Zhang, Y.; Shi, P.; Song, J.; Li, Q. Application of Nitrogen and Oxygen Isotopes for Source and Fate Identification of Nitrate Pollution in Surface Water: A Review. *Appl. Sci.* **2019**, *9*, 18. [CrossRef]

102. Amberger, A.; Schmidt, H.L. Naturliche Isotopen-gehalte von nitrat als indikatoren fur dessen herkunft. *Geochim. Cosmochim. Acta* **1987**, *51*, 2699–2705. [CrossRef]

103. Voerkelius, S.; Schmidt, H.L. Natural oxygen and nitrogen isotope abundance of compounds involved in denitrification: Mitteilungen der Deut. *Bodenkundlichen Gesselschaft* **1990**, *60*, 364–366.

104. Burns, D.A.; Boyer, E.W.; Elliott, E.M.; Kendall, C. Sources and Transformations of Nitrate from Streams Draining Varying Land Uses: Evidence from Dual Isotope Analysis. *J. Environ. Qual.* **2009**, *38*, 1149–1159. [CrossRef]

105. Jeen, S.W.; Lee, H.; Kim, R.H.; Jeong, H.Y. A Review on Nitrate Source Identification using Isotope Analysis. *J. Soil Groundw. Environ.* **2017**, *22*, 1–12.

106. Zak, D.R.; Groffman, P.M.; Pregitzer, K.S.; Christensen, S.; Tiedje, J.M. The vernal dam: Plant-microbe competition for nitrogen in northern hardwood forests. *Ecology* **1990**, *71*, 651–656. [CrossRef]

107. Bottomley, D.J.; Craig, D.; Johnston, L.M. Oxygen-18 studies of snowmelt runoff in a small Precambrian shield watershed: Implications for streamwater acidification in acid-sensitive terrain. *J. Hydrol.* **1986**, *88*, 21–234. [CrossRef]

108. McHale, M.R.; McDonnell, J.J.; Mitchell, M.J.; Cirmo, C.P. A field based study of soil- and groundwater nitrate release in an Adirondack forested watershed. *Water Resour. Res.* **2002**, *38*, 1029–1038. [CrossRef]

109. Piatek, K.B.; Mitchell, M.; Silva, S.R.; Kendall, C. Sources of Nitrate in Snowmelt Discharge: Evidence from Water Chemistry and Stable Isotopes of Nitrate. *Water Air Soil Pollut.* **2005**, *165*, 13–35. [CrossRef]

110. Schleppi, P.; Hagedorn, F.; Providoli, I. Nitrate leaching from a mountain forest ecosystem with Gleysols subjected to experimentally increased N. deposition. *Water Air Soil Pollut.* **2004**, *4*, 453–467. [CrossRef]

111. Ohte, N.; Sebestyen, S.D.; Shanley, J.B.; Doctor, D.H.; Kendall, C.; Wankel, S.D.; Boyer, E.W. Tracing sources of nitrate in snowmelt runoff using a high-resolution isotopic technique. *Geophys. Res.* **2004**, *31*, L21506. [CrossRef]

112. Barnes, R.T.; Raymond, P.A.; Casciotti, K.L. Dual isotope analyses indicate efficient processing of atmospheric nitrate by forested watersheds in the northeastern U.S. *Biogeochemistry* **2008**, *90*, 15–27. [CrossRef]

113. Spoelstra, J.; Schiff, S.L.; Elgood, R.J.; Semkin, R.G.; Jeffries, D.S. Tracing the sources of exported nitrate in the Turkey Lakes Watershed using $^{15}N/^{14}N$ and $^{18}O/^{16}O$ isotopic ratios. *Ecosystems* **2001**, *4*, 536–544. [CrossRef]

114. Hales, H.C.; Ross, D.S.; Lini, A. Isotopic signature of nitrate in two contrasting watersheds of Brush Brook, Vermont, USA. *Biogeochemistry* **2007**, *84*, 51–66. [CrossRef]

115. Buda, A.R.; DeWalle, D.R. Dynamics of stream nitrate sources and flow pathways during stormflows on urban, forest and agricultural watersheds in central Pennsylvania, USA. *Hydrol. Process.* **2009**, *23*, 3305–3392. [CrossRef]

116. Wexler, S.K.; Goodalea, C.L.; McGuire, K.J.; Bailey, S.W.; Groffman, P.M. Isotopic signals of summer denitrification in a northern hardwood forested catchment. *Proc. Natl. Acad. Sci. USA* **2014**, *111*, 16413–16418. [CrossRef]

117. Divers, M.A.; Elliott, E.M.; Bain, D.J. Quantification of Nitrate Sources to an Urban Stream Using Dual Nitrate Isotopes. *Environ. Sci. Technol.* **2014**, *48*, 10580–10587. [CrossRef]

118. Klaus, J.; McDonnell, J.J.; Jackson, C.R.; Griffiths, N.A. Where does streamwater come from in low-relief forested watersheds? A dual-isotope approach. *Hydrol. Earth Syst. Sci.* **2015**, *19*, 125–135. [CrossRef]

119. Griffiths, N.A.; Jackson, C.R.; McDonnell, J.J.; Klaus, J.; Du, E.; Bitew, M.M. Dual nitrate isotopes clarify the role of biological processing and hydrologic flowpaths on nitrogen cycling in subtropical low-gradient watersheds. *J. Geophys. Res. Biogeosci.* **2016**, *121*, 422–437. [CrossRef]

120. Seiler, R.L. Combined use of ^{15}N and ^{18}O of nitrate and ^{11}B to evaluate nitrate contamination in groundwater. *Appl. Geochem.* **2005**, *20*, 1626–1636. [CrossRef]

121. Widory, D.; Kloppmann, W.; Chery, L.; Bonnin, J.; Rochdi, H.; Guinamant, J. Nitrate in groundwater: An isotopic multi-tracer approach. *J. Contam. Hydrol.* **2004**, *72*, 165–188. [CrossRef] [PubMed]

122. Widory, D.; Petelet-Giraud, E.; Negrel, P.; Ladouche, B. Tracking the sources of nitrates in groundwater using coupled nitrogen and boron isotopes: A synthesis. *Environ. Sci. Technol.* **2005**, *39*, 539–548. [CrossRef] [PubMed]

123. Saccon, P.; Leis, A.; Marca, A.; Kaiser, J.; Campisi, L.; Bottcher, M.E.; Savarino, J.; Escher, P.; Eisenhauer, A.; Erbland, J. Multi-isotope approach for the identification and characterization of nitrate pollution sources in the Marano lagoon (Italy) and parts of its catchment area. *Appl. Geochem.* **2013**, *34*, 75–89. [CrossRef]

124. Puig, R.; Soler, A.; Widory, D.; Mas-Pla, J.; Domènech, C.; Otero, N. Characterizing sources and natural attenuation of nitrate contamination in the Baix Ter aquifer (NE Spain, using a multi-isotope approach). *Sci. Total Environ.* **2017**, *580*, 518–532. [CrossRef]

125. Martinelli, G.; Dadomo, A.; De Luca, D.A.; Mazzola, M.; Lasagna, M.; Pennisi, M.; Pilla, G.; Sacchi, E.; Saccon, P. Nitrate sources, accumulation and reduction in groundwater from Northern Italy: Insights provided by a nitrate and boron isotopic database. *Appl. Geochem.* **2018**, *91*, 23–35. [CrossRef]

126. Vitòria, L.; Otero, N.; Soler, A.; Canals, A. Fertilizer characterization: Isotopic data (N, S, O, C, and Sr). *Environ. Sci. Technol.* **2004**, *38*, 3254–3262.

127. Nestler, A.; Berglund, M.; Accoe, F.; Duta, S.; Xue, D.; Boeckx, P.; Taylor, P. Isotopes for improved management of nitrate pollution in aqueous resources: Review of surface water field studies. *Environ. Sci. Pollut. Res.* **2011**, *18*, 519–533. [CrossRef]

128. Komor, S.C. Boron content and isotopic composition of hog manure, selected fertilizer, and water in Minnesota. *J. Environ. Qual.* **1997**, *26*, 1212–1222. [CrossRef]

129. Leenhouts, J.M.; Bassett, R.L.; Maddock Iii, T. Utilization of intrinsic boron isotopes as Co-migrating tracers for identifying potential nitrate contamination sources. *Ground Water* **1998**, *36*, 240–250. [CrossRef]

130. Sacchi, E.; Acutis, M.; Bartoli, M.; Brenna, S.; Delconte, C.A.; Laini, A.; Pennisi, M. Origin and fate of nitrates in groundwater from the central Po plain: Insights from isotopic investigations. *Appl. Geochem.* **2013**, *34*, 164–180. [CrossRef]

131. Vengosh, A.; Heumann, K.G.; Juraske, S.; Kasher, R. Boron isotope application for tracing sources of contamination in groundwater. *Environ. Sci. Technol.* **1994**, *28*, 1968–1974. [CrossRef]

132. Eisenhut, S.; Heumann, K.G.; Vengosh, A. Determination of boron isotopic variations in aquatic systems with negative thermal ionization mass spectrometry as a tracer for anthropogenic influences. *Fresenius' J. Anal. Chem.* **1996**, *354*, 903–909. [CrossRef] [PubMed]

133. Barth, S. Application of boron isotopes for tracing sources of anthropogenic contamination in groundwater. *Water Res.* **1998**, *32*, 685–690. [CrossRef]

134. Barth, S.R. Boron isotopic compositions of near-surface fluids: A tracer for identification of natural and anthropogenic contaminant sources. *Water Air Soil Pollut.* **2000**, *124*, 49–60. [CrossRef]